

Properties of contrails from aircraft with modern engines and alternative fuels

Dissertation zur Erlangung des Grades
„Doktor der Naturwissenschaften“

am Fachbereich Physik, Mathematik und Informatik
der Johannes Gutenberg-Universität
in Mainz

Raphael Satoru Märkl
geb. in München
Mainz, den 28. November 2024

-
1. Gutachten: Prof. Dr. Christiane Voigt
 2. Gutachten: Prof. Dr. Stephan Borrmann

Datum der mündlichen Prüfung: 31. Januar 2025

Angefertigt am Deutschen Zentrum für Luft- und Raumfahrt e.V.
Institut für Physik der Atmosphäre, Oberpfaffenhofen

Abstract

Contrails forming from aircraft engine emissions can evolve into long-living contrail cirrus when ambient conditions are ice-supersaturated. Their net effective radiative forcing has been shown to directly correlate with the number of contrail ice particles under similar atmospheric conditions. As one of the largest single contributors to radiative forcing from aviation, contrail ice crystal reduction is a major lever in mitigating aviation's climate impact.

In the course of this work, the first ever in-situ measurements of contrails and emissions from the combustion of 100 % sustainable aviation fuel (SAF) were conducted within the framework of the ECLIF3 project. In a series of research flights, the DLR-operated Dassault Falcon served as the measurement platform in chasing the emission source aircraft Airbus A350-941 equipped with Rolls-Royce Trent XWB-84 engines and burning 100 % HEFA-SPK (Hydro-processed Esters and Fatty Acids - Synthetic Paraffinic Kerosene) fuel. The resulting contrails were probed by in-situ instrumentation for the detection of contrail ice particles, (non-)volatile particulate matter, trace gases, and water vapor onboard the DLR Falcon. Hereby, a 56 % reduction of ice particle numbers per mass of burned fuel compared to the combustion of reference Jet A-1 fuel was measured at cruise conditions. Simultaneously, a lower reduction of 35 % for soot particle numbers was detected, thereby suggesting less ice activation by the low aromatics and low sulfur HEFA-SPK fuel. Beyond CO₂ footprint reductions of 100 % non-fossil origin SAF, global climate model simulations based on these experimental results estimate an additional decrease in contrail radiative forcing. Modern aircraft engines employing lean-burn combustion technology are expected to reduce soot emissions into the low-soot regime of $10^{11} - 10^{14}$ particles per kg of burned fuel. The implications for the formation of contrails by the use of SAF and modern lean-burn aircraft engines are investigated in the German-French NEOFUELS-VOLCAN (VOL avec Carburants Alternatifs Nouveaux) project. In the course of two research campaign phases, an Airbus A319neo and an Airbus A321neo equipped with lean-burn CFM LEAP-1A engines served as emission source aircraft which were chased by the DLR Falcon measurement platform. Despite large soot particle emission reductions for the lean-burn combustion mode compared to the forced rich-burn mode in non-contrail forming conditions, a high number of contrail ice particles is measured in both combustion modes. At the same time, a correlation of ice particle numbers is found to total aerosol particle (nonvolatile + volatile) emissions. SAF use in lean-burn combustors showed a decrease in contrail ice particle numbers compared to conventional jet fuel combustion in the lean-burn and forced rich-burn combustion modes.

The results of this work will contribute to the assessment of benefits and caveats of the use of sustainable aviation fuels and modern combustion technologies regarding contrail formation and properties as well as the associated contrail climate forcing. This will help industry and policy-makers to make informed decisions on the development of future technologies and the regulation of non-CO₂ effects currently burdened by large uncertainties.

Contents

1	Introduction	1
2	Background	9
2.1	Contrails	9
2.1.1	Contrail formation	9
2.1.2	Condensation nuclei	11
2.1.3	Stages of contrail development	13
2.1.4	Contrail microphysical and optical properties	14
2.1.5	Climate impact of contrails and contrail cirrus	16
2.1.6	Experiments on contrail mitigation	18
2.2	Sustainable aviation fuels	20
2.2.1	Chemical properties	21
2.2.2	Production pathways	22
2.2.3	Climate impact of SAFs	23
2.2.4	SAF outlook	25
2.3	Modern combustion technologies	26
3	Instrumentation	31
3.1	Light-particle interaction	31
3.1.1	Scattering cross section	32
3.1.2	Spherical and aspherical particles	33
3.2	Cloud Aerosol Spectrometer: Scattering instruments	39
3.2.1	Measuring principle	39
3.2.2	Calibration	44
3.2.3	Size distribution	51
3.2.4	Comparison of CAS-DPOL and CAPS-DPOL instruments	52
3.3	Aerosol measurement systems	57
3.4	Trace gas and water vapor measurements	60
3.5	Research aircraft DLR Falcon and contrail chasing	63
4	Data analysis	65
4.1	Contrail ages, microphysical parameters and T_{SA}	65
4.2	Definition of plumes/contrails	68
4.3	Corrections and uncertainties	70
4.4	Emission indices (EI) and apparent ice emission index (AEI)	74
4.5	Uncertainties of AEI	76
4.6	Filtering of AEI	77
4.7	Structuring of data by domains	78
5	Contrails from 100 % SAF in rich-burn engines	89
5.1	The ECLIF3 campaign	89
5.1.1	Ambient conditions of the ECLIF3 campaign	93
5.2	Influence of 100 % HEFA on AEI	94
5.2.1	Measurement of contrails at cruise altitude	94

5.2.2	Impact of 100% HEFA-SPK on the apparent ice number emission index AEI	98
5.2.3	Impact of fuel composition and engine type on the apparent ice number emission index AEI	101
5.2.4	Variability in ice particle size distribution	105
5.2.5	Conclusions and outlook	108
6	Contrails from lean-burn engines	111
6.1	Measurements of lean-burn emissions and contrails	111
6.1.1	VOLCAN1	112
6.1.2	VOLCAN2	114
6.2	Influence of combustion modes on AEI	118
6.2.1	Contrail formation on emitted aerosols	119
6.2.2	Statistical analysis of combustion mode effects on contrail ice particles . . .	122
6.2.3	Size distributions depending on combustion mode	125
6.3	Fuel effects at different conditions	129
6.4	Contrail dependence on ambient conditions	134
6.5	Warm contrails	138
6.6	Ice nucleation in lean-burn engines	142
6.6.1	Engine comparison	142
6.6.2	Types of contrail ice condensation nuclei	145
6.7	Ice processing	147
6.7.1	Effects of ice formation on aerosol numbers	147
6.7.2	Influence of ambient conditions on processing	152
7	Summary and Outlook	155
7.1	Summary	155
7.2	Outlook	161
7.2.1	Open questions and future contrail campaigns	161
7.2.2	Future developments in instrumentation and data analysis	164
7.2.3	Technology outlook	166
	Contributions to this study	169
	Appendix A: Additional VOLCAN information	171
	Appendix B: Sensitivity of T_{SA} and ΔT_{SA} on ambient conditions	183
	Appendix C: Additional information for instrumentation	185
	Bibliography	191
	Abbreviations and Symbols	213
	List of Figures	219
	List of Tables	221
	Acknowledgments	223
	Curriculum Vitae	225

CHAPTER 1

Introduction

When birds fly, they leave behind turbulent air, happy ornithologists and perhaps some not so happy pedestrians unlucky enough to intercept their droppings. Jet airplanes delight the souls of aviation enthusiasts and are indispensable in today's transport of goods, tourists and business travelers. Unfortunately, they leave behind some more unwelcome byproducts such as very loud noise, greenhouse gases, and condensation trails, also known as contrails. It is well established and scientific consensus that anthropogenic greenhouse gases like CO₂ are responsible for increasingly warmer average global temperatures (Eyring et al., 2021), resulting in more frequent and intense adverse weather, rising sea levels, reduced biodiversity, higher uncertainty in food production, and many other effects endangering Earth's ecosystem and humankind's living conditions (Urban, 2015; Fox-Kemper et al., 2021; Seneviratne et al., 2021; Mirón et al., 2023).

Of all anthropogenic climate warming contributions, the aviation sector is responsible for 3 to 4 % (Lee et al., 2021), even though only 11 % of the world's population traveled by air in 2018 (Gössling and Humpe, 2020). This applies when comparing net effective radiative forcing (ERF) (a metric considering the perturbation of a certain influencing factor to Earth's radiation budget including rapid adjustments) from aviation to net anthropogenic ERF. Aviation's climate impact results from different effects with varying shares depending on the type of metric used, the considered time horizon, and the specific emission scenario (Fuglestvedt et al., 2010; Grewe and Dahlmann, 2015). A number of studies (Burkhardt and Kärcher, 2011; Chen and Gettelman, 2013; Schumann and Graf, 2013; Teoh et al., 2024) have quantified aviation's radiative impact contributions with varying values. For example, Lee et al. (2021) estimate the global ERF from aviation at 100.9 mW m⁻². Of those, they attribute only about a third (34.3 mW m⁻²) to CO₂ emissions, while the majority is determined by the non-CO₂ effects from NO_x emissions (17.5 mW m⁻²) and contrail cirrus (57.4 mW m⁻²). In contrast to the long time scales CO₂ remains in the atmosphere, contrails have life times on the scale of hours (Vázquez-Navarro et al., 2015; Lee et al., 2023). This means that a hypothetical elimination of contrail formation would result in a virtually instant zero contrail radiative forcing. The international community has agreed to slow down and ideally stop harmful climate warming, for example within the Paris climate agreement (United Nations, 2015) or the European Green Deal (EASA, 2023). While it is furthermore a high priority to reduce CO₂ emissions, the short-term climate forcing reduction potential of contrails has been recognized and work has been

conducted to assess the implementation of non-CO₂ effects into the European Unions Emissions Trading Scheme (ETS) and the International Civil Aviation Organization (ICAO) led Carbon Offsetting and Reduction Scheme for International Aviation (CORSIA) program on an international level beyond Europe (Niklaß et al., 2020).

Contrails form when hot jet engine exhaust gases (composed mainly of water vapor and CO₂ and small amounts of other gases including SO_x and NO_x (Schumann et al., 1996; Schulte et al., 1997)) are emitted together with aerosol particles (nonvolatile and volatile) into sufficiently cold and moist air (Schumann, 1996). When the ambient temperature lies below the T_{SA}, water vapor first condenses mostly on emitted aerosol particles to liquid droplets, which then rapidly freeze and form contrail ice crystals (Kärcher, 2018). If ambient conditions are ice-supersaturated, i.e., the relative humidity over ice (RH_i) is above 100 %, these contrails can become persistent and develop into long-living contrail cirrus (Minnis et al., 2004; Immler et al., 2008; Vázquez-Navarro et al., 2015).

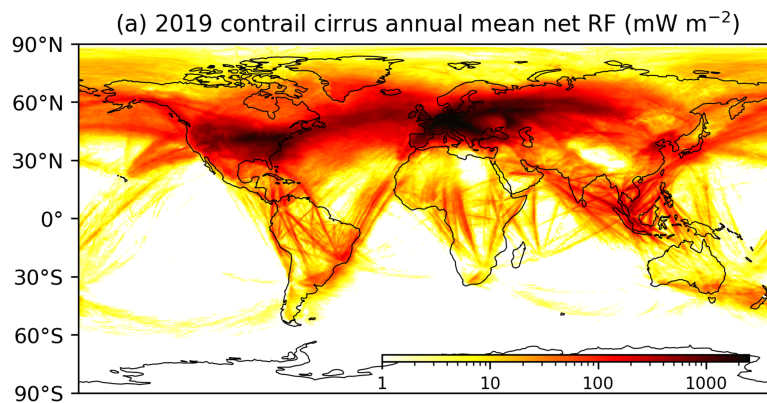


Figure 1.1: Global distribution of annual mean contrail cirrus net radiative forcing of 62.1 mW m^{-2} (range from 34.8 to 74.8 mW m^{-2} based on sensitivity analysis) for the year 2019. Figure and caption information from Teoh et al. (2024), used under CC BY 4.0 (<https://creativecommons.org/licenses/by/4.0/>)

A number of contrail parameters such as ice particle size, concentration, or shape, but also the contrail's surrounding surface and cloud albedo, temperature, or altitude determine if a specific contrail cirrus has a net warming or cooling effect (Meerkötter et al., 1999; Schumann et al., 2012). Most importantly, the level of solar irradiance influences the sign of contrail cirrus radiative forcing. During the day, the reflection of incoming shortwave solar radiation can lead to a cooling effect while absorption and re-emission of longwave radiation from the Earth's surface results in net atmospheric warming during the night (Meerkötter et al., 1999; Schumann et al., 2012; Teoh et al., 2022a). The sign and magnitude of contrail cirrus radiative forcing is characterized by strong regional and temporal variability with an overall global warming net radiative effect as illustrated for the year 2019 in Figure 1.1 from Teoh et al. (2024). The study also found that only 14 % of the contrail cirrus formed in 2019 had a net warming effect and that 80 % of the annual contrail energy forcing could be attributed to only 2 % of performed flights (Teoh et al., 2024). This shows that

some contrails are more climatically relevant than others, offering an opportunity to target these specifically in mitigation measures (Burkhardt et al., 2018).

Aviation climate mitigation options

The simplest and most effective way to avoid all emissions, non-CO₂ effects, and other adverse environmental and health effects from aviation would be to avoid flying or to fly less. While some individuals may choose this path, it is unlikely to become established in an impactful manner on a global scale in the current economic landscape (Gössling et al., 2019). The aviation sector has grown rapidly by many measures in the past (Lee et al., 2021) and passenger numbers are projected to approximately double by the year 2040 compared to 2019 (IATA, 2023). Market-based measures such as the EU's ETS and ICAO's CORSIA are levers that can generate a financial incentive to reduce aviation's climate impact (Niklaß et al., 2020; EASA, 2023), possibly creating some variability in aviation growth. However, even in the smallest growth scenarios, a steady increase in passengers is projected until 2050 (Fleming et al., 2022). It therefore seems inevitable that technological solutions will need to complement political measures to reduce aviation's climate impact. Advancements in sustainable aircraft design aim at improving fuel efficiency as well as particle and noise emissions but realization is limited by long technology development and certification cycles (Goobie et al., 2022).

Another solution requiring no modification to the aircraft and targeting contrails specifically is the optimization of flight routes to avoid regions where warming contrails form. As mentioned, only 2 % of all flights cause 80 % of annual contrail energy forcing (Teoh et al., 2024), offering the opportunity to achieve a large mitigation impact by avoiding contrail formation in these flights by rerouting. Recent studies have shown the feasibility and potential of flight rerouting to avoid contrails while also discussing the possible risk of negating the climate benefit of contrail avoidance with higher CO₂ emissions from the additional fuel needed to take the alternative route (Schumann et al., 2011; Teoh et al., 2020a,b; Lee et al., 2023; Sausen et al., 2023; Martin Frias et al., 2024).

Approaches that have the potential to tackle CO₂ emissions and non-CO₂ effects are novel propulsion technologies. Electric propulsion creates no local emissions but faces challenges of low storage energy density and associated high weight so that it is currently only seen as a possible solution mostly for urban and regional traffic (Ying, 2022; Hungerland et al., 2024). Additionally, the CO₂ reduction benefit strongly depends on the source of used electricity.

Hydrogen (H₂) is currently being investigated as fuel for direct combustion or in hybrid-electric propulsion using fuel cells (Llewellyn and Miftakhov, 2022). With this fuel, water (in liquid or gaseous form) is the main emission so that no CO₂ or soot is emitted locally. While some studies expect the lack of soot to reduce contrail formation, this has not been proven experimentally and it is possible that other emitted or ambient particles could act as condensation nuclei instead (Gierens, 2021; Ungeheuer et al., 2022; Bier et al., 2024). The higher water vapor emission index could also lead to contrail forming regions at warmer temperatures, with the potential contrail cover depending strongly on latitude and altitude (Kaufmann et al., 2024). Hydrogen is also only

sustainable if produced from renewable sources and not from fossil fuels as is currently the main source (Nikolaidis and Poullikkas, 2017).

According to Hungerland et al. (2024), the only feasible technology option in the near and mid-term future for reducing the aviation climate impact for mid- and long-haul flights is the use of SAFs. These alternative fuels have a variable CO₂ reduction potential depending on their feedstock and production pathway (ICAO, 2022a). Also, SAF blends up to certain blending ratios (ASTM, 2024b) are currently already approved for use in today's aircraft without the need for modifications to aircraft, thereby making them so-called drop-in fuels, while 100 % SAF use requires additional certification for commercial airliners (EASA, 2023).

Finally, modern lean-burn engine technology such as the Twin Annular Premixing Swirler (TAPS) combustor in the General Electric GEnx engine or the TAPSII combustor for the CFM International LEAP engine have been designed to improve engine efficiency and reduce NO_x emissions (Liu et al., 2017). From engine test stand based measurements, lower nonvolatile particulate matter (nvPM) emissions have been found for the Landing and Take Off Cycle (LTO) cycle as stated in ICAO (2024), so that lower soot emissions at cruise can be expected for the lean-burn combustion mode. Beyond fuel savings and associated CO₂ emission reductions, it has so far not been proven experimentally if a strong soot particle reduction in the lean-burn combustion mode translates to lower contrail ice particles numbers and lower contrail radiative forcing.

Research questions

Recent in-situ campaigns (Moore et al., 2017; Bräuer et al., 2021b; Bräuer et al., 2021a; Voigt et al., 2021) have investigated the influence of SAF blends on particle emission and contrail formation and have found that both can be reduced mostly due to the lower aromatics content compared to conventional jet fuel. Regulations have so far prevented the combustion of 100 % SAF in flight (ASTM, 2024b), so that up until now, the following question had not been answered experimentally:

RQ1 What is the effect of 100 % SAF combustion on particle emissions and contrail formation?

Building upon the past experience and expertise of the DLR Cloud Physics department, in-situ chase flight measurements were conducted with the DLR Falcon equipped with the suite of instrumentation for the measurement of water vapor, trace gases, aerosol particles and contrail ice particles. This instrumentation was either installed in the aircraft cabin and fed by inlets mounted on the fuselage or mounted below the wings as was the case for the two Cloud and Aerosol Spectrometer (CAS) instruments used for the detection of contrail ice particle number concentrations and size distributions. To answer **RQ1**, the DLR Falcon chased an Airbus A350 during the ECLIF3 campaign at typical cruise altitudes under controlled engine parameters. This emission source aircraft burned either a hydrotreated esters and fatty acids (HEFA) type SAF or a conventional reference Jet A-1 fuel in its Trent XWB-84 engines so that emitted soot particle numbers and nucleated ice particle numbers could be compared and differences attributed to fuel properties.

Previous research has showed and assumed soot particles to be the dominant condensation nuclei for contrail formation in the soot-rich regime (Kärcher and Yu, 2009; Wong and Miake-Lye, 2010; Kärcher et al., 2015; Rojo et al., 2015). This is also reflected in the parcel model simulations by Kärcher and Yu (2009) and a nearly linear relationship between soot particles and nucleated contrail ice particles is expected as shown in Figure 1.2 from Kärcher (2018). There, the number of nucleated ice particles for a given number of emitted soot particles is higher for ambient temperatures further below T_{SA} . For conditions closer to T_{SA} , a strong reduction in contrail ice particles is simulated. For the low-soot regime ($< 10^{14} \text{ kg}^{-1}$), the simulations expect a linear anticorrelation between nucleated contrail ice crystal numbers and emitted soot particles for cold conditions well below T_{SA} due to the activation of ultrafine aqueous particles (UAP)s. This low-soot regime is expected from modern lean-burn engine technology but so far, neither particle emissions nor contrail ice particles have been measured in flight in this regime so that the contrail ice particle to soot relationship described in Kärcher (2018) remains unconfirmed experimentally. This therefore raises the second major research question of this work:

RQ2 Can contrail ice particle numbers be reduced by the use of modern lean-burn combustion technologies and if so, how much?

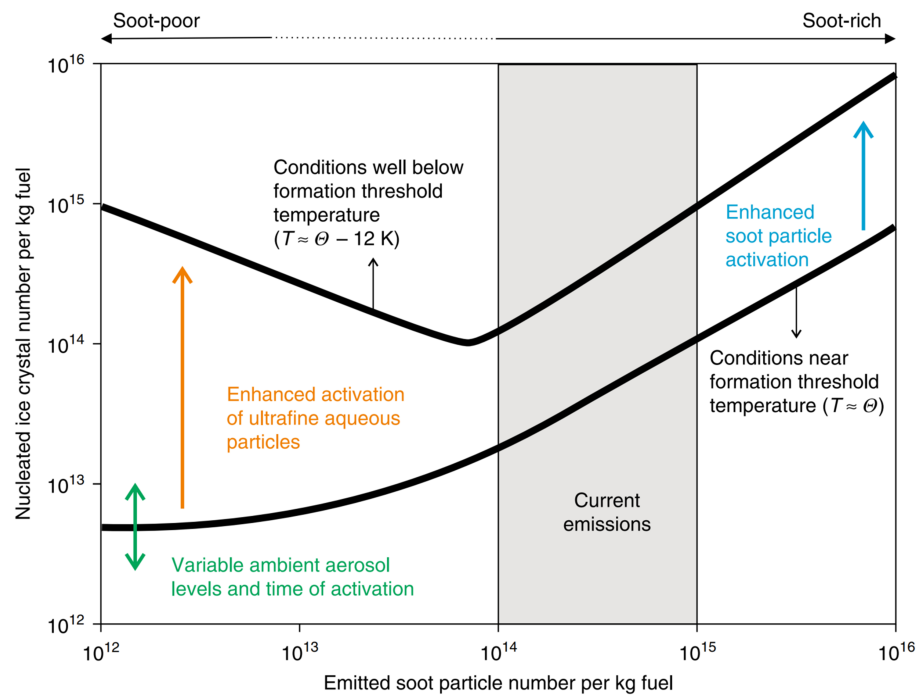


Figure 1.2: Number of nucleated contrail ice crystals per kg of fuel burned as a function of the number of emitted soot particles per kg of fuel burned based on parcel model simulations (Kärcher and Yu, 2009). The lower curve shows the function for conditions close to the contrail formation threshold, while the upper curve is for cold temperatures well below the contrail formation threshold. Figure and caption information from Kärcher (2018), used under CC BY 4.0 (<https://creativecommons.org/licenses/by/4.0/>)

This question was explored in the course of the Neofuels/VOL avec Carburants Alternatifs Nou-

veaux (VOLCAN) campaigns where the DLR Falcon research aircraft chased an Airbus A319neo and A321neo. Both emission source aircraft were equipped with CFM LEAP-1A engines that could be operated either in a lean-burn mode or a forced rich-burn combustion mode at typical cruise conditions. This way, the influence of these two combustion modes on nucleated contrail ice particle numbers in relation to the number of emitted nvPM and total particles (nonvolatile and volatile particles) could be studied from data recorded across a broad range of ambient conditions.

In light of **RQ1**, the question is raised if a fuel effect for 100 % SAF use can also be found for modern lean-burn combustion technologies, especially in the lean-burn combustion mode where soot is not expected to be the dominant nucleating particle. The third research question is thereby formulated:

RQ3 Can contrail ice particle numbers be reduced by the use of SAFs in modern lean-burn combustion technologies in the lean-burn and forced rich-burn combustion mode?

Contrails from several types of 100 % SAF were measured in both combustion modes during the Neofuels/VOLCAN campaigns as well so that the contrail reduction potential using SAF in these types of engines could be quantified.

Structure of the work

This work is structured into seven chapters. After this introduction, a short overview will be given over the scientific and technical background of contrails and contrail cirrus by establishing the prerequisites of contrail formation such as meteorological conditions and types of possible condensation nuclei. The climate impact and current status of knowledge about contrails is then discussed by reviewing current and past literature and research. The technical basics of SAFs and modern combustion technologies will then be presented to lay the groundwork for the later discussed results.

The third chapter will introduce the physical and technical principles of the measurements conducted in this work. The focus will lie on the CAS instruments used for the detection of contrail ice particle number concentrations and sizes and differences between the two used instruments Cloud and Aerosol Spectrometer with Depolarization (CAS-DPOL) and Cloud, Aerosol, and Precipitation Spectrometer with Depolarization (CAPS-DPOL). Measurement techniques for the detection of aerosols, trace gases, water vapor and ambient conditions will be briefly introduced as well.

Chapter 4 will subsequently focus on the processing of measured data to obtain central parameters such as the Apparent Ice Emission Index (AEI). Corrections, uncertainties, and data filtering are discussed and a method of structuring and statistically interpreting data is introduced.

In chapter 5, the results of the Emission and Climate Impact of Alternative Fuels (ECLIF)³ campaign are presented in which for the first time, the influence of 100 % SAF combustion on aerosol particle emissions and contrail formation was investigated. After introducing the flights and fuels of this campaign, AEI from HEFA SAF and reference Jet A-1 combustion are related to their fuel properties

and nvPM emissions. These results are then put into the context of previous measurements of SAF blends. The publication Märkl et al. (2024) was the product of the collaborative ECLIF3 campaign and is reproduced in large parts in this chapter.

The following chapter 6 focuses on measurement results obtained during the VOLCAN campaigns. Using a statistical method to ensure comparability and statistical significance of data across a wide range of conditions, contrail formation and properties in the low-soot regime from lean-burn combustion could be compared to the soot-rich regime in rich-burn combustion. Several fuels including different SAFs were combusted in the course of the campaigns so that their influence on contrail formation in modern lean-burn engines could be studied. These results are then discussed and put into context of previous and current research to aid in interpreting these novel findings.

The central results and findings of the entire work are finally summarized in chapter 7, followed by a discussion of possible future research in contrails from SAF and modern combustion technology.

Publications

Large parts of the following publication have been adapted into this thesis:

Märkl, R. S., C. Voigt, D. Sauer, R. K. Dischl, S. Kaufmann, T. Harlaß, V. Hahn, A. Roiger, C. Weiß-Rehm, U. Burkhardt, U. Schumann, A. Marsing, M. Scheibe, A. Dörnbrack, C. Renard, M. Gauthier, P. Swann, P. Madden, D. Luff, R. Sallinen, T. Schripp, and P. Le Clercq (Mar. 2024). "Powering aircraft with 100% sustainable aviation fuel reduces ice crystals in contrails". In: *Atmospheric Chemistry and Physics* 24.6, pp. 3813–3837. doi: 10.5194/acp-24-3813-2024.

Work conducted during the ECLIF campaign led to co-authorship in the following publications:

Dischl, R., D. Sauer, C. Voigt, T. Harlaß, F. Sakellariou, R. Märkl, U. Schumann, M. Scheibe, S. Kaufmann, A. Roiger, A. Dörnbrack, C. Renard, M. Gauthier, P. Swann, P. Madden, D. Luff, M. Johnson, D. Ahrens, R. Sallinen, T. Schripp, G. Eckel, U. Bauder, P. Le Clercq (Oct. 2024). "Measurements of particle emissions of an A350-941 burning 100 % sustainable aviation fuels in cruise". In: *Atmospheric Chemistry and Physics* 24.19, pp.11255-11273. doi: 10.5194/acp-24-11255-2024.

Harlass, T., R. Dischl, S. Kaufmann, R. Märkl, D. Sauer, M. Scheibe, P. Stock, T. Bräuer, A. Dörnbrack, A. Roiger, H. Schlager, U. Schumann, M. Pühl, T. Schripp, T. Grein, L. Bondorf, C. Renard, M. Gauthier, M. Johnson, D. Luff, P. Madden, P. Swann, D. Ahrens, R. Sallinen, C. Voigt (Oct. 2024). "Measurement report: In-flight and ground-based measurements of nitrogen oxide emissions from latest-generation jet engines and 100% sustainable aviation fuel". In: *Atmospheric Chemistry and Physics* 24.20, pp.11807-11822. doi: 10.5194/acp-24-11807-2024.

The following award was also obtained:

ODAS Award: "The best paper prepared and presented by young scientists" for: Maerkl, R., C. Voigt, D. Sauer, R. Dischl, S. Kaufmann, T. Harlaß, M. Scheibe, A. Marsing, V. Hahn, T. Bräuer, A. Roiger, T. Jurkat-Witschas, A. Dörnbrack, D. Delhayé, I. Ortega, K. Seeliger, C. Renard, J. Moreau, G. Le Chenadec, E. Requena-Esteban, O. Basset (Jun. 2023). "Inflight measurements of contrail ice crystals of Airbus aircraft with lean-burn engine technology", 23rd ONERA – DLR Aerospace Symposium, ODAS 2023 Paris, talk and conference paper (not published).

CHAPTER 2

Background

The research questions formulated in this work relate to the effects of SAF and modern combustion technologies on contrail formation and properties as well as the associated climate impact. This chapter will therefore provide the background necessary to comprehend the discussed results and put them into context. First, the theories behind contrail formation, the life cycle and climate impact will be discussed before an overview of SAF chemical properties, production pathways and their climate impact as well as market projections is given. Finally, the difference between jet engine Rich-Quench-Lean (RQL) combustors and lean-burn combustors is presented, as well as the different operating modes of lean-burn combustors.

2.1 Contrails

2.1.1 Contrail formation

Aircraft jet engines generate thrust by combusting jet fuel, consisting mostly of hydrocarbon molecules in various configurations and several other contaminants such as sulfur. These hydrocarbons are converted to the main exhaust gases H_2O and CO_2 . These are emitted together with other gases such as NO_x , forming mainly from the thermal oxidation of nitrogen from ambient air, SO_x from oxidation of fuel sulfur, and others (Schumann, 2002; Bergthorson and Thomson, 2015; Liu et al., 2017). Incomplete combustion in the engine can lead to the formation of soot particles, which are emitted together with (semi-)volatile aerosols such as chemi-ions (Yu and Turco, 1997; Arnold et al., 1999), UAPs (Kärcher and Yu, 2009; Kärcher, 2018), or emissions not resulting from combustion such as lubrication oil droplets (Fushimi et al., 2019; Ungeheuer et al., 2022; Ponsonby et al., 2024a).

The formation of contrails requires cold and humid conditions that are quantified by the Schmidt-Appleman contrail formation threshold (T_{SA}) (Schmidt, 1940; Appleman, 1953; Schumann, 1996), which is a threshold temperature below which contrail ice particles form.

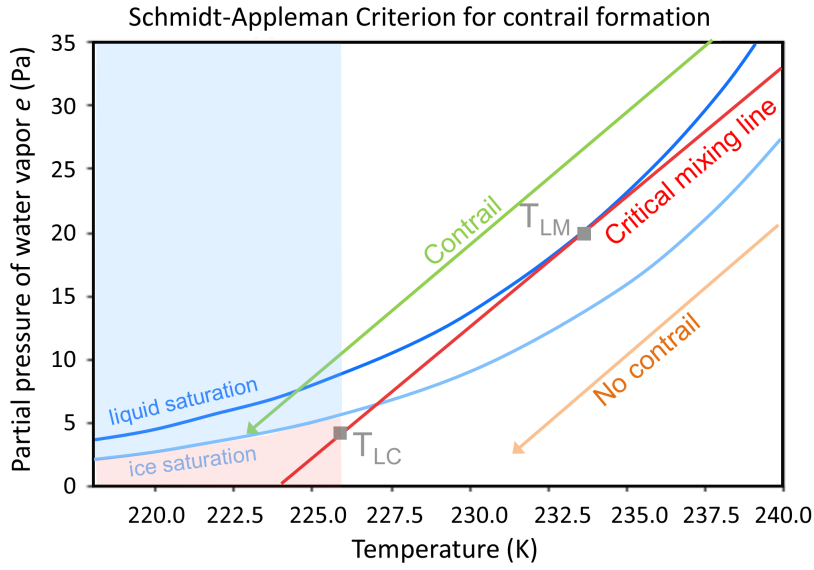


Figure 2.1: Illustration of T_{SA} derivation with curves for saturation vapor pressure above liquid water (dark blue) and saturation vapor pressure above ice (light blue). Linear mixing lines indicate the different scenarios of no contrail formation (orange), the borderline case (red), and contrail formation (green). T_{SA} is T_{LC} for $U < 1$ and T_{LM} for $U = 1$ (Schumann, 1996). The parameter space of contrail formation and ice supersaturation (subsaturation) is shaded in blue (red). Figure and caption information adapted from and based on Dischl et al. (2022), used under CC BY 4.0 (<https://creativecommons.org/licenses/by/4.0/>)

The calculation of T_{SA} is illustrated in Figure 2.1 (Dischl et al., 2022). Aircraft engine exhaust gases and particles are emitted at high temperatures (~ 800 K) (Onissen, 2014) and with high partial pressures of water vapor e due to the low level of dilution directly behind the engine exit. Conditions right after emission would therefore lie far beyond the upper right corner of the figure. These hot emissions mix with ambient air and are diluted and cooled down until ambient conditions are reached. Mixing can be described in the partial pressures of water vapor and temperature space with mixing lines along which the conditions move towards lower partial pressures of water vapor and lower temperatures.

Following the derivation in Schumann (1996), the slope G of mixing lines can be defined as:

$$G = \frac{\Delta e}{\Delta T} = \frac{e_p - e_{amb}}{T_p - T_{amb}} = \frac{EI_{H_2O} c_p p_{amb}}{(M_{H_2O}/M_{air})Q(1 - \eta)} \quad (2.1)$$

where e_p and T_p are the water vapor pressure and temperature of the plume, EI_{H_2O} is the water vapor emission index, c_p is the specific heat capacity at constant pressure, M_{H_2O} and M_{air} are the molar masses of water and dry air, Q is the combustion heat of fuel, and η the engine's propulsion efficiency (Schumann, 1996).

Three examples of mixing lines are shown in Figure 2.1. Contrails are only able to form if these mixing lines intersect with the dark blue curve of saturation vapor pressure above liquid water

(short: liquid saturation curve), which is determined by the Clausius-Clapeyron relation (Rogers and Yau, 1989c). Then, liquid water droplets can form by condensation on emitted or entrained aerosol particles which then rapidly freeze due to cold temperatures below the homogeneous freezing threshold of approximately -40°C (Rogers and Yau, 1989a). The borderline case where this is fulfilled is illustrated by the red critical mixing line in Figure 2.1. All mixing lines above the critical mixing line intersect the liquid saturation curve (e.g. green mixing line). Liquid droplets form even though the ice supersaturation curve is intersected first. This is due to the low requirements of particles to act as condensation nuclei for the relatively unordered arrangement of liquid water molecules compared to the highly ordered crystal structure in ice, which require specific properties of the condensation nucleus (Gierens et al., 2012). The mixing lines end (illustrated by arrow tip) when ambient conditions have been approximately reached. If these ambient conditions are ice-supersaturated, the contrail ice particles can persist and continue to form contrail cirrus. In ice-sub-saturated conditions, formed contrail ice crystals sublime quickly and do not form persistent contrails. If ambient conditions are higher than the Schmidt-Appleman contrail formation threshold temperature T_{LC} (also: T_{SA}), the mixing lines (e.g. orange mixing line) would not intersect the liquid saturation curve and no liquid droplets would form.

In order to calculate T_{LC} , equation 2.1 can be reformulated to relate the threshold temperatures T_{LC} and T_{LM} shown in Figure 2.1 by (Schumann, 1996):

$$T_{LC} = T_{LM} - \frac{e_L(T_{LM}) - U e_L(T_{LC})}{G}, \quad (2.2)$$

where $e_L(T_{LM})$ and $e_L(T_{LC})$ are the saturation vapor pressures over liquid water at temperatures T_{LM} and T_{LC} and U is the relative humidity over liquid water. This equation can be solved numerically or approximated using the equations given in Appendix 2 of Schumann (1996), taking into account the correction implemented in Schumann (2012) following the hint of Ferrone (2011).

2.1.2 Condensation nuclei

When a mixing line intersects with the liquid saturation curve, supersaturation with respect to liquid water is reached and water droplets form. Supersaturation is defined as:

$$s = \frac{e}{e_L} - 1 \quad (2.3)$$

with the vapor pressure e and saturation vapor pressure over liquid water e_L (Wallace and Hobbs, 2006). However, e_L is only valid over a flat surface of water while for contrail formation, the nucleation sites are non-flat aerosol particles. Therefore, a physical effect described by the Kelvin effect and a chemical effect described by Raoult's Law determine the level of supersaturation over an aerosol particle of given size and composition (Wallace and Hobbs, 2006).

Water molecules at curved surfaces are bonded less strongly to each other compared to those

at flat surfaces (Rogers and Yau, 1989b). The molecules therefore require less energy to escape the molecular bonds and transfer to the gas phase, hence the vapor pressure is higher for curved surfaces (smaller radii), which is described by the Kelvin equation (Rogers and Yau, 1989b). Thus, the smaller the radius, the higher the level of supersaturation with respect to a flat surface must be in order to achieve supersaturation with respect to the curved surface.

If another component is dissolved in water and thereby forms a solution, the vapor pressure is influenced as well, which is described by Raoult's Law (Rogers and Yau, 1989b). There, an ideal solution is assumed where solute molecules are present at the liquid surface and thereby reduce the amount of water molecules exposed to the surrounding environment, thus reducing the vapor pressure. Finally, the Köhler theory combines the principles of vapor pressure over a flat surface with the vapor pressure increase for small radii and the vapor pressure reduction from the presence of solutes (Rogers and Yau, 1989b). This way, the saturation vapor pressure for a curved surface (water droplet) including a solute is given.

Many different types of particles are emitted from jet engines but not all are equally suited as condensation nuclei. In the soot-rich regime of ($> 10^{14} \text{ kg}^{-1}$), previous studies have shown that larger soot particles (several tens of nm) act as preferential condensation nuclei (Kärcher and Yu, 2009; Wong and Miake-Lye, 2010; Kärcher et al., 2015; Rojo et al., 2015), even in the presence of smaller (semi-) volatile aerosol. This occurs largely due to the Kelvin effect (Lewellen et al., 2014; Kärcher, 2018) despite low hygroscopicity of soot particles (Kärcher et al., 2015).

Jet fuels however contain varying levels of sulfur, so that soot particles can be coated by sulfate and condensed sulfuric acid after emission (Kärcher, 1998; Kärcher et al., 2015), thereby enhancing their hygroscopicity (Popovicheva et al., 2004; Petzold et al., 2005; Wong and Miake-Lye, 2010; Kärcher et al., 2015). An increased propensity of soot to act as a condensation nucleus with increasing sulfur content is thus predicted by Jones and Miake-Lye, 2023.

In the soot-poor regime ($< 10^{14} \text{ kg}^{-1}$), (semi-)volatile particles can become more relevant and UAPs are predicted to act as condensation nuclei (Kärcher and Yu, 2009; Kärcher, 2018) despite their smaller sizes in the range of 1 to 10 nm (Kärcher et al., 2000; Rojo et al., 2015). Studies by Fushimi et al. (2019), Ungeheuer et al. (2022), and Ponsonby et al. (2024a) mention lubrication oil particles, present in high number concentrations but low overall mass, as further potential contrail ice condensation nuclei, which however is so far unconfirmed experimentally. Near the contrail formation threshold T_{SA} under soot-poor conditions, Kärcher and Yu (2009) predict contrail ice particle numbers to be determined by the number of entrained ambient aerosol particles, which can be compared against observations with the results presented in this work in chapter 6.

2.1.3 Stages of contrail development

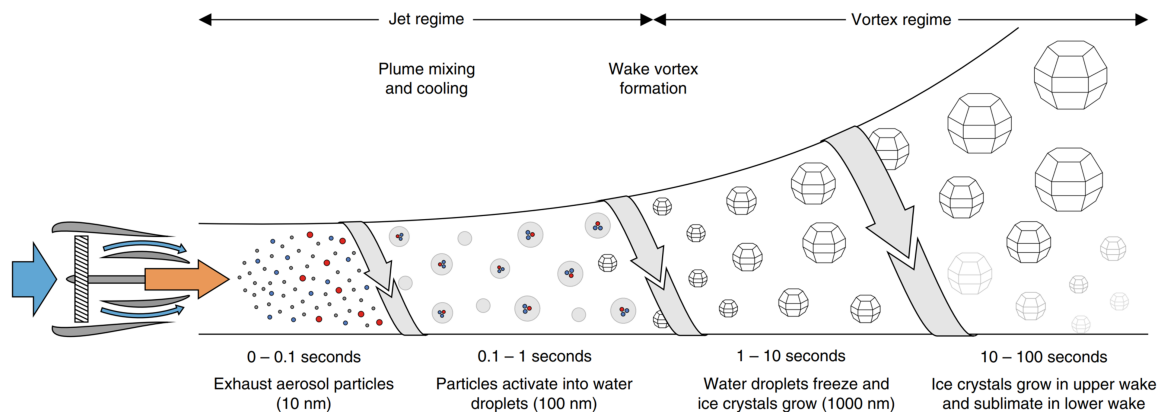


Figure 2.2: Stages of contrail formation, where gaseous combustion products are emitted together with exhaust aerosol particles. The three different particle colors represent soot particles from incomplete combustion, aqueous aerosol particles, and entrained aerosol particles. Under supersaturated conditions with respect to liquid water, these particles are then activated into water droplets and subsequently freeze. Ice crystals then grow and persist if conditions are ice-supersaturated in the upper secondary wake and sublimate in the lower primary wake. Figure from and caption information based on Kärcher (2018), used under CC BY 4.0 (<https://creativecommons.org/licenses/by/4.0/>)

At the left end of Figure 2.2 (Kärcher, 2018) an aircraft jet engine and the multitude of particles and gases emitted is pictured. This hot exhaust first expands behind the engine before it is caught and trapped in the wing tip vortices (Gerz et al., 1998). If ambient conditions are cold and humid enough, inmixing of ambient air into the plume can lead to an activation of aerosol particles into water droplets within the first second of emission, which concludes the so called jet regime (Gerz et al., 1998; Kärcher, 2018). The formed water droplets then rapidly freeze and the resulting ice crystals can grow if ambient conditions are supersaturated with respect to ice. The counter-rotating vortex pair leads to a separation of the vortex into a downward-propagating primary vortex and a secondary wake remaining roughly at emission altitude. The downward propagation of the primary vortex leads to adiabatic warming, thereby reducing relative humidity and increasing the probability of ice particle sublimation (Paoli and Shariff, 2016). This phase is called the vortex regime, which concludes on the order of approximately 100 s with the appearance of instabilities such as the Crow instability (Crow, 1970; Paoli and Shariff, 2016). During the subsequent dissipation regime, the primary vortex and secondary wake begin to break up into turbulence (Gerz et al., 1998; Paoli and Shariff, 2016). When all aircraft-induced motion has dissipated, the diffusion regime begins where atmospheric processes and sedimentation dominate the transport of contrail ice crystals, particles and gases over the course of several hours (Gerz et al., 1998; Paoli and Shariff, 2016). A number of atmospheric processes and parameters such as wind shear, turbulence, radiative effects, horizontal and vertical transport of air masses, ice particle sedimentation, the presence of natural cirrus clouds or other contrails, temperature, relative humidity, etc. finally determine the further contrail life cycle (Unterstrasser and Gierens, 2010b,a; Paoli and Shariff, 2016; Bier et al.,

2017; Schumann and Heymsfield, 2017).

2.1.4 Contrail microphysical and optical properties

Several methods exist to observe microphysical and optical properties of contrails. While remote sensing methods (e.g. satellites and light detection and ranging (LIDAR)) are used to detect large scale effects, in-situ measurements allow small-scale observations of contrail structure and particles. These in-flight experiments involve an emission source aircraft and a chasing research aircraft, making these types of measurements challenging organizationally (managing two aircraft and crews, airspace, schedules, maintenance, operational restrictions, etc.) from an experimental standpoint (assuring comparable operating and ambient conditions, adverse conditions such as turbulence and low visibility, ensuring a statistically significant high quality dataset), and financially (fuel, crew, travel, maintenance, insurance, etc.). Over the years, a large number of remote sensing and in-situ measurements on microphysical properties of contrails have taken place, some of which are highlighted in the following.

The first in-situ observations of contrails are reported by Knollenberg (1972), where an optical-array spectrometer mounted on the National Center for Atmospheric Research (NCAR) Sabreliner aircraft measured contrails and natural cirrus at cruise altitudes. For these experiments, the aged contrails produced by the research aircraft itself were measured and compared to nearby natural cirrus clouds. Knollenberg (1972) found similar particle concentrations and ice water content (IWC) for both types of clouds, albeit limited by the instrument's lower size detection limit of $75 \mu\text{m}$ so that the concentrations are underestimated. During the International Cirrus Experiment performed in 1989, in-situ, LIDAR, and infrared radiometer measurements were employed on several research aircraft to compare natural cirrus and aged contrail cirrus (Gayet et al., 1996). They found that contrail cirrus and natural cirrus form under similar conditions but that contrails have significantly higher particle concentrations.

Microphysical properties of contrails forming behind a Boeing 757 were then probed in 1996 and compared to the properties of wave clouds formed at similar ambient conditions (Baumgardner and Gandrud, 1998). These measurements confirmed significantly higher particle concentrations in the contrails, while liquid water content (LWC) was much higher in the wave clouds due to larger particles (around $10 \mu\text{m}$) compared to the small (around $1 \mu\text{m}$) contrail ice particles (Baumgardner and Gandrud, 1998). They also found that despite these differences in microphysical properties, the backscatter to extinction relationship and hence, radiative properties, were similar for the contrails and wave clouds. This led them to conclude that the particle shapes of both cloud types might be similarly aspherical (Baumgardner and Gandrud, 1998).

Schröder et al. (2000) used data from several airborne experiments performed in 1996 and 1997 to describe the evolution of fresh contrail ice particle size distributions (diameter around $1 \mu\text{m}$) with

age into young cirrus clouds (around 10 μm) as well as a shrinking case for the case of subsaturated conditions with associated evaporation. In these measurements, typical contrail number concentrations of over 100 cm^{-3} and approximately spherical shapes were found (Schröder et al., 2000). However, more recent measurements (Voigt et al., 2011; Gayet et al., 2012) have confirmed a growing level of asphericity of contrail ice particles with age. These measurements were performed during the CONtrail and Cirrus ExpeRimenT (CONCERT) campaign where contrails forming behind a number of commercially operating aircraft were probed by the Deutsches Zentrum für Luft- und Raumfahrt / German Aerospace Center (DLR) Falcon research aircraft (Voigt et al., 2010, 2011). Probability distributions of extinction, optical depth, and IWC are presented in Voigt et al. (2011) from a wide range of measurements so that optical properties of contrails and the implications for radiative forcing could be constrained by these results. In the course of this campaign, Jeßberger et al. (2013) found increasing ice particle number concentration and vertical contrail depth and thereby higher optical depths for higher aircraft weight, while at the same time, particle sizes remained similar. Additionally, Schumann et al. (2013) describe smaller contrail ice particle sizes in the descending primary wake due to particle losses compared to the secondary wake.

Using remote sensing methods, e.g. a ground-based scanning LIDAR (Freudenthaler et al., 1995) or satellite observations (Vázquez-Navarro et al., 2015), the spatial growth of contrails could be determined, which can be used for determining extinction and optical depth of contrails (Bräuer et al., 2021b).

A series of experiments in the 1990's under the name of SULFUR aimed at investigating the influence of fuel sulfur content (FSC) on particle and contrail formation (Schumann et al., 2002). In this context, Busen and Schumann (1995) found no visible difference between contrails from fuels with 2 ppm and 250 ppm sulfur content, however only utilizing visual methods, so that differences on a small scale would likely not be detectable. In the next experiment of the series however, an increased contrail optical thickness was found for high-sulfur fuel compared to low-sulfur fuel using in-situ instrumentation capable of measuring particle number concentrations (Schumann et al., 1996).

During the ML-CIRRUS (Voigt et al., 2017) campaign, aircraft measurements performed by a broad in-situ instrumentation onboard the High Altitude and Long Range Research Aircraft (HALO) were combined with cloud data obtained from satellite observations and ground-based measurements to investigate the microphysical and radiative properties of contrail cirrus and differences to natural cirrus. During the flight campaign, aged contrail cirrus were encountered and showed higher concentrations of smaller ice particles (diameter < 30 μm) compared to natural cirrus despite having grown in similar ambient conditions (Voigt et al., 2017). The smaller ice particle sizes of contrails and contrail cirrus compared to natural cirrus were confirmed by Wang et al. (2023) based on in-situ data obtained during the ML-CIRRUS campaign combined with satellite data of a contrail cirrus outbreak.

By compiling in-situ measurements and remote sensing data from many campaigns and research

projects, Schumann et al. (2017) confirm the described trends in microphysical parameters across a large time range from ages of several seconds to several hours. For example, particle number concentrations decrease from over 10^3 cm^{-3} to below 10^0 cm^{-3} over the course of aging while diameters increase from the order of $1 \mu\text{m}$ to tens of μm (Schumann et al., 2017). The study also describes a continuous increase in contrail width and depth over time while optical extinction decreases (Schumann et al., 2017).

2.1.5 Climate impact of contrails and contrail cirrus

Earth's energy budget is characterized by the interaction of incoming shortwave solar radiation and outgoing radiation, composed of reflected solar radiation and longwave thermal radiation, with Earth's surface and atmosphere (Forster et al., 2021). In an equilibrium state, incoming and outgoing energy flux would balance in the global long-term mean. However, reflection, scattering, absorption, re-emission, phase changes etc. all influence the net energy flux and are determined by surface properties, greenhouse gases and the presence of clouds and aerosols (Wild et al., 2015; Forster et al., 2021). Any change in the energy balance due to a perturbation is described by radiative forcing as the change in energy flux at the top of the atmosphere (TOA) relative to pre-industrial times (usually the year 1750) (Myhre et al., 2013). Clouds play a major role in this energy balance but have different effects depending on the type of cloud. While low-level liquid clouds with high optical thickness mainly reflect incoming shortwave radiation back to space, high altitude ice clouds such as cirrus and contrail cirrus are typically optically thinner and therefore do not reflect as much solar radiation (Kärcher, 2018). Additionally, these colder ice clouds absorb and re-emit more longwave radiation compared to warmer low-level liquid clouds and therefore have a globally averaged net warming effect (Chen et al., 2000; Kärcher, 2018).

Contrail radiative forcing on the local scale however depends on a number of factors. The contrail's optical density and ice crystal microphysical properties have a large influence on the ratio of shortwave radiation reflection and longwave radiation absorption and emission (Meerkötter et al., 1999). The contrail's position and surrounding conditions play a role as well. Radiative properties of the Earth's surface, like the presence of low-level natural clouds, affect the radiation budget by determining the amount of longwave radiation emitted from Earth's surface (Meerkötter et al., 1999; Schumann et al., 2012). The level of incoming solar radiation depending on the time of day, season, and latitude strongly influences the contrail cirrus climate relevance (Meerkötter et al., 1999; Schumann et al., 2012). During the day, the amount of shortwave radiation energy reflected back to space can exceed the amount of longwave energy emitted towards Earth's surface or deposited in the atmosphere, hence resulting in a net cooling effect (Stuber et al., 2006). With decreasing incoming solar radiation, the longwave radiation contribution begins to outweigh shortwave radiation reflection and the radiative forcing becomes positive with a net warming effect (Stuber et al., 2006; Newinger and Burkhardt, 2012). Globally averaged, the warming effect outweighs the

cooling effect but the strong spatial and temporal variation in radiative forcing suggests that not all contrails and contrail cirrus are equally climatically relevant. In fact, according to Teoh et al. (2024), only 14 % of formed contrail cirrus in 2019 resulted in a warming effect while 2 % of flights were responsible for 80 % of annual contrail energy forcing. This circumstance offers the opportunity to target net warming contrails specifically in climate impact mitigation approaches.

Persistent contrails forming in ice-supersaturated regions are the most climatically relevant as they can transform into contrail cirrus and cover large surface areas (Haywood et al., 2009; Vázquez-Navarro et al., 2015). Ice-supersaturated regions and hence, contrail occurrence and persistence, are distributed not only geographically (Bier and Burkhardt, 2019; Dischl et al., 2022; Kaufmann et al., 2024), with more contrails forming at mid latitudes compared to the tropics at typical flight altitudes, but also temporally, as colder conditions in winter are more favorable for ice-supersaturation compared to summer (Gierens et al., 2012).

While radiative forcing aims at quantifying changes in the Earth system energy balance from a specific perturbation, this is not achieved well for all forcing agents (Myhre et al., 2013). This can be improved by including the effects of rapid adjustments to parameters in the troposphere such as atmospheric temperature, water vapor, and clouds, which are taken into account in ERF (Myhre et al., 2013). When comparing time horizons in the Global Warming Potential (GWP) metric as seen in Figure 2.3, it can be seen that the shares of contrail cirrus and NO_x decrease over time while the significance of CO_2 increases due to the long CO_2 residence time and resulting accumulation in the atmosphere (Lee et al., 2021). Even though the share of contrail cirrus contribution decreases with increasing time horizon, it remains a significant portion of the overall GWP, signifying its importance in being addressed by mitigation options, no matter which time horizon is considered. This shows however that the magnitude of climate impact depends on the used metric and time horizon (Megill et al., 2024).

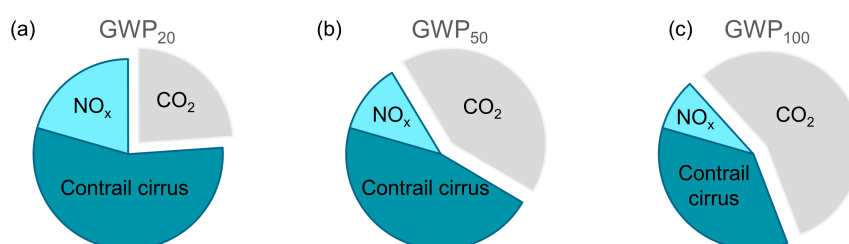


Figure 2.3: Comparison of CO_2 emission, NO_x emission, and contrail cirrus contributions (not considering other contributions) to GWP for the time horizons (a) 20 years, (b) 50 years, and (c), 100 years, based on CO_2 -equivalent emissions in Tg CO_2 per year for 2018. Data from Lee et al. (2021).

The prediction of contrail and contrail cirrus occurrence, life cycles, radiative forcing, and energy forcing has been researched extensively and implemented in the prediction tool Contrail Cirrus Prediction Tool (CoCiP) (Schumann et al., 2011; Schumann, 2012; Schumann et al., 2017) to predict the occurrence and properties of contrails for a given time and place (Teoh et al., 2022a, 2024).

Further, global climate models (GCMs) like the ECHAM5 model (Roeckner et al., 2003) coupled to the contrail cirrus module CCMod can be used to gain insight into contrail cirrus cover and associated radiative forcing utilizing historic traffic data and assumptions on the number of emitted soot particles acting as condensation nuclei (Bock and Burkhardt, 2016; Bier et al., 2017; Burkhardt et al., 2018; Bock and Burkhardt, 2019).

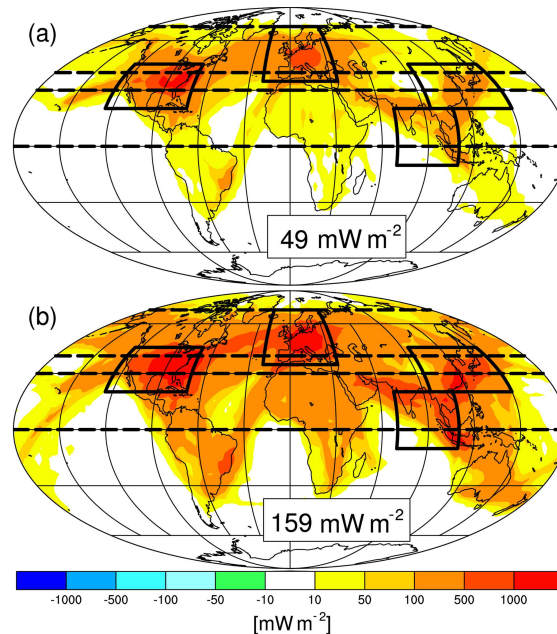


Figure 2.4: Contrail cirrus radiative forcing for the years (a) 2006 and (b) 2050 based on ECHAM5-CCMod calculations performed by Bock and Burkhardt (2019). Figure and caption information adapted (cropped) from and based on Bock and Burkhardt (2019), used under CC BY 4.0 (<https://creativecommons.org/licenses/by/4.0/>)

For example, the ECHAM5-CCMod calculations performed by Bock and Burkhardt (2019) shown in Figure 2.4 illustrate the increase in radiative forcing from 49 mW m^{-2} in the year 2006 to 159 mW m^{-2} in 2050. This comparison accounts for increased air traffic but does not consider changing background climate or the increases in fuel and propulsion efficiency as well as the use of SAF. This case is also discussed in Bock and Burkhardt (2019) and reduces the contrail cirrus radiative forcing increase to 137 mW m^{-2} for the year 2050. Beyond model calculations, the possibility to reduce contrail radiative forcing with the use of SAFs has however also been investigated experimentally.

2.1.6 Experiments on contrail mitigation

Significant research progress has been made in the measurement of particle emissions and contrail formation from the use of alternative jet fuels in ground-based and in-flight measurements. Ground-based measurements investigating the influence of alternative jet fuels include those of

Lobo et al. (2011) where a Fischer-Tropsch based fuel and a 50 % blend based thereon was combusted in a CFM56-7B jet engine and resulted in a 34 % reduction in nvPM numbers for the blend and 52 % reduction for the pure Fischer-Tropsch fuel. Similarly, Timko et al. (2010a) found significant reductions in SO_2 and soot particle emissions for a Fischer-Tropsch based fuel compared to JP-8 jet fuel as well as intermediate reductions for a 50 % blend. In both studies, the highest reduction potential was found for lower engine thrusts (Timko et al., 2010a; Lobo et al., 2011). Further studies (Beyersdorf et al., 2014; Brem et al., 2015; Schripp et al., 2018) confirm the influence of fuel composition and especially aromatics and sulfur content and the resulting particulate and gaseous jet engine emissions from ground-based measurements.

In-flight measurements investigating the influence of alternative fuel blends on particle emissions and contrail formation include the ACCESS campaign where the NASA DC-8 source aircraft, equipped with CFM56-2-C1 engines, was chased by the NASA HU-25 Falcon research aircraft in order to quantify particulate matter emissions from conventional Jet A fuel and a 50 % biofuel blend at cruise altitudes (Moore et al., 2017). In those measurements, Moore et al. (2017) found a reduction in total particles as well as 48 % lower nvPM numbers for the 50 % blend as well as a shift towards smaller particles. Contrail and particle emissions from alternative fuel blends were further investigated during the ECLIF1 (in 2015) and ECLIF2/NDMAX (in 2018) campaigns in a cooperation between DLR and NASA (Voigt et al., 2021; Bräuer et al., 2021a; Bräuer et al., 2021b), where the DLR Falcon research aircraft served as the chasing research aircraft behind the DLR Advanced Technology Research Aircraft (ATRA) Airbus A320 aircraft during ECLIF1, while the ATRA was chased by the NASA DC-8 research aircraft during ECLIF2/NDMAX. Results from both campaigns can be found in Voigt et al. (2021) from which two plots are shown in Figure 2.5.

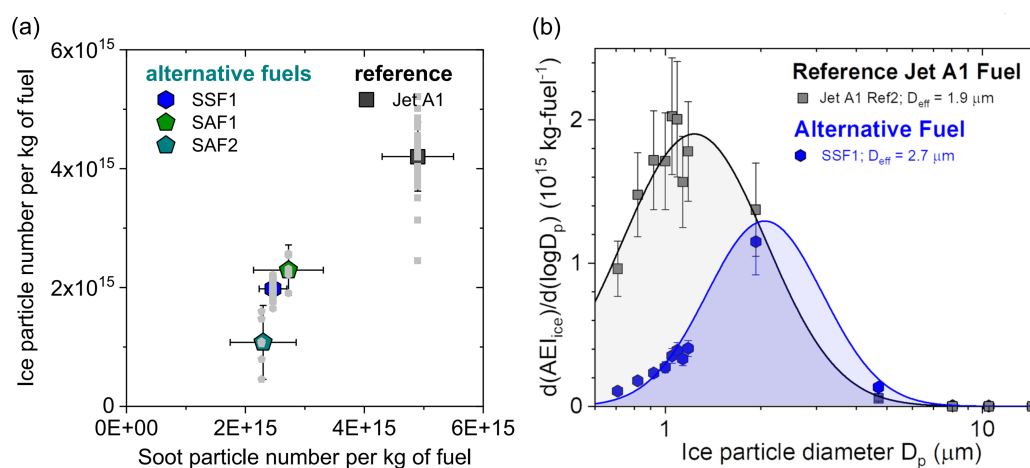


Figure 2.5: (a) AEI vs soot Emission Index (EI) for fuels investigated during the ECLIF1 and ECLIF2/ND-MAX campaigns and (b) AEI size distribution of reference Jet A-1 (Ref2) and Fischer-Tropsch based semisynthetic jet fuel blend (SSF1) of the ECLIF1 campaign. Figures and caption information adapted (two figures combined) from (Voigt et al., 2021), used under CC BY 4.0 (<https://creativecommons.org/licenses/by/4.0/>).

There, an approximate halving of ice particle and soot emissions can be found for the SAF blends compared to the reference Jet A-1 fuel due to their reduced aromatic content and higher hydrogen content. This also translates to an increased ice particle size for the semisynthetic fuel blend compared to the reference Jet A-1 fuel shown in panel (b). Voigt et al. (2021) argue that this increase in ice particle size is due to less nucleating particles competing for water vapor so that more water vapor is available for the particles to grow. Also in the course of the ECLIF1 campaign, Kleine et al. (2018) found contrail ice particle formation to be largely soot-controlled and that ice particle losses are dominated by sublimation in vertical profiles with respect to the emission altitude.

Several in-situ campaigns have been conducted to investigate the influence of different fuel compositions and alternative fuel blends on particle emissions and contrail formation. While reductions in nvPM emissions for modern lean-burn engines can be measured during the LTO (ICAO, 2024), the particle emission reduction potential at cruise levels remains unconfirmed experimentally for systematic measurements under controlled engine parameters. This gap will be closed in the course of this work together with first measurements of contrail ice particle numbers from the combustion of 100 % SAF.

2.2 Sustainable aviation fuels

Virtually all jet aircraft in commercial, private and military use today are fueled by liquid kerosene-based aviation fuels. Jet A-1 is the most common jet fuel used almost worldwide, while Jet A is the most common civil jet fuel in the US (Chevron Products Company, 2007). The high climate impact (CO₂ and non-CO₂ effects) from fossil aviation fuel use motivates a transition towards SAF, which are chemically similar to conventional jet fuels but are derived from non-fossil origin. New SAF technology pathways have been developed and approved in recent years (Csonka et al., 2022) and SAF use is projected to increase strongly in the near future (EASA, 2019; U.S. Department of Energy et al., 2022). This chapter will give an overview over the different production pathways, chemical properties and climate impact of alternative jet fuels, commonly referred to as SAFs.

Currently, SAF blends up to 50 % blending ratio with conventional jet fuel and minimum volumetric share of 8 % aromatics (ASTM, 2024b) are certified for all commonly used jet engines and aircraft, depending on the SAF type. This justifies it to be regarded as "drop-in" fuel, meaning that it can be fueled and used without any modifications to the aircraft or current fueling infrastructure. 100 % SAF use currently requires special approval as the elastomer seals used in the aircraft's fuel system require aromatics typically found in fossil-based fuels to swell and retain their ability to properly act as seals (Liu et al., 2013; Pechstein and Zschocke, 2017). Regulation bodies however are currently working on enabling 100 % SAF use in the near future (EASA, 2023). As hydrogen fuel is at a lower technology readiness level, with broad commercial availability projected not before 2035 (Llewellyn and Miftakhov, 2022), it can not be considered a drop-in fuel or current solution.

2.2.1 Chemical properties

Jet fuels in general are a complex mixture of thousands of chemical compounds, mostly hydrocarbons, which differ for each production process and feedstock (Pechstein and Zschocke, 2017). This is the case for SAFs as well as for conventional jet fuel where different crude oil origins are associated with different chemical compositions (e.g. sulfur content) (EIA, 2012). Generally, jet fuels are required to fulfill certain chemical (e.g. sulfur content, aromatics content) and physical properties (e.g. flash point, viscosity, freezing point), defined for Jet A-1 and Jet A in American Society for Testing and Materials (ASTM) Standard D1655 (ASTM, 2024a).

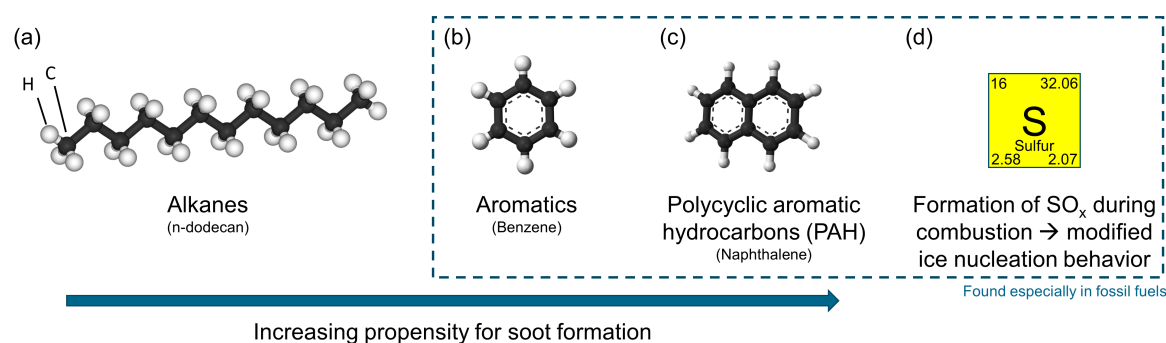


Figure 2.6: Schematic of the main constituents of jet fuel (a) alkanes consisting of mostly linear chains of hydrogen and carbon atoms and typical chain lengths of 10 to 18 C atoms (Pechstein and Zschocke, 2017), (b) aromatics consisting of cyclic hydrocarbon compounds with conjugated electron bonds, (c) polycyclic aromatic hydrocarbons consisting of several aromatic rings, and (d) sulfur which forms SO_x during combustion. Note: Images in (a), (b), and (c) based on graphics created by Benjah-bmm27 (username) (2006, 2007, 2009), released into the public domain via Wikimedia Commons.

The main jet fuel constituents (~ 50 v%) are alkanes (Pechstein and Zschocke, 2017). These are saturated hydrocarbons which can occur either in linear form (n-alkanes) or branched (iso-alkanes) and an example of a linear alkane molecule is shown in Figure 2.6 (a). Alkanes have the highest hydrogen-to-carbon ratio with highest heat of combustion of all hydrocarbons and relatively little energy is required to break the chemical bonds, leading to a "clean" (i.e. complete) combustion (Pechstein and Zschocke, 2017). Around 30 % of the volumetric share of conventional jet fuel is made up of saturated cyclo-alkanes with a lower hydrogen-to-carbon ratio and lower heating value compared to alkanes (Pechstein and Zschocke, 2017). Compounds with even lower hydrogen-to-carbon ratio and a volumetric share of up to 25 % (ASTM, 2024a) are the ring-shaped aromatics, made up of conjugated electron bonds (alternating single and double electron bonds). Benzene is the simplest aromatic and shown in Figure 2.6 (b). The increased energy required to break the chemical bonds is associated with less complete combustion and soot formation (Cain et al., 2013; Brem et al., 2015; Schripp et al., 2022). The soot formation propensity is even larger for polycyclic aromatic hydrocarbons (PAH) like naphthalene (Chin and Lefebvre, 1990) shown in panel (c), which can make up to 3 v% of the fuel (ASTM, 2024a).

The non-hydrocarbon constituent in jet fuel most relevant for particulate emissions and contrail formation is sulfur, which is represented in Figure 2.6 (d). Sulfur can occur either in pure form

or bound chemically (Pechstein and Zschocke, 2017) and its content is limited to 0.3 w% (ASTM, 2024a). During combustion, sulfur oxides (SO_x) can form, which then interact with other combustion products such as soot and have been shown to alter the behavior of contrail ice nucleation (Petzold et al., 1997; Schumann et al., 2002; Jones and Miake-Lye, 2023). Note that the exact volumetric shares of alkanes, cyclo-alkanes, and aromatics of conventional jet fuels differ strongly between different fuels depending on crude oil origin and production process. As for conventional fossil jet fuel, SAFs can have a wide range of chemical compositions depending on used feedstock and production process.

2.2.2 Production pathways

There are several pathways in the production of SAF with different feedstocks, production processes, and resulting fuel types (ICAO, 2018; EASA, 2023). While the Fischer-Tropsch process can use fossil origin feedstock as well as biogenic feedstock, the other processes described in this subsection exclusively use biogenic feedstock. Below, a selection of conversion processes for the production of drop-in SAF is given. There are further methods (e.g. co-processing of biogenic feedstock in petroleum refineries) that are not listed and new methods are constantly being developed.

- **Fischer-Tropsch process (FT):** In the Fischer-Tropsch process, first syngas (hydrogen and carbon monoxide) is produced from the various feedstock options (lignocellulose, energy crops, solid waste, coal, natural gas) and (preferably renewable) energy (Rauch et al., 2017; ICAO, 2018; EASA, 2023). The syngas is then catalytically converted to the desired Synthetic Paraffinic Kerosene (SPK) fuel (Rauch et al., 2017). Aromatics derived by alkylation of light aromatics from non-petroleum sources can also be added to produce an FT-fuel with aromatics (ICAO, 2018; EASA, 2023).
- **Hydrotreated Esters and Fatty Acids (HEFA):** In the HEFA process, oils and fats of plant or animal origin (waste oils and fats also possible) consisting mainly of triglycerides are converted to jet fuel by catalytic conversion using hydrogen (Neuling and Kaltschmitt, 2017b). The hydrogen thereby saturates esters and double bonds (hydrogenation) and removes oxygen using metal catalysts in an exothermal reaction, resulting in saturated alkanes (Neuling and Kaltschmitt, 2017b,a). This is followed by isomerization where linear n-alkanes are cracked and formed into branched iso-alkanes, resulting in a mixture of both and an SPK type fuel (Neuling and Kaltschmitt, 2017b,a).
- **Direct Sugar to Hydrocarbon (DSHC):** For the direct sugars to hydrocarbon (DSHC) process, sugar is extracted from sugar-containing crops and converted to alkenes via fermentation (Neuling and Kaltschmitt, 2017b). In contrast to mostly non-branched chains in SPK

fuel, the subsequent hydrotreatment results in branched hydrocarbon chains in the synthetic isoparaffins (SIP) fuel (Neuling and Kaltschmitt, 2017b).

- **Alcohol to Jet (AtJ):** Feedstock of the AtJ process is alcohol, which first needs to be produced from crops containing sugar, starch, or lignocellulose by fermentation (Neuling and Kaltschmitt, 2017b; EASA, 2023). The alcohol is then dehydrated (i.e. removal of water), oligomerized (i.e. catalytic merging of short-chain alkenes to longer molecules) and the resulting products separated by distillation (Neuling and Kaltschmitt, 2017b). During the final hydrogenation step, unsaturated bonds are saturated to achieve alkanes and an SPK-type fuel (Neuling and Kaltschmitt, 2017b).
- **Catalytic Hydrothermolysis Jet (CHJ):** Catalytic hydrothermolysis takes place by exposing the pretreated feedstock mixed with water to high pressures and temperatures (Neuling and Kaltschmitt, 2017a). Under these supercritical conditions, the feedstock's triglycerides are broken down into shorter molecules (e.g. alkenes) and n-alkane structure is modified to cyclo-alkanes (Neuling and Kaltschmitt, 2017a). These products are then hydrotreated to remove oxygen and saturate the bonds, resulting in alkanes (Neuling and Kaltschmitt, 2017a). Finally, the different fuel fractions are distilled (Neuling and Kaltschmitt, 2017a).

SPK type fuels, as obtained for example in the HEFA process, are made up mostly of n-alkanes and iso-alkanes and contain almost no cyclo-alkanes, aromatics, naphthalene, and sulfur. While SIP fuel contains almost only one type of iso-alkane, Synthetic Kerosene with Aromatics (SKA) fuels contain aromatics (Pechstein and Zschocke, 2017). This allows current drop-in use of SAF by meeting the minimum aromatics content and blends of HEFA and SKA are currently marketed as a drop-in solution (Virent, 2024). All discussed pathways are currently certified for a maximum blending ratio of 50 % and 10 % for SIP fuel (ASTM, 2024b).

Additionally, conventional jet fuel from fossil feedstock can also be hydrotreated to have chemical properties closer to SAFs. There, aromatics can become saturated and converted to alkanes and sulfur can react to gaseous hydrogen sulfide (H_2S), which can then be separated from the liquid (Neuling and Kaltschmitt, 2017a).

2.2.3 Climate impact of SAFs

SAFs offer the opportunity to reduce aviation's climate impact from CO_2 and non- CO_2 effects. CO_2 emissions in-flight are determined by the fuel's hydrogen-to-carbon ratio, which is similar for conventional jet fuel and SAF. The strongly reduced aromatic, naphthalene, and sulfur content of SAFs however have been experimentally shown to lead to a decrease in non- CO_2 radiative forcing from contrails (Voigt et al., 2021; Bräuer et al., 2021b; Märkl et al., 2024).

This is also expected from model calculations such as from ECHAM5-CCMod results in Burkhardt et al. (2018). There, a reduction in initial ice particle numbers leads to a reduction in contrail radiative forcing as can be seen in Figure 2.7. The reference case with normalized radiative forcing and ice particle numbers of 1 refers to what Burkhardt et al. (2018) call a "present-day soot number scenario" and corresponding relative radiative forcing is shown for a reduction by 50 %, 80 %, and 90 %. Soot particle reductions, for example through the use of SAF, therefore result in lower contrail radiative forcing (Burkhardt et al., 2018).

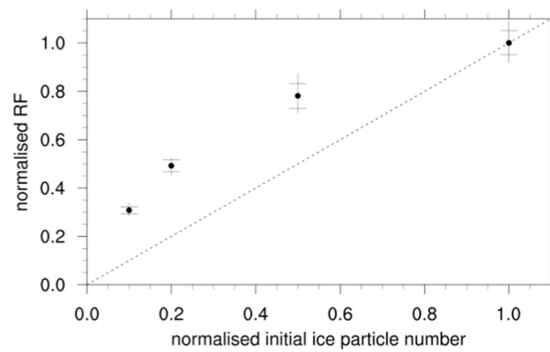


Figure 2.7: Global net radiative forcing and initial ice particle numbers normalized to a current soot emission scenario as calculated with ECHAM5-CCMod. Figure and caption information adapted (cropped) from Burkhardt et al. (2018), used under CC BY 4.0 (<https://creativecommons.org/licenses/by/4.0/>).

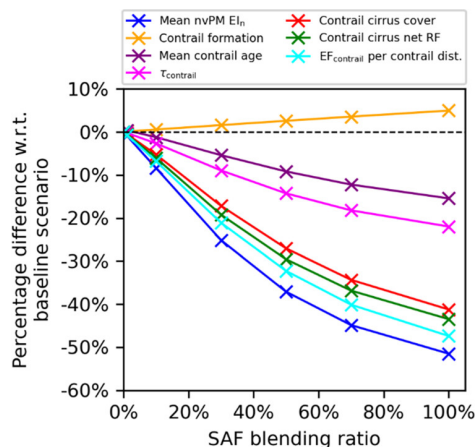


Figure 2.8: SAF blending ratio dependent relative differences in particle emissions, contrail properties, and climate forcing compared to a conventional fuel baseline scenario. Figure and caption information taken from Teoh et al. (2022b), used under CC BY 4.0 (<https://creativecommons.org/licenses/by/4.0/>).

Model calculations by Teoh et al. (2022b) based on CoCiP predictions created a link between emissions, contrail properties and contrail radiative forcing for different SAF blending ratios as shown in Figure 2.8. There, contrail formation increases with higher blending ratios due to higher water vapor emission indices, while nvPM EI, contrail cirrus cover, and contrail cirrus net radiative forcing decrease for higher SAF blending ratios. Teoh et al. (2022b) therefore predict an increasing climate forcing mitigation potential for higher SAF blending ratios while they at the same time also discuss the current availability of SAF so that the optimal blending ratio considering limited supply is not necessarily the highest.

There is, nevertheless, a large difference in CO₂ and CO₂ equivalent emissions (CO₂e) between fossil jet fuel, where all of the released carbon was previously stored underground, and SAFs, where the carbon released by combustion was ideally previously bound from the atmosphere. The exact carbon footprint reduction with SAF however depends on a number of factors that are considered in a full life cycle assessment (LCA).

In the course of the CORSIA framework developed by ICAO, the LCA is performed by treating "core LCA" emissions and induced land use change (ILUC) emissions separately and defining the

total life cycle green house gas emissions by the sum of both (Malina et al., 2022; ICAO, 2022b). For core LCA emissions, the single contributions are listed in Malina et al. (2022), which include the cultivation, harvesting, and collection of feedstock together with its processing, extraction and transportation. The emissions from conversion of feedstock to SAF, as well as its subsequent transportation and combustion are included as well and complete the core LCA emissions (Malina et al., 2022). These can then be compared to the baseline well-to-wake emissions (not including the effects from contrails) for conventional jet fuel of 89.0 g CO₂e/MJ (although this value is also subject to variations in reality (Jing et al., 2022)). Compared to this baseline emission scenario, core LCA emission reductions between 26 % and 94 % are achieved for SAF depending on feedstock and conversion process¹ (ICAO, 2022b).

One step before feedstock cultivation stands the consideration of land area needed to cultivate the respective feedstock crop and to obtain the (ideally renewable) energy for the chosen type of SAF and production method. The associated environmental effect is termed land use change (LUC), which again can be divided into direct land use change (dLUC) and indirect land use change (iLUC) (Malina et al., 2022). Czyrnek-Delêtre et al. (2016) describe dLUC as the environmental effects from direct changes to the land area used for cultivation, for example when converting a forest to fields for energy crop cultivation. Further, they define iLUC as the necessary conversion of land area other than the land used for energy crop cultivation. For example, if land area previously used for food crop cultivation is now used for energy crop cultivation, other land area needs to be converted to land for food crop cultivation. Model calculations estimate ILUC emissions depending on geographic location, crop type and conversion process, which can range from -54 g CO₂e/MJ to +39 g CO₂e/MJ (ICAO, 2022b).

The overall life cycle emission factors in ICAO (2022a), including core LCA emissions and ILUC, range from -23 g CO₂e/MJ to 101 g CO₂e/MJ,¹ which demonstrates the wide range of emissions associated with SAF production and use. Compared to the baseline scenario emissions for conventional jet fuels of 89.0 g CO₂e/MJ, SAF can offer significant emission reductions and even be negative while it is also possible to have higher emissions than those associated with conventional jet fuel use. Overall, the exact quantification of the climate and environmental impact of any given SAF is highly complex and depends on many factors. Generalized statements on the sustainability of SAFs as a whole should be taken with caution and instead, a differentiated analysis of single fuel types and production pathways is needed to assess a fuel's environmental and climate impact.

2.2.4 SAF outlook

In the year 2022, only 0.1 to 0.15 % of global fuel demand (approximately 240 million tons) was covered by 240 thousand to 280 thousand tons of SAF (IATA, 2023). However, policymakers on

¹excluding Fischer-Tropsch (FT) municipal solid waste with non-biogenic carbon content > 0 %

national and supranational level have set goals aimed at increasing the share of SAF (Becken et al., 2023). For example, the ReFuelEU initiative of the European Union aims for a 5 % SAF share by 2030 and 63 % by 2050, while the US has targeted 100 % SAF by 2050 (Boshell et al., 2022; U.S. Department of Energy et al., 2022). Considering a growing aviation sector, this would mean a SAF demand of 2.3 million tons in 2030 and 28.6 million tons in 2050 in the European Union (EU) alone (EASA, 2023). This ramp-up of SAF production will be influenced by the fact that different types of SAF have different scaling capabilities. For example, it is questionable if an increased demand for used cooking oil as SAF feedstock will lead to an increased supply. Roth et al. (2017) estimates a maximum global production capacity of 4 to 5 million tons of HEFA from used cooking oil, a relatively small contribution compared to the global fuel demand. Several fuel production pathways and feedstock will therefore have to be explored and developed in parallel to reach the SAF supply goals. These goals also need to be seen under the context of an additionally growing aviation sector and projected approximate doubling of fuel demand by 2050 (Fleming et al., 2022). While the price of SAF is currently between 1.5 and 6 times higher (depending on the type of SAF (Pavlenko et al., 2019)) compared to conventional jet fuel, prices are projected to fall once production is scaled (EASA, 2023). On the other hand, it can be argued that the immense costs of climate change effects outweigh the additional costs of SAF compared to conventional jet fuel (Newman and Noy, 2023; Kotz et al., 2024).

2.3 Modern combustion technologies

Beyond the influence of fuel on aerosol particle emissions and contrail formation, the impact of modern combustion technologies is investigated in the course of this work. Special focus lies on lean-burn combustion technologies, as is implemented for example in the CFM International LEAP engine series. In this section, the conceptual differences between RQL combustors and lean-burning combustors and their operation under rich-burn and lean-burn conditions are presented in order to facilitate the interpretation and comprehension of results presented in the corresponding results chapters 5 and 6.

Engine technologies are continuously developed to enhance efficiency and reduce emission of unwanted substances. On the ground as well as during landing and takeoff, this especially concerns NO_x , CO, unburned hydrocarbons (UHC), and soot, which affect air quality and human health (ICAO, 2010). While many parts of the engine are continuously further developed, this section will only focus on the combustor and combustion chamber located after the engine's compressor and before the turbine.

Combustor designs have evolved from classical fully rich-burning combustors to various configurations of Low-Emissions Combustor (LEC)s in order to reduce NO_x and particle emissions (Liu et al., 2017). Current examples of LECs are RQL combustors, double annular combustor (DAC)s, and TAPS combustors (Liu et al., 2017). RQL combustors have rich-burn and lean-burn zones and make

up the majority of engines listed in ICAO (2024) currently in production, while TAPS combustors can be seen as lean-burn systems (Stickles and Barrett, 2013) implemented in the LEAP and GENx engine series. These two systems are the combustor technologies used during the campaigns of this work and are therefore compared in the following.

RQL combustors

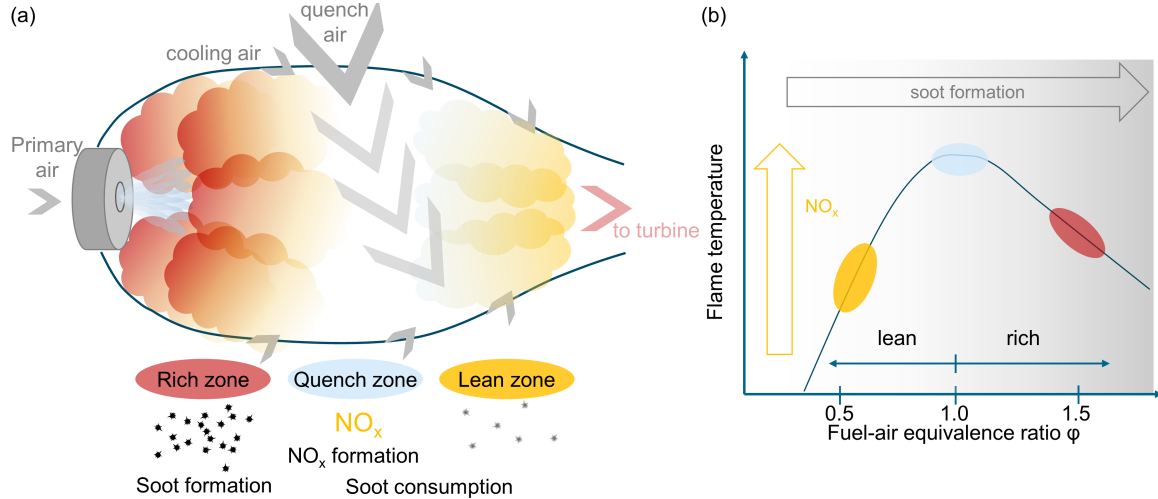


Figure 2.9: (a) Schematic of an RQL combustion chamber where fuel injected together with primary air is first burned in a rich zone, after which the fuel-air mixture is then quenched with quench air so that finally a lean mixture is combusted. (b) Rich-burn, quench zone, and lean-burn sequences indicated on a plot relating flame temperature to the fuel-to-air equivalence ratio ϕ . Increased thermal NO_x production is indicated for higher flame temperatures and increased soot formation is indicated for higher values of ϕ . Panel (a) inspired by Stickles and Barrett (2013) and Bergthorson and Thomson (2015) and panel (b) inspired by Pavri and Moore (2001), Foust et al. (2012), and Stickles and Barrett (2013).

An example of an engine with RQL combustion technology (Rolls-Royce Phase 5 combustor) is the Rolls-Royce Trent XWB in use on the Airbus A350 and the engine type used during the ECLIF3 campaign (Liu et al., 2017; ICAO, 2024). As the name suggests, this combustor technology relies roughly on three different combustion zones, which are shown in Figure 2.9. Panel (a) shows a rough conceptual schematic of the combustion chamber with the fuel/air injector on the left side through which primary air and fuel are atomized into the swirling flow entering the combustion chamber (Stickles and Barrett, 2013; Bergthorson and Thomson, 2015). There, rich combustion takes place with an fuel-to-air equivalence ratio $\phi > 1$. In this zone, the most soot production takes place and the approximate position on the ϕ dependent flame temperature curve is indicated by the red oval in panel (b) at high values of ϕ .

In this conceptually depicted relationship based on Pavri and Moore (2001), Foust et al. (2012), and Stickles and Barrett (2013), flame temperature rises for increasing ϕ under lean-burn conditions ($\phi < 1$) until approximately stoichiometric mixture ($\phi \approx 1$) and then is reduced again for larger values of ϕ under rich-burn conditions ($\phi > 1$). In this simplified representation, NO_x production

is roughly proportional to flame temperature and soot formation increases with larger values of ϕ . Following the rich-burn combustion zone, quench air is introduced into the combustion chamber in the quench zone as shown in panel (a) and indicated by the light blue oval in panel (b) (Stickles and Barrett, 2013; Bergthorson and Thomson, 2015). This influx of air reduces the fuel-to-air equivalence ratio to nearly stoichiometric mixtures and increases the flame temperature, leading to increased NO_x production. Simultaneously, previously produced soot is beginning to be consumed, facilitated by high temperatures and low values of ϕ . Following the quench zone and accompanying dilution, the final lean-burn combustion zone is reached at lower combustion temperatures than in the quench zones and lower values of ϕ (Stickles and Barrett, 2013; Bergthorson and Thomson, 2015). There, soot is consumed even further and NO_x production is low. Therefore, in reality, the high temperature point in the quench zone is attempted to be avoided as much as possible to reduce NO_x production during dilution to lean-burn conditions. The hot combustion products then exit the combustion chamber where part of the energy is used to drive the turbine and propulsion is created by expulsion of the exhaust gases (Onissen, 2014).

Lean-burn TAPS combustors

Lean-burn combustors, such as the TAPS II combustor implemented in the CFM International LEAP engine series, are able to operate in rich-burn and lean-burn conditions. This is achieved by employing two separate pilot and main fuel circuits so that optimized combustor operation can be assured across the entire flight envelope (Foust et al., 2012). During cruise conditions, the engine will usually operate under lean-burn conditions but transition to rich-burn combustion under low thrust conditions such as descent and taxi to avoid flameout. This is achieved by so-called staging where certain fuel injection sites are shut off.

The lean-burn combustor design is shown in Figures 2.10 and 2.11 where (a) a rough conceptual schematic of the combustion chamber is shown (Stickles and Barrett, 2013; Bergthorson and Thomson, 2015) together with (b) a conceptual ϕ dependent flame temperature function (Pavri and Moore, 2001; Foust et al., 2012; Stickles and Barrett, 2013) analogous to the representation in Figure 2.9. Compared to the RQL combustor, the two fuel circuits can be seen where the pilot injection site is located at the center of the fuel injector and several main injection sites arranged annularly around the fuel injector but with injection into a spatially separate circuit.

During the rich-burn combustion mode represented in Figure 2.10, fuel and air are injected into the combustion chamber only through the pilot injection site (Stickles and Barrett, 2013; Bergthorson and Thomson, 2015). In this pilot zone with high ϕ fuel-to-air equivalence ratio, there is soot production analogous to the rich-burn zone in an RQL combustor, which is marked by the red oval in panel (b). Main air entering the combustion chamber then mixes with the pilot flame in the so-called premixing flame zone, indicated by the blue crossed arrows in panel (a), and the fuel-air mixture is diluted to a lean-burning mixture. In this lean-burn combustion zone, ϕ is small and flame temperature is relatively low, as indicated by the yellow oval in panel (b) (Stickles

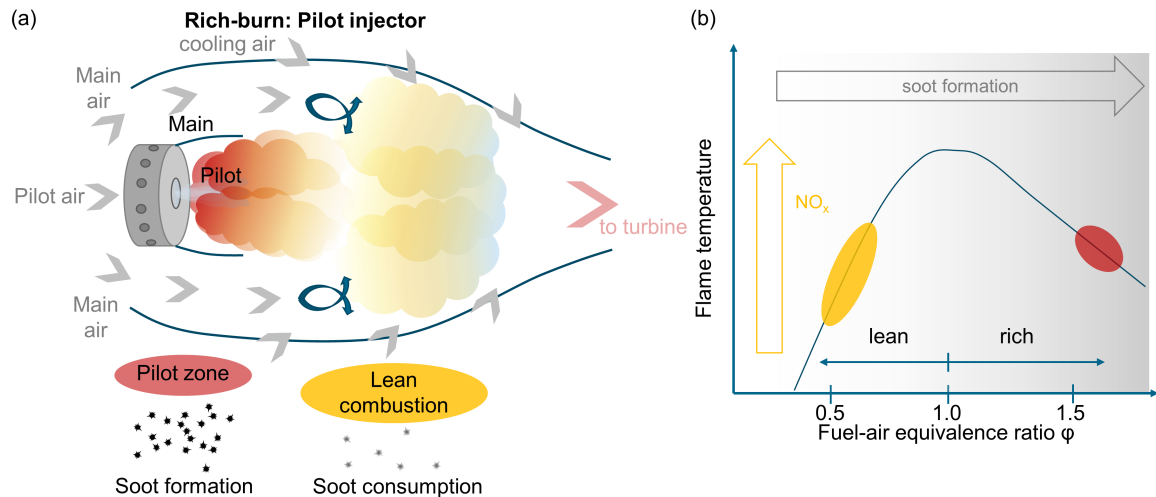


Figure 2.10: (a) Schematic of a lean-burn combustion chamber operating in rich-burn combustion mode where fuel is injected together with pilot air through the pilot injector forming a rich-burning air-fuel mixture with significant soot formation. Main air is then mixed in, forming a lean-burning mixture where soot is consumed. (b) Rich-burning pilot zone and lean-burning zone indicated on a plot relating flame temperature to the fuel-to-air equivalence ratio ϕ . Increased thermal NO_x production is indicated for higher flame temperatures and increased soot formation is indicated for higher values of ϕ . Panel (a) inspired by (Stickles and Barrett, 2013; Bergthorson and Thomson, 2015) and panel (b) inspired by Pavri and Moore (2001), Foust et al. (2012), and Stickles and Barrett (2013).

and Barrett, 2013). This combustion technology avoids the high temperature quench zone found in RQL combustors so that NO_x production is reduced. Following the lean-burn combustion, the combustion products exit the combustion chamber and enter the turbine.

The same combustor can be operated in a lean-burn combustion mode, where the mentioned annularly arranged main fuel injection sites are activated as depicted in Figure 2.11 (a) (Stickles and Barrett, 2013; Bergthorson and Thomson, 2015). Fuel injected through these sites mixes with incoming main air and is premixed when entering the combustion chamber together with fuel and air injected through the pilot injection site. By using the main and pilot injectors simultaneously, a lean-burning mixture is immediately achieved without a rich-burn zone (Bergthorson and Thomson, 2015). This lean primary combustion is indicated by the yellow oval in panel (b) for small values of ϕ and relatively low flame temperatures, so that NO_x and soot production are relatively low (Stickles and Barrett, 2013). Further along the combustion chamber the flame transitions to even lower values of ϕ and lower flame temperatures in the secondary lean combustion zone as marked by the light green oval in panel (b) (Stickles and Barrett, 2013). By assuring a lean mixture throughout the combustion chamber, there is a long path along which potentially formed soot can be consumed again, reducing soot emissions even further.

During the VOLCAN campaign parts (see chapter 6), it was possible to operate the engines in both combustion modes (normal lean-burn operation and forced rich-burn operation) at comparable conditions during cruise at high altitudes. Forced rich-burn operation is not the normal operation

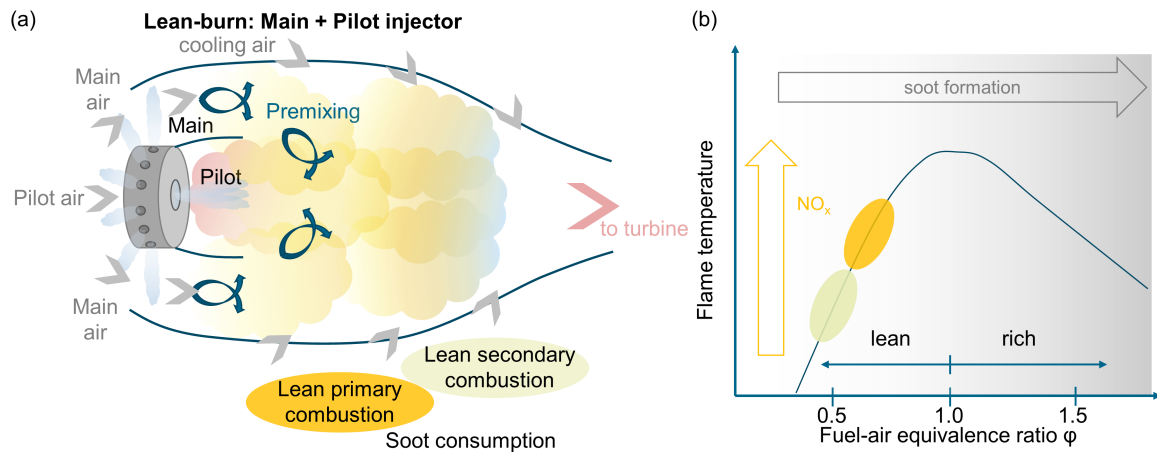


Figure 2.11: (a) Schematic of a lean-burn combustion chamber operating in lean-burn combustion mode where fuel is injected together with pilot air through the pilot injector and through injectors arranged annularly which mixes with main air and is premixed. This forms a lean-burn mixture in a primary and subsequent secondary combustion zone, which are indicated on a (b) plot relating flame temperature to the fuel-to-air equivalence ratio ϕ . Increased thermal NO_x production is indicated for higher flame temperatures and increased soot formation is indicated for higher values of ϕ . Panel (a) inspired by (Stickles and Barrett, 2013; Bergthorson and Thomson, 2015) and panel (b) inspired by Pavri and Moore (2001), Foust et al. (2012), and Stickles and Barrett (2013).

mode of an engine in commercial use and therefore, the rich-burn combustion sequences are to be seen as a forced rich-burn combustion mode. Additionally, a modified fuel-split mode (henceforth referred to as split mode) was also achieved by employing an intermediate pilot/main fuel share compared to nominal fuel split operation.

CHAPTER 3

Instrumentation

This work is based on in-situ measurements performed at cruise altitudes onboard the DLR Falcon research aircraft equipped with a wide suite of in-cabin instrumentation, inlet systems, underwing-mounted probes and additional instruments for navigation and determination of ambient conditions. This chapter is intended to give an overview over the most important systems used during these in-situ measurements and to illustrate their operating principles and functions.

3.1 Light-particle interaction

In the course of this work, two types of ice particle instrumentation, optical array probes and forward-scattering probes, were used. Optical array probes create a shadow image of the measured particle and provide insight into the shape, size and number concentration of large particles ($> \sim 10 \mu\text{m}$), while forward-scattering instruments detect light scattered on particles, thereby allowing conclusions on size distribution and number concentration of particles down to the sub-micrometer range (Baumgardner et al., 2017). This section focuses on the physical principles behind forward-scattering instruments and will provide the background necessary to understanding and interpreting the results presented later in this work.

Forward-scattering probes such as the CAS-DPOL, measure the intensity of light scattered on the particle of interest (Baumgardner et al., 2001; DMT, 2018). By counting the number of these scattering events and correlating them with the time and flown distance, a particle concentration can be calculated. The more complex operation is the size determination of encountered particles. The exact interaction of light with a given particle depends strongly on the light properties as well as size, shape, material, and orientation of the particle together with the interface created by the medium surrounding the particle (Wiscombe, 1980; Bohren and Huffman, 1998a; Borrmann et al., 2000; Rosenberg et al., 2012). Relevant light properties include the wavelength, polarization, wave front shape, coherence, and type of light source (e.g. point source or quasi-parallel) (Wiscombe, 1980; Bohren and Huffman, 1998a; Rosenberg et al., 2012). By controlling some of these variables such as the light wavelength, polarization, and the detected scattering angles and making informed assumptions on the type of particles, information on the size of the particles can be gained. For the

applications discussed in this work, it is reasonable to assume elastic scattering from a monochromatic light source.

3.1.1 Scattering cross section

Following the derivations presented comprehensively in Wendisch and Yang (2012) and Bohren and Huffman (1998a), the total scattering cross section C_{sca} is defined as:

$$C_{sca} = \int_{4\pi} \left(\frac{dC_{sca}}{d\Omega} \right) d\Omega = \frac{\Phi_{sca,4\pi}}{I_i}, \quad [C_{sca}] = \text{m}^2 \quad (3.1)$$

where $\Phi_{sca,4\pi}$ is the radiant energy flux scattered into the entire solid angle with dimension $[\Phi_{sca,4\pi}] = \text{W}$ and I_i is the incident energy flux density with dimension $[I_i] = \text{Wm}^{-2}$. The total scattering cross section C_{sca} relates the power scattered into the entire solid angle (secondary radiation) to the incoming power density (primary radiation), resulting in a quantity with the dimension of an area. This area is not a physical surface area but can be rather viewed as the hypothetical surface area through which the primary radiation would have to pass in order to result in the same power or energy flux that was scattered into the chosen solid angle. This means that a particle's scattering cross section C_{sca} can be seen as a measure of its effectiveness in scattering light (Wendisch and Yang, 2012).

However, the distribution of the scattered light is usually not uniform. The angular distribution of scattered light is therefore described by the term $\left(\frac{dC_{sca}}{d\Omega} \right)$, encountered in Equation 3.1 and commonly known as the differential scattering cross section with dimension $\left[\left(\frac{dC_{sca}}{d\Omega} \right) \right] = \text{m}^2 \text{sr}^{-1}$. This function is the link between impinging primary radiation and the secondary radiation scattered into a certain solid angle $\Delta\Omega$ in a given direction (Bohren and Huffman, 1998a). Therefore, the differential scattering cross section relates an angle-dependent (θ, ϕ) scattered radiant energy flux $\Phi_{sca,\Delta\Omega}$ to the incident energy flux density, which is reduced to only θ dependence when assuming axially symmetrical scattering (Wendisch and Yang, 2012).

The assumption of axially symmetrical scattering is trivially valid for spherical particles and is approximated for non-spherical particles by assuming non-preferential orientations of the particles. For the probes used in the course of this work, light scattered in forward direction in an angle of $4^\circ \leq \theta \leq 12^\circ$ is detected. The resulting probe scattering cross section is therefore determined by:

$$C_{probe} = \int_0^{2\pi} d\phi \int_{4^\circ}^{12^\circ} d\theta \left(\frac{dC_{sca}}{d\Omega} \right) = \frac{\Phi_{detector}}{I_i} \quad (3.2)$$

Here, the power $\Phi_{detector}$ impinging on the detector is the quantity measured by the probe, which is directly related to the scattering cross section. Therefore, the relationship between scattering cross section and particle size is the missing link that can be used to determine the particle's size. For the assumption of spherical particles and light wavelength in a similar order of magnitude as

the particle's size, Mie scattering theory provides this link. In the case of non-spherical particles, the relationship between particle size and scattering cross section is approximated by T-matrix calculations. Both will be described briefly in the following subsection.

3.1.2 Spherical and aspherical particles

The calculation of scattered electromagnetic fields is done by solving the Maxwell equations (Maxwell, 1865) using suitable boundary conditions. These boundary conditions depend on the geometry of the scattering problem and result in analytical solutions for spherical particles with isotropic scattering, which is described by the Lorenz-Mie theory (Mie, 1908). Derivations of these solutions have been discussed at length in literature (Bohren and Huffman, 1998a) and will not be discussed further here. All size-dependent scattering cross sections shown here and used in the course of this work were obtained using the Mie Scattering Conversion Table Generator v1.1.8 software by Philip Rosenberg (Rosenberg et al., 2012), which in turn is based on the work of Wiscombe (1980).

Figure 3.1 shows two of these scattering cross sections as a function of the spherical water droplet diameter ($n = 1.33 + i \cdot 0$) (absorption of zero assumed for simplicity) and an incident wavelength of $\lambda = 658$ nm, which is the wavelength used by the probes employed in this work. For the red curve, the total scattering cross section as a result of scattering into the entire solid angle (corresponding to $0^\circ \leq \theta \leq 180^\circ$) is shown. This red curve lies significantly above the scattering cross section (SCS) curve for a scattering angle of $4^\circ \leq \theta \leq 12^\circ$ as only part of the scattered light is probed for the constrained probing angle. Additionally, the approximations for particle sizes much smaller than the incident wavelength ($D \ll \lambda$) and for particle sizes much larger than the incident wavelength ($D \gg \lambda$) are shown. For very small particles, the function asymptotically approaches the scattering cross section described by Rayleigh scattering and with a r^6 proportionality, where r is the particle radius (Wendisch and Yang, 2012).

When the spatial extension of the charges is much smaller than the wavelength of electromagnetic radiation they are exposed to, all charges in the particle oscillate more or less in sync. This leads to a nearly homogeneous electromagnetic field within the particle and re-radiation from oscillators in phase as from an oscillating dipole (Wendisch and Yang, 2012).

When the particle size however is similar to the incident wavelength, light scattering is described by the Mie scattering regime (Seinfeld and Pandis, 2006). Unlike for the Rayleigh regime, the electromagnetic field within the particle cannot be assumed to be homogeneous in this case (Mie, 1908), so that the single oscillators within the particle oscillate with phase differences to each other. The re-radiation from these phase-shifted oscillators results in constructive and destructive interference, which can be seen in the oscillations of the SCS curves describing Mie scattering in Figure 3.1 and are henceforth referred to as Mie resonances.

Finally, for particle sizes much larger than the incident wavelength, the SCS function approaches geometric scattering where light is described macroscopically as a bundle of linear localized rays.

The basic principles are described by the Fresnel formulas on reflection and transmission and Snell's law of refraction (Bohren and Huffman, 1998b).

There, the scattering cross section is proportional to r^2 . This can be illustrated by introducing the scattering efficiency factor (Wendisch and Yang, 2012):

$$Q_{sca} = \frac{C_{sca}}{A_{proj}} \quad (3.3)$$

where A_{proj} is the projection of the geometric cross section onto a plane, which is πr^2 for a sphere. This scattering efficiency exhibits oscillations when shown against particle size but approaches $Q_{sca} \rightarrow 2$ for large particle sizes (Wendisch and Yang, 2012). The scattering cross section for geometric scattering is therefore described by $C_{sca,geo} = 2\pi r^2$, which is plotted as the dashed-dotted line in Figure 3.1 and appears very similar to the red SCS curve, especially for larger particle diameters.

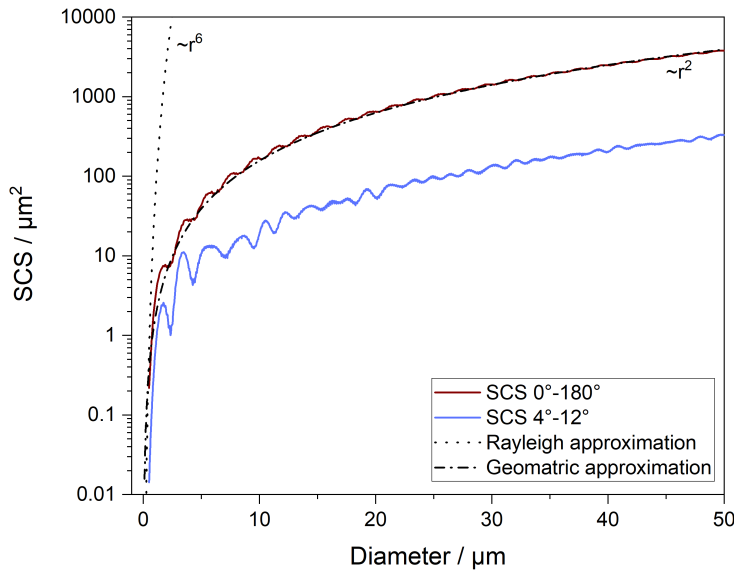


Figure 3.1: Size dependent scattering cross sections for $\lambda = 658 \text{ nm}$ light scattering on spherical water droplets in a scattering angle of $0^\circ\text{-}180^\circ$ and of $4^\circ\text{-}12^\circ$ with additional asymptotic indications of Rayleigh and geometric scattering. SCS data are from Mie Scattering Conversion Table Generator v1.1.8 software by Phil Rosenberg (Wiscombe, 1980; Rosenberg et al., 2012).

It was mentioned that the scattered radiant energy flux measured by a probe's detector can be related directly to a scattering cross section. Now that it has been established that for a given refractive index, light wavelength and scattering angle, a SCS can be mapped to every particle diameter of a spherical particle via Mie scattering, it is possible to create a link between measured scattered radiant energy flux and particle size. By using spherical particles of known material and with defined refractive index (polystyrene latex, sodalime glass, and borosilicate glass) the

probe's measured quantity can be allocated to the SCS of the respective calibration particle size. By interpolating between these known values, a continuous mapping function is achieved for the probe, which is called the transfer function. These are discussed in further detail in subsection 3.2.2. However, when performing in-situ measurements, the inverse operation is conducted where a given SCS, determined by measurement of radiant energy flux and mapped via the transfer function, needs to be allocated to the particle size. For this, assumptions on the type of particle need to be made. For liquid clouds it is reasonable to assume spherical water droplets and spherical ice for freshly formed contrail ice particles. Over time, the ice particles however grow into non-spherical shapes and can be approximated by spheroids that can be quantified by their aspect ratios (ARs) (Borrmann et al., 2000; Gayet et al., 2012).

For non-spherical particles, the orientation under which the particles encounter the incident light, as well as the particle's aspect ratio, have a strong influence on the particle's SCS. To be able to achieve a size-dependent SCS function, a homogeneous distribution of all orientations is assumed, which is reasonable in the dynamic environment a contrail ice particle is exposed to. Symmetrical scattering around the optical axis, similar to scattering on spherical particles, is therefore assumed. As the scattering solution of the Maxwell equations is not analytically solvable for non-spherical particles, numerical methods are needed to be able to quantify the size dependent SCS. For this, results from the T-matrix method are used in the course of this work, as implemented by Borrmann et al. (2000) (specific calculations conducted by Beiping Luo, ETH-Zürich). Thereby, an arbitrary orientation of spheroids with given AR is assumed due to the large number of particles. The result is a mean SCS for every AR and volume equivalent diameter. Works by Gayet et al. (2012) and Voigt et al. (2011) have shown that contrail ice crystals that originate as quasi-spherical particles evolve into aspherical shapes in the minutes following contrail ice formation. Similar contrail ice particle measurements by Kleine (2019) assumed an AR of 0.75, which is done likewise in this work.

Figure 3.2 (a) shows the SCS for spherical ice particles ($n = 1.31 + i \cdot 0$) in dark blue together with a fourth order polynomial fit in light blue. The different refractive index for ice compared to liquid water leads to the slightly different SCS curve compared to the blue curve in Figure 3.1. The fourth order polynomial fit was chosen to achieve a smoothed function without resonances in order to facilitate the mentioned reverse allocation of SCS to particle size. This is necessary as the reverse mapping of SCS to particle diameter is not a bijective function but rather in the case of the resonances, one SCS can correspond to several particle diameters. For example, for a SCS of $10 \mu\text{m}^2$, there are at least three possible particle diameters. Due to this physically limited measurement resolution, the forward scattering instruments therefore measure particle sizes in so-called bins where ranges of SCS are allocated to ranges of particle diameters. The choice of these bins is visualized in Figure 3.2 (b). There, the SCS is shown for aspherical ice particles with an aspect ratio of 0.75 from T-matrix calculations in red together with a fourth order polynomial fit in orange, similar to the fit done for spherical ice in panel (a). In panel (b), dashed black lines indicate exemplarily where bin boundaries were set for the CAS-DPOL instrument during the VOLCAN2

campaign to achieve a uniform distribution of size bins with a high resolution for particle sizes ($<10 \mu\text{m}$), which are especially of interest for contrail ice particles. In the parts of the SCS function where it is bijective, the bins can be chosen freely to match the desired size resolution. For the parts of the function with resonances and non-bijective mapping, the bins were chosen to span a SCS range that completely encompasses the areas of ambiguous mapping. An example of this are the upper ($3.2 \mu\text{m}^2$) and lower ($1.7 \mu\text{m}^2$) bins boundaries surrounding the resonance at smallest particle diameters. Any SCS measured in this range correspond to particle diameters between $1.35 \mu\text{m}$ and $2.85 \mu\text{m}$ with no possibility to increase size measurement accuracy in this size range with the used instrument. As will be discussed further in subsection 3.2.2, the CAS-DPOL instrument requires a certain number of bins within defined size ranges. Therefore, bin boundaries need to be placed where no physical increase in size resolution is possible. These bins with ambiguous size allocation are indicated as blue dotted horizontal lines in Figure 3.2 (b). The corresponding sizes are the middle intersection in the case of the first (smallest sizes) ambiguity and the intersection with the fourth order polynomial for all larger sizes. In general, for the size allocation, the original T-matrix SCS function is used for very small particle sizes, after which the fourth order polynomial of the T-matrix function is used. For particles larger than $20 \mu\text{m}$ the fourth order polynomial for spherical ice is used as no T-matrix calculations are available for particles larger than this size. Details on the exact size allocation are presented in subsection 3.2.2.

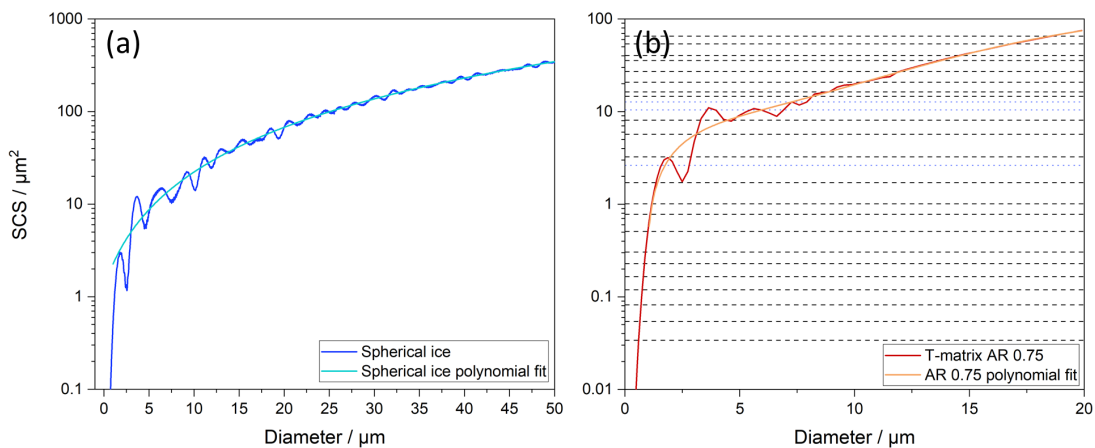


Figure 3.2: Size-dependent scattering cross sections for $\lambda = 658 \text{ nm}$ light scattering on (a) spherical ice particles with a fourth order polynomial fit for a scattering angle of 4° - 12° , and (b) aspect ratio of 0.75 non-spherical ice particles with a fourth order polynomial fit for a scattering angle of 4° - 12° together with horizontal lines that indicate a favorable subdivision for size binning for a forward-scattering instrument. Black lines were chosen due to favorable size division and blue lines indicate additional subdivisions. SCS data in panel (a) is from Mie Scattering Conversion Table Generator v1.1.8 software by Phil Rosenberg (Wiscombe, 1980; Rosenberg et al., 2012) and T-matrix data was created by Beiping Luo, ETH Zürich (Borrmann et al., 2000).

The shown SCS functions were total scattering cross sections over the 4° - 12° scattering angle. To visualize the angular SCS variability, polar diagrams of the scattered light intensity from 1 W m^{-2} incident light at a distance of 1 m from the scattering particle are shown in Figure 3.3. The

scattering on four different sizes of monodisperse spherical water droplets is shown from (a-c, e, f) unpolarized and (d) polarized light. In these diagrams, the incident light comes from the 180° direction and impinges on the particle which is situated at the center of the circle. All light scattered in forward direction is from 90° to 270° and the other circle half signifies backscattered light.

The first effect illustrated in this figure is the particle size dependence of the angular scattering intensity, which can be seen by comparing panels (a), (b), (c), and (e). For the smallest particle size in panel (a) the Mie resonances are hardly visible, indicating the asymptotical approach to Rayleigh scattering mentioned in Figure 3.1 and the majority of light scattered in forward direction. For increasing particle sizes in panels (b), (c), and (e), the number of resonance peaks increases as could also be observed in the one-dimensional diagrams in Figures 3.1 and 3.2.

The scattering angle of 4° - 12° from which the instruments used in this work detect scattered light is highlighted in panel (c). As this is a two-dimensional (2D) representation of the scattering event and assuming scattering symmetrical around the optical axis, the volume stretched by the scattering angle is a hollow cone in three dimensions. Therefore, the angle is not only indicated from 4° - 12° , but also from the symmetrical angle of 348° - 356° in the θ plane.

The scattering instrumentation used in this work operates with p-polarized light, which is why it is worth comparing scattered intensity from (c) unpolarized and (d) polarized light for the same particle size. The general shape and resonance structure is similar between the different modes of polarization with differences being mainly the amplitudes of resonance peaks. Especially for the relevant scattering angle of 4° - 12° the mode of polarization has little influence. Therefore, for calibration and SCS to size allocation of the used scattering instruments, unpolarized light was assumed.

Finally, it is also worth changing perspective to get a feeling for the ratios of forward and backward scattering by comparing the angular scattering function for one particle size in (e) logarithmic and (f) linear representation. The details of the resonance structure are very clear in the logarithmic representation, but are not visible in the linear representation. Instead, one can see how the first main mode in the direction of the optical axis dominates the scattered intensity.

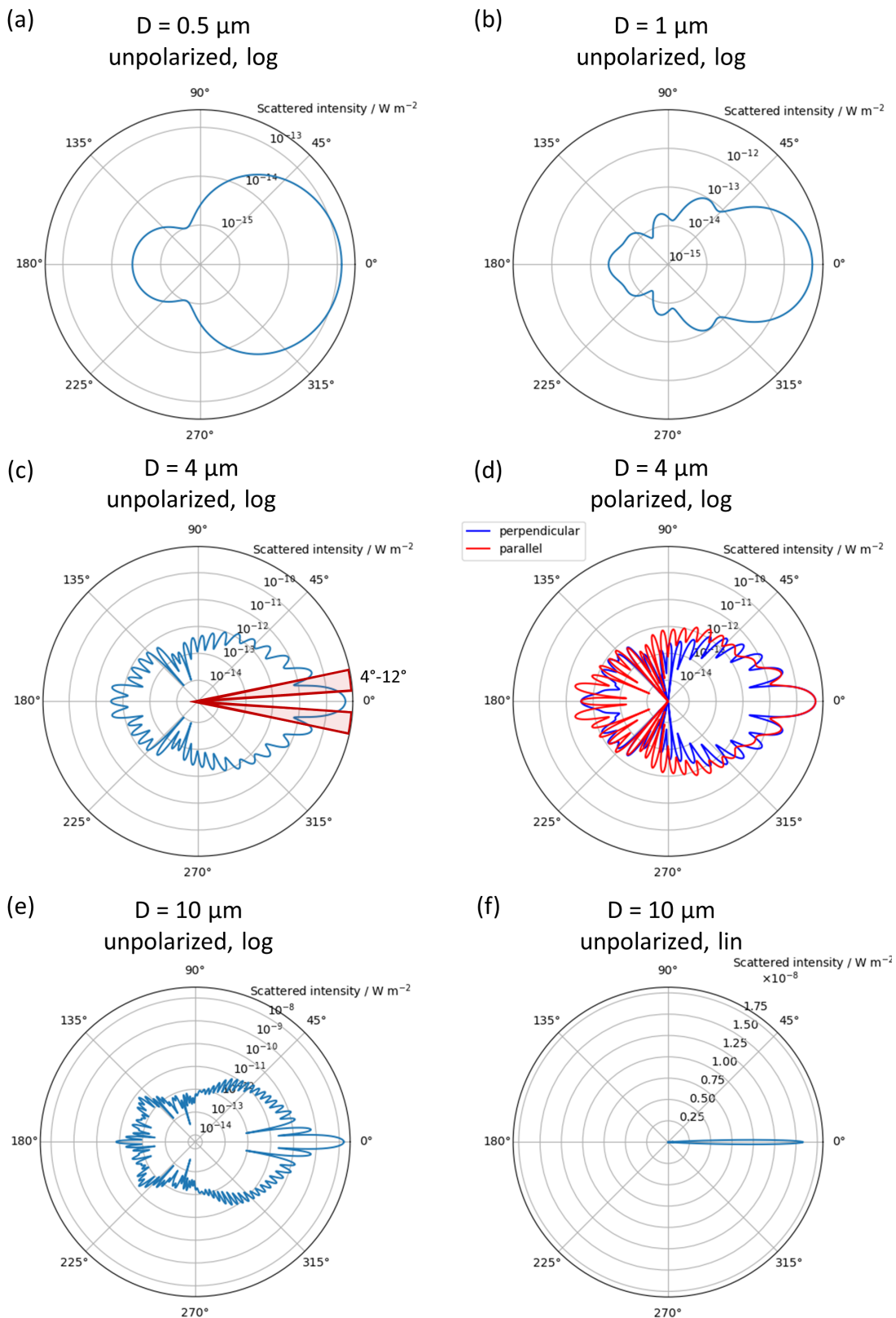


Figure 3.3: Polar diagrams of light intensity scattered on monodisperse spherical water particles suspended in vacuum from a plane wave point light source with 658 nm wavelength and an incident intensity of 1 W m^{-2} . Scattered intensity is given at 1 m distance from the scattering particles. Particle diameters are indicated for each subplot together with information of polarization of incident light and if a logarithmic (log) or linear (lin) radial axis was chosen. The three-dimensional forward scattering angle of $4^\circ\text{-}12^\circ$ is marked red in panel (c). Scattering data obtained using Philip Laven’s MiePlot v4.6.21 software (Laven, 2021).

3.2 Cloud Aerosol Spectrometer: Scattering instruments

In the course of this work, number concentrations and size distributions of contrail ice particles were measured. To achieve this, several underwing probes for in-situ measurements come into question. Previous work probing contrails has been conducted with the Fast Forward Scattering Spectrometer Probe (FF-SSP) by manufacturer Stratton Park Engineering (SPECinc) (Bräuer et al., 2021b) as well as with the CAS-DPOL (Kleine, 2019). Optical array probes such as the CIP provide direct shadow images of the measured particles and thereby enable insights into particle size and shape. The measurement range of this type of imagers (15 – 900 μm for the CIP) however lies beyond the typical sizes of contrail ice particles (Voigt et al., 2010, 2011; Voigt et al., 2017; Bräuer et al., 2021b). An excellent overview over imaging and scattering probes is given in Baumgardner et al. (2017).

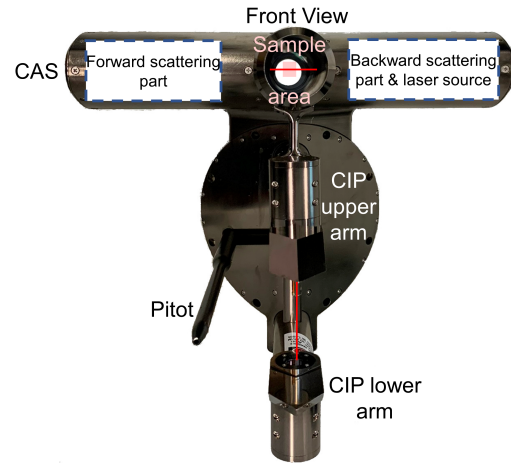


Figure 3.4: Front view of the CAPS-DPOL instrument. In the CAS part, the laser beam enters the sample area in the continuous tube and light scattered on particles is detected in forward (backward) direction in the left (right) part. In the open-path Cloud Imaging Probe (CIP) instrument, the laser beam travels between the upper and lower CIP arms. The pitot tube is used for dynamic pressure measurements.

Two probes containing CAS instruments, the CAS-DPOL and CAPS-DPOL by manufacturer Droplet Measurement Technologies (DMT), were mounted below the wings of the DLR Falcon and used to obtain ice particle data in flight in the course of this work. The CAS-DPOL (Baumgardner et al., 2001) is an older version of the instrument that has been updated with more modern electronics and data processing in the CAPS-DPOL, which is also equipped with an CIP in addition to the CAS part. A front view image of the CAPS-DPOL can be found in Figure 3.4 where the CAS part is located at the top and the two arms of the CIP instruments are arranged vertically below the CAS part. The laser beam of the CAS part passes horizontally through the hollow sampling tube while the CIP beam runs vertically in an open path configuration.

3.2.1 Measuring principle

The general CAS measurement principle representative for the CAS-DPOL and CAPS-DPOL will be described in the following. The CAS instruments sample contrail ice particles passively, i.e. the probed gas volume including particles enters the hollow inlet tube of the instrument without the assistance of any pumps. The probed particles then continuously pass through the instrument in

a straight path, are counted and sized in the sample area located approximately in the center of the particle's path through the probe and finally exit the probe through the rear. This is illustrated schematically on the left hand side of Figure 3.5 in the top view photograph of a CAS with indicated contrail ice particles entering the instrument in the front and exiting out the back. The photograph is overlaid with a schematic showing a backward scattering part and laser source on the left side of the instrument and a forward scattering part on the right side. Between these instrument parts, the sample area is located in the middle where the laser beam interacts with the contrail ice particles passing through the continuous tube. To illustrate the processes within the instrument, a simplified schematic of the beam paths and most important components of the instrument are shown to the right of the instrument photograph in Figure 3.5.

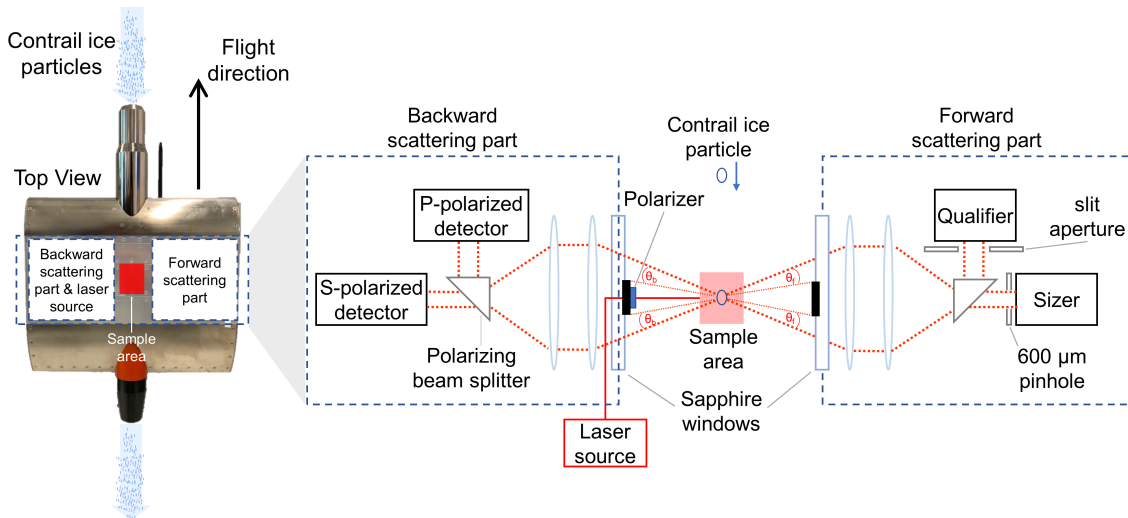


Figure 3.5: Top view of the CAS instrument with most important parts indicated in the photograph on the left side. The right side is a zoomed in schematic of the CAS instrument working principle. A laser beam is polarized and scattered on particles in the sample area in forward and backward direction. There, detectors record the intensity of the scattered light in $4^\circ \leq \theta_f \leq 12^\circ$ in forward direction and in $168^\circ \leq \theta_b \leq 176^\circ$ backward direction. Inspired by Baumgardner et al. (2001) and Baumgardner et al. (2017) and personal communication with the manufacturer DMT and Darrel Baumgardner.

The measurement begins with the laser source shown on the left hand side. From here, a laser beam with wavelength $\lambda = 658$ nm passes through a polarizer, resulting in a linearly p-polarized beam (Kleine, 2019). This polarized laser beam impinges on particles passing through the instrument's sampling tube and is scattered in forward and backward direction under scattering angles $4^\circ \leq \theta_f \leq 12^\circ$ and $168^\circ \leq \theta_b \leq 176^\circ$ (DMT, 2018). Light scattered in backward direction is depolarized to a certain degree depending on the shape and orientation of the particle. It then enters the backward scattering part through a sapphire window and is focused by a lens system onto a polarizing beam splitter after which p-polarized and s-polarized light impinge on their respective detectors. Light scattered in forward direction analogously passes through a sapphire window and is focused onto a beam splitter by a lens system. This beam splitter directs 70 % of impinging light towards the qualifier detector masked by a slit aperture and 30 % of impinging light towards the sizer detector

(DMT, 2018) masked by a 600 μm pinhole. The mentioned sapphire windows can be extracted from the instrument and cleaned to avoid unwanted scattering on accumulated dust, oil or other pollution, which was done regularly during measurement campaigns. The installed detectors are avalanche photodiodes that detect the intensity of impinging photons and output a proportional detector voltage.

The slit aperture masking the qualifier detector is smaller than the pinhole aperture in front of the sizer detector. When a measured particle passes close to or within the center of focus, the scattered light covers a small surface area so that it fully passes through the slit mask and pinhole aperture respectively. When particles do not pass within a certain distance of the center of focus, the scattered beam is widened and masked stronger by the qualifier's small slit mask compared to the sizer's larger pinhole aperture. The resulting qualifier detector voltage U_Q is therefore reduced stronger than the sizer detector voltage U_S (Baumgardner et al., 2017). If the ratio of detector voltages $\frac{U_Q}{U_S}$ falls below the depth of field threshold value of $\text{DoF}_{\text{thresh}} = 0.5$, the particle is not qualified anymore but rejected due to not being in focus (Kleine, 2019). By comparing the signal from the qualifier detector and the sizer detector, particles can be qualified, i.e. it is evaluated if the particle was "in focus" by fully passing through the sample area (Baumgardner et al., 2017). As 70 % of light is directed towards the qualifier detector, the resulting detector voltage U_Q is higher than that of the sizer detector for in-focus particles. If a particle is hence qualified, it is accepted and the intensity impinging on the sizer signal is used to determine the particle's size according to the signal intensity to size allocation provided by calibrations using Mie scattering theory.

Sample area

From this criterion of particle qualification, a probe's sample area is reduced from the entire area in which the detector is sensitive to a qualified sample area (Kleine, 2019). This area is further reduced by detector sampling efficiencies, resulting in an effective sample area. Kleine (2019) conducted a detailed mapping of the CAS-DPOL sample area from data obtained in the calibration stand of manufacturer DMT in 2015 where the instrument was still equipped with an 800 μm pinhole. The instrument was then equipped with a 600 μm pinhole at a later stage and a sample area beam mapping was conducted by Valerian Hahn at the DLR Institute of Atmospheric Physics with the calibration stand AQUAmax developed and built by him (Hahn, 2019). For the CAS-DPOL in the 600 μm pinhole configuration, he found a sample area of:

$$S_{\text{CAS-DPOL}} = 0.22 \pm 0.04 \text{ mm}^2 \quad (3.4)$$

This sample area was used for all calculations of the CAS-DPOL sampling volume in this work. For the CAPS-DPOL instrument, the sample areas measured during calibrations performed by manufacturer DMT were used. For all measurements of the ECLIF campaigns and the first VOLCAN1

campaign, the following sample area was used:

$$SA_{\text{CAPS-DPOL},1} = 0.247 \pm 0.05 \text{ mm}^2 \quad (3.5)$$

For the VOLCAN2 campaign, the sample area was:

$$SA_{\text{CAPS-DPOL},2} = 0.278 \pm 0.06 \text{ mm}^2 \quad (3.6)$$

This change in sample area resulted from the repairs and maintenance conducted by DMT in the time period between campaigns. The CAS-DPOL sample area is given with an uncertainty resulting from sample area measurements while CAPS-DPOL uncertainty is from personal communications between Valerian Hahn (DLR, IPA) and DMT.

Data acquisition

The CAS-DPOL and CAPS-DPOL instruments can be operated in laboratories, wind tunnels, and onboard research aircraft. Laboratory setups are generally used for size calibrations and troubleshooting and don't require the use of a closed Knollenberg canister as is used in wind tunnel measurements in cold and wet conditions. In aircraft operation, the rear part of the instrument is mounted in cylindrical containers connected to the underwing pylons of the aircraft. In all cases, the instrument is controlled and data recorded by the manufacturer DMT's data acquisition software Particle Analysis and Display System (PADS). On the ground, the instruments are directly connected to a computer running PADS via a lab cable. This cable has three main bundles, the first being an RS-422 connector for data transmission, and the other two for power. The instrument's internal computer, laser and other electronic components use 28 V direct current (DC), while the anti-ice system uses 115 V alternating current (AC). For the CAPS-DPOL, an additional data connection for the CIP instrument is needed, for which a SeaLevel PCI express interface card needs to be installed in the receiving computer in order to process 2D CIP data. For the acquisition of CAS and one-dimensional (1D) CIP data, a SeaLevel SeaLINK to USB serial adapter is needed to connect the RS-422 output to either a lab-based or aircraft mounted computer. Onboard the DLR Falcon, the instruments are connected via wiring through the aircraft wings into the cabin. There, the CAS-DPOL connects to the so-called optical particle counter (OPC) rack mounted at the front of the cabin and controlled via PADS installed on one of the rack-mounted computers. The CAPS-DPOL is connected to an Advantech MIC-7500 industrial computer, from which it is also controlled by PADS and data is recorded.

The detected raw analog voltage signal in CAS instruments is processed and amplified in analog-to-digital converters resulting in discrete measurement units of analog-to-digital counts (ADC). To ensure proper signal amplification across the nominal particle size measurement range of 0.5 – 50 μm and the associated several orders of magnitude in scattering cross section (s. Figures 3.1 and

3.2), the older CAS-DPOL uses three gain stages (high gain stage (HGS) for small particles, mid gain stage (MGS) for intermediately sized particles, low gain stage (LGS) for large particles), while the newer CAPS-DPOL uses two (HGS for small particles and LGS for large particles). Each of these gain stages has a linear relationship between scattering cross section and ADC, which is called a transfer function. These transfer functions have small slopes for the smaller particle ranges and larger slopes for larger particles. The determination of transfer functions is done in particle size calibrations and will be discussed in further detail in subsection 3.2.2.

Before a measurement is started, there are several parameters that need to be set. For this, a configuration file ("ini-file") is used where operating parameters of the instrument are defined. These include the sampling rate (set to 1 Hz in this work), settings for communication with the computer (e.g. Baud rate), the probe's sample area, the allocation of instrument ADC to particle size and a number of calibration constants for instrument pressure and temperature sensors. During a measurement, PADS displays a number of instrument parameters such as temperature, pressure, particle air speed (PAS), as well as particle number concentration, size distribution, etc. This allows monitoring of the measurement by the instrument operator and reaction/correction of measurement conditions if contrail particles are not measured successfully. Several files are recorded and saved by PADS, where the two most important ones are the so-called bulk file and the particle-by-particle (pbp) file.

The bulk file records all qualified particles in the defined sampling frequency, which was 1 Hz in the course of this work. This means that for every second, there is a data entry where the number of counted particles in each of the defined size bins is recorded. Hereby, 30 bins are available, where 10 bins are reserved for each gain stage in the CAS-DPOL. Additionally, derived quantities such as number concentration and median volume diameter (MVD) (defined in section 4.1) as well as a number of housekeeping parameters (voltages, baseline values, temperatures, pressures, etc.) are recorded. The exact parameters recorded in the bulk files differ between the CAS-DPOL and CAPS-DPOL while the most important parameters needed for size distribution and number concentration determination are the same.

In the pbp file, a data entry is created for every detected particle. For the CAS-DPOL, the 1 Hz time sequence, in which the qualified particle was detected, is recorded together with the corresponding ADC values in forward and backward scattering direction, the inter-particle time (IPT) (time between detection of two particles) and several other parameters. For the CAPS-DPOL, the ADC values are further split into the signals from the sizer and qualifier detector, as well as in which gain stage the signal was detected together with a number of other parameters that will not be discussed in detail here. For every individual detected particle, the pbp file offers more information. However, only the first 292 particles in the CAS-DPOL sampling interval and the first 734 (ECLIF3 & VOLCAN1) or 511 (VOLCAN2) particles in the CAPS-DPOL sampling interval are recorded in the pbp file. At high particle concentrations as are often times encountered during

contrail measurements, not all particles are therefore recorded in the pbp file. While both files offer the possibility of calculating particle number concentrations, the pbp file can offer a higher resolution that goes beyond the bulk file sampling rate. In section 4.1 these two methods with their advantages and disadvantages are discussed further. The pbp file also proves to be useful for size calibrations. From there, histograms of measured ADCs of every detected particle can be formed and compared to the nominal size of used calibration particles.

3.2.2 Calibration

Due to aging of instrument components such as the laser and detector, and by exposure to vibrations and external forces during transportation and in-situ operation, the original allocation of ADC to particle sizes can change over time. Therefore it is necessary to perform regular size calibrations, preferably directly before measurement campaigns. For all campaigns discussed in this work, calibrations were performed before the first measurements to obtain the most current gain stage transfer functions. A further calibration was performed after the campaigns to ensure that no misalignment or damage had occurred during the measurement flights and the size allocation remained stable throughout the campaign.

The calibrations followed the procedure according to Rosenberg et al. (2012) and were performed either in the DLR cloud physics laboratory in Oberpfaffenhofen, in the Falcon aircraft hangar or in the field during campaigns. In all cases, the conditions were attempted to be as similar as possible for all calibrations. When performed in the laboratory, the instrument was confined in an instrument stand and connected to an external power source and portable computer for data acquisition. When performed on an instrument installed in the aircraft, power was provided by the aircraft and data acquisition performed by the onboard computer used to control the instrument. A hollow calibration tube is inserted into the CAS sampling tube before the calibration procedure to deliver the used calibration particles directly to the instrument's sampling area and to maximize the number of qualified particles. To achieve this, the calibration tube has a diameter much smaller than that of the CAS inlet tube and a length such that it ends directly before the place where the sample area begins. To achieve a continuous air flow through the instrument inlet tube, an industry vacuum cleaner (Bosch Professional GAS 35 L SFC+) is connected to the back of the CAS inlet tube. While the CAS-DPOL is in principle able to measure particles during calibrations without the use of the vacuum cleaner, the CAPS-DPOL has a lower particle speed detection threshold that does not allow calibration particle detection without the acceleration of calibration particles to a certain speed by the vacuum cleaner.

Several types of calibration particles were used depending on the particle size range. For particles in the size range of 510 nm to 2002 nm, polystyrene latex (PSL) beads suspended in ultrapure water are atomized using a Topas GmbH aerosol generator ATM 228. The atomized beads then pass through antistatic tubing into a drying system consisting of a hollow tube embedded in desiccant silica gel in order to absorb any excess water and isolate the PSL beads. The beads then enter the

instrument's calibration tube via an antistatic rubber tube connected thereto. For larger sizes, 9000 Series Glass Particle Standards by Thermo Fisher Scientific were used. For sizes between 1.9 μm to 23.0 μm , the glass type is borosilicate (BS) and for the largest bead sizes between 29.5 μm and 49.0 μm the glass was soda-lime (SL). A small amount (heaped tip of a laboratory spatula) is transferred from the original container to a glass vial equipped with a lid through which two independent metal tubes enter the vial. In order to pass the glass particles through the CAS instrument, one of the metal tubes is inserted into the CAS calibration tube and a controllable gas pressure source (compressed air duster, nitrogen, dry air) is applied to the other metal tube. Just enough gas flow should be applied to the vial to swirl up the beads and create a homogeneous "cloud" of glass beads that are well-separated and slowly exit the glass vial through the other metal tube into the probe's calibration tube. During the calibration process, the respective beads are passed through the CAS instrument while it is recording a continuous measurement. The time periods of spraying the respective bead sizes together with all bead parameters (size, size uncertainty, lot number, etc.) are documented so that the recorded data can later be correlated to the used calibration particles.

At the end of a calibration procedure, the recorded pbp file and the calibration protocol containing bead properties and spray times are further processed to achieve probe transfer functions. The processing differs slightly between CAS-DPOL and CAPS-DPOL and will be discussed first conceptually for the CAS-DPOL in the following. Figure 3.6 shows the sequential processing of calibration pbp data from calibration glass beads used in the CAS-DPOL. In panel (a), the measured ADC of single particle encounters are seen for the entire calibration measurement sequence. Darker areas show where many particles with the corresponding ADC were encountered. When comparing these ADC patterns for different calibration bead sizes, a main mode can be seen that lies at higher ADC for large particles and decreasing ADC for decreasing particle size. For each given calibration bead size, histograms are plotted over all measured ADC and an example for the 5.4 μm calibration beads can be found in panel (b). There, the main peak is determined as being the highest peak in an ADC range where it is expected for the respective calibration bead size. In some cases, peaks from instrument artifacts can be higher but usually remain at constant ADC values while the main peaks of calibration beads change for different sizes. In order to determine the position of the main peak, a Gauss-fit is performed on the kernel smooth fit of the histogram, which is marked in light green. The peak center of this Gauss curve gives the central ADC value corresponding to the 5.4 μm borosilicate glass beads. The connection between ADC and SCS is created by consulting the Mie scattering relationship of SCS to particle diameter for borosilicate glass as shown in panel (c). In this function, the SCS corresponding to 5.4 μm particles is extracted, which is marked by the central red lines in this figure. The calibration bead manufacturer provides uncertainties on bead size so that the minimum and maximum size with corresponding SCS is indicated in Figure 3.6 (c) as well. The central ADC value determined in panel (b) and the corresponding SCS from panel (c) are finally plotted together with the mentioned uncertainties for each of the calibration bead sizes as shown in panel (d). For every gain stage, a linear fit is conducted with the available data points using an instrumental weighted method, meaning that each data point is weighted by the inverse

squared uncertainty in y-direction. These linear fits are the transfer functions of the instrument and unambiguously relate SCS to ADC.

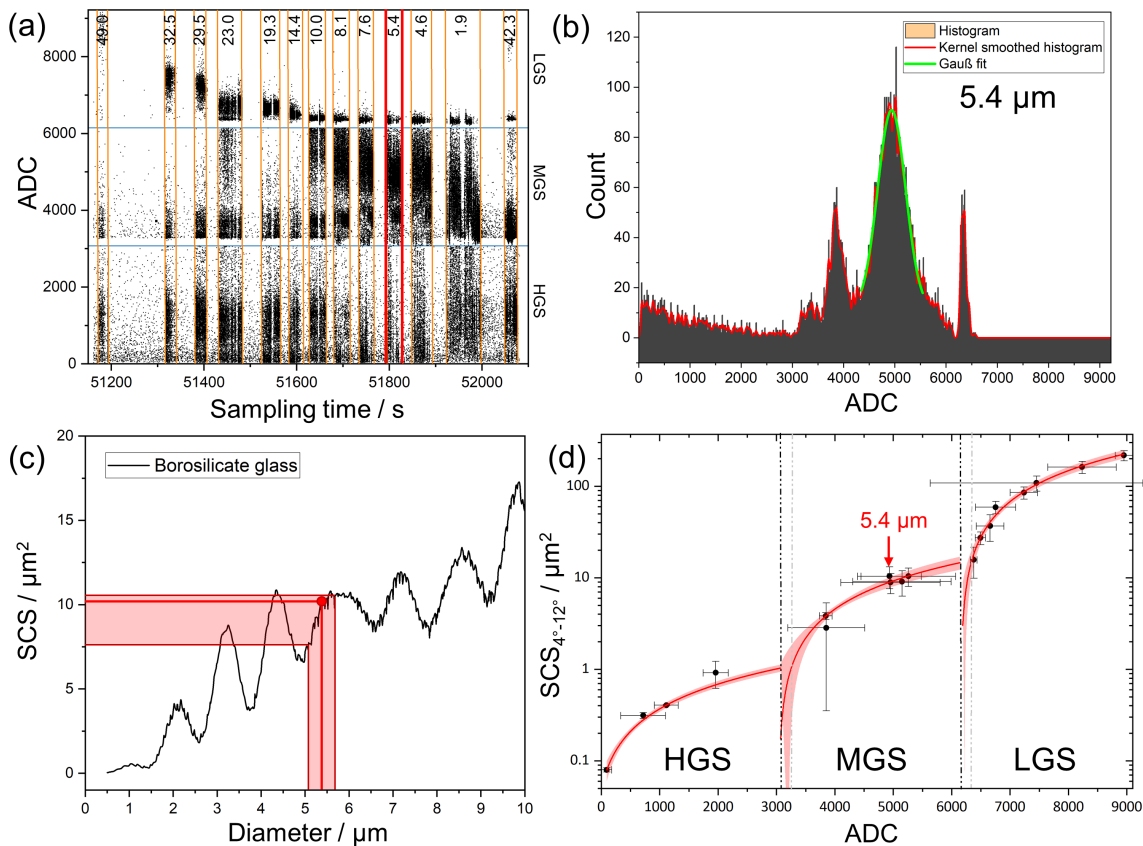


Figure 3.6: CAS-DPOL calibration data processing steps for glass calibration bead measurements. (a) pbp file counts vs sampling time with measured glass bead sizes ($5.4 \mu\text{m}$ highlighted) indicated at the top (in μm) and confined by orange vertical lines. Gain stages are delimited by horizontal blue lines. (b) Histogram over $5.4 \mu\text{m}$ bead counts with red kernel smoothed function and green Gauss fit over the main peak. (c) Mie SCS curve for borosilicate glass (from Mie Scattering Conversion Table Generator v1.1.8 software (Wiscombe, 1980; Rosenberg et al., 2012)) with allocation from bead size to SCS marked in light red and uncertainty resulting from manufacturing size uncertainty marked as a band. (d) Resulting linear fits (transfer functions) with 95% confidence interval bands for the three gain stages and $5.4 \mu\text{m}$ measurement pointed to in red.

When examining the ADC of one size of calibration particles as shown in Figure 3.6 (a) and (b), it quickly becomes apparent that for a given calibration particle size there are ADC apart from the main mode. This phenomenon can have several origins. In the spaces of time between calibration bead spraying, a wide range of ADCs is seen mainly across the HGS and MGS. This results from background aerosol particles passing through the instrument as the air flow was maintained between calibration bead spraying. Another reason for deviation from Gaussian distributions of ADC around the main mode for given particle size lies in the size distribution of calibration particles. For a given particle size, there is a manufacturing uncertainty indicated exemplarily by the size width in x-direction in panel (c) together with the resulting span of SCS. This range of SCS results

in a non-Gaussian distribution of ADC when transferring them to ADC using the transfer functions. Additionally, instrument artifacts can be found that can not be fully explained. For example for glass bead sizes between 14.4. and 49.0 μm , ADC clusters can be seen in all three gain stages while the main ADC peak is expected in the LGS. Likely in some cases, measured encounters are not allocated to the correct gain stages, leading to counts in the gain stages they are not expected. These instrument artifacts introduce an uncertainty to the correct sizing of measured particles but are assumed to not influence the counting of particles as each pbp file entry should stem from a qualified particle scattering event.

An additional artifact seen in Figure 3.6 (a) are counting gaps directly above the gain stage boundaries. These gaps correspond to gain stage overlap areas, so-called "dead zones", of the instrument which are also marked by the two gray vertical dashed lines in panel (d). In these ADC ranges, the SCS of the transfer function lies below the maximum SCS of the previous gain stage. Therefore, no counts are expected for these ADC ranges as they should be allocated to the previous gain stage. This seems to be fulfilled in most cases but for some particle sizes, counts can be found in the dead zones, especially the one between MGS and HGS, as is also the case in the 5.4 μm example. This shows that in some cases, the probe electronics do not allocate particle encounters to the correct sizes. This phenomenon is sensitive to the exact setting of the probe electronics, an example of which can be found in Figure C1 in Appendix C.

CAS-DPOL

The main result of instrument calibration is the determination of transfer functions for each of the instrument's gain stages. While every gain stage ranges from 1 to 3072 ADC, the ADCs of subsequent gain stages are added, leading to a total ADC range of 1 to 9216 (3×3072) for the CAS-DPOL. The linear transfer functions for these gain stages relating ADC to SCS of the CAS probe in the forward-scattering angle range of 4° to 12° are defined as (Kleine, 2019):

$$\text{SCS}_{\text{CAS}} = c_i \cdot \text{ADC} - a_i, \text{ with } i \in \{HGS, MGS, LGS\} \quad (3.7)$$

where the slope c_i and y-axis intersect a_i are determined from the linear fits of the SCS to ADC relations. The transfer function parameters resulting from the calibrations for every campaign investigated in this work are shown in Table 3.1. Except for the transfer function slope c_i of the HGS, all parameters increase continuously over time. The fitting standard errors are approximately one order of magnitude smaller than c_i and a_i such that in some cases, the differences of the parameters across campaigns lie within each other's fitting uncertainty. From this comparison it is therefore not possible to determine if instrument aging effects are systematically reflected in the transfer function parameters or if the parameters simply remain within their measurement uncertainties.

Originally, before the ECLIF3 (Q2 and Q4) and VOLCAN1 campaigns, binnings for spherical liquid water or spherical ice were chosen for the CAS-DPOL. After completion of these campaigns it was

Table 3.1: Transfer function parameters of the CAS-DPOL instrument across the investigated campaigns.

Gain Stage	ECLIF3 Q2		ECLIF3 Q4 / VOLCAN1		VOLCAN2	
	c_i / cm^2	a_i / cm^2	c_i / cm^2	a_i / cm^2	c_i / cm^2	a_i / cm^2
HGS	3.20×10^{-12}	-4.97×10^{-10}	3.05×10^{-12}	-2.32×10^{-10}	3.23×10^{-12}	-1.88×10^{-10}
MGS	4.71×10^{-11}	1.43×10^{-7}	5.11×10^{-11}	1.52×10^{-7}	5.24×10^{-11}	1.59×10^{-7}
LGS	8.03×10^{-10}	4.94×10^{-6}	8.97×10^{-10}	5.49×10^{-6}	9.09×10^{-10}	5.58×10^{-6}

decided that as the measurement focus is on contrail ice crystals of several minutes age, a size binning for aspherical ice particles with an AR of 0.75 will be used. Once ADC boundaries have been chosen, they can't be changed anymore in the bulk file for completed measurements. The size allocation of these ADC boundaries however can still be modified. The existing transfer functions are used for this size conversion so that the SCS are fixed as well. In principle, one could also convert the allocated size to SCS by using the Mie SCS function for liquid water droplets if one is certain that this was the material the original binning was based on and that the instrument transfer functions have not changed. However, using the transfer functions from the most recent calibration and instead converting ADC to SCS takes possible changes and modifications to the instrument into account. The conversion takes place by allocating these SCS to sizes of AR 0.75 ice particles, which would be ambiguous due to Mie resonances for some sizes if only the T-matrix function were used. Therefore, the T-matrix function was used for the size allocation for small particle sizes where the function is unambiguous. As soon as the ambiguities begin, a fourth order polynomial fit to the function as was shown previously in Figure 3.2 (b) is used. T-matrix calculations were only available up to sizes of 20 μm , so that the Mie function of spherical ice particles as shown in Figure 3.2 (a) was used for that size range. In Table C1, the resulting allocation of ADC to aspherical AR 0.75 ice particle volume equivalent diameters for the different campaigns of this work is shown.

CAPS-DPOL

For the CAPS-DPOL, sizes of AR 0.75 ice particles were allocated to an existing and slightly modified binning during the ECLIF3 and VOLCAN1 campaigns. For the VOLCAN2 campaign, an own calibration was performed, which is described in the following.

The physical steps needed to calibrate the CAPS-DPOL instrument are nearly identical to those for the CAS-DPOL. One difference lies in the minimum particle speed needed to record calibration particles. While in principle, particles could be directly injected into the CAS-DPOL sampling tube without an additionally provided air flow, this is not the case for the CAPS-DPOL. A minimum particle sampling speed set in the CAPS-DPOL requires the mentioned vacuum cleaner to be attached to the back of the sampling tube to create an air flow and sufficiently accelerate injected calibration beads.

Data processing of obtained calibration data on the other hand differs slightly between the two

instruments. As mentioned, the CAPS-DPOL pbp file records signals from the sizer and qualifier detector and separately records the gain stages. For size calibration, only the sizer signals are used. However, the ADC signals from the two gain stages are not recorded on the same ADC scale. The sizer high gain stage signal ranges from 0 to 16383 ADC, although realistic signals are found from approximately 90 ADC to approximately 11800 ADC after which a large gap in signals is found before a thin line of artifactual counts at exactly 16383 ADC marks the upper recording range of the sizer high gain stage signal. The sizer low gain stage signal ranges from 0 ADC to 2097024 ADC which is not on the same scale as the sizer high gain stage signal. One of the size binnings preset by the manufacturer spanned from 83 ADC to 30689 ADC across both gain stages so that the size high signal in the pbp file cannot be directly compatible with the sizer low gain stage signal. In order to combine the signals from the two gain stages, the sizer low gain stage signals are divided by 128 which converts the signal range to 0 to 16383 ADC and is the same as in the sizer high gain stage signal. To receive a complementary and continuous signal range, 16383 is finally added to the sizer low gain stage so that both gain stages together span a range from 0 to 32766 ADC. After combining these two columns, further processing of data for calibration is analogous to that for the CAS-DPOL.

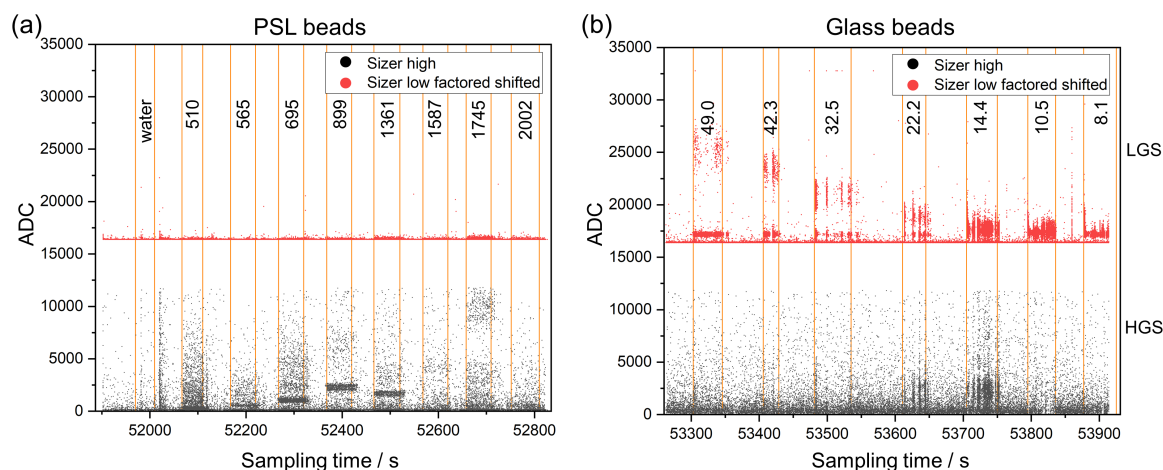


Figure 3.7: ADCs of calibration bead counts during CAPS-DPOL calibration sequence of (a) PSL beads and (b) glass beads performed before the VOLCAN2 campaign. Sizer high gain stage data is shown in black in the bottom half of both graphs and the scaled and shifted sizer low gain stage data is shown in red in the top half. Sequences of used calibration particle sizes are indicated within orange vertical lines in (a) nm and (b) μm . Not all bead sizes used for calibration are shown.

A representation of VOLCAN2 calibration sequences for (a) PSL and (b) glass calibration beads is shown in Figure 3.7. There, the factoring and shifting of the sizer low gain stage and combination with the sizer high gain stage has been completed so that the entire ADC range is shown on the same scale. There it can be nicely seen that the small PSL bead's main signal lies in the HGS and the glass bead main signals are in the LGS. Also, the main ADC mode with an accumulation of counts for 1361 nm PSL beads lies at smaller ADC compared to the 899 nm beads due the Mie resonances in this size range. For glass calibration beads in panel (b), the main mode ADC position

continuously moves towards smaller values for smaller calibration beads. Nonetheless, there are always counts in the HGS resulting from background aerosol ingested by the vacuum cleaner and also from the measured calibration beads that are registered in both gain stages (there is always a HGS and LGS value for each particle in the pbp file). Finally, there are no counts registered in the HGS between approximately 11830 and 16383 ADC. As there was no experience calibrating the CAPS-DPOL in the research group, it was not clear at the time of the campaign that this might be a cause of concern. However, during processing of CAPS-DPOL data from the VOLCAN2 campaign, several suspicious results were found that did not match those of the CAS-DPOL. These differences will be discussed in subsection 3.2.4 and likely originate at least partially from this gap in data in the CAPS-DPOL sizer high gain stage.

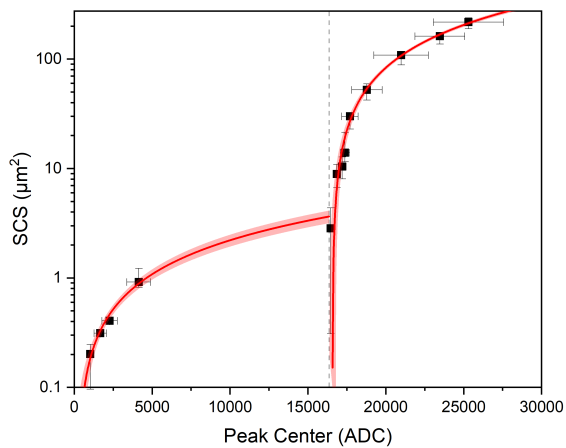


Figure 3.8: Linear fits (transfer functions) of CAPS-DPOL calibration data obtained before the VOLCAN2 campaign with 95 % confidence interval bands for the two indicated gain stages in red. Note: No error weighting was used for these linear fits, see alternative parameters in Table 3.2

to that of the CAS-DPOL. However, as will be discussed in subsection 3.2.4, the CAPS-DPOL had technical issues during the VOLCAN2 campaign that don't allow the obtained data to be used reliably. Nonetheless, the binning used during the campaign for aspherical AR 0.75 ice binning is shown in Table C2.

Table 3.2: Transfer function parameters of the CAPS-DPOL for the VOLCAN2 campaign without instrument error weighting and with instrument error weighting.

Gain Stage	VOLCAN2 no weight		VOLCAN2 with weight	
	c_i / cm^2	a_i / cm^2	c_i / cm^2	a_i / cm^2
HGS	2.26×10^{-12}	4.79×10^{-10}	1.87×10^{-12}	1.86×10^{-10}
LGS	2.44×10^{-10}	4.04×10^{-6}	2.19×10^{-10}	3.62×10^{-6}

With the shown calibration performed before the VOLCAN2 campaign, the two transfer functions (without the instrumental weighted method) for the respective gain stages were obtained. It was attempted to increase the fitting accuracy by resolving the different errors in positive and negative y-direction but these two different y-uncertainties were not accepted by the fitting algorithm of the software Origin as an input value for error weighting. Fits using the instrumental weighted method based on the larger of the two y-errors are shown together with the parameters of the non-weighted fits in Table 3.2 to illustrate the impact of error weighting. In principle, with these function parameters, the size binning for the CAPS-DPOL could be adapted to be similar

During both campaign parts of ECLIF3 and VOLCAN1, the same binning was used for the CAPS-DPOL. The size allocation was originally for water and was converted to sizes for aspherical AR 0.75 ice particles using the Mie SCS function for liquid water droplets and converting those SCS to the T-matrix, fourth order polynomial, and spherical ice particle SCS functions as described for the CAS-DPOL (s. 3.2.2 CAS-DPOL) (this allocation was done directly from the calibrated transfer functions for VOLCAN2). The ADC bins stem from a calibration performed by the manufacturer DMT and were not replaced by ADC bins from an own calibration as pbp file data handling for the two-gain stage CAPS-DPOL with updated data processing and recording was not known to the research group at the time. Therefore, only the calibrated transfer function from VOLCAN2 is shown in Table 3.2.

3.2.3 Size distribution

With the performed calibrations, the CAS-DPOL and CAPS-DPOL instruments are used to measure size distributions of the encountered contrail ice crystals in a size resolution defined by the ADC bins. This size information is recorded for every sampled second during measurements but generally, longer time sequences are considered to draw conclusions on the obtained results. For example, size distributions for different test points in a measurement flight or single contrail encounters could be a sensible time sequence. In Figure 3.9, the measured (a) total ice number concentration is shown together with the (b) number concentrations per size bin and (c) time-averaged size distribution of a single contrail encounter during measurement flight 16 of the VOLCAN2 campaign. The shown total ice number concentration is the sum over the particle concentrations measured in all 30 bins of the CAS-DPOL. These single concentrations are resolved in panel (b) where it can be seen that the main share of particle concentration is found in a small number of bins, while the entire distribution spans up to around 10 μm . By averaging over the shown time sequence, the particle size distribution (PSD) in panel (c) is obtained where each step corresponds to one bin.

The quantity shown in panel (c) is the concentration N_i in each bin normalized by the difference of the logarithmic upper ($\log D_{u,i}$) and lower bin ($\log D_{l,i}$) size boundaries for every respective bin i and is calculated as follows (TSI Incorporated, 2012):

$$(dN/d \log D)_i = \frac{N_i}{\log D_{u,i} - \log D_{l,i}} \quad (3.8)$$

By normalization by the difference of the logarithmic bin boundaries, the effect of different bin widths is considered, making concentrations in different bins comparable to each other, especially when combining size distributions with different sizes, e.g. from several instruments. The detailed processing of PSDs is described in Appendix C and illustrated in Figure C2. While particle size distributions shown in this work have been processed in the described way, calculated total ice particle number concentrations are based on all 30 bins and conserve all particles measured therein.

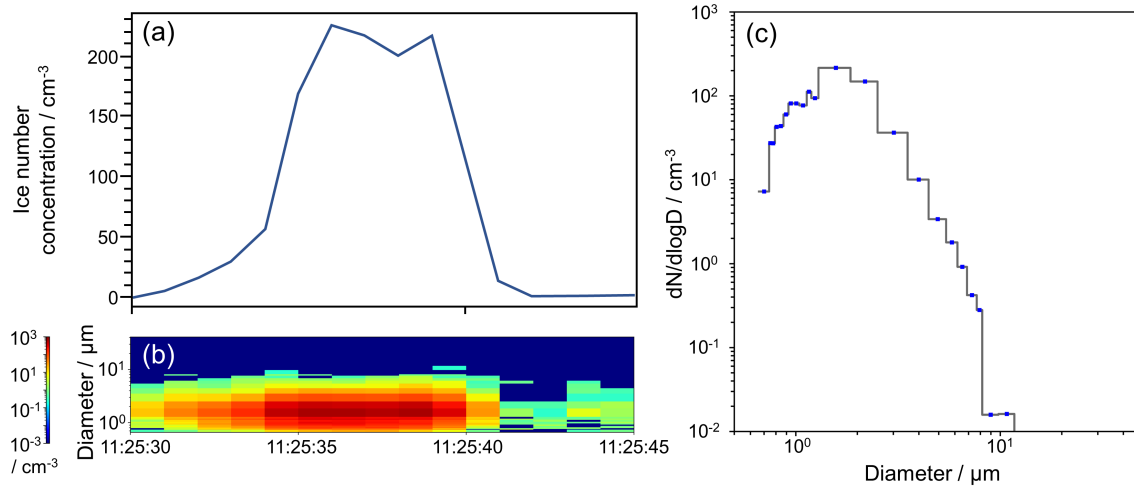


Figure 3.9: (a) Total ice particle number concentration and (b) number concentrations per size bin time-resolved for a contrail encounter sequence with (c) average particle size distribution for this sequence.

As gain stage overlaps were not always isolated in the used binnings, it was decided to consistently use all 30 bins for both instruments across all campaigns to ensure comparability.

All shown PSDs in this work are from the CAS-DPOL instrument. During the VOLCAN2 campaign, the CAPS-DPOL had several technical issues that are discussed in subsections 3.2.4 and led to the dismissal of CAPS-DPOL data for this campaign. For the ECLIF3 and VOLCAN1 campaigns, no own CAPS-DPOL calibration was available and the CAS-DPOL had a higher size resolution in the size range up until 10 μm . Therefore, while PSDs generally matched between the two instruments, discussed trends in PSDs depending on ambient conditions were more clearly discernible in the CAS-DPOL data and it was thus chosen as the primary instrument for size distributions.

In order to better visualize trends depending on parameters such as ΔT_{SA} , RHi or Δz , several PSDs of individual contrail encounters from specified fuels or combustion modes and defined conditions can be plotted together in one respective figure. To be able to discern trends in the "small" and "large" contrail ice particle size range, PSDs are normalized to their respective bin with the highest $(dN/d\log D)_i$ value, which usually lies between 1 μm and 4 μm . All particle sizes smaller than this highest bin are classified as "small" and all particles larger than this bin are classified as "large". Results presented in this way are found in chapters 5, 6, and in Appendix A.

3.2.4 Comparison of CAS-DPOL and CAPS-DPOL instruments

During the campaigns discussed in this work, systematic differences in number concentration counting were found between the two cloud probes CAS-DPOL and CAPS-DPOL with varying severity. The extent of these differences and possible reasons for them will be discussed in the following.

The spatial extension of contrails is only slightly larger compared to the size of the DLR Falcon

research aircraft. It is therefore likely that ice particle concentration differences are measured by instruments mounted at different positions on the aircraft. The CAS-DPOL and CAPS-DPOL were mounted symmetrically in the horizontal aircraft axis and contrail probing in measurement sequences was conducted from below the contrail without horizontal bias. It is therefore unlikely that a systematic difference between the instruments would result from their difference in mounting position onboard the Falcon aircraft and would not be averaged out over the course of a measurement.

The two cloud probes also cover a similar particle size detection range as can be seen by comparing Tables C1 and C2. The CAPS-DPOL's detection size range covers slightly smaller and larger particles compared to the CAS-DPOL. However, very large particle sizes above approximately 10 μm are irrelevant for contrails, while the contribution of very small particles below approximately 0.6 μm is approximately two orders of magnitude smaller than the main contrail particle size mode. Therefore, for the purpose of contrail ice particle measurements, the two instruments can be seen as measuring in the same size range.

In an exemplary flight of the ECLIF3 Q4 (November 2021) campaign, the relationship between the two instruments did not exactly follow the ideal 1:1 line. Instead, it appears to show two domains, with one domain showing good agreement and the other a systematic deviation. To better understand the nature of these two domains, the sequence of matching number concentrations is isolated and compared against the adjacent sequence in which the two instruments deviate in their number concentrations. This comparison is shown in Figure 3.10, where plots in the left column ((a), (c), (e)) correspond to the matching measurements and plots in the right column ((b), (d), (f)) correspond to deviating measurements. These deviations are shown in panels (a) and (b) for the measured number concentrations during the respective time sequences by the two instruments. The subsequent plots show ADC histograms over the pbp files during measurement sequences of the CAS-DPOL in the second row ((c), (d)) and for the CAPS-DPOL in the third row ((e), (f)). As absolute y-axis values depend on the histogram bin width, the axes are in arbitrary units. Hence, the relationship of counts is more relevant than the absolute heights of histograms.

During the matching measurement sequence, there is a significant number of counts in the CAS-DPOL high gain stage and the mid gain stage, while during the sequence of non-matching measurements between the instruments, counts are found almost exclusively in the mid gain stage. Similarly, the high gain stage of the CAPS-DPOL detects a significant number of counts while an apparent peak is found at the transitions between high and mid gain stage. In panel (f), the share of counts in the low gain stage increases. This indicates that for the plots in the right hand column, measured particles were larger than on the left hand side. It can therefore be concluded that there is a size-dependent sampling bias in at least one of the instruments.

Two options come to mind in order to explain this phenomenon. As almost all counts fall into the CAS-DPOL's mid gain stage when the instruments deviate (s. panel (d)), it is possible that this gain stage counts too many particles or that the instrument's sample area is underestimated for larger particles. The other option could be that the CAPS-DPOL misses a certain number of particles,

especially when the particle's sizes correspond to ADCs in or around the gain stage transition. There, an obvious gap is found between the highest ADCs recorded in the high gain stage and the beginning of the low gain stage, as mentioned in subsection 3.2.2.

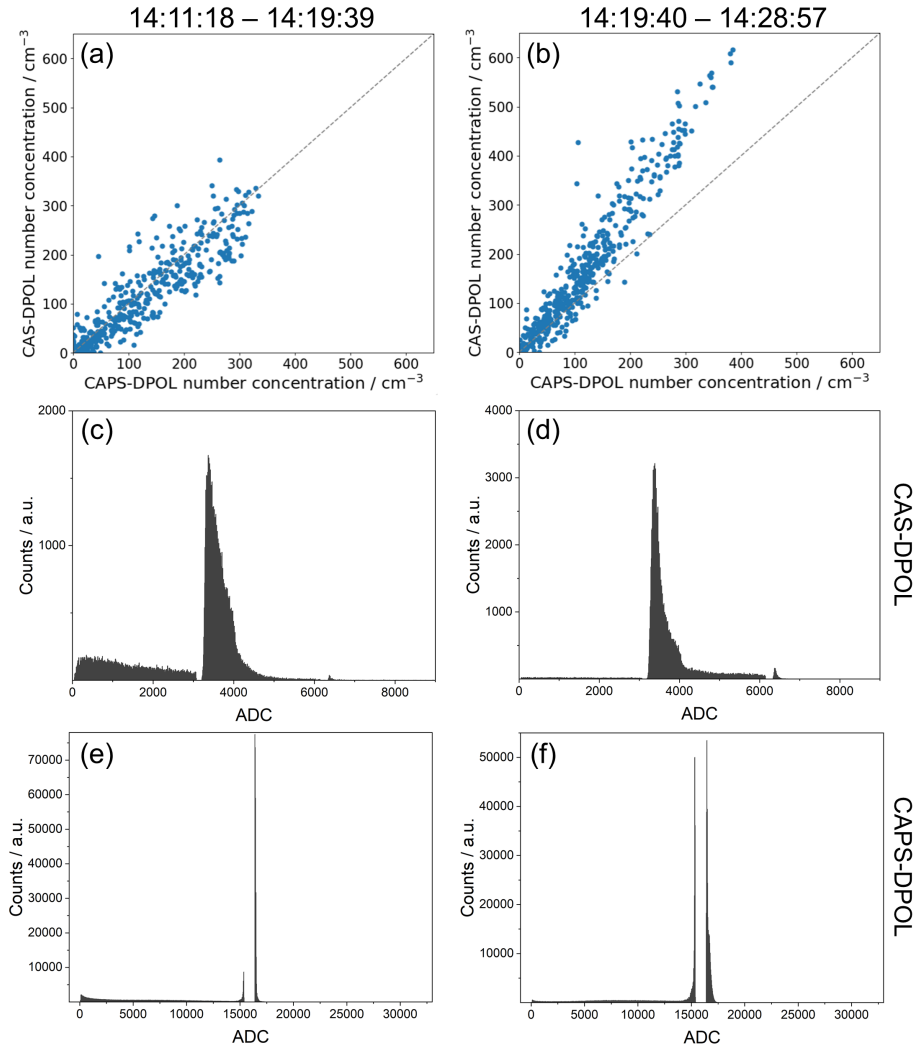


Figure 3.10: 1 Hz CAS-DPOL vs. CAPS-DPOL number concentrations ((a), (b)) during the respective measurement sequences indicated at the top of the plot columns ((a), (c), (e) and (b), (d), (f)) with corresponding CAS-DPOL pbp histograms ((c), (d)) and CAPS-DPOL pbp histograms ((e), (f)).

This gap between the CAPS-DPOL's high and low gain stage was found to vary during different measurements and campaigns. While no gap was observed during calibration measurements in preparation for the VOLCAN1 and ECLIF3 Q4 campaigns (not used to obtain transfer functions), a gap was found during mentioned campaigns. This shows that it is possible in principle to record data across the entire ADC range of the high gain stage.

In Figure 3.11, an overview is given over the agreement between CAS-DPOL and CAPS-DPOL during the ECLIF3 Q2 ((a), (d), (g)), VOLCAN1 ((b), (e), (h)), and VOLCAN2 ((c), (f), (i)) campaigns.

The first row ((a), (b), (c)) again shows the ice particle number concentrations measured by the CAS-DPOL and CAPS-DPOL during contrail measurements of the respective flights. Corresponding CAS-DPOL pbp ADC histograms are shown in the second row ((d), (e), (f)), and CAPS-DPOL pbp ADC histograms in the third row.

During ECLIF3 Q2, the two instruments match relatively well. The spread in data points is likely a result of the mentioned inhomogeneities encountered in contrails that however do not appear to result in a systematic bias. By comparing plots in the first row, it can be seen that disagreement between the two instruments increases from left to right so that a strong disagreement with systematically much higher CAS-DPOL number concentrations is found in the shown VOLCAN2 flight.

When comparing the corresponding histograms of the CAS-DPOL in the second row, it can again be seen that many counts are detected in the high gain stage in panel (d), almost all counts are found in the mid gain stage in panels (e) and (f), and a higher share of counts is found in the upper half of the mid gain stage in panel (f). This again indicates larger average particle sizes in every subsequent compared flight. A similar trend is observed for the CAPS-DPOL in the third row. There, the ratio of counts in the high gain stage to counts in the low gain stage decreases from left to right, indicating a particle size peak shifting towards higher ADC values and thereby increasing particle size. This increasing particle size is not attributed to the campaigns in general but to the specific compared flights. The ADC histogram (not shown) of flight F09 of VOLCAN2 for example appears similar to that of ECLIF3 Q2 MF4 and good agreement between the two instruments is found (s. Figure C3 (b)). This further reinforces the hypothesis that the mismatch in number concentration detection between the two instruments is related to the particle size.

However, the CAPS-DPOL histograms in the third row also reveal a varying gap size between gain stages in the different campaigns. This gap is 1469 ADC wide in panel (g), 982 ADC in panel (h) and 3522 ADC in panel (i). As the main particle size mode wanders from small ADC values towards the gain stage transition, the disagreement between instrument increases. In panel (g), many small particles are detected in the high gain stage and likely a small number of counts falls into the gap area. For the larger particles in panel (h), a significant peak is found around the gap area and in panel (i), the left half of the peak seems to be completely missing. The size related bias of instrument disagreement coinciding with the particle main size mode lying in the gain stage gap raises the suspicion that certain particles with allocated ADC in the gap might not be counted. This could be an explanation for the strong disagreement of the instruments during VOLCAN2 where the gap is largest and larger particles are expected at ADCs in the gap.

At the time of writing, the exact source of the gap and its significance are still under investigation and in discussion with the manufacturer. From laboratory experiments, the exact setting of gain stage baselines appears to be a likely reason for this gap, but physical changes within the instrument over time likely also play a role. The pbp files of the histograms in panels (g) and (h) were recorded using the same configuration file, i.e. the same "D/A Controller" values (baseline settings)

and the same ADC and size binnings. Yet, the gap width differs for these two measurements, suggesting changing conditions (e.g. aging, misalignment of optics) within the instrument.

From these comparisons, it can not be finally and conclusively clarified which of the instruments may have counted too many or too little particles. The ADC of the CAPS-DPOL strongly suggests that this instrument misses particles but it can also not be excluded that the CAS-DPOL counts too many. As there is no independent counting reference measurement, it was decided to use the measurements from both instruments together for the evaluation of ECLIF3 and VOLCAN1.

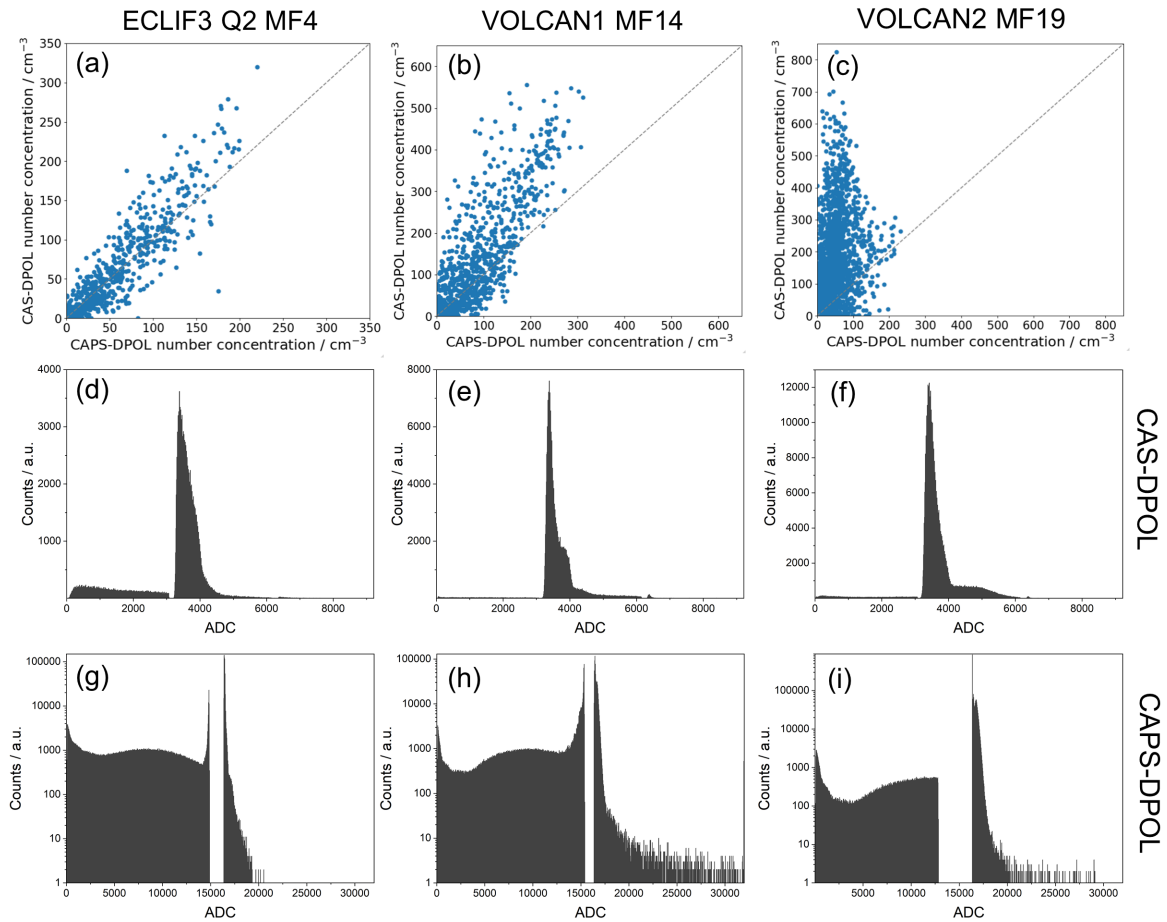


Figure 3.11: 1 Hz CAS-DPOL vs. CAPS-DPOL number concentrations during the respective contrail measurement sequences in (a) flight MF4 of ECLIF3 Q2, (b) flight MF14 of VOLCAN1, and (c) flight F19 of VOLCAN2 with corresponding CAS-DPOL pbp ADC histograms (d), (e), (f) and CAPS-DPOL pbp ADC histograms (g), (h), (i).

For VOLCAN2 however, there was a number of reasons not to use data from the CAPS-DPOL for further analyses. A faulty dynamic pressure sensor in the instrument led to unrealistic PAS readings, which however is unlikely to affect the measured number concentration as the aircraft true air speed (TAS) is used in data processing. However, during flight F11, one of the fuses responsible for the instrument heaters had blown, which led to a dramatic drop in the probe's internal temperature. As a result, the sizer high gain stage baseline ran into saturation and nothing was recorded

during the chase flight sequence. Generally, the CAPS-DPOL's baselines behaved in an unpredictable way during the campaign but with a temperature and pressure correlation to a certain degree in parts of the measurement flights. During flight F17, the CAPS-DPOL measured systematically higher concentrations than the CAS-DPOL but with no discernible contrail peak structure. Instead, the first bin of the instrument showed signs of strong noise and unrealistically high values for no apparent reason. This behavior was not found again during the subsequent flight the next day. Examples of different levels of agreement between the two instruments during the VOLCAN2 campaign can be found in Figure C3 in Appendix C.

While size calibration of the instruments is possible, there was no access to a reliable counting calibration in the course of this work. Calibrating the number concentration detection of the two instruments would be an extremely valuable tool in detecting overcounting and undercounting. One attempt at comparing the particle counting values of the two instruments was conducted before the ECLIF3 Q2 campaign and again during VOLCAN2 by connecting the inlet tube of one instrument to the outlet of the other and repeating the measurements in a vice versa configuration. In principle, calibration beads injected into the first instrument should also be detected in the second instrument. Several measurements were conducted with various particle bead sizes but results were not conclusive and depended on the order of the instrument configuration. It is unclear if the concentration of injected particles in the respective instrument sample volumes remains constant and also if calibration beads impact on the tube walls and get stuck there. Both would lead to differing particle number concentrations.

In another configuration, the two inlet tubes of both instruments faced each other and calibration beads were injected via a flow splitter to both instruments. This led to a broad distribution of number concentrations of the two instruments with no discernible trend. Likely, no equal and homogeneous splitting of bead particle numbers into both instruments was achieved in this configuration. Therefore, this method could not be confirmed as a suitable method to reliably compare number concentration measurements between two CAS instruments.

3.3 Aerosol measurement systems

Parts of the methods described in this section have been published in the journal article "Powering aircraft with 100 % sustainable aviation fuel reduces ice crystals in contrails" (Märkl et al., 2024) in Atmospheric Chemistry and Physics, 24, 3813-3837, 2024, doi: 10.5194/acp-24-3813-2024. The descriptions have been extended here and are valid for ECLIF3 and VOLCAN measurements.

During the flight campaigns described in this work, aerosol measurements play a large role in interpreting contrail ice particle number concentrations, as they constitute the condensation nuclei needed for ice particle formation. The measurements differentiate between nvPM and total aerosol

particles (nvPM + volatile particulate matter (vPM)). Soot and other incompletely combusted organic particles make up the majority of nvPM, while volatile particles condense from exhaust gases containing lubrication oil, hydrocarbons, sulfate and other constituents after dilution and cooling in the plume (Timko et al., 2010b; Yu et al., 2019). Unlike the ice particle instrumentation, the aerosol measurement instrumentation is not mounted at the bottom of the DLR Falcon's wing. Rather, the particles enter an inlet mounted at the top of the Falcon's fuselage and pass through a tubing system into the aerosol measurement system in the cabin. There, a flow splitter directs one part of the sampled air and particles directly to condensation particle counters (CPCs) for the measurement of total particles, while the other part of the sampled air first passes through a thermodenuder (TD) set at 250°C in which volatile compounds are evaporated so that nvPM can be measured in the CPCs (Märkl et al., 2024).

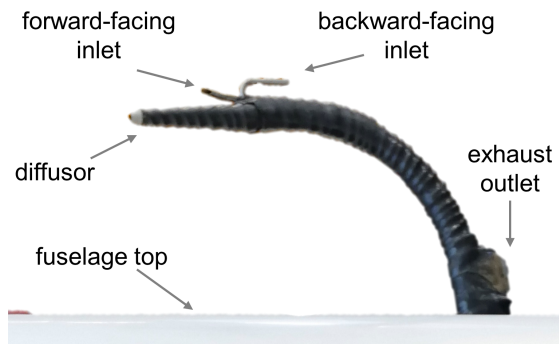


Figure 3.12: Side view of the aerosol inlet system mounted on the top of the DLR Falcon fuselage. Photograph modified from original, courtesy of Georg Dietz of DLR FX department.

The DLR Falcon inlet is described in Fiebig (2001) and consists of a diffuser intended to reduce the air stream speed by roughly a factor of 7, which then enters the forward-facing inlet. During the VOLCAN2 campaign, a configuration was also available with a backward-facing inlet with which some of the measurements were conducted. By reducing the air stream speed in the inlet, turbulence within the inlet tube can be avoided that could lead to particle loss by impacting the inlet tube walls. At the base of the inlet after having passed the inlet curve, the airstream then enters the cabin

quasi-isokinetically (i.e. at aircraft speed TAS reduced by the diffuser factor without boundary layer effects). In this way, even larger particles like contrail ice crystals are able to pass the curve of the inlet and are not lost by impacting the inlet walls. However, TAS values encountered during the flights discussed in this work exceed those where isokinetic conditions are ensured so that contrail ice particles (together with the aerosol particles contained therein) are enriched in the inlet (Schöberl et al., 2024). Therefore, a correction factor to this enrichment of 76 % was calculated based on the equations in Krämer and Afchine (2004) and Hinds (1999) and a typical contrail ice particle size distribution found during the ECLIF3 campaign (Märkl et al., 2024). This correction factor is applied to 96 % of each median nvPM EI value from far-field contrail measurements, assuming a nucleation efficiency of 96 % according to Kärcher et al. (2018) (Märkl et al., 2024). This correction was only applied to flight MF4 of ECLIF3, discussed in Chapter 5 and the underlying publication Märkl et al. (2024). The exact correction factor is sensitive to the assumed size distribution, which varied for the different conditions encountered during the VOLCAN campaigns. Schöberl et al. (2024) describe the inlet's overall sampling efficiency as a combination of the competing enrichment and particle losses, for example due to sampling system size cutoffs. These efficiencies are

TAS and size-dependent. For typical TAS during the discussed campaigns and typical size distributions of VOLCAN2, the overall sampling efficiency ranges between approximately 80 % to 120 % with a large indicated uncertainty. As a detailed discussion of absolute far-field aerosol EI is not the focus of this work, the inlet correction was omitted for the VOLCAN campaigns. The backward-facing inlet is simply a backward-facing tube, in which the procedure of diffusion and isokinetic probing is not implemented as larger particles (e.g. ice crystals) can't enter the backward-facing inlet. A photograph of the described inlet system can be found in Figure 3.12.

After the particle containing air stream has entered the aerosol measurement system in the Falcon cabin, the part of the air stream to be sampled as nvPM is directed towards a thermodenuder. There, the air stream and particles are heated to 250°C so that any volatile material and/or ice surrounding nonvolatile particles is evaporated. After passing the heated section of the thermodenuder, the air stream passes a cooled section where any gaseous volatile material or water vapor condenses and is removed from the sampling system. For the used measurement system, 250°C was determined in laboratory experiments by Daniel Sauer and Rebecca Dischl (DLR Institute of Atmospheric Physics (IPA)) to sufficiently remove semivolatile material and to reduce the risk of sublimating previously condensed volatile material and reintroducing it to the measurement system compared to higher temperatures.

Finally, the thermodenuded (for nvPM measurement) or non-thermodenuded (for total particle measurement) sample air stream enters a set of CPCs (custom made based on TSI Inc. CPC model 3010). These are in principle optical scattering instruments in which a laser is focused on particles and the intensity of scattered light detected in forward-scattering direction. However, the aerosol particles intended for measurement are initially too small to be detected in this way due to low scattering intensity. Therefore, the particles first pass through a saturated butanol atmosphere and are subsequently cooled in a condensation section. There, the sample is strongly supersaturated and the small particles are activated so that butanol droplets form on them. These then grow further by several orders of magnitude until they enter the measurement chamber where the laser scatters on the butanol droplets and counts them. However, no information on the size distribution of particles is obtained using this measurement technique. Several CPCs are used where each has a different lower cutoff diameter D_{50} , defined as the particle diameter at which counting efficiency reaches 50 %. The different lower cutoff diameters of 12-14 nm, 35 nm, and 90 nm for nvPM during the flight experiments are achieved by the use of diffusion screen separators (Feldpausch et al., 2006) located within the inlet lines before the CPCs (Märkl et al., 2024). The two CPCs used for measurement of total particles had a hard lower cutoff of 5 nm (Märkl et al., 2024) and D_{50} of approximately 7 nm. As the pressure inside the measurement chamber is nearly at ambient pressure, the CPCs experience a counting efficiency loss (Noone and Hansson, 1990) which have been characterized by Daniel Sauer and Rebecca Dischl (DLR, IPA) in laboratory experiments (Märkl et al., 2024). Thereby, they used a setup similar to that of Hermann and Wiedensohler (2001), resulting in a parameterized correction function for each individual CPC (Märkl et al., 2024). The overall

uncertainties occurring during far-field aerosol measurements discussed in this work amount to approximately 18 % (Märkl et al., 2024) and approximately 10 % during near-field measurements (Dischl et al., 2024).

Aerosol measurements were performed and processed by Daniel Sauer, Rebecca Dischl and Felicitas Sakellariou (DLR, IPA). I processed 1 Hz nvPM and total particle concentration time series to calculate far-field EI for the VOLCAN2 campaign. Far-field EI for VOLCAN1, ECLIF3, as well as all near-field aerosol EI were calculated and provided by Rebecca Dischl.

3.4 Trace gas and water vapor measurements

Parts of the methods for NO_y and water vapor measurements described in this section have been published in the journal article "Powering aircraft with 100 % sustainable aviation fuel reduces ice crystals in contrails" (Märkl et al., 2024) in Atmospheric Chemistry and Physics, 24, 3813-3837, 2024, doi: 10.5194/acp-24-3813-2024. The descriptions have been extended here and are valid for ECLIF3 and VOLCAN measurements.

In the context of contrail measurements, trace gases are an important measured quantity. The gases CO_2 and NO_y can both be used as quasi-inert tracers to gauge the level of dilution in the measured contrail. The amount of CO_2 emitted per kg of burned fuel depends on the fuel's H:C ratio while the amount of NO_x emitted per kg of burned fuel depends mainly on the combustion temperature (Blakey et al., 2011). With this knowledge of expected CO_2 and NO_y concentrations in an undiluted plume, the level of dilution can be calculated from measured concentrations in the diluted plume. Therefore, said trace gases are essential in the analysis of in-situ contrail data and their measurement principles are briefly explained in the following. Trace gas measurements were performed and processed by Theresa Harlass, Tiziana Bräuer and Monika Scheibe (DLR, IPA). I processed 1 Hz CO_2 and NO_y time series to calculate AEIs and far-field aerosol EIs from the VOLCAN2 campaign.

CO_2 measurements

CO_2 was measured using two different instruments onboard the Falcon, the Licor LI-7000 and the Cavity Ring-Down Spectrometer (CRDS) from Picarro Inc. Both instruments are mounted in the DLR Falcon's cabin and receive sample air through an inlet on the aircraft's fuselage top close to the aerosol inlet. Usually, a backward-facing inlet is used for the CO_2 measurements. During the VOLCAN2 campaign however, technical issues with pressure fluctuations at high altitudes made the use of a forward-facing inlet necessary so that it needed to be closed during sequences where liquid water droplets were expected, in order to avoid liquid water entering. The CRDS is able to measure CO , CH_4 and CO_2 , while the LI-7000 measures CO_2 and H_2O . For all further processing of

far-field contrail measurement data, only Licor LI-7000 data was used due to its faster reaction time and higher sampling rate compared to the CRDS (0.5-1 Hz for CRDS and up to 10 Hz for LI-7000). Therefore, only the LI-7000 measurement principle will be discussed.

The Licor LI-7000 is a high-speed precision differential nondispersive infrared sensor (NDIR) gas analyzer used for the measurement of CO₂ concentrations during in-flight measurements. According to the instrument's manual (*LI-7000 CO₂ /H₂O Analyzer Instruction Manual 2007*), the CO₂ and H₂O measurements are conducted by comparing the difference in infrared radiation absorption passing through two gas sampling cells. There, the reference cell has a known CO₂ or H₂O concentration and the sample cell contains the sample gas with unknown CO₂ and H₂O concentration. Depending on the CO₂ concentration present in the sampling cell, the intensity of source infrared radiation is reduced in the characteristic 4.255 μm absorption band. The instrument was calibrated extensively on the ground before and during the discussed campaigns between every couple of flights and as often as logistically possible. The instrument's precision varied across the different measurement flights based on the performed calibrations and ranged from 0.04 ppm to 0.08 ppm and the accuracy is constant at 0.2 ppm.

NO_y measurements

The sum of NO_x (NO and NO₂) and other nitrogen oxides such as HNO₃ and HONO makes up total reactive nitrogen (NO_y) (Ziereis et al., 2022). NO_y is measured onboard the DLR Falcon by probing sample air through a backward-facing inlet mounted on top of the aircraft's fuselage, which then passes through a tubing system to the instrumentation within the cabin. There, the reactive nitrogen species are first catalytically reduced to NO by a heated gold converter and H₂ reducing agent (Ziereis et al. (2022), and contained references). The air sample containing NO as only nitrogen species then enters the chemiluminescence detector (CLD) 780TR by Eco Physics AG, modified for in-flight use. There, NO reacts with high concentrations of O₃ to an electronically excited state NO₂^{*}, which emits photons via chemiluminescence when transitioning to its ground state. The intensity of light from this chemiluminescence is proportional to the NO concentration in the air sample (Harlass et al., 2024). During the discussed campaigns, the instrument probed with a sampling rate of 1 Hz (Märkl et al., 2024). Its precision was constant at 0.5 ppb, while accuracy depends on the counting rate and dilution of the sample air. Extensive ground-based calibrations were performed in between flights as often as logistically possible and zero air measurements were performed during measurement flights in sequences without contrail or emission plume encounters.

Water vapor measurements

The Schmidt-Appleman contrail formation threshold is a function of, among others, RH_i, while contrail ice particle persistence depends strongly on the level of ice supersaturation. Therefore, an accurate measurement of RH_i is essential to evaluating and interpreting recorded contrail encoun-

ters.

In principle, several instruments can be used to measure water vapor concentrations and relative humidity. In the course of this work, water vapor mixing ratios measured by the Airborne Mass Spectrometer (AIMS) (Kaufmann et al., 2016, 2018) were used for calculations of RH_i and all further analyses. This cabin-mounted instrument receives ambient air through a backward-facing inlet on the DLR Falcon's fuselage top and tubing connecting the inlet to the instrument. AIMS has been designed for high-frequency water vapor measurements in the upper troposphere and lower stratosphere and operates by ionizing the air sample and detecting the formed ions in a linear quadrupole mass spectrometer (Kaufmann, 2013).

As RH_i is a function of water vapor mixing ratio, ambient pressure, and temperature, it is also sensitive to altitude changes during measurement flights. Generally, the undisturbed atmosphere at the time and point of contrail formation would be the desired quantity for the calculation of T_{SA} and to assess the level of atmospheric ice supersaturation. However, reliable measurements onboard the source aircraft are not available and AIMS water vapor concentration and Falcon pressure and temperature measurements are used instead. In principle, one could try to define background sequences before and after contrail encounters to approximate RH_i of the undisturbed atmosphere. In reality, RH_i fluctuates strongly along the flight path even at constant altitudes due to probing of different air masses. These differences in RH_i far outweigh possible fluctuations due to emitted water vapor when measuring within a contrail. In typical far-field contrail measurement sequences (several minutes old and ice particle forming), it can be assumed that emitted water vapor has been almost completely processed to contrail ice particles as this happens on the order of tens of seconds (Kaufmann et al., 2014). Therefore, all given RH_i and T_{SA} based thereon in this work are from AIMS measurements onboard the DLR Falcon at the time of contrail detection.

The uncertainty of RH_i is dominated by the uncertainties in water vapor concentration measurements of 8-12 % depending on the actual mixing ratio and Falcon temperature uncertainty of approximately 0.5 K, while the influence of the static pressure uncertainty is negligible (Märkl et al., 2024). Overall, the uncertainty of RH_i can be approximated with 15 % (Märkl et al., 2024). This estimate pertains to absolute RH_i values, which are relevant especially for the determination of ice supersaturation. Uncertainties of the difference between RH_i values are likely much smaller and are estimated to 2 % due to statistical uncertainties of measurement sequences, which are primarily from signal noise. For water vapor concentrations above approximately 150 ppm, the sensitivity of the instrument decreases and it has to be evaluated on a case-by-case base if measured values are still reliable, leading to increased uncertainty. In this work, such high water vapor concentrations were encountered only during flight F21 of the VOLCAN2 campaign where the exact measured values had significantly higher uncertainties.

Water vapor measurements were performed by Stefan Kaufmann, Andreas Marsing and Laura Tomsche (DLR, IPA) and processed by Stefan Kaufmann. I used 1 Hz mixing ratio and RH_i time series to evaluate the level of ice supersaturation or subsaturation during contrail measurements by averaging over each plume encounter and assessing if this average lies above or below 100 %.

3.5 Research aircraft DLR Falcon and contrail chasing

Parts of this section have been published in the journal article "Powering aircraft with 100 % sustainable aviation fuel reduces ice crystals in contrails" (Märkl et al., 2024) in *Atmospheric Chemistry and Physics*, 24, 3813-3837, 2024, doi: 10.5194/acp-24-3813-2024. The descriptions have been extended here and are valid for ECLIF3 and VOLCAN measurements.



Figure 3.13: DLR Falcon aircraft from a (a) side view with inlets visible and from a (b) front view with underwing instrumentation and nose boom visible. Photographs taken during a refueling stop during the VOLCAN2 campaigns at the general aviation terminal of Málaga Airport (ICAO code: LEMG) on 04 March 2023.

The DLR Falcon 20E-5 (registration D-CMET and referred to as DLR Falcon in this work) is a versatile twin-engine business jet class research aircraft and has been in service for DLR since 1976 on a large number of scientific research campaigns (Schulte and Schlager, 1996; Arnold et al., 1999; Schumann et al., 2002; Newman et al., 2012; Kleine et al., 2018). This highly modified aircraft is able to accommodate a wide array of instrumentation for atmospheric measurements related to water vapor, trace gases, aerosols, cloud particles, and a large set of ambient conditions (Krautstrunk and Giez, 2012). Figure 3.13 shows a (a) side view and (b) front view of the aircraft with the fuselage-top mounted inlets visible in panel (a) and the four underwing probes visible in panel (b) mounted in so-called Knollenberg pylons. The CAS-DPOL and CAPS-DPOL instruments are located approximately 2.8 m below the fuselage-top inlets in the vertical axis and approximately

2.7 m from the inlets in the horizontal axis. Therefore, the two cloud probes are 5.3 m¹ apart horizontally and approximately 4 m from the inlets in a direct line. Aside from added scientific instrumentation, the Falcon's onboard instrumentation measures highly resolved aircraft position data (latitude, longitude, altitude) and dynamics data (e.g. TAS), together with data on ambient meteorological conditions such as temperature, pressure and wind field (Bögel and Baumann, 1991; Krautstrunk and Giez, 2012; Giez et al., 2017, 2020, 2021, 2023)². Temperature and pressure accuracy is given with 0.5 K and 0.5 hPa respectively (Kaufmann et al., 2014). Positional data are combined with those from the respective investigated emission source aircraft to calculate distances between the aircraft and associated plume and contrail ages (see subsection 4.1).

The aircraft is operated by two pilots and one flight engineer and there is seating for four scientists to operate their respective instruments. With a range of up to 3700 km and a ceiling altitude of 12.7 km together with structural and aerodynamical robustness make this aircraft ideal for measurements in challenging environments such as in contrails and highly turbulent near-field chase sequences behind large passenger aircraft (Krautstrunk and Giez, 2012). During chase sequences for contrail measurements, flight levels (altitudes) were chosen based on meteorological predictions where contrail forming conditions were expected as well as where there was little or no cloud cover. High altitude clouds can drastically impair visual conditions, making it difficult for the Falcon crew to find the produced contrails. Therefore, contrails were often times probed directly above high altitude cloud covers where humidity was high enough for contrail formation and visibility was sufficient to find the contrails. In order to aid the pilots in finding contrails in far-field measurements, the so-called Breadcrumb tool was used. There, the Falcon's own position from a separate GPS receiver is compared to positional data of aircraft in the vicinity from their Automatic Dependent Surveillance–Broadcast (ADS-B) signals, received by a Open Flight Solutions Flightbox Plus (now distributed by Falken Avionics). By selecting the source aircraft, its flight path together with wind field data from European Centre for Medium-Range Weather Forecasts (ECMWF) or Global Forecast System (GFS) predictions is used to predict the position of potentially forming contrails so that finding contrails in the far-field regime without visual contact with the source aircraft is greatly facilitated. The tool was developed by Robert Baumann and Monika Scheibe (DLR, IPA) and deployed and operated by Monika Scheibe during the discussed flight campaigns.

¹In Märkl et al. (2024), 7 m was given. This minor error does not justify a corrigendum of the publication but is presented correctly here.

²Data from the Falcon onboard instrumentation was processed and provided by Andreas Giez, Christian Mallaun, Vladyslav Nenakhov, and/or Martin Zöger (DLR FX department).

CHAPTER 4

Data analysis

During contrail measurement flights, data files are obtained for every used instrument. Data files relevant for contrail evaluation include files from the two separate contrail ice particle measurements (CAS-DPOL and CAPS-DPOL), trace gas measurements (CO_2 and NO_y), aerosols, water vapor measurements, as well as data on position, dynamics, and meteorological parameters of the Falcon and emissions source Airbus aircraft. At the beginning of each data evaluation, these single files are read and processed by the Python Jupyter Notebook developed in the course of this work. Before performing a measurement flight, the instrument's data acquisition computers are synchronized to the central time reference of the Falcon. However, due to delays in measurement from long inlet tubing, different instrument reaction times and possible data acquisition computer crashes, the recording times can become desynchronized. Therefore, time series of each instrument file need to be manually synchronized by plotting them together and determining the time shift of characteristic peaks (e.g. from contrail encounters, low cloud encounters, takeoff, landing, etc.). With this time shift, all instrument time series can be synchronized to the Falcon timeline. Finally, all time series are merged together in one master Pandas DataFrame, which is used for all further time series processing.

4.1 Contrail ages, microphysical parameters and T_{SA}

This section extends information described in shorter form in the journal article "Powering aircraft with 100 % sustainable aviation fuel reduces ice crystals in contrails" (Märkl et al., 2024) in Atmospheric Chemistry and Physics, 24, 3813-3837, 2024, doi: 10.5194/acp-24-3813-2024. The descriptions are valid for ECLIF3 and VOLCAN measurements.

Plume/contrail ages

The time between plume emission (\sim contrail formation) and detection is calculated with two independent methods based on World Geodetic System 1984 (WGS84) GPS latitude and longitude

data from the two aircraft (Märkl et al., 2024). In both methods, horizontal aircraft distances are the great circle distances assuming the Earth's radius as $r_{Earth} = 6368.31$ km and adding the flight altitude (Märkl et al., 2024). Vertical distances are simply the difference between the WGS84 GPS altitudes of both aircraft (Märkl et al., 2024). The total distance between the two aircraft is then the Pythagorean distance using the horizontal and vertical distance (Märkl et al., 2024).

For the first plume age calculation method, the wind field at the Airbus emission source aircraft is calculated with the three input values heading, wind speed and wind direction, measured at time of emission (Märkl et al., 2024). This way, the drift of the contrail between the time of formation and detection is considered (Märkl et al., 2024). The plume age is then calculated iteratively for each point in time by taking the total distance between the two aircraft and calculating how many time steps are needed for the Falcon to cover this distance considering the Falcon's ground speed along the flight path added to the previously calculated head wind component (assumed constant from the point of emission). This method iterates in forward direction as it begins with the total distance at point i and saves the time difference $t(j) - t(i)$ at which this distance is covered j at that position in the DataFrame. This way, a (hypothetical) plume/contrail age is calculated for every point in time during a measurement flight, so that aircraft and engine parameters at the time of emission can be allocated to times of detected plumes/contrails (Märkl et al., 2024).

In a second plume age calculation method written by Andreas Marsing (IPA, DLR), the source aircraft's TAS is used instead of measured wind speed and wind direction to quantify the wind field. This method iterates backwards from the time of detection to the point of emission and matches the ages from the first method in chase sequences. However, due to their different iteration directions, the resulting plume/contrail ages diverge for non-chase sequences. Therefore, the difference in plume/contrail age between these two methods can be used to quantify if the contrail was measured in a straight chase sequence.

Microphysical parameters

From CAS time series, several quantities can be calculated that are central to the further analyses. All quantities discussed here are given for ambient conditions encountered at the point of measurement and no conversion to standard temperature and pressure (STP) conditions is conducted. The most important is the total ice particle number concentration. The CAS bulk file records the number of detected particles in each of their respective size bins. That means that for every second, there are 30 channels with the number of detected particles in that respective size range. To obtain the total particle number concentration, the counts in all 30 bins i are summed and divided by the sample volume SV (based on DMT (2011)):

$$N = \sum_{i=1}^{30} \frac{n_i}{SV} = \sum_{i=1}^{30} \frac{n_i}{SA \cdot \Delta t \cdot TAS}. \quad (4.1)$$

The sample volume is spanned by the probe's sample area SA and the sampling length, defined

by the chosen time interval Δt and the Falcon's TAS. For the 1 Hz data considered in this work, $\Delta t = 1$ s. The Falcon's TAS is chosen as a proxy for the actual sample air speed (SAS) based on computational fluid dynamics (CFD) simulations and wind tunnel measurements performed by Valerian Hahn (DLR, IPA) (Märkl et al., 2024). These show that particle flow in the CAS inlet tube is approximated better by the aircraft's TAS than the probe's PAS (Märkl et al., 2024), which is influenced by ram pressure effects due to the sensor's position. It was chosen to always use all 30 bins, as there were no unusually high counts in the first bin that could be expected from electronic noise. Also, gain stage overlap bins were not eliminated to ensure comparability between different binnings and between CAS-DPOL and CAPS-DPOL as discussed in subsection 3.2.3. This method of calculating the total ice particle number concentration uses the CAS bulk file. Alternatively, it is also possible to calculate N using the pbp file by using the recorded IPT. The number of particles recorded in a 1 s interval is limited to 292 particles in the CAS-DPOL and 734 (ECLIF3 & VOLCAN1) or 511 (VOLCAN2) particles in the CAPS-DPOL so that not all particles are recorded. Therefore, in order to calculate total number concentrations using the pbp file, the total number of recorded particles in the 1 Hz interval is divided by the summed IPT values, which gives an average counting rate for the 1 s interval. The equation then changes to (based on Baumgardner (1986)):

$$N = \frac{\sum_{1s} n_{i,pbp}}{SA \cdot TAS \cdot \sum_{1s} IPT_{i,pbp}}. \quad (4.2)$$

In principle, this method has advantages regarding coincidence effects when many particles lie close together and several particles are counted as one, due to the numerator and denominator in equation 4.2 being reduced. In sequences of high particle number concentrations where the number of counts exceeds those recorded in the pbp file, calculating total particle number concentration in this way is an extrapolation. For the count limits in the CAPS-DPOL, the pbp file records < 10 % of counts in the bulk file and for the CAS-DPOL, the pbp file records \ll 10 % of counts in the bulk file. Therefore, in sequences with strong concentration variability within one second, the alternative IPT based method extrapolates the concentration encountered in the first counts up until the aforementioned counting limit for the entire second. It was therefore decided to calculate contrail ice particle number concentrations with the classical method in equation 4.1 and apply the additional coincidence correction described in subsection 4.3. Additionally, it was found that number concentrations calculated with the classical method had a better time series correlation with measured trace gases in contrail sequences.

Further, the quantity IWC is introduced, which gives the mass of ice found in a defined volume of air, analogous to the LWC for liquid water (based on DMT (2011)):

$$IWC = \rho_{ice} \cdot \sum_{i=1}^{30} N_i \cdot \frac{4\pi}{3} \cdot \left(\frac{D_i}{2}\right)^3, \quad (4.3)$$

where $\rho_{ice} = 917 \text{ kg m}^{-3}$ (Feistel and Wagner, 2006), N_i is the number concentration in bin i and D_i is the bin center of bin i and thereby the volume-equivalent diameter of the respective ice particles.

Based on IWC, another useful measure for the size of measured particles is the median volume diameter (MVD), which denotes the diameter where 50 % of the IWC is from particles smaller than the MVD and the other 50 % is from particles larger than the MVD (DMT, 2011):

$$\text{MVD} = D_{l,i^*} + \left(\frac{0.5 - \text{cum}_{i^*-1}}{\text{pro}_{i^*}} \right) \cdot (D_{u,i^*} - D_{l,i^*}), \quad (4.4)$$

where $\text{pro}_i = \frac{\text{IWC}_i}{\text{IWC}}$ is the proportion of the IWC in bin i of the total IWC, $\text{cum}_n = \sum_{i=1}^n \text{pro}_i$ is the cumulative sum of proportions from bin 1 until bin n , and i^* is the lowest bin for which $\text{cum}_{i^*} > 0.5$. $D_{l,i}$ ($D_{u,i}$) denote the lower (upper) bin boundaries of bin i .

Schmidt-Appleman threshold calculation

For the calculation of T_{SA} in the course of this work, six input variables were used in a Python code written by Jonas Kleine (formerly DLR IPA) based on the equations described by Schumann (1996), including the correction made aware of by Ferrone (2011) and implemented in Schumann (2012). The ambient temperature and pressure measured by the emission source aircraft at the time of contrail formation and RH_i at the time of detection (as proxy for RH_i at time of formation) from measurements onboard the DLR Falcon were used. The other three variables propulsion efficiency η , combustion heat Q , and water vapor emission index $\text{EI}_{\text{H}_2\text{O}}$ were kept at the constant default values $Q = 43.2 \text{ MJ kg}^{-1}$ and $\text{EI}_{\text{H}_2\text{O}} = 1.23 \text{ kg kg}^{-1}$ (Schumann, 2000) for all calculations of the ECLIF3 campaign while fuel resolved values of Q and $\text{EI}_{\text{H}_2\text{O}}$ were used for the VOLCAN campaigns. The propulsion efficiency for modern high bypass ratio engines lies between $\eta = 0.3$ and $\eta = 0.4$ (Schumann, 1996; Epstein, 2014) and is therefore conservatively estimated at $\eta = 0.36$ for the modern aircraft engines investigated in the discussed campaigns.

4.2 Definition of plumes/contrails

This section extends information described in shorter form in the journal article "Powering aircraft with 100 % sustainable aviation fuel reduces ice crystals in contrails" (Märkl et al., 2024) in Atmospheric Chemistry and Physics, 24, 3813-3837, 2024, doi: 10.5194/acp-24-3813-2024.

From 1 Hz timelines of the different measurements, the times of contrail encounters must be defined for all further calculations pertaining to contrail properties. To achieve this, the timelines of ice particle measurements, trace gases, aerosols, RH_i and ambient pressure and temperature are plotted above one another in an interactive plot using the Python Bokeh package. Using this tool, it is possible to quickly adjust the zoom level and determine x-axis (time) and y-axis (concentration, RH_i, etc.) values with the cursor. By simultaneously using flight protocols written by

instrument operators on board the measurement flights, contrail encounters can be determined. A contrail encounter for the ice particle evaluation is defined as the times where the contrail ice particle number concentration departs from background levels to the time when it returns to background levels (Märkl et al., 2024). In cases where several contrail encounters are measured in quick succession, the ice particle concentration might not drop back to background levels in some cases. In order to still be able to separately investigate the contrail encounters, they were separated when the ice particle concentration dropped to approximately 15 % of the maximum ice particle concentration in neighboring peaks. These plume encounter times are the foundation of the plume definition file, in which all plume/contrail parameters are saved and used for further analysis and plotting.

Other instrument teams of aerosol and trace gas measurements define their own plume times based on their instrument response times and departures of and returns back to their respective backgrounds. This is also done in the near-field mode in emission measurements where no ice particles are measured. For ECLIF3 and VOLCAN1, aerosol contrail times were defined by the aerosol team Rebecca Dischl and Felicitas Sakellariou (DLR, IPA) and allocated to the respective defined contrail ice times, while the contrail ice particle times were used to calculate nvPM and total particle emission indices for the VOLCAN2 campaign.

With the defined plume/contrail times, relevant parameters at time of detection can be calculated such as mean engine parameters and ambient conditions, but also the preparatory values such as trapezoidal integrations over ice particle number concentrations and trace gases (minus their backgrounds). One important parameter used to assess the quality of contrail ice measurements is the Pearson correlation between ice particle time series and trace gas time series, which is calculated for every contrail encounter. Ice particle time series and trace gas time series are expected to correlate well under the assumption of full immersion of the Falcon in a contrail. Under those circumstances, the fuselage top mounted trace gas inlets and the wing mounted ice particle instrumentation probe an assumed quasi-homogeneous spatial distribution of ice particles (Märkl et al., 2024). This assumption does not hold true near the edges of contrails where one of the mentioned instrumentation can probe higher particle concentrations than the other (Märkl et al., 2024). In this case, the time series shapes of ice particle and trace gas measurement disagree, which can be quantified by the Pearson correlation. Contrail encounters with a correlation < 0.6 are excluded from further investigation as they would lead to unrealistic and misleading results (Märkl et al., 2024).

Using the calculated contrail ages, engine parameters, fuels, or ambient conditions at the time of emission/contrail formation can also be determined. Ambient pressure and temperature measured onboard the source aircraft for example are used for the calculation of T_{SA} . The emission times are also used to determine if the engine was in a stable condition based on T30 fluctuations.

4.3 Corrections and uncertainties

This section extends information described in shorter form in the journal article "Powering aircraft with 100 % sustainable aviation fuel reduces ice crystals in contrails" (Märkl et al., 2024) in Atmospheric Chemistry and Physics, 24, 3813-3837, 2024, doi: 10.5194/acp-24-3813-2024. The descriptions are valid for ECLIF3 and VOLCAN measurements.

Counting and sizing measurements from the CAS instruments come with uncertainties and artifacts that can be corrected to some extent. Uncertainties of other measurements discussed in this work are included in the AEI uncertainty calculation discussed in subsection 4.5. This subsection will begin with the discussion of artifacts before moving on to the quantification of uncertainties in counting and sizing of the CAS instruments and uncertainties of trace gas measurements.

Coincidence

At high particle number concentrations, the probability increases that more than one particle is present in the instrument's sample area at once. In this case, these several particles are detected as only one but are oversized. This effect of undercounting is called classical coincidence and is a common artifact in forward-scattering particle detection instruments, which has been quantified using instruments with differing sizer detector pinhole apertures (Lance, 2012; Kleine, 2019). In the comparison performed by Kleine (2019), a CAS with 800 μm pinhole aperture was compared to a CAS with a 500 μm aperture, for which much less coincidence effects are expected, so that a correction function for the 800 μm pinhole aperture instrument could be derived. The CAS-DPOL and CAPS-DPOL instruments used in the course of this work were both equipped with 600 μm pinhole apertures so that coincidence effects are expected but on a much smaller scale than with a 800 μm pinhole probe or one without a pinhole aperture. This also means that the correction functions determined by Lance (2012) and Kleine (2019) can't be applied to the instruments used in this work. Instead, a correction function determined specifically for the CAS-DPOL by Valerian Hahn (DLR, IPA) in laboratory experiments is used to obtain coincidence-corrected ice particle number concentrations (Märkl et al., 2024):

$$N_{\text{coinc}} = \frac{N \cdot 6323}{6527 - N}, \quad (4.5)$$

with N and N_{coinc} in cm^{-3} . As the same pinhole aperture size was installed in the CAPS-DPOL, this correction was also applied to that instrument.

Shattering

The CAS inlet tube in principle provides a site at which impinging ice crystals could shatter and thereby form many smaller secondary ice particles (Baumgardner et al., 2017). These could be detected and create a false bias towards higher particle number concentrations and smaller particle sizes. Due to the high concentration of many small particles together with a lower concentration of the original larger particles, a bimodal IPT distribution would be expected (Field et al., 2003). As the IPT mode from shattering is on the order of the main single mode from contrail ice particles (Field et al., 2003; Kleine, 2019), shattered particles from larger cirrus ice crystals would directly lead to a seemingly higher contrail ice particle concentration. However, it is also possible to simply measure contrail ice particles and cirrus ice particles at the same time, which would lead to a bimodal IPT distribution also without shattering.

In order to investigate the possibility of shattering during contrail ice particle measurements with and without cirrus clouds in the background, two exemplary IPT distributions are shown in Figure 4.1. There, a typical single mode IPT distribution averaged across a contrail encounter is seen without any second mode at smaller IPT values in panel (a). When viewing all IPT histograms of a measurement flight, there are however also bimodal distributions where the second mode is always at larger IPT values than the main contrail mode. Therefore, the second mode must result from larger background particles and does not indicate shattering of contrail ice particles. It can therefore be concluded that shattering of contrail ice particles is not found for the CAS instruments.

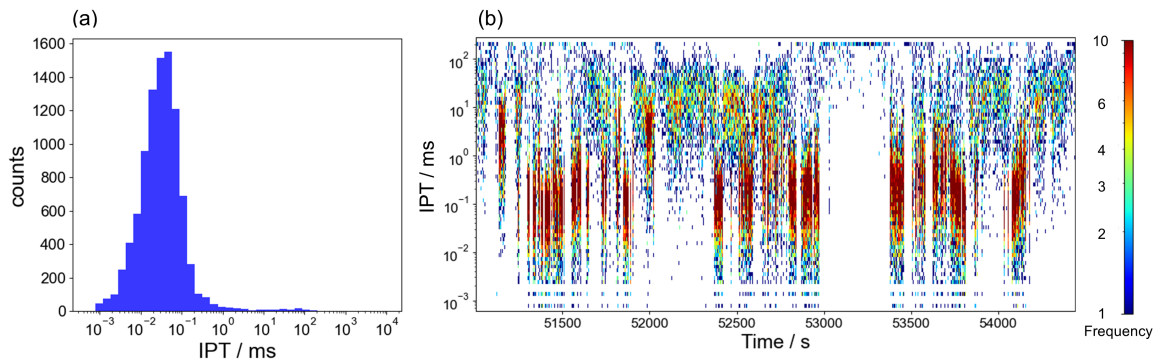


Figure 4.1: (a) Single contrail IPT histogram during flight F08 of the VOLCAN2 campaign from 13:24:56 - 13:25:29 UTC and (b) curtain IPT plot during the contrail measurement sequence of flight F09 of the VOLCAN2 campaign.

Now, it must also be excluded that larger background particles shatter and increase counts in the contrail ice particle IPT mode. For this, the IPT curtain diagram is shown during flight F09 of the VOLCAN2 campaign in Figure 4.1 (b). During this flight, hazy conditions and many cirrus clouds were encountered. Their IPT modes are seen for IPT values large than 10^0 ms and the peak of contrail ice particles is centered approximately around 10^{-1} ms. While there are sequences where both modes coexist, there are clearly also sequences of the larger cirrus particles without a second

mode at smaller IPT (e.g between 52000 and 52300 s). This lack of a second IPT mode indicates that shattering did not occur for the CAS instrument even when cirrus particles were present, so that it can be assumed that shattering also does not occur when both particle types are present simultaneously. Data discussed in this work was therefore not corrected for shattering.

Ice particle number concentration uncertainty

It was mentioned that the TAS is used as SAS in the calculation of ice particle number concentration. From the mentioned CFD calculations and wind tunnel measurements, the uncertainty of this substitution is quantified as $u_{TAS} = 7 \%$ (Märkl et al., 2024). As discussed in section 3.2 and mentioned in Märkl et al. (2024), the CAS-DPOL sample area uncertainty from calibration stand measurements performed by Valerian Hahn (DLR, IPA) was determined as $u_{SA,CAS} = 18.2 \%$, while CAPS-DPOL sample area uncertainty is given as approximately $u_{SA,CAPS} = 20 \%$ from personal communications between Valerian Hahn and DMT. Finally, a counting uncertainty is calculated, which scales inversely with the number of particle counts n in every second under the assumption of Poisson statistics (Baumgardner et al., 2017):

$$u_n = \frac{1}{\sqrt{n}}. \quad (4.6)$$

This quantifies that concentrations based on few data points (counts) have a higher uncertainty than those with many data points. For every contrail encounter sequence, the mean counting uncertainty is calculated under the conditions that the detected number concentration is higher than 1 cm^{-3} . This avoids slight fluctuations in the ice particle background disproportionately affecting the mean counting uncertainty. With these three uncertainties, the total CAS number concentration measurement uncertainty is calculated for every contrail encounter, so that the sum over counts n_i in equation 4.1 is replaced by the mean number of counts $\bar{n}_{\text{contrail}}$ and the total number concentration measurement uncertainty is given as:

$$\Delta N_{\text{meas}} = \pm \sqrt{\left(\frac{\partial N}{\partial \bar{n}_{\text{contrail}}} u_n\right)^2 + \left(\frac{\partial N}{\partial SA} u_{SA}\right)^2 + \left(\frac{\partial N}{\partial TAS} u_{TAS}\right)^2} \quad (4.7)$$

The resulting mean number concentration uncertainty is 19.8 % for the CAS and 21.5 % for the CAPS for the discussed contrail measurement flight during the ECLIF3 campaign (Märkl et al., 2024) and similar values are found for the VOLCAN campaigns. The uncertainty is resolved for every contrail encounter in all measurement flights and is used to calculate the AEI uncertainty discussed in subsection 4.5, which in turn is used for filtering of data. Therefore, a detailed breakdown of single number concentration uncertainties is not conducted here.

Ice particle size uncertainty

The determination of ice particle sizes with CAS instruments is limited by physical and technical constraints. As discussed in subsection 3.1.2, Mie resonances lead to ambiguities in the mapping of scattering cross sections to particle sizes, so that the size can't be determined with perfect accuracy even with perfectly adjusted and calibrated instrumentation (using only one wavelength of light). Further, assumptions are made on the shape and orientation of the particles, which determines the refractive index and thus the mapping of SCS to size. In reality, the measured particles are likely not all perfect spheroids with aspect ratios of exactly 0.75 so that the assumed SCS curve from T-matrix calculations is only a good approximation for the bulk of measured particles. Also, the collection angles of 4° to 12° in forward-scattering direction and a homogeneous distribution of laser intensity across the sample area are assumed, which are not perfectly realized. Through continued use of the instruments in conditions with vibrations and rough handling, it is in principle possible that the quality of alignment in the optical system diminishes and changes the actual collection angles. Similarly, the laser source and detectors can be subject to aging effects. While a coincidence correction function is applied for the calculation of particle number concentration, no correction is applied to the particle sizing so that this effect constitutes a source of uncertainty in size determination. The extent of the sizing uncertainties can be reduced through periodic size calibrations of the instruments, especially during measurement campaigns with heavy instrument use.

Baumgardner et al. (2017) discuss these uncertainty sources in greater detail and estimates a sizing uncertainty between 10 % and 50 % for forward-scattering instruments from the mentioned uncertainty sources. For the specific CAS instrumentation, Kleine (2019) gives an uncertainty of ± 20 % based on estimates by the manufacturer DMT. As a similar instrumentation was used in the course of this work, this is a reasonable approximation for the used CAS-DPOL and CAPS-DPOL.

Trace gas uncertainties

Trace gas instrument accuracy and precision were mentioned in subsection 3.4. Here, it shall briefly be discussed how CO₂ and NO_y uncertainties are determined for each contrail encounter. Generally, for both trace gas measurements, mean measurement uncertainty $\Delta\text{NO}_{y\text{meas}}$ or $\Delta\text{CO}_{2\text{meas}}$ and background uncertainty u_{bckgr} are determined. For the background uncertainty, background sequences are defined where no contrail encounters occur and other conditions such as flight altitude and temperature are as similar as possible to the contrail measurement sequences. The mean and standard deviation of each background sequences are then calculated for NO_y, while the background values for CO₂ are determined manually. As the chosen background sequences each have different lengths, their contribution to the final background and background uncertainty is then weighted by calculating the mean of each background sequence and subsequent sequence weighted by their respective lengths. These mean weighted backgrounds and corresponding standard deviations u_{stdv} are then allocated to the appropriate contrail encounters in

between. Additionally, the mean difference between trace gas concentrations at the beginning and end of a contrail encounter to the used background is calculated. This way, the uncertainty $u_{mean\Delta}$ from fluctuating background levels during a contrail encounter with one background value is quantified. The CO_2 background usually fluctuates stronger than the NO_y background, making automated background determination difficult. However, background uncertainties are still quantified based on background sequences as is done for NO_y . Finally, the total background uncertainty $\Delta\text{NO}_{y\text{bckgr}} = u_{\text{bckgr}}$ or $\Delta\text{CO}_{2\text{bckgr}} = u_{\text{bckgr}}$ is calculated by propagating the weighted background standard deviation u_{stdv} and the deltas of measured values at plume beginning and end $u_{mean\Delta}$:

$$u_{\text{bckgr}} = \sqrt{(u_{mean\Delta})^2 + (u_{stdv})^2} \quad (4.8)$$

The mean measurement uncertainty $\Delta\text{NO}_{y\text{meas}}$ or $\Delta\text{CO}_{2\text{meas}}$ is simply the mean instrument accuracy across the contrail encounter for NO_y measurements while it is constant for CO_2 .

For the ECLIF3 and VOLCAN1 campaigns, the backgrounds and uncertainties were determined by Theresa Harlaß (DLR, IPA), while they were determined by me with the described algorithm for the VOLCAN2 campaign. A detailed discussion on trace gas uncertainty calculations for NO_x determination can be found in Harlass et al. (2024).

4.4 Emission indices (EI) and apparent ice emission index (AEI)

This section extends information described in the journal article "Powering aircraft with 100 % sustainable aviation fuel reduces ice crystals in contrails" (Märkl et al., 2024) in Atmospheric Chemistry and Physics, 24, 3813-3837, 2024, doi: 10.5194/acp-24-3813-2024 in order to be valid for ECLIF3 and VOLCAN measurements. Verbatim passages (figure, table, and equation numbers adapted) are marked by quotation marks and used under CC BY 4.0 (<https://creativecommons.org/licenses/by/4.0/>).

"In order to be able to compare measurements at different contrail ages, stages of contrail vortex dynamics, and positions in the contrail, a dilution-corrected metric is needed. Generally, for particles of type X, an emission index is defined by (Beyersdorf et al., 2014)

$$\text{EI}_X = \left(\frac{\Delta X}{\Delta \text{Tr}} \right) \cdot \left(\frac{M_{\text{air}}}{M_{\text{tracer}} \cdot \rho_{\text{air}}} \right) \cdot \text{EI}_{\text{tracer}}. \quad (4.9)$$

Here, ΔX and ΔTr are the enhancement of the particle number and the mixing ratio of a gaseous tracer, which are assumed to have the same mixing behavior as the particles above their respective background. M_{air} and M_{tracer} are the molar masses of air and the tracer gas, ρ_{air} is the density of ambient air, and $\text{EI}_{\text{tracer}}$ is the emission index of the used tracer gas." (Märkl et al., 2024)

nvPM and total particle concentration time series can be converted to STP conditions or ambient

conditions from the conditions within the measurement chamber. When using STP time series for EI calculation, the factor $\frac{M_{\text{air}}}{\rho_{\text{air}}}$ in equation 4.9 becomes the molar volume V_m of an ideal gas at STP conditions (Moore et al., 2017).

"Analogous to the emission index for particle number concentrations, the apparent contrail ice emission index (AEI) describes the number of contrail ice particles formed from aircraft exhaust per kilogram of fuel burned. By using a dilution tracer and measuring in the secondary wake, a dilution-corrected metric is achieved, which can be used to draw conclusions for the two probed fuels independent of contrail age. The AEI is sensitive to processes affecting ice particle number concentrations such as sublimation, thereby resolving small-scale variations in ice particle number concentrations as well as ice particle loss due to entrainment of ice-subsaturated ambient air." (Märkl et al., 2024)

In principle, CO_2 and NO_y can both be used as dilution tracers. In the case of the investigated ECLIF3 flight, the average enhancement of CO_2 in contrails during the measurements was in the range of the background variability of CO_2 . NO_y on the other hand had a relatively low background concentration with low variations at the flown cruise altitudes. "At high engine power settings, emitted nitrogen compounds mainly consist of NO (>80%) and NO_2 , while NO rapidly reacts with O_3 to form NO_2 (Schulte et al., 1997). Therefore, in order to minimize induced uncertainties due to CO_2 background variability, NO_y was chosen as a dilution tracer. Measured NO_y contains all nitrogen species processed in the atmosphere from the initial NO_x emissions. As stated in Schulte et al. (1997), the NO_x emission index is defined in mass units of NO_2 . Therefore, NO_2 molar mass is used for the NO_y tracer together with the molar mass of air and the gas constant, resulting in the following equation dependent on measured parameters:

$$\text{AEI} / \text{kg}^{-1} = 1.807 \cdot 10^{12} \text{J kg}^{-1} \text{K}^{-1} \cdot \left(\frac{\Delta N / \text{cm}^{-3}}{\Delta \text{NO}_y / \text{ppbv}} \right) \cdot \left(\frac{T_{\text{amb}} / \text{K}}{p_{\text{amb}} / \text{hPa}} \right) \cdot \text{EI}_{\text{NO}_x} / \text{g kg}^{-1}. \quad (4.10)$$

During a chosen contrail measurement interval, ΔN and ΔNO_y are the time integrals over ice particle number concentration and NO_y concentration enhancements over their respective atmospheric backgrounds, and T_{amb} and p_{amb} are the mean ambient temperature and pressure. EI_{NO_x} refers to the NO_x emission index, which is mainly determined by thermal origin NO_x related to the combustion state rather than fuel-related effects such as fuel-bound nitrogen and H:C content-dependent peak flame temperature (Blakey et al., 2011)." (Märkl et al., 2024)

For the investigated ECLIF3 flight, EI_{NO_x} predictions conducted by engine manufacturer Rolls-Royce using their P3T3 method and corresponding to the relevant T30 ranges were used. The resulting EI_{NO_x} values are 17.4 g/kg for the T30 values corresponding to Jet A-1 sequences and 17.5 g/kg for the T30 values corresponding to HEFA-SPK sequences. (Märkl et al., 2024)

For all analyses of data from the VOLCAN campaigns, CO_2 was used as tracer. One reason was the lack of EI_{NO_x} predictions at the time of analysis and also fluctuations of the CO_2 background were lower in many cases compared to the investigated ECLIF3 flight. The used equation depending on measured parameters for CO_2 then becomes:

$$\text{AEI} / \text{kg}^{-1} = 1.888 \cdot 10^9 \text{J kg}^{-1} \text{K}^{-1} \cdot \left(\frac{\Delta N / \text{cm}^{-3}}{\Delta \text{CO}_2 / \text{ppmv}} \right) \cdot \left(\frac{T_{\text{amb}} / \text{K}}{p_{\text{amb}} / \text{hPa}} \right) \cdot \text{EI}_{\text{CO}_2} / \text{g kg}^{-1}, \quad (4.11)$$

where ΔCO_2 is now the time integral of CO_2 concentration enhancements of the atmospheric background and EI_{CO_2} is the fuel dependent CO_2 emission index. The factor at the beginning of the equation is now also different due to the different molar mass of CO_2 and due to ΔCO_2 given in ppmv instead of ppbv.

4.5 Uncertainties of AEI

This section extends information described in the journal article "Powering aircraft with 100 % sustainable aviation fuel reduces ice crystals in contrails" (Märkl et al., 2024) in Atmospheric Chemistry and Physics, 24, 3813-3837, 2024, doi: 10.5194/acp-24-3813-2024 in order to be valid for ECLIF3 and VOLCAN measurements. Verbatim passages (figure, table, and equation numbers adapted) are marked by quotation marks and used under CC BY 4.0 (<https://creativecommons.org/licenses/by/4.0/>).

Considering the dependencies of AEI in equations 4.10 and 4.11, the individual contributions to the total uncertainty for NO_y based AEI are: "(a) ice particle measurements ($\partial \Delta N_{\text{meas}}$), (b) NO_y measurement ($\partial \Delta \text{NO}_{y\text{meas}}$), (c) NO_y background determination ($\partial \Delta \text{NO}_{y\text{bckgr}}$), (d) ambient temperature measurements ($\partial \Delta T_{\text{amb}} = 0.5 \text{ K}$), (e) ambient pressure measurements ($\partial \Delta P_{\text{amb}} = 0.5 \text{ hPa}$), and (f) EI_{NO_x} prediction uncertainty ($\partial \Delta \text{EI}_{\text{NO}_x} = 10\%$." (Märkl et al., 2024) From these single uncertainty contributions discussed in subsection 4.3, the total uncertainty for AEI can be determined according to Märkl et al. (2024)¹:

$$\partial \text{AEI} = \pm \sqrt{\left(\frac{\partial \text{AEI}}{\partial \Delta N} \partial \Delta N_{\text{meas}} \right)^2 + \left(\frac{\partial \text{AEI}}{\partial \Delta \text{NO}_y} \partial \Delta \text{NO}_{y\text{meas}} \right)^2 + \left(\frac{\partial \text{AEI}}{\partial \Delta \text{NO}_y} \partial \Delta \text{NO}_{y\text{bckgr}} \right)^2 + \left(\frac{\partial \text{AEI}}{\partial T_{\text{amb}}} \partial T_{\text{amb}} \right)^2 + \left(\frac{\partial \text{AEI}}{\partial P_{\text{amb}}} \partial P_{\text{amb}} \right)^2 + \left(\frac{\partial \text{AEI}}{\partial \text{EI}_{\text{NO}_x}} \partial \text{EI}_{\text{NO}_x} \right)^2}. \quad (4.12)$$

For CO_2 -based AEI, NO_y is replaced by CO_2 in equation 4.12. Additionally, no uncertainty in EI_{CO_2} determination is considered as its calculation is based on highly precise fuel composition measurements and its negligible contribution to propagated uncertainties has been shown in Harlass et al. (2024).

As for the work in this study, relative differences in AEI for different fuels or combustion modes are most relevant, a separate calculation of non-systematic errors was conducted. There, ΔN_{meas} is reduced to only include the CAS counting uncertainty u_n , no EI_{NO_x} uncertainty is considered for NO_y -based AEI, and no CO_2 measurement uncertainty is considered for CO_2 -based AEI as it is

¹In Märkl et al. (2024), there was a Δ before T_{amb} , P_{amb} , and EI_{NO_x} . As there is no fluctuating background for these quantities, the Δ is unnecessary and is also not included in Equation 4.10 on which the uncertainty calculation is based. As this is a minor error, it does not justify a corrigendum of the publication but is presented correctly in this thesis and is also corrected in equation 4.12.

constant.

The median uncertainties found during the different campaigns are listed in table 4.1, where the uncertainties of the investigated ECLIF3 measurement flight are shown together with the uncertainties of all contrail flights of VOLCAN1 and VOLCAN2 after filtering (s. subsection 4.6).

Table 4.1: Median AEI uncertainties during investigated campaigns.

Campaign	Tracer	Absolute uncertainty /%		Non-systematic uncertainty /%	
		CAS-DPOL	CAPS-DPOL	CAS-DPOL	CAPS-DPOL
ECLIF3 Q2 MF4	NO _y	33	33	24	24
VOLCAN1	CO ₂	40	41	28	28
VOLCAN2	CO ₂	32	-	18	-

ECLIF3 Q2 MF4 values from Märkl et al. (2024).

4.6 Filtering of AEI

This section extends information described in shorter form in the journal article "Powering aircraft with 100 % sustainable aviation fuel reduces ice crystals in contrails" (Märkl et al., 2024) in Atmospheric Chemistry and Physics, 24, 3813-3837, 2024, doi: 10.5194/acp-24-3813-2024. The descriptions are valid for ECLIF3 and VOLCAN measurements.

Contrail encounters are defined according to the ice particle number concentration behavior as described in section 4.2. This in principle defines all contrail encounters independent of ambient conditions, engine parameters, and other influencing factors. To ensure comparability of AEI from contrails in a stable state from valid contrail measurements, the defined contrails are filtered in the course of data processing.

Unless noted otherwise, contrail encounters were filtered to only include those where RH_i during the encounter was >100 % (Märkl et al., 2024). Further, only "valid" contrail encounters are considered. This is a qualitative measure for the rough correlation between ice particle number concentrations and trace gas concentration (Märkl et al., 2024). For example, if there is a significant ice particle signal but no trace gas signal or one with a completely different shape, no significant correlation is given so that it must be assumed that the encounter was at the edge of the contrail or during other inhomogeneous conditions and the encounter is classified as invalid (Märkl et al., 2024). The correlation between ice particle concentration and trace gas concentration is then further quantified as described in section 4.2 and contrail encounters are only considered if the correlation between ice particle number concentration and chosen tracer is > 0.6 (Märkl et al., 2024). To avoid the influence and possible bias of very uncertain measurements, contrail encounters with a determined AEI uncertainty of > 100 % are also excluded. Finally, by using the calculated contrail age, the engine stability at time of emission based on T30 fluctuations (stable when within 4 K of

stable T30 values (Märkl et al., 2024)) is determined. If fluctuations exceed the threshold, the engine is classified as not being in a stable testing mode and the corresponding contrail encounter is not considered.

For aerosol EI calculated for VOLCAN2 data, an additional filter was applied to only account for nvPM data obtained using the forward-facing aerosol inlet. Therefore, the data set of contrail encounters with far-field nvPM data is a subset of the total contrail encounter data set. Plots that show AEI against nvPM EI might therefore not include all available AEI but only those with a direct correspondence to nvPM measured with the forward-facing inlet. This is explained in more detail in section 6.7.

4.7 Structuring of data by domains

During the VOLCAN campaigns (see section 6.1), a broad range of ambient conditions, including ΔT_{SA} , was encountered. Ambient pressure, temperature and relative humidity are the ambient factors influencing T_{SA} , which is why these parameters along with the total water vapor mixing ratio and their relation to ΔT_{SA} during VOLCAN2 are explored in Figure 4.2. There, all x-axes have the same ΔT_{SA} range and y-axes vary from panel to panel.

In panel (a), the strongly linear relationship between ambient temperature and ΔT_{SA} on the larger scale spanning the shown ΔT_{SA} range becomes apparent. On a smaller scale, domains with slightly differing slope and slightly offset vertically to one another are suggested. A similar phenomenon is seen in panel (b) where RH_i is plotted against ΔT_{SA} . On a local scale of only several K ΔT_{SA} , strongly linear relationships can be seen with higher humidity corresponding to lower ΔT_{SA} . On a global scale however, maximum RH_i are found around -9 K to -10 K ΔT_{SA} , which are reduced again for ΔT_{SA} below approximately -10 K.

Another interesting relationship is the one between water vapor mixing ratio and ΔT_{SA} shown in panel (c). Here, the lowest mixing ratios with the lowest vertical spread of data can be found for very low ΔT_{SA} values, both of which increase towards warmer temperatures in an apparently exponential manner. This shows that most water vapor is available at high temperatures close to T_{SA} and decreases the further ambient conditions are from T_{SA} . Finally, from panel (d) it can be seen that ambient pressure is quasi constant for the very cold contrail encounters below approximately -13 K ΔT_{SA} . For higher temperatures, the ambient pressures were generally also higher, i.e. at lower flight levels, but a wide range of ΔT_{SA} can be observed for any given pressure level. In this panel, clearly separated domains can also be observed where measurements were taken at relatively similar conditions relative to points in the other domains.

Additionally, as part of the sampling strategy, conditions were sought out with a high likelihood of contrail formation and simultaneously good visibility (preferentially no natural cirrus clouds). These could be found in clear skies as well as short distances above or below existing cirrus clouds.

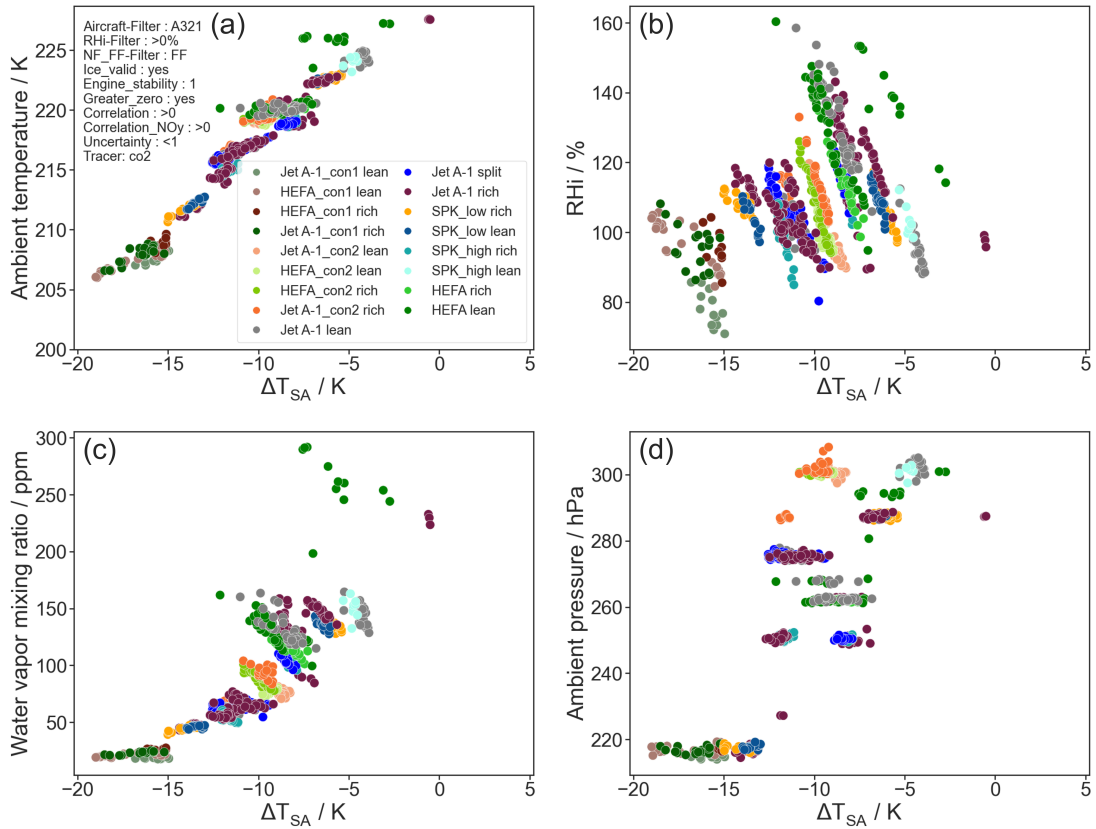


Figure 4.2: Ambient conditions at time and point of contrail detection shown against delta to Schmidt-Appleman threshold temperature from the VOLCAN2 campaign for all fuels in all combustion modes. (a) Ambient temperature, (b) relative humidity over ice, (c) water vapor mixing ratio, and (d) ambient pressure. The applied filters can be found in the top left corner of panel (a). Note: a small subsection of panel (b) has been shown by Jonas Schmidt (formerly DLR IPA) in his master's thesis (Schmidt, 2023) for flights F04 and F19.

In two of the flights with the coldest conditions (F02, F09) visual conditions were quite hazy so that the presence of natural ice clouds is likely. Inside natural cirrus clouds, RHi usually approaches 100 % as the ice particles take up ambient water vapor (Krämer et al., 2009; Voigt et al., 2017) so that in these cases, the low RHi are likely attributed to the presence of natural cirrus ice particles. The gap in RHi for temperatures colder than approximately -10 K below T_{SA} is therefore due to the sampling strategy and conditions present during the measurement sequences rather than a direct physical relationship.

To be able to answer the research questions of this work and to conduct valid comparisons, ambient conditions need to be restricted. This reduces the variability in parameters and enables a comparison of data to find effects of fuel and combustion mode depending only on a single parameter ΔT_{SA} or RHi. For this, domains were defined in plots of ambient pressure and ambient temperature vs. ΔT_{SA} as shown in Figure 4.3. These parameters were chosen as the resulting clusters of data can then be analyzed depending only on RHi or ΔT_{SA} , which also have a linear relationship on the local

scale. Additionally, aerosol properties such as nvPM size can be pressure-dependent (Dischl et al., 2024) so that possible influences on nucleation can be excluded by comparing contrail encounters at similar altitudes.

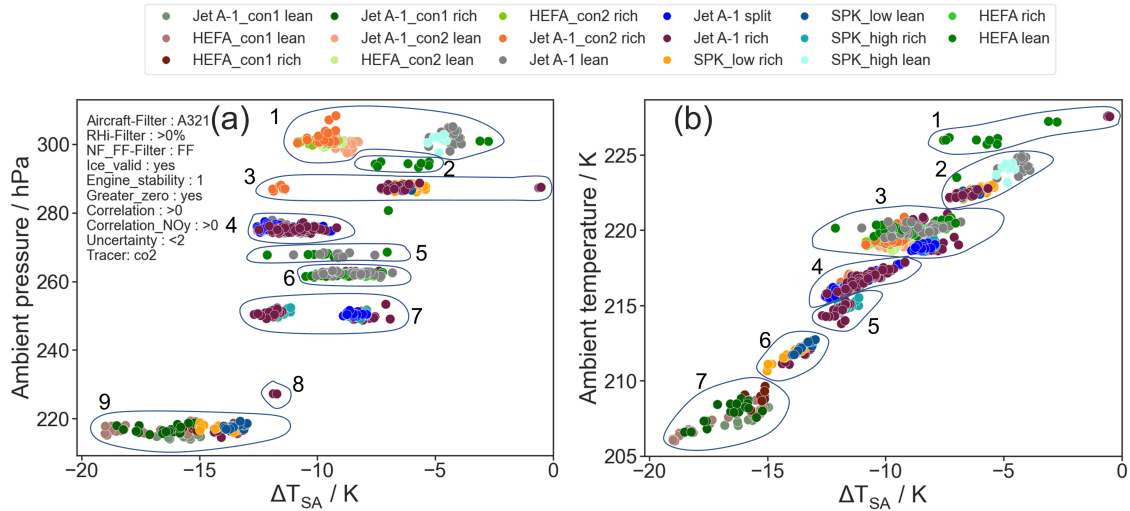


Figure 4.3: VOLCAN2 data from contrail encounters vs. ΔT_{SA} . Ambient conditions shown are (a) ambient pressure and (b) ambient temperature. Additionally, domains in the respective parameter space are marked and numbered. Filters shown in panel (a) also apply to panel (b).

The horizontal structures seen in panel (a) indicate data measured at similar altitude. Data is first sorted by these pressure domains as indicated by the numbered outlines surrounding data points. In panel (b), measured ambient temperatures are plotted against ΔT_{SA} and defined domains are likewise indicated by numbered outlines around data. Temperature domains were defined where clusters of data were clearly separated from each other either by a horizontal or vertical offset and/or by a clear break in the slope of data points.

Domains in T_{amb} vs ΔT_{SA} space do not necessarily contain the same set of data as in P_{amb} vs. ΔT_{SA} space as can be seen exemplarily for orange Jet A-1 con2 rich and turquoise SPK High lean data points, which are both included in P-domain 1 but separated into T-domains 2 and 3. To define the final domains for which further analyses are conducted, the intersections of P-domain and T-domain sets are created. The list of resulting domains for the VOLCAN2 campaign can be found in Table A1 in Appendix A. Intersection domains are named as the number of the P clusters followed by a dot and the number of the T domain, e.g. domain 1.2 is the intersection of P domain 1 and T domain 2 and therefore contains lean burn Jet A-1 (gray) and SPK High (light blue) data points. The data contained in each of these intersection domains were measured at similar pressures and temperatures and temperature ranges are mapped by the locally linear relationship to ΔT_{SA} . They therefore allow a quasi two-dimensional analysis without the influence of many simultaneously varying external parameters. This also means that findings are generally results of a small phase space case study that might be different under different conditions. Comparisons of data across intersection domains should therefore be avoided or made with utmost caution. The same procedure was done for VOLCAN1 data and is shown in Figure A11 in Appendix A.

Comparisons for different fuels and combustion modes will be conducted in chapter 6 for respective domains to elucidate the effect of rich- and lean-burn combustion using various fuels on contrail ice particle formation.

Exemplary data reduction process for one domain

In the following, the further data processing of P-T domains will be demonstrated on domain 6.3 in order illustrate the steps taken towards the final results of the combustion mode and fuel comparisons presented in sections 6.2 and 6.3. AEI locally (e.g. for one P-T domain) depend linearly on ΔT_{SA} and RH_i. This is illustrated clearly in Figure 4.4 where RH_i of contrail encounters in domain 6.3 are shown against ΔT_{SA} . The entire VOLCAN2 ΔT_{SA} range is shown to better put into context what conditions were encountered in domain 6.3.

While the parameter space is now reduced to a linear relation between RH_i and ΔT_{SA} , data points measured at strongly different ΔT_{SA} or RH_i cannot be compared to each other, even within one domain. Rather, the conditions must be similar enough to allow comparisons to find fuel or combustion mode effects. Therefore, I developed a data processing procedure where data is grouped into ΔT_{SA} or RH_i bins of 1 K or 5 % in which the data points can be assumed to have similar enough conditions for a valid comparison. In order to ensure robustness of this method to the position of data in the respective bins, a second analysis is conducted with bins shifted by 0.5 K or 2.5 %. This results in four binnings in total, which are henceforth called the ΔT_{SA} binning for the integer ΔT_{SA} steps, alternative ΔT_{SA} binning for the bins shifted by 0.5 K, RH_i binning for the integer RH_i steps, and alternative RH_i binning for the bins shifted by 2.5 %.

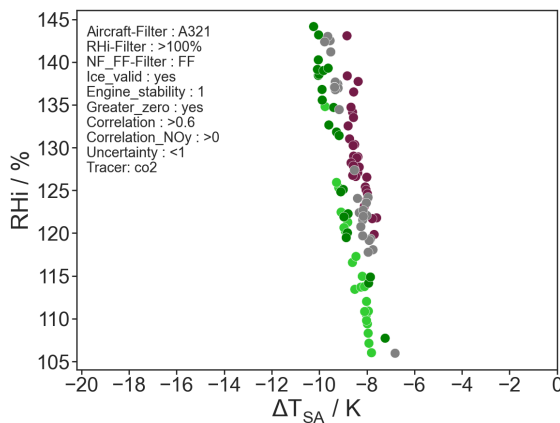


Figure 4.4: VOLCAN2 P-T domain 6.3 linear relationship between RH_i and ΔT_{SA} .

The results of these different binning methods can be found exemplary in Figure 4.5 where the fully ΔT_{SA} resolved AEI in panel (a) are grouped according to ΔT_{SA} binning in panel (c) and by alternative ΔT_{SA} binning in panel (e), while the fully RH_i resolved AEI in panel (b) are grouped according to RH_i binning in panel (d) and by alternative RH_i binning in panel (f). In these plots, the negative linear correlation for AEI and ΔT_{SA} and the positive linear correlation for AEI to RH_i can be clearly seen. In the different binning methods, not every bin enables a comparison of all available fuel-combustion mode combinations. For example in panel (c) of Figure 4.5, HEFA lean can be compared to Jet A-1 lean in the three middle bins while combustion mode comparisons of Jet A-1 are only possible for two of the middle bins.

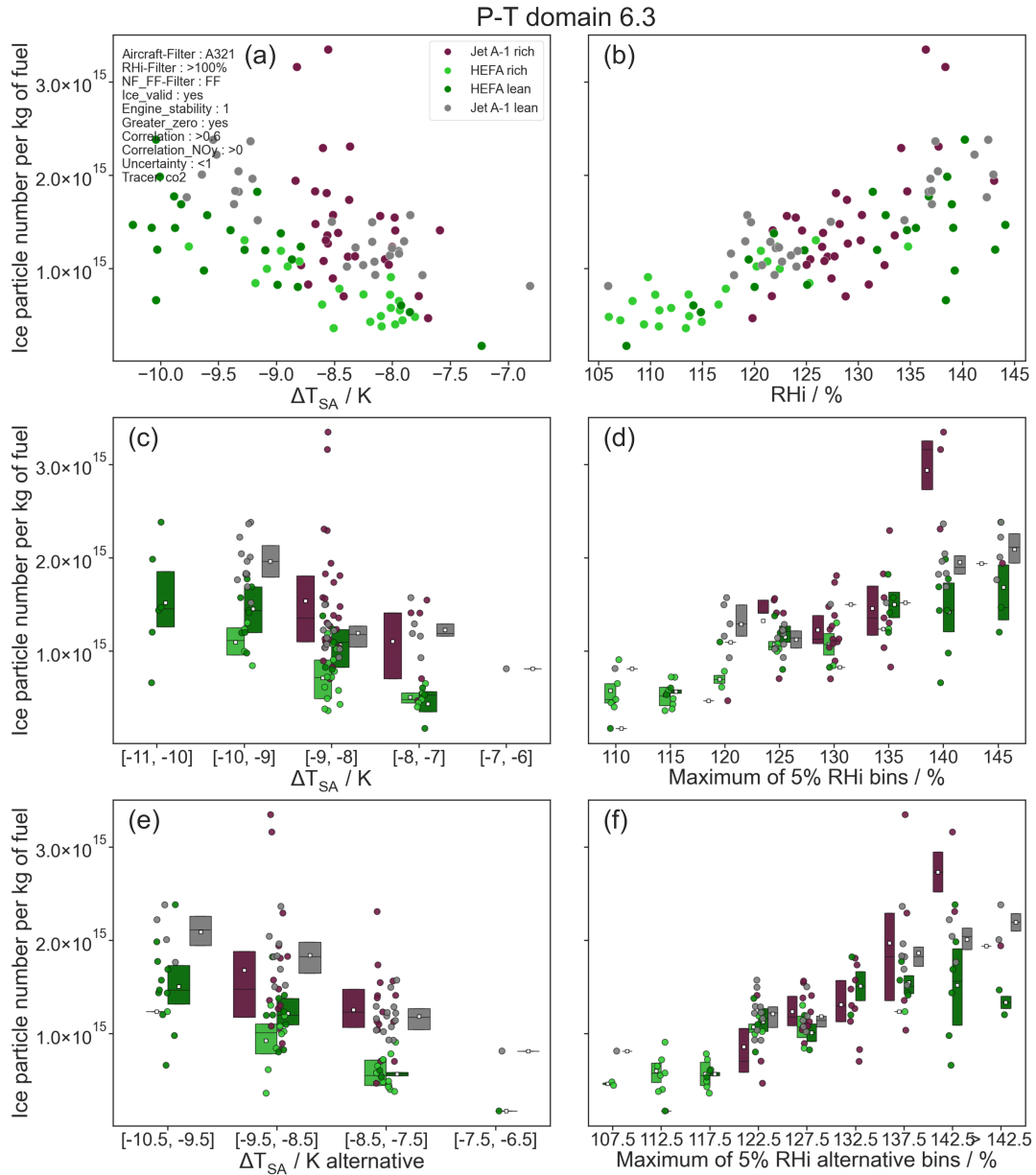


Figure 4.5: AEI of P-T domain 6.3 shown against ΔT_{SA} (a) scattered including applied filters, (c) in box plot form in standard ΔT_{SA} bins, and (e) in alternative ΔT_{SA} bins and against RHi (b) scattered, (d) in box plot form in standard RHi bins, and (f) in alternative RHi bins. Note: The data subset for rich-burn combustion in panels (a) and (b) has been shown by Jonas Schmidt (formerly DLR IPA) in his master's thesis (Schmidt, 2023).

Comparison of two species and normalization

Therefore as a next step in data processing, two fuel-combustion modes (combination of fuel and combustion mode during operation) to be compared are chosen. For this example case, the fuel comparison of HEFA rich to Jet A-1 rich in domain 6.3 is chosen. The resulting available data points are shown in Figure 4.6 exemplary for (a) ΔT_{SA} binning and (b) RHi binning. In both panels,

bins exist in which both species are not present so that only bins are considered where data points of both species are found.

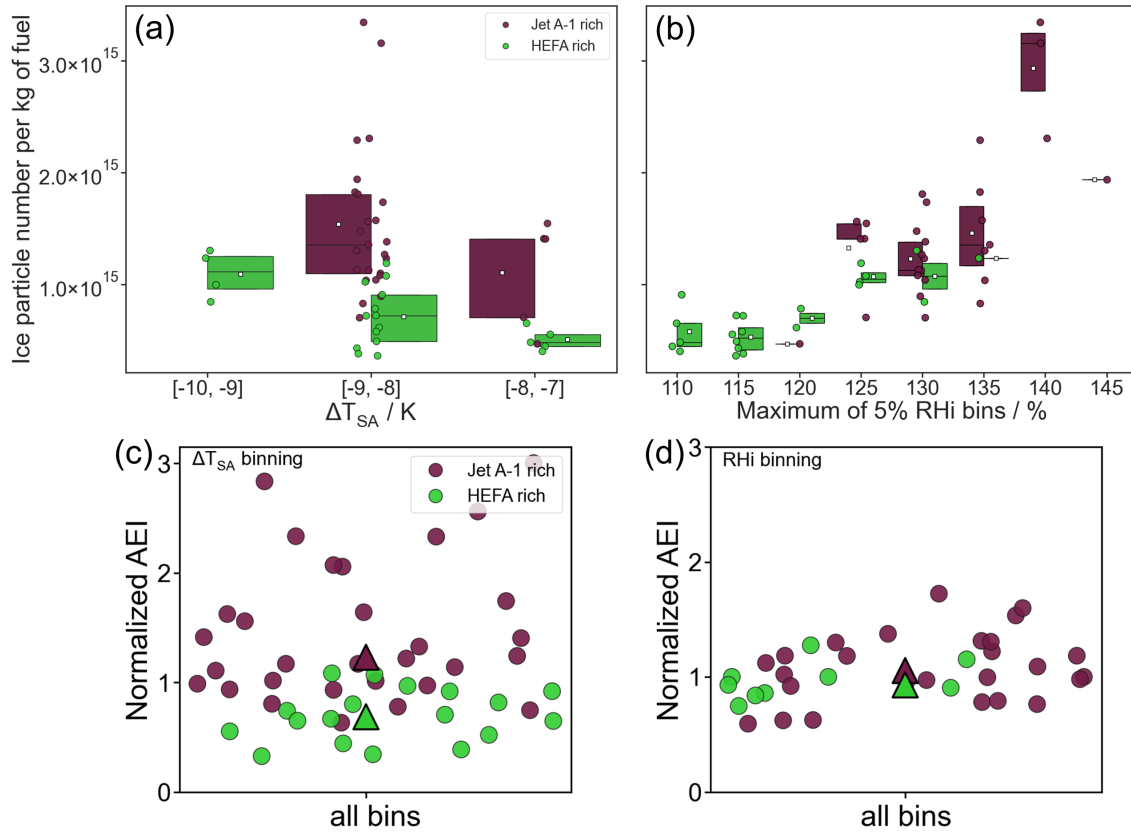


Figure 4.6: VOLCAN2 domain P-T domain 6.3 AEI binned for (a) ΔT_{SA} and (b) RHi. Normalization to respective bin medians leads to normalized AEI from (c) ΔT_{SA} binning and (d) RHi binning. The medians of the respective species are shown as triangles.

At this point, one could conduct a bin-wise comparison of both species. This would lead to a large number of relations between the two species for every bin with varying sample size and unclear statistical significance. This could be partially rectified by using statistical weights but would still not solve the need for a measure of statistical significance and standard deviation for the difference between both species across the available data point space. As a solution, the data was normalized. The median of all data points within one bin is the reference against which all data within one bin is normalized. The reason for choosing this reference point will be illustrated in this subsection by using Figure 4.7.

As a result of normalizing the data, a data set is achieved in which all points can be compared to each other independent of ΔT_{SA} or RHi influence. Before discussing the choice of normalization reference, it is worth examining panels (c) and (d) of Figure 4.6, where the normalized AEI from (c) ΔT_{SA} binning and from (d) RHi binning are shown. Comparing these two panels reveals that the set of compared data varies, as does the distribution of normalized data points and the medians shown as triangles. Normalized data from ΔT_{SA} binning (panel (c)) has a larger distribution of single data

points and the HEFA median is reduced by 44 % compared to Jet A-1, while the data points have a more narrow distribution for RHi binning (panel (d)) and show only a 12 % reduction of the HEFA median compared to Jet A-1. Also, the difference between the two species is statistically significant by measure of Mann-Whitney U rank test p-values (Mann and Whitney, 1947; Fay and Proschan, 2010) when using ΔT_{SA} binning while it isn't when using RHi binning. In this example, only the ΔT_{SA} and RHi binning are shown but for a full analysis, all four binning methods are conducted. This example also illustrates why this is necessary. For ΔT_{SA} binning shown in panel (a), almost all available data points are used while for RHi binning, the only bins with an overlap of both species are those for medium RHi. These points are strongly influenced by RHi but are possibly compared against each other when using ΔT_{SA} binning. Therefore, a difference between two species is only accepted as valid when all four binning methods yield statistically significant results.

Discussion of normalization reference

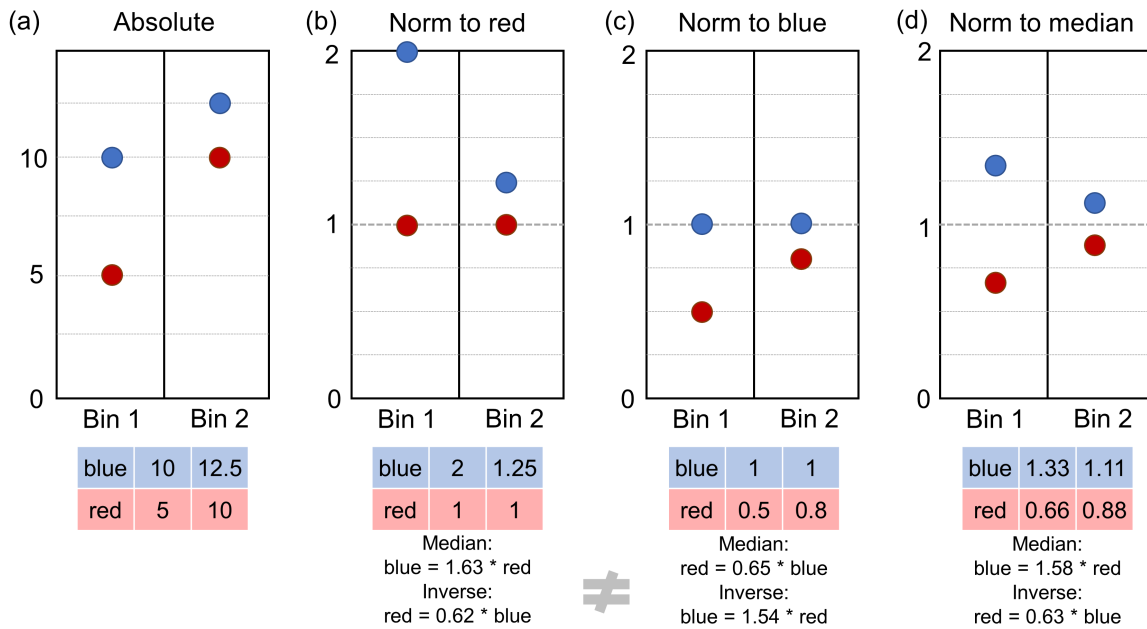


Figure 4.7: Exemplary illustration of the dependence of relative relations between two species (red and blue) across bins on the chosen reference for normalization. (a) Absolute values, (b) values normalized to red data, (c) values normalized to blue data, and (d) values normalized to the median of all values in one bin. The mean relative relations are given below the tables and it is shown that they are not equal for the different chosen references.

Several references for normalization could be chosen and the consequences of the most obvious references are discussed in the following. In Figure 4.7, a minimal example is shown where the data set consists of two species (red and blue) in two bins. Panel (a) shows the absolute values illustrated in the top diagram and additionally given in the table below the diagram. The same structure is used to illustrate the values from different normalizations, using (b) red data as reference in every bin, (c) blue data as reference in every bin, and (d) the median of all values in one bin as reference in every bin. For panels (b) to (d), the relative relations of red to blue and blue to red are given below

the respective tables. Normalizing to either the blue or red values is an analog for normalizing against a fuel-combustion mode species for VOLCAN data. This is the most obvious choice at first glance, as the goal is to compare two species and a normalization against one of the species yields a direct relative relation between the two species. However, the resulting relative comparisons do not yield the same result. By normalizing against red, blue values are larger than red values by 1.63 on average and the inverse relation obtained by dividing 1 by 1.63 yields that red values are 62 % of blue values on average. However, when normalizing against blue values, blue values are larger than red values by 1.54 on average and inversely, red values are 65 % of blue values on average which is not the same.

In a realistic case where each bin contains more than just one data point, normalization would be done against the median of the respective species against which the other species could be directly compared. There is no single reference fuel-combustion mode that is available for all fuel-combustion mode comparisons, therefore it would be inconsistent to switch references across different comparisons. A solution is given by using the median of all data within one bin as the respective reference for normalization as illustrated in panel (d) of Figure 4.7. This is a point usually lying between data points of the two species and can be calculated for every comparison in the same way independent of the compared species. The relations between red and blue values for this example yield that blue values are larger than red values by 1.58 and inversely, red values are 63 % of blue values on average. The use of the bin median of the two species however requires an additional step in order to achieve the comparison given by the aforementioned relations.

The normalization method presented schematically in panel (d) is then conducted for each binning method bm . This results in a median $\tilde{AEI}_{norm, bm}$ of all normalized values for each species. From these, the mean $AEI_{norm, mean}$ is calculated for each of the two compared species, which can then be compared to each other:

$$AEI_{norm, mean} = \frac{1}{4} (\tilde{AEI}_{norm, RHi} + \tilde{AEI}_{norm, RHi alt} + \tilde{AEI}_{norm, \Delta T_{SA}} + \tilde{AEI}_{norm, \Delta T_{SA alt}}) \quad (4.13)$$

For the comparison of $AEI_{norm, mean}$, one of the two species is arbitrarily chosen as the "reference" and the $AEI_{norm, mean}$ of the other species is divided by the "reference". The inverse can also be conducted, in both cases yielding mutually translatable results. Another possibility would be to first calculate ratios of $\tilde{AEI}_{norm, bm}$ between one species and the reference for every binning method and then calculating the mean. Switching reference fuels for this method however would not produce the inverse value, therefore giving non mutually translatable results. The chosen method of calculating the mean for every species and comparing them is therefore seen as the better approach to calculating a unified value for the difference between two species.

As an exemplary illustration, the $\tilde{AEI}_{norm, bm}$ are shown for the comparison of HEFA rich to Jet A-1 rich in Figure 4.8. Here, medians of normalized AEI are shown with standard deviations as error bars against medians of normalized nvPM EI in panel (a) and against medians of normalized total particle EI in panel (b). Every data point is the median for one binning method. Additionally in panel (b), the large circles show the respective means $AEI_{norm, mean}$ for each species corresponding

to the respective mean total particle EI from the shown medians. In panel (a), only two data points can be found because nvPM data is only considered where the forward-facing aerosol inlet was used and in this case, there was no overlap of HEFA rich and Jet A-1 rich data in the same bins for two binning methods. Therefore for this comparison, no nvPM comparison is done.

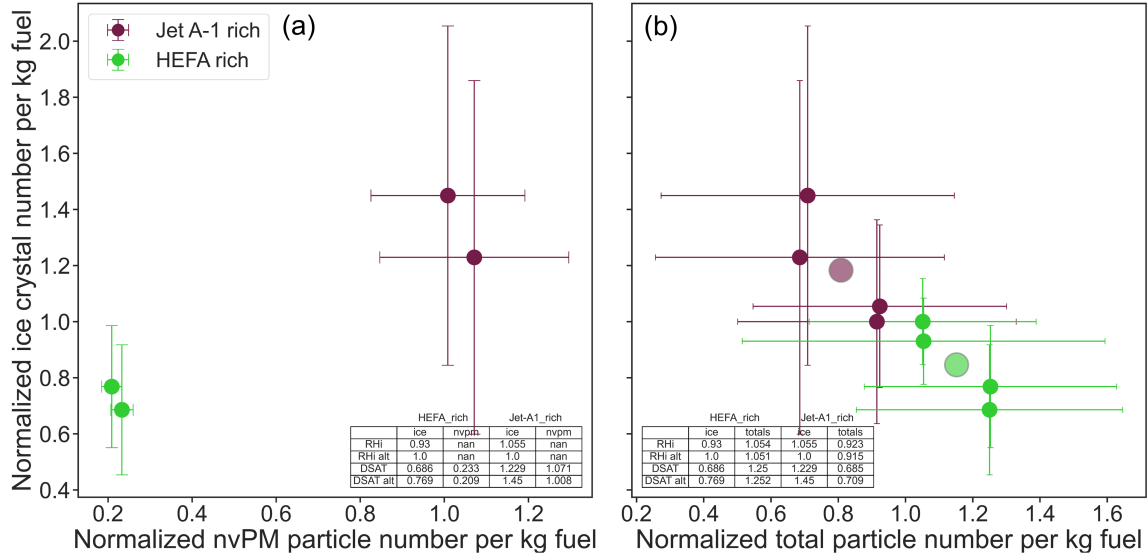


Figure 4.8: Medians of normalized AEI from different binning methods against medians of (a) normalized nvPM EI from ΔT_{SA} and ΔT_{SA} alt binning and (b) total particle EI from all four binning methods. Large circles are the means of median normalized AEI and total particle EI. Note: as only nvPM data obtained using the forward-facing inlet are used, there were only two bins containing HEFA rich and Jet A-1 data points, therefore only two data points are shown for each fuel-combustion mode.

Statistical measures

From the comparison of $\tilde{AEI}_{norm, bm}$ for each compared species, a relative relation is obtained, which denotes a reduction or increase of AEI compared to the "reference" fuel-combustion mode. However, given the varying distribution widths and sample sizes of compared fuel-combustion modes, no information about statistical significance is contained in the difference of normalized AEI. For example, if single data points of two compared species have wide distributions with a large overlap, a large difference of their medians may be yielded, which however might not be statistically significant. The same can happen for small sample sizes. In order to have a quantitative measure for assessing the statistical significance of the difference between normalized AEI for two species, the two-sided Mann-Whitney U rank test (Mann and Whitney, 1947; Fay and Proschan, 2010) is employed, which does not require normally distributed data.

This test is performed on the entire set of normalized data points for each binning method to test the null hypothesis that it is equally probable that a randomly selected value from one population is smaller or larger than a randomly selected value of the other population. Therefore, if the null hypothesis is rejected (p-value smaller than threshold), the difference between two populations is statistically significant. Medians of two populations are only compared if the variance of the

distributions are equal (Divine et al., 2018). As this is not strictly the case for the data in this study, the Mann-Whitney U rank test is to be seen as an approximate quantification of the measurement data statistics. Resulting p-values are given in the results in sections 6.2 and 6.3. If all four p-values lie below the threshold value of $p_{thresh} = 0.05$, the difference of normalized values is accepted as being statistically significant.

In order to gain additional insight into the sample sizes of compared species, a statistical weight is calculated by summing the products of respective samples sizes N_1 and N_2 of species A and B within each bin b : $w_{stat} = \sum_b N_{A,b} * N_{B,b}$. This is a measure that gives higher weight to a higher number of available data points, as well as to the equality of distribution. For example, for a total number of 10 data points in a given bin, the statistical weight is higher for the equal distribution of five points in species A and 5 points in species B with a statistical weight of 25, while the unequal distribution of 1 point in species A and 9 points in species B gives a lower statistical weight of 9. By nature of the metric, only bins are considered where both of the compared species have data points, as one of the factors is zero otherwise.

The method presented in this section can be summarized as:

- **VOLCAN data is grouped into data domains of similar ambient conditions (P-T domains) where only a dependence on RH_i and ΔT_{SA} remains. Using these domains, influences of combustion mode and fuel can be investigated.**

CHAPTER 5

Contrails from 100 % SAF in rich-burn engines

Large parts of this chapter have been published in the journal article "Powering aircraft with 100 % sustainable aviation fuel reduces ice crystals in contrails" (Märkl et al., 2024) in Atmospheric Chemistry and Physics, 24, 3813-3837, 2024, doi: 10.5194/acp-24-3813-2024. Verbatim citations (figure, table, and equation numbers adapted) are indicated as such where possible. All text, tables, figures and other content from the mentioned publication shown in this chapter are used under CC BY 4.0 (<https://creativecommons.org/licenses/by/4.0/>). Several people have contributed to this study and a detailed statement of contributions is found in Contributions to this study after chapter 7.

5.1 The ECLIF3 campaign

The ECLIF (Emissions and Climate Impact of Alternative Fuels) campaigns are a series of in-situ campaigns aimed at investigating the impact of alternative fuels on particle and trace gas emissions and contrail formation and the associated climate impact. The campaign series was preceded by the Alternative Fuel Effects on Contrails and Cruise Emissions Study (ACCESS) campaign performed in 2013 and 2014 where particle emissions from a SAF blend fuel were compared to medium- or low-sulfur conventional Jet A fuel emissions (Moore et al., 2017). The ECLIF series began with ECLIF1 in 2015 where the DLR Falcon performed chase flights behind the DLR Airbus A320 ATRA aircraft equipped with International Aero Engines (IAE) V2527 engines and combusting a blend of Fischer-Tropsch based synthetic kerosene and Jet A-1, as well as a reference Jet A-1 fuel (Kleine et al., 2018; Voigt et al., 2021). The series continued with ECLIF2/ND-MAX, a cooperation between DLR and National Aeronautics and Space Administration (NASA) in 2018 where the same DLR Airbus A320 ATRA aircraft served as the emission source aircraft while combusting different blending ratios of Jet A-1 and HEFA-based kerosene compared against a Jet A-1 reference fuel (Bräuer et al., 2021b; Bräuer et al., 2021a; Voigt et al., 2021; Schripp et al., 2022).

During the ECLIF3 campaign presented in this work, emissions and contrails from the combustion of 100 % HEFA-SPK SAF were measured for the first time behind a large passenger aircraft in a cooperation between DLR, Airbus, Rolls-Royce, and Neste (Märkl et al., 2024; Dischl et al.,

2024; Harlass et al., 2024). These in-situ measurements were conducted at cruise conditions by the DLR-operated Falcon 20E research aircraft chasing an Airbus A350-941 equipped with Rolls-Royce Trent XWB-84 engines. The ECLIF3 campaign took place across two campaign parts in April (second quarter (Q2)) and November (fourth quarter (Q4)) 2021 with the DLR Falcon based in Oberpfaffenhofen and Toulouse. Contrails were measured in the far-field regime with contrail ages ranging from approximately 60 s to 375 s. Emissions were measured in the near-field regime as close as approximately 100 m behind the emission aircraft. This work focuses on measurements in contrails conducted in the far-field regime. In this section, an overview will be given over all flights performed during ECLIF3 and the properties of corresponding fuels and ambient conditions before presenting the results obtained during this campaign in the subsequent sections.



Figure 5.1: Source aircraft during the ECLIF3 campaign. Airbus A350-941 equipped with Rolls-Royce Trent XWB-84 engines as viewed from the DLR Falcon. Taken during ECLIF3 measurement flight 02 on 10 April 2021.

"The first-ever built Airbus A350-941 (registration: F-WXWB) equipped with two Rolls-Royce Trent XWB-84 engines and operated by Airbus served as the emission source aircraft. Fuel was supplied selectively from the two wing fuel tanks containing a reference fuel and 100% HEFA-SPK, respectively. This allowed for in-flight switching between two fuels for each engine and the operation of both engines on a single fuel using cross-feed valves. The DLR Dassault Falcon 20-E5 research aircraft followed the emission source aircraft to measure exhaust gases, volatile and nonvolatile aerosol particles, and contrail ice particles (Voigt et al., 2023a,b)." (Märkl et al., 2024) In Figure 5.1, the

source aircraft can be seen forming a contrail during an ECLIF3 measurement flight on 10 April 2021 above a layer of high altitude cloud cover where favorable conditions for contrail formation were often found during the campaign.

In total, nine measurement flights were conducted during the ECLIF3 campaign, three in Q2 and six in Q4. Of these, contrails were measured during five flights in either exclusively far-field conditions or flights in which far-field contrail as well as near-field emission measurements were carried out. An overview over the flights containing contrail measurements is given in Table 5.1. While Jet A-1 and HEFA fuel were used during Q2 flights, an additional blend of Jet A-1 and HEFA was available during Q4 flights. Q2 flights took place in an area over the Mediterranean Sea off the French southern coast as well as West of Corsica and Sardinia with the Falcon taking off from Oberpfaffenhofen for both flights. The exact flight paths taken by the DLR Falcon are illustrated in Figure 5.2 where race track patterns in North-South and East-West directions can be clearly seen for the chase sequences. The flight paths for Q4 can also be seen, which are off the French Atlantic

Table 5.1: Overview of far-field contrail flights during the 2021 ECLIF3 campaign.

Flight Number	Date	Area	Type of flight	Fuel
ECLIF3 Q2				
02	10.04.	Mediterranean	Contrails, Emissions	Jet A-1
04	16.04.	Mediterranean	Contrails, Emissions	Jet A-1 HEFA
ECLIF3 Q4				
13	24.11.	Bordeaux, Atlantic	Contrails	Jet A-1 HEFA
14	25.11.	Bordeaux, Atlantic	Contrails	Blend HEFA
17	27.11.	Bordeaux, Atlantic	Contrails, Emissions	Jet A-1 HEFA

Coast in the area of the city of Bordeaux. For flights 13 and 14, the Falcon operated from Toulouse Blagnac airport, while for flight 17 it took off from Nantes and returned to Oberpfaffenhofen after the measurement sequence. The exact flight patterns and routes were chosen due to a combination of factors, including airspace restrictions from air traffic control (ATC), predicted contrail forming areas, and on-site evaluation of contrail visibility and conditions for contrail probing such as discernability of primary and secondary wakes.

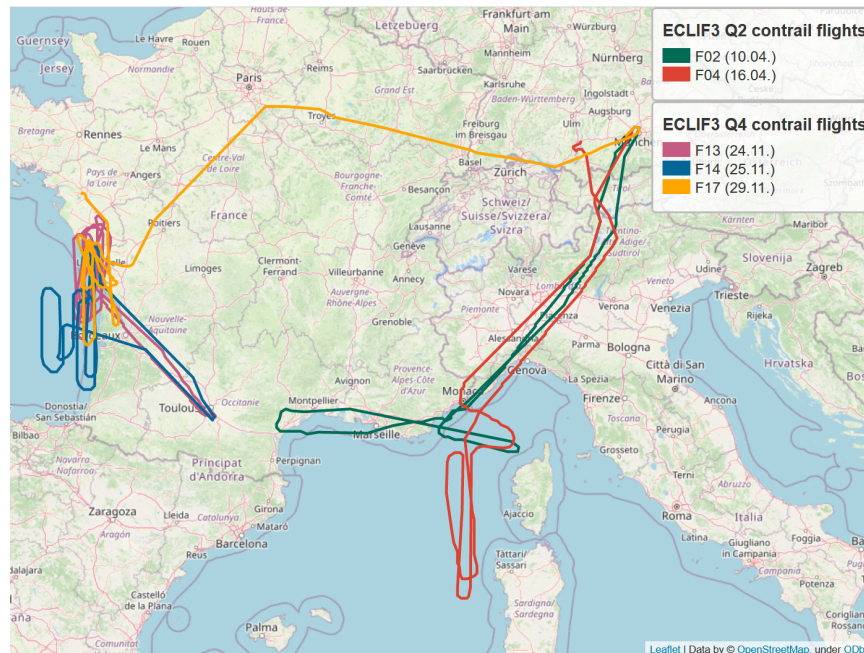


Figure 5.2: Overview of DLR Falcon flight paths from the five far-field contrail flights during the ECLIF3 campaign in April (Q2) and November (Q4) 2021. The brackets denote the flight date in the year 2021. Note that flights 13 and 14 were combined flights of the VOLCAN1 and ECLIF3 Q4 campaigns and measurement sequences of both campaigns are shown in this map. Map data from OpenStreetMap (<https://www.openstreetmap.org/copyright/en>).

Five different fuels were investigated during the ECLIF3 flight campaign in Q2 and Q4, with the most important fuel properties at the point of use and after logistics given in Table 5.2. The conventional Jet A-1 used as reference fuel for both campaign parts was the standard jet fuel available at Toulouse Blagnac airport at the time of fueling supplied by TotalEnergies (Märkl et al., 2024). The 100 % HEFA fuel was produced by Neste Corporation (Märkl et al., 2024), which was also used for the blend fuel. However, a Jet A-1 different from the one used as reference fuel was used for the blend, which can be seen for example by the higher naphthalene and sulfur content of the blend compared to the reference Jet A-1. The HEFA fuel in both campaign parts can be considered nearly free of aromatics, naphthalene and sulfur and in fact, aromatics and naphthalene contents lie below the ASTM D6379 and ASTM D1840 detection limits (Märkl et al., 2024). Therefore, results from GCxGC measurements given in mass% are used for these quantities for HEFA. For the interpretation of results, it is helpful to mention that the used reference Jet A-1 has a lower aromatic content compared to the global mean (Hadaller and Johnson, 2006) but aromatics as well as naphthalene contents are more than an order of magnitude higher compared to those of HEFA fuel (Märkl et al., 2024). Similarly, the sulfur content of Jet A-1 is at least a factor of 30 higher compared to the HEFA during the respective campaign part but lies well below the maximum permitted value of 0.3 mass% (ASTM D5453) (Märkl et al., 2024). The reductions in aromatics and naphthalene content for HEFA fuel compared to Jet A-1 are reflected in the lower CO₂ emission index (EI_{CO₂}) and higher hydrogen content (Märkl et al., 2024). Due to the aromatics content of the blend lying between those of Jet A-1 and HEFA but the naphthalene content being the highest, EI_{CO₂} of the blend is closer to that of Jet A-1.

Table 5.2: Properties of fuels used during ECLIF3 far-field measurements. Q2 values from Märkl et al. (2024). Parts of Q4 values published in Dischl et al. (2024).

	unit	Jet A-1 Q2	HEFA Q2	Jet A-1 Q4	HEFA Q4	Blend Q4
Fuel composition (Jet:HEFA for blend)	%	100	100	100	100	62:38
Aromatics (ASTM D6379)*	vol%	13.4	0.41	13.4	0.62	10.8
Naphthalenes (ASTM D1840)*	vol%	0.35	0.002	0.5	0.06	0.58
Hydrogen content (ASTM D3701)	mass%	14.08	15.11	14.25	15.18	14.39
Carbon content**	mass%	85.90	84.89	85.74	84.82	85.56
H:C mole fraction ratio		1.95	2.12	1.98	2.13	2.00
EI _{CO₂}	g/kg	3149	3111	3143	3108	3137
Sulfur Total (ASTM D5453)	mass%	0.0211	0.0007	0.0125	0.0003	0.0505

Fuel composition of blends refer to Jet:HEFA blending.

* The aromatic (naphthalene) content of HEFA-SPK is given (mass %) and determined by GCxGC measurements due to the contents being below the ASTM D6379 (D1840) detection limits.

**Carbon content based on the difference between 100% and hydrogen and sulfur content

5.1.1 Ambient conditions of the ECLIF3 campaign

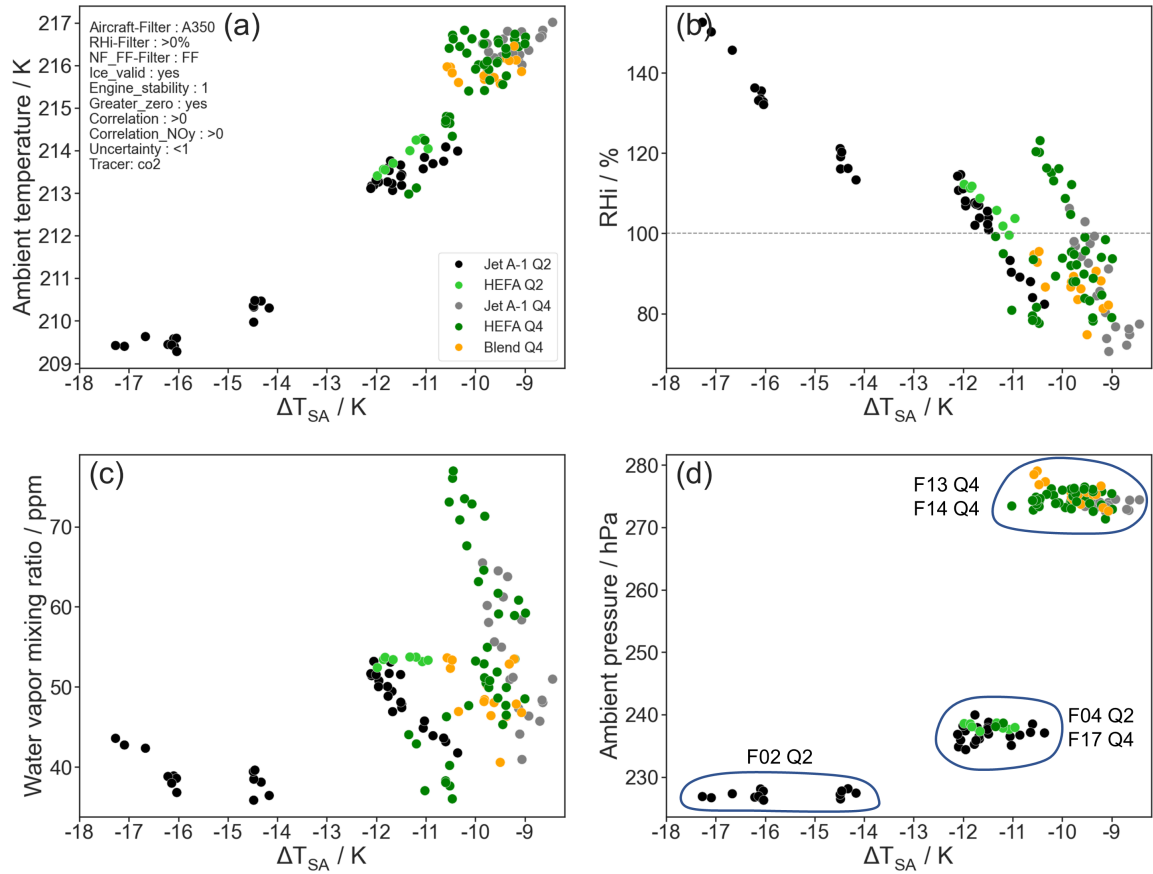


Figure 5.3: Ambient conditions at time and point of contrail detection shown against ΔT_{SA} from the ECLIF3 campaign for all fuels. (a) Ambient temperature, (b) relative humidity over ice, (c) water vapor mixing ratio, and (d) ambient pressure. The applied filters can be found in the top left corner of panel (a). Flights and campaign part are indicated for the circled data points in panel (d).

During the measurement flights of the ECLIF3 campaign, a wide range of ambient conditions was encountered. Sorting data by ambient conditions is important to prevent unwanted biases when determining the influence of different fuels on contrail ice crystal numbers and properties. In order to visualize the most important ambient conditions present during contrail encounters of ECLIF3, (a) ambient temperature, (b) RHi, (c) water vapor mixing ratio, and (d) ambient pressure are shown against ΔT_{SA} in Figure 5.3. All contrail encounters occurred well below the contrail formation threshold T_{SA} and span a ΔT_{SA} range of approximately 9 K from -8.5 K to -17.5 K. A direct correlation between ambient temperature and ΔT_{SA} can be seen in panel (a), which is not surprising as lower temperatures are the most direct connection to ΔT_{SA} . The relationship between RHi and ΔT_{SA} shown in panel (b) is more multifaceted as nearly linear anticorrelations can be seen locally. This is the result of T_{SA} dependence on RHi and water vapor mixing ratio (shown in panel (c)). These three locally nearly linear relationships additionally correspond to the roughly three flight levels / pressure levels shown in panel (d).

Flight 02 in Q2 took place at the lowest pressure level (highest altitude), while flight 04 in Q2 and flight 17 in Q4 at slightly higher pressure and flights 13 and 14 of Q4 at the highest pressure levels. During flight 02, only Jet A-1 with no comparison fuel was probed at similar conditions. Therefore, these data points can not be used for any fuel-based comparison. As a result, only flights 13 and 14 from Q4 with Jet A-1, HEFA and blend remain for one pressure level and flight 04 from Q2 and flight 17 from Q4 with Jet A-1, Q2 HEFA and Q4 HEFA for the other pressure level. To be able to compare contrail encounters at stable conditions without strong influences of sublimation due to ice-subsaturated air, data is filtered to only compare contrail encounters where RH_i was above 100 %. This threshold is marked by a dashed horizontal line in panel (b) and separates the data into data points useable for the conventional fuel-based comparison above the line and data points where sublimation effects must be expected below the line. This filters out data points from flight 17 of Q4 for the medium pressure level measurements and all of the blend data points from the high pressure level measurements. The final data points available for a fuel-based comparison are the HEFA and Jet A-1 data points from flight 04 in Q2 and HEFA and Jet A-1 data points from flight 13 in Q4.

However, for flight 13 from Q4, there are only two Jet A-1 data points with a sampling length of 6 s and 7 s respectively, resulting in a total Jet A-1 sampling time of 13 s, which is a very low statistical sample size not suitable for drawing statistically significant conclusions on the influence of fuel on contrail ice crystal numbers. It is in principle thinkable to conduct comparisons for the subsaturated data points by restricting RH_i and contrail ages and thereby comparing data points at similar stages of sublimation. To do this, the correlation between ice crystal measurements and trace gas can't be used as the data will inherently correlate less well than for supersaturated conditions. This however also adds additional uncertainty because a differentiation of bad correlation due to sublimation effects or non-homogeneous contrail probing cannot be distinguished. It was therefore decided to focus the fuel-based comparison on the data from flight 04 (16.04.2021) from Q2. The resulting analysis culminated in the publication "Powering aircraft with 100% sustainable aviation fuel reduces ice crystals in contrails" (Märkl et al., 2024) in *Atmospheric Chemistry and Physics*, Vol. 24, No. 6, p. 3813-3837, 2024, doi: 10.5194/acp-24-3813-2024, from which excerpts will be presented in the following sections.

5.2 Influence of 100 % HEFA on AEI

5.2.1 Measurement of contrails at cruise altitude

This subsection is composed of verbatim parts (figure, table, and equation numbers adapted) of Märkl et al. (2024). The individual parts are marked by quotation marks.

"This section presents an in-depth analysis of in situ contrail ice particle measurements under cruise conditions during the contrail flight on 16 April 2021 behind an Airbus A350-941 equipped

with Rolls-Royce Trent XWB-84 engines and burning 100 % reference Jet A-1 and 100 % HEFA-SPK successively. One other flight from ECLIF3-1 focused on emission measurements, and the other contrail flight did not have the option of providing 100 % HEFA-SPK to the two engines, as this was the first test flight. Far-field contrail measurements (distance between 19 and 35 km) of Jet A-1 fuel were conducted between 11:18:22 and 11:33:00 UTC, while contrails from burning HEFA-SPK were measured between 11:42:16 and 11:52:55 UTC. A detailed time series plot of this measurement sequence is shown in Fig. 5.4 where the sequences of Jet A-1 and HEFA-SPK are shaded in gray and green, respectively. Contrail encounters are marked by strong increases in ice crystal numbers and soot numbers, in line with enhanced CO_2 and NO_y measurements. The contrail measurements are clearly identified in the measurement time series.

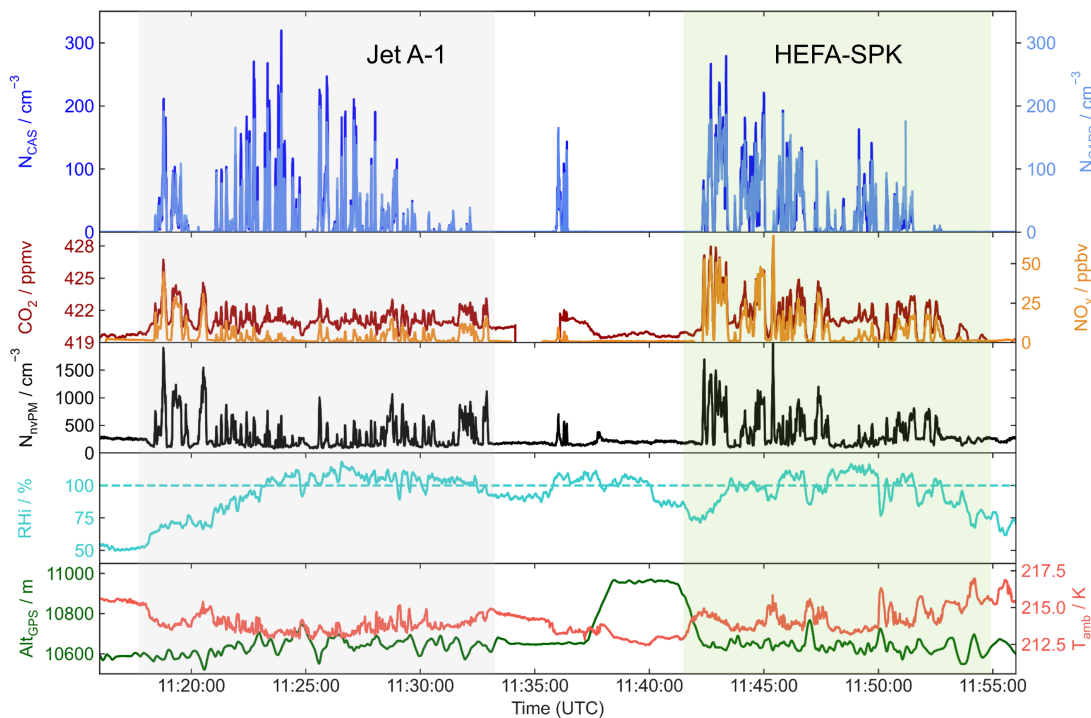


Figure 5.4: Time series of 1 Hz data during far-field measurement sequences of Jet A-1 (gray shading) and HEFA-SPK fuel (green shading) showing number concentrations of ice crystals larger than at least $0.5 \mu\text{m}$ measured by the CAS (N_{CAS}) and CAPS (N_{CAPS}) instruments, CO_2 and NO_y mixing ratios, and number concentrations of nonvolatile particles $> 14 \text{ nm}$. (N_{NvPM}), relative humidity over ice (RHi) during the measurements with indicated saturation (dashed line), and the GPS altitude of Falcon (Alt_{GPS}) with the Falcon-measured ambient temperature (T_{amb}). Source: Märkl et al. (2024)

The difficulty of drawing any reliable conclusions from time series alone illustrates the need for the dilution-corrected apparent contrail ice emission index. In the time series, groups of peaks can be seen where each individual peak of ice particle measurements constitutes a contrail encounter with a peak defined as the time period between the departure from and return to ice particle background concentrations. However, not all of the collected data shown in Fig. 5.4 can be used to calculate valid apparent ice emission indices." (Märkl et al., 2024)

"Sequences where the Falcon was not fully immersed in the contrail lead to a strong mismatch between ice particle concentrations on the one side and trace gas and nvPM concentrations on the other, an example of which is demonstrated from 11:30:00 to 11:33:00 UTC, where ice particle number concentrations are very low, while trace gas and nvPM concentrations are at similar levels to the previous parts of the Jet A-1 sequence. Together with strongly differing time series curve shapes, a preferential immersion of the Falcon fuselage top, where the aerosol and trace gas inlets are located, compared to only partial immersion of the wing-mounted ice particle instrumentation, is suggested. As a result, the ice particle measurement in this sequence is classified as invalid. Further, for a valid comparison of the AEI, we must ensure that ice particles are in a quasi-stable state and that ice number concentrations do not change significantly on measurement timescales by sublimation. As ice crystals form under ice-supersaturated conditions and are measured about 1 min later under ice-supersaturated conditions in the secondary wake, we hypothesize that no ice crystal loss has occurred, e.g., due to vortex loss processes (Unterstrasser, 2014). By only further analyzing data under ice-supersaturated conditions with $RHi > 100\%$, this focus on quasi-stable ice particle numbers is achieved. Finally, only data are chosen where the engine was determined to have operated under a stable condition at the time of emission, defined as emission sequences where high-pressure compressor outlet temperatures T30 stay within 4 K of stable T30 values. After filtering data according to the criteria described above, a data set remains with quality-controlled valid data points, which can be used to calculate comparable AEI values. This reduces the sampling times from the original 750 to 183 s for Jet A-1 and from 522 to 123 s for HEFA-SPK." (Märkl et al., 2024)

"Table 5.3 lists the ranges, means, and standard deviations as computed for the reduced data set. Here, in addition to the columns for Jet A-1 and HEFA-SPK, a third column shows the values for HEFA-SPK when applying a filter to the data set that only accepts contrail encounters where the time series of ice particle measurements and NO_y correlate better than 60 %. In this way, aforementioned sequences with preferential contrail immersion of either the aerosol and trace gas inlets or the ice particle instrumentation are quantified and can be disregarded for further analysis. Jet A-1 data are coincidentally not influenced by this filter, and therefore no separate column is given.

For Jet A-1, measured contrails were between 104 and 142 s old, while HEFA-SPK contrails were slightly younger, between 73 and 92 s. While performing far-field measurements in contrails, the distance between the source aircraft and the DLR Falcon continuously increases due to the limited propulsion performance of the Falcon compared to the Airbus A350, thereby intentionally leading to the range of contrail ages for each fuel sequence. As the measurements were taken under ice-supersaturated conditions within the vortex regime in the secondary wake of the contrail near flight altitudes, ice particle number concentrations and tracers are assumed to be diluted similarly, so that the AEIs are not expected to be affected by the age difference. The total sampling time in all the valid contrails shown in Table 5.3 has the largest discrepancy between the two fuels and affects the statistical significance of data. As the data were filtered to only include

Table 5.3: Contrail measurement conditions for the respective fuel measurement sequences. An ice-NO_y time series correlation filter of 60 % further reduces HEFA-SPK data (last column), while Jet A-1 data are not further reduced by this filter. Adapted from: Märkl et al. (2024)

	unit	Jet A-1	HEFA-SPK	HEFA-SPK (correlation > 60%)
Contrail age	s	104–142	73–92	75–87
Sampling time with/without filtering	s	183/750	123/522	55/522
Ambient RH _i	%	101–115	102–113	102–112
Ambient T	K	213.3 (±0.2)	213.8 (±0.3)	213.7 (±0.3)
ΔT _{SA}	K	-11.8 (±0.2)	-11.6 (±0.4)	-11.7 (±0.3)
Altitude of source aircraft	m	10626 (±4)	10621 (±4)	10622 (±2)
Speed of source aircraft	Mach	0.846 (±0.004)	0.852 (±0.001)	0.852(±0.001)
Fuel flow per engine	kg h ⁻¹	FF _{Jet} (±0.6%)	FF _{Jet} + 1.9% (±0.2%)	FF _{Jet} + 1.8% (±0.1%)
Engine T30	K	T30 _{Jet} (±0.9)	T30 _{Jet} + 6.5 (±0.8)	T30 _{Jet} + 6.2 (±0.4)

Measurement conditions filtered for RH_i > 100%. The sampling time is the sum of valid contrail encounters. The arithmetic standard deviation (± a.s.d.) given in parentheses. The original sampling time before the filters is given behind the slash.

ice-supersaturated data points, all the shown measurements were taken at $RH_i > 100\%$ with very similar ranges between Jet A-1 and HEFA-SPK. The temperature-related parameters such as ambient temperature and the difference to the Schmidt-Appleman threshold temperature (ΔT_{SA}) were within each other's standard deviations from the respective means. The emitting Airbus A350 was flying at nearly constant altitudes on flight level FL350 at steady Mach numbers for the two fuel burning sequences. Engine combustion conditions are described by the parameters high-pressure compressor outlet temperature T30 and the fuel flow FF. Their fluctuations are relatively small for each individual fuel sequence where average fuel flow and T30 were, respectively, 1.9 % and 6.5 K higher for HEFA-SPK burning sequences compared to Jet A-1. The differences in the ice- NO_y correlation-filtered HEFA-SPK data points and the non-filtered data points are negligible except for the sampling time, which reduces the overall statistics of HEFA-SPK measurements. However, this step leads to an increased quality of data by quantifying spatial inhomogeneities and focusing on homogeneous contrail encounters.

Overall, the quality-controlled and reduced data set with the conditions shown in Table 5.3 provides a solid basis for comparison of the AEI for HEFA-SPK fuel burning compared to Jet A-1, considering fluctuations of relevant atmospheric and aircraft parameters are statistically distributed." (Märkl et al., 2024)

5.2.2 Impact of 100% HEFA-SPK on the apparent ice number emission index AEI

This subsection is taken verbatim (figure, table, and equation numbers adapted) from Märkl et al. (2024).

"With the quality-controlled data set described in previous sections (filtered for $> 60\%$ ice- NO_y correlation), it is possible to compare the AEI for Jet A-1 and HEFA-SPK. Figure 5.5 shows comparisons of the AEI for Jet A-1 and HEFA-SPK (individual data points, medians, and arithmetic standard deviations) versus a set of parameters relevant in ice particle formation. Figure 5.5a relates contrail ice particle numbers to measured soot particle emission indices corresponding to the contrail measurement data, while further panels compare the AEI depending on the fuel parameters (b) naphthalene, (c) aromatics, and (d) sulfur.

Figure 5.5a shows a reduction in the median AEI for 100 % HEFA-SPK compared to Jet A-1 of 56%. The absolute AEI decreases from 7.8×10^{14} to $3.4 \times 10^{14} \text{ kg}^{-1}$. At the same time, the median nvPM EIs are reduced by 35% from 9.5×10^{14} to $6.1 \times 10^{14} \text{ kg}^{-1}$. Both fuels were probed under very similar conditions within a single flight, and therefore it is reasonable to attribute these reductions to properties of the probed fuels, which are explored in the following. Due to the higher binding energy between atoms in aromatics compared to aliphatic compounds, incomplete combustion and subsequent soot formation are enhanced for these compounds (Cain et al., 2013; Brem et al., 2015; Schripp et al., 2022). Naphthalene as a polycyclic aromatic compound is especially conducive to soot formation, and a reduction in naphthalene has been experimentally demonstrated to reduce

apparent contrail ice emission indices (Voigt et al., 2021; Bräuer et al., 2021b). As shown in Fig. 5.5b and c, the naphthalene and aromatic contents are reduced to below their ASTM D1840 and ASTM D6379 detection limits for HEFA-SPK compared to Jet A-1. Hence, the soot reduction of 35% can be explained by this reduction in aromatics and naphthalene in the SAF. It is also worth mentioning that, despite a strong or almost complete reduction in aromatics and naphthalene, there is still a residual amount of soot particle emissions of 6×10^{14} nvPM EI per kilogram of fuel that contribute to contrail formation from the combustion of HEFA-SPK. Also, the question arises why the 56% reduction in ice particles is larger than the corresponding 35 % reduction in soot number emissions. The reduction in the sulfur content of the HEFA-SPK from 0.0211 to 0.0007 mass %, corresponding to a reduction of 97% for HEFA-SPK compared to Jet A-1 shown in Fig. 5.5d could give one possible explanation. Sulfur contained in fuels can result in emissions of gaseous SO_2 , which can lead to the formation of very small sulfuric acid droplets (Petzold et al., 1997; Schumann et al., 2002; Jurkat et al., 2011; Kärcher, 2018). Moreover, models show that sulfur can activate the initially hydrophobic soot particles (Jones and Miake-Lye, 2023). Thereby it facilitates ice particle nucleation by increasing the hydrophilicity of the soot particles (Wong and Miake-Lye, 2010). Our results point towards a possibly reduced soot particle activation into ice particles due to the low fuel sulfur content and might explain stronger reduction in ice particles than from the reduction in soot alone. A similar effect has been suggested by Jones and Miake-Lye (2023) to explain observations of reduced soot activation into ice for a low-sulfur HEFA-SPK blend measured during the ECLIF2 campaign (Voigt et al., 2021).

At the same time, a larger spread in AEI values is observed for the Jet A-1 data points compared to HEFA-SPK due to the larger sample size of Jet A-1 measurements taken under cruise conditions. A large range of ice crystal number concentrations has been measured in young contrails (Heymsfield et al., 2010; Voigt et al., 2010, 2011; Voigt et al., 2017; Schumann et al., 2013, 2017; Jeßberger et al., 2013; Gayet et al., 2012; Chauvigné et al., 2018) due to the strong dynamical variations in humidity and temperature in the expanding plume as well as dilution in the vortex phase. The entrainment of ambient air in the primary vortex and the secondary wake leads to a multitude of conditions within the contrail, which can lead to sublimation locally, reflected in variations in ice crystal number concentrations (Lewellen et al., 2014). This explains the observed variations and shows that the assumption of AEI values not being influenced by vortex phase dynamics is not entirely true in reality. In addition, variations in altitude, position in the contrail, age of the contrail, and resulting state of development add to the distribution of AEI values due to ice crystal loss or measurement fluctuations as described in subsection 4.4.

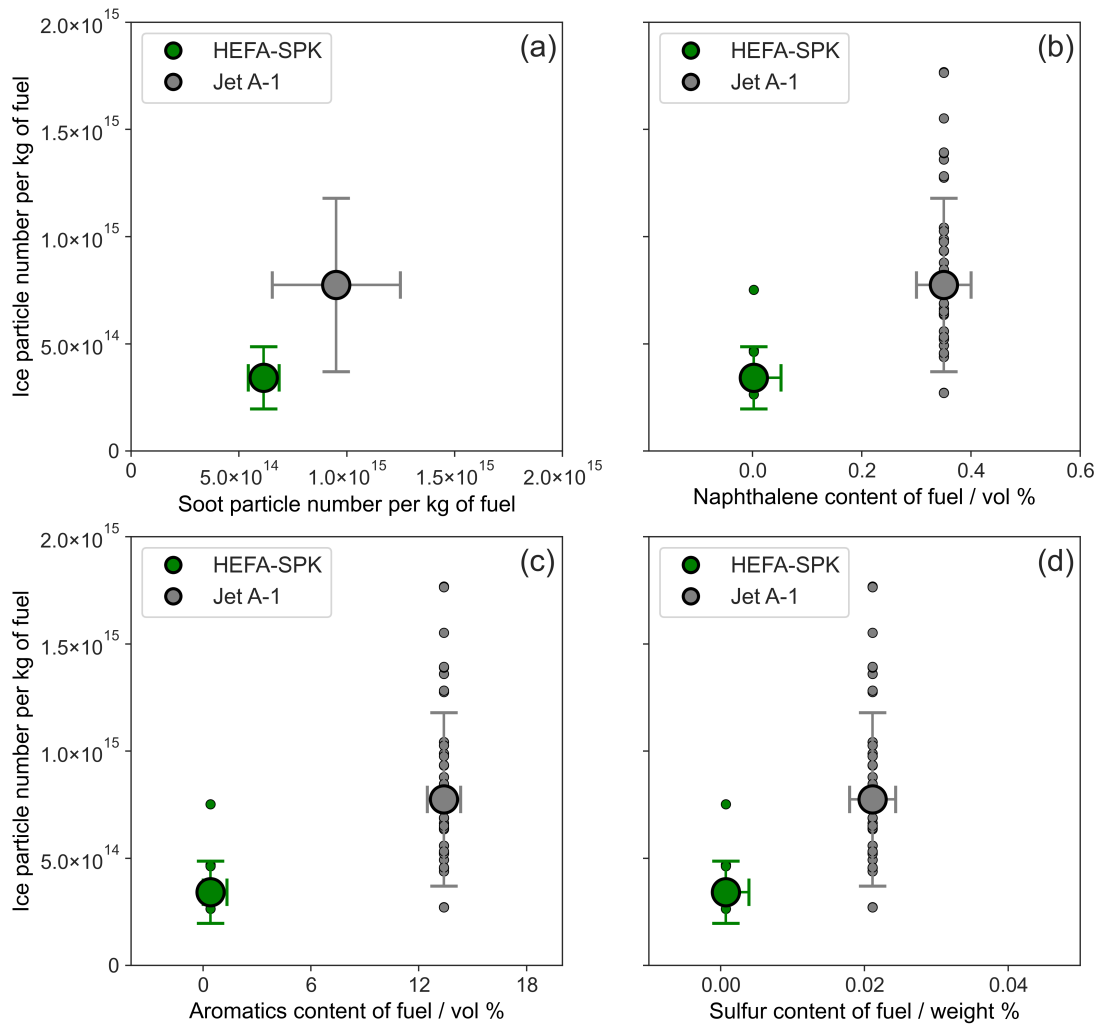


Figure 5.5: The AEI of ECLIF3 (flight on 16 April 2021) contrail measurements of Jet A-1 and HEFA-SPK fuels versus (a) nvPM emission indices and versus the respective fuel parameters (b) naphthalene content, (c) aromatic content, and (d) sulfur content. *x*-axis values are shown in Table 5.2. Single-scattered data points show data from individual contrail crossings, large circles represent the respective medians, and the bars give the arithmetic standard deviation. Note: the aromatic (naphthalene) content of HEFA-SPK is based on GCxGC measurements (%w w⁻¹) and not ASTM D6379 (D1840) due to being below the detection limit of these methods. *x* axis error bars are the reproducibility of the respective ASTM fuel property detection method (also used as a conservative proxy for GCxGC uncertainty). Source: Märkl et al. (2024)

Medians and means of soot data are based on nvPM emission indices in far-field contrail measurements at the same time as the presented apparent ice emission indices. Although nvPM emissions are preferentially measured under ice-free near-field emission conditions, data from far-field contrail sequences were chosen due to their sensitivity to the Mach number of the source aircraft and the lack of near-field data at similar Mach numbers in the far-field ice measurements. However, nvPM emission indices are slightly higher than their corresponding AEI values, which indicates the presence of interstitial soot, resulting possibly from a reduction in nucleation efficiency for the

low sulfur fuel, local sublimation effects, and/or fluctuations in nucleation efficiency. Further, the correction factor accounting for particle enrichment in the aerosol inlet is based on assumptions of ice particle size and nucleation efficiency, and effects such as particle trajectory deviations due to streamline compression and expansion at the fuselage (Afchine et al., 2018) are not considered. This highlights the need for ice-free near-field emission measurements for detailed analyses of aerosol emissions. Although the nvPM EI values in the case presented in Figure 5.5a are subject to the described sampling uncertainties, they nonetheless are a valuable indicator of soot particle activation, which is assumed to be the dominant ice particle activation mechanism in the soot-rich regime (Kleine et al., 2018; Kärcher, 2018)." (Märkl et al., 2024)

5.2.3 Impact of fuel composition and engine type on the apparent ice number emission index AEI

This subsection is taken verbatim (figure, table, and equation numbers adapted) from Märkl et al. (2024).

"These data can now be compared with results from the preceding ECLIF1 and ECLIF2/NDMAX campaigns where particle emissions and apparent contrail ice particle emissions were investigated in a similar manner to ECLIF3. It needs to be kept in mind that we are not able to independently and systematically vary single parameters and investigate their isolated influence on ice particle concentrations. This is amplified when comparing results from several campaigns where different engines, fuels, and measurement platforms were used. Aerosol inlet systems were not identical, and we estimate a 20% uncertainty for the intercomparison between campaigns for soot particle measurements. During the ECLIF1 and ECLIF2/NDMAX campaigns, the blends of a Fischer-Tropsch-based synthetic jet fuel with Jet A-1 (SSF1) and two blends of 30 % and 50 % biomass-based HEFA-SPK alternative jet fuel with Jet A-1 (SAF2 and SAF1) (Schripp et al., 2022) were compared to a reference Jet A-1 fuel (Ref2) as described in Voigt et al. (2021). However, a qualitative assessment of the influence of fuel composition and the type of engine used can be achieved by comparing the AEIs from different campaigns against their respective soot emissions (Fig. 5.6) and fuel constituents (Fig. 5.7).

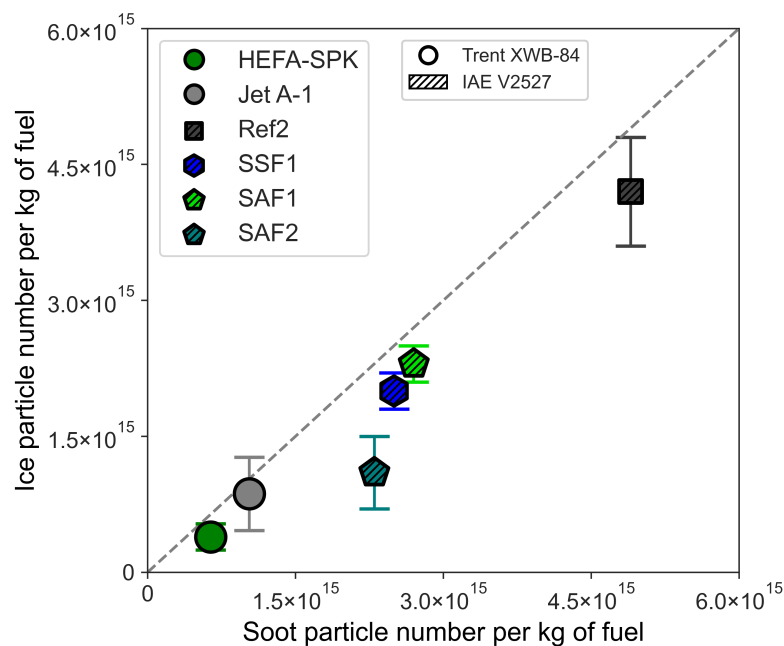


Figure 5.6: Apparent ice emission indices versus nvPM emission indices for Jet A-1 and HEFA-SPK fuel from the ECLIF3 campaign using a Rolls-Royce Trent XWB-84 engine (circles) compared to fuels investigated during ECLIF1 and ECLIF2/NDMAX (Ref2, SSF1, SAF1, SAF2) using an IAE V2527 engine (hatched symbols) (Voigt et al., 2021). The symbols represent means of the respective quantities in order to facilitate comparability between ECLIF1, ECLIF2/NDMAX, and ECLIF3 data. The dashed line shows the ideal 1 : 1 relationship between the AEI and nvPM EI. Source: Märkl et al. (2024)

In Figure 5.6, mean apparent ice emission indices versus mean nvPM EIs of these fuels are shown together with the mean AEI and nvPM EI of ECLIF3 as described in Table 5.4. We find a nearly linear relationship between ice particle numbers and nvPM particle numbers for the different fuels and different engines. Measurements during ECLIF1 and ECLIF2/NDMAX were conducted behind the DLR A320 Advanced Technology Research Aircraft (ATRA) equipped with IAE V2527-A5 engines with higher soot emissions compared to the Rolls-Royce Trent XWB-84. Many relevant measurement conditions were similar for the ECLIF1 and ECLIF2/NDMAX data, and the data were also filtered to only include data points with a relative humidity over ice of > 100%. The fuel-engine combinations investigated during ECLIF3 have a lower nvPM EI and therefore a lower AEI compared to the fuel-engine combination probed during ECLIF1 and ECLIF2. In particular, the newer Rolls-Royce Trent XWB-84 engine exhibits lower soot particle emissions compared to the old IAE V2527 engine probed during ECLIF1 and ECLIF2. Also, the aircraft were different, with the smaller and lighter A320 ATRA chased previously and the A350-MSN1 probed during ECLIF3. It is especially interesting that soot and apparent ice particle emissions of the ECLIF3 Jet A-1 lie below the SAF blends from previous campaigns. In order to disentangle fuel and engine effects on the emissions, relevant fuel properties are compared in Figure 5.7.

Table 5.4: The AEI and EI_{nvPM} for Jet A-1 and HEFA-SPK (based on 60 % correlation filtered data) for the ECLIF3 flight on 16 April 2021. Adapted from: Märkl et al. (2024)

Property	unit	Jet A-1	HEFA-SPK
AEI median	10^{14} kg^{-1}	7.8 ± 4.0	3.4 ± 1.5
AEI mean	10^{14} kg^{-1}	8.7 ± 4.0	3.9 ± 1.5
nvPM EI median	10^{14} kg^{-1}	9.5 ± 3.0	6.1 ± 0.7
nvPM EI mean	10^{14} kg^{-1}	10.3 ± 3.0	6.4 ± 0.7

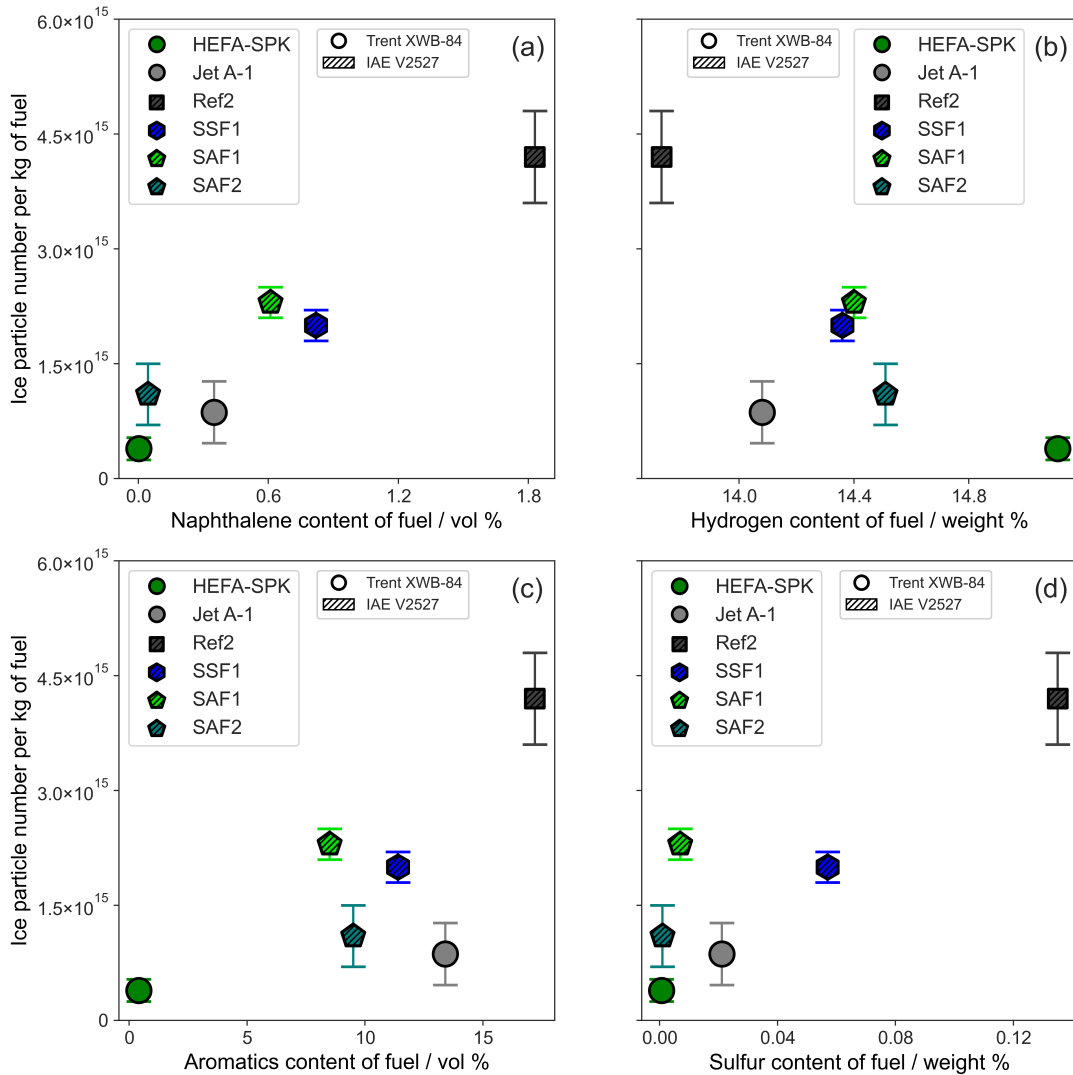


Figure 5.7: The AEI of ECLIF1, ECLIF2/NDMAX, and ECLIF3 campaigns versus fuel parameters (a) naphthalene content, (b) hydrogen content, (c) aromatic content, and (d) sulfur content. ECLIF3 fuels (HEFA-SPK, Jet A-1) were burned in a Rolls-Royce Trent XWB-84 engine (circles), while ECLIF1 and ECLIF2/NDMAX fuels (Ref2, SSF1, SAF1, SAF2) were burned in an IAE V2527 engine (hatched symbols) (Voigt et al., 2021). Note: the aromatic (naphthalene) content of HEFA-SPK is based on GCxGC measurements ($\%w w^{-1}$) and not ASTM D6379 (D1840) due to being below the detection limit of these methods. y-axis error bars are standard deviations of the means of the measurements shown as symbols. Source: Märkl et al. (2024)

AEI values from the three ECLIF campaigns from both aircraft and engines are shown in Figure 5.7 plotted against the fuel parameters (a) naphthalene, (b) hydrogen content, (c) aromatic content, and (d) sulfur content. The stronger bonding of the monocyclic and polycyclic aromatic compounds explains their propensity to form soot precursors. An increase in hydrogen content thus correlates with decreasing naphthalene or aromatic contents and can be seen as a unified measure attributed to the sooting propensity of the fuels. Therefore, we show the AEI versus the fuel's hydrogen content, which is also used in models to calculate the engine's nvPM particle emissions for specific thrust settings (Teoh et al., 2022b). Of all the fuels, the 100 % HEFA-SPK has the lowest naphthalene, aromatics, and sulfur content and at the same time the highest hydrogen content. Therefore, apparent ice particle emissions from this fuel-engine combination are the lowest in the set of compared fuels. For Jet A-1 from ECLIF3, on the other hand, it is no surprise that its AEI values are lower than those of the Ref2 fuel as Jet A-1 has a much lower naphthalene, aromatics, and sulfur content. However, it becomes more interesting how ECLIF3 Jet A-1 performs compared to the SAF blends SSF1, SAF1, and SAF2. Focusing on the fuel constituents mainly responsible for soot and volatile particle formation, naphthalene, aromatics, and sulfur, ECLIF3 Jet A-1 had a lower naphthalene content but a higher aromatic content compared to SSF1 and SAF1 and lies between those two fuels regarding the sulfur content. However, ECLIF3 Jet A-1 has a lower AEI compared to both fuels, indicating that the Rolls-Royce engine leads to reduced nvPM particle emission indices compared to the older IAE V2527 engine. Finally, ECLIF3 Jet A-1 has a higher naphthalene content, more aromatics, and more sulfur than SAF2, with at the same time a lower AEI. The same relation holds true for the two SAF blends SSF1 and SAF1, where SSF1 has a higher naphthalene, aromatics, and sulfur content but also lower AEI values. This shows that considered fuel constituents alone are not the only parameters that influence soot and ice crystal formation. Soot formation is strongly dependent on the engine cycle, combustion parameters, and combustor design. The Trent XWB-84 engine installed on the Airbus A350 during ECLIF3 is a latest-generation engine on a latest-generation aircraft compared to the IAE V2527-A5 engine installed on the Airbus A320 ATRA. This is also seen in the ICAO engine emissions database, which delivers engine emission indices from different engines probed at four thrust settings for the landing-take off cycle. While to some extent correlations between fuel constituents and apparent contrail ice particle emissions are suggested, other parameters such as the engine cycle, combustion parameters, combustor design, and atmospheric conditions may influence soot emissions as well. A direct cross-campaign comparison can therefore give hints on trends, but differences in ambient conditions and measurement setups impede a direct comparison based solely on the fuel effect, as is done for HEFA-SPK and Jet A-1 in ECLIF3. Here, the reduction of 56% from the rigidly reduced data set within one flight can be seen as the reduction potential when a flight is conducted with 100% HEFA-SPK instead of Jet A-1. However, an important fact to consider when interpreting reductions is the reference fuel to which a sustainable aviation fuel or blend is compared. The Jet A-1 used as a reference fuel in ECLIF3 was relatively clean by measures of naphthalene, hydrogen, aromatic, and sulfur content compared to the Ref2 fuel and even compared to the blends by some of the fuel properties. A comparison of ECLIF3 HEFA-SPK to Ref2 from ECLIF1 would lead to higher reduction in soot and

ice particles simply due to the higher emissions from the Ref2 fuel." (Märkl et al., 2024)

5.2.4 Variability in ice particle size distribution

This subsection is composed of verbatim parts (figure, table, and equation numbers adapted) of Märkl et al. (2024). The individual parts are marked by quotation marks and a citation.

"In addition to the fuel-engine-dependent reduction in overall contrail ice particle numbers, we investigate the variability of the ice particle size distributions in contrails and relate this to the vertical distance to the contrail-producing aircraft to account for vortex descent. This study extends beyond the fuel effects on apparent ice emission indices and aims to provide a deeper insight into the ice particle microphysics encountered during ECLIF3 contrail measurements. During the contrail vortex regime, exhaust is entrained in the two counter-rotating vortices, which propagate downward below the flight level. These vortices produce a wake into which some of the exhaust is detrained at altitudes above the primary wake (Gerz et al., 1998). To avoid measuring particles that sublimate in the descending primary wake, we focused our measurements on flight altitudes in the secondary wake at +96/−48 m vertical distance to the engine of the A350 aircraft. For this purpose, particle size distributions (PSDs) of single encounters of contrails formed on Jet A-1 emissions are viewed depending on the difference of detection altitude and emission altitude (Δz) and are shown in Fig. 5.8. For the analysis of ice particle size distributions, we concentrate on contrail encounters from Jet A-1 emissions, as a larger Δz is covered and no significant differences in size distribution can be attributed to the different fuels. Due to a better size resolution, we focus on CAS PSDs under ice-supersaturated conditions.

For this study, a mean PSD is calculated for every contrail encounter, and the corresponding mean Δz is indicated as a color in Fig. 5.8a. The PSDs are normalized to the respective size bin with the highest number concentration in order to be able to compare size ratios independent of absolute number concentrations. As ice particle sizes in contrails a few minutes old are typically below 10 μm and the contribution of larger ice particles was negligible, the PSDs are shown for sizes up to 10 μm . On the y axis is the number concentration normalized to the logarithmic width of the respective size bin, which allows comparison of concentrations over various bin widths. While the majority of the ice particle sizes lie in the range of 1.3 to 2.5 μm , ice particles with sizes below 1.3 μm down to 0.66 μm are henceforth classified as "small", and ice particles with sizes above 2.5 μm up to 8.2 μm are classified as "large". The highest concentration of small ice particles is measured in contrails encountered at large negative distances and hence below the emission altitude, and this concentration gradually decreases with increasing Δz . To illustrate this more clearly, the bins of the respective small and large ice particle size areas are summed up for every contrail encounter. These normalized distributions are plotted against the respective Δz in Fig. 5.8b and facilitate in relating small ice particle size concentrations to large ice particle size concentrations. Relative

to the bin with the highest concentration, there are many small and few large particles for low altitudes below the emission altitude. The share of small ice particles decreases with growing Δz , while the share of large ice particles grows.

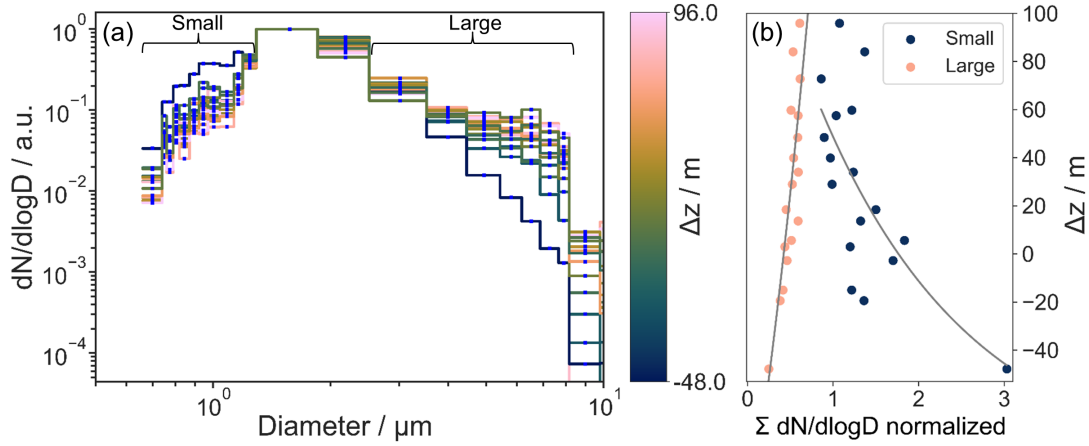


Figure 5.8: Ice particle size distributions (PSDs) of contrail crossings from Jet A-1 emissions measured by the CAS-DPOL instrument. The color bar shows the difference between the detection altitude and the emission altitude (Δz) in meters with positive values (negative values) defined as detected above (below) the emission altitude. Panel (a) shows the PSDs in number concentrations per logarithmic bin width normalized to the bin with the highest concentration. Bins are classified as "small" sizes and "large" sizes and are marked as such. Panel (b) shows the summed bins of small and large particle sizes of the normalized PSDs versus Δz . Gray lines are fits of the exponential function $f(x) = a \cdot b^x + c$, with a , b , and c being the variable parameters in order to illustrate the trends. Source: Märkl et al. (2024). Scientific color map: batlow (Crameri et al., 2020; Crameri, 2021).

From this analysis it becomes clear that, in this case, more small ice particles are found below the emission altitude, while the occurrence of large ice particles grows with increasing Δz within the secondary wake. Ice particles detected at different Δz have experienced different temperatures and humidity values along their trajectories from formation of ice in the jet phase and subsequent vortex processing, leading to the variations in ice particle size distributions. This variability in PSD shapes leads to various degrees of deviations from lognormal distributions, with the PSD at the lowest Δz having the largest deviation. While there is no discernible trend of the AEI depending on Δz for $RH_i > 100\%$, there appears to be a linear reduction in the total ice particle concentration with growing Δz when the summed $dN/d\log D$ of all the bins is regarded as shown in Fig. 5.9" (Märkl et al., 2024)

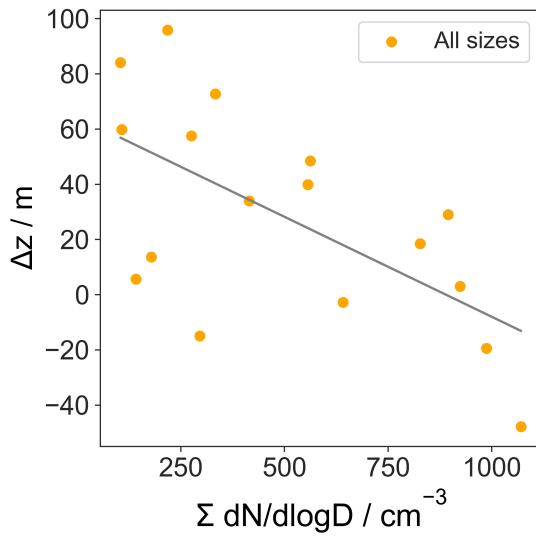


Figure 5.9: Summed bin-normalized number concentrations $dN/d\log D$ of all sizes from contrail encounters shown in Fig. 5.8 together with a linear fit function in gray. Source: Märkl et al. (2024)

"The values are calculated to illustrate trends in the shown particle size distributions also given in $dN/d\log D$ and do not reflect the absolute number concentrations N . The trend of growing ice particle number concentrations with smaller Δz is indicated by a linear fit function in gray." (Märkl et al., 2024) "The measurements thereby confirm simulations by Paugam et al. (2010) that are discussed by Paoli and Shariff (2016), which predict the locations of the largest ice crystals at the top of the secondary wake. There, fewer particles compete for the available water vapor, thereby allowing the growth of larger particles, while water vapor is distributed among more particles at the higher ice crystal number concentrations found at lower Δz , resulting in smaller ice crystals.

Unterstrasser (2014) finds from LES that number concentration distributions in the vertical contrail profiles of 5 min old contrails are non-symmetrical, with concentrations decreasing more rapidly for altitudes above the emission level compared to altitudes below the emission level. Similar results were found in the observations (Jeßberger et al., 2013; Schumann et al., 2013). Consistent with these findings, we observe that total number concentrations are systematically lower for $\Delta z \geq 40$ m. We find contrail ice crystals up to 96 m above the flight altitude of the source aircraft, which can be explained by uplift of ice crystals in the secondary wake and the primary vortex caused by vertical oscillation of the plume interacting with the stratified ambient atmosphere (Brunt-Väisälä dynamics). In addition, the adiabatic increase in temperature during the vortex-related descent contributes to the decrease in ice particle size with increasing distance below the emission altitude.

The ice particle size distributions also show for most encounters in the secondary wake that very small ice particles with sizes below $1 \mu\text{m}$ contribute little to the total size distribution. Similar results are found by Voigt et al. (2021) for the semisynthetic jet fuel with lower AEI values, while higher AEI values for Jet A-1 lead to smaller ice particle sizes due to more initial ice particles competing for the same amount of water (ambient and from the engine) and thus stay smaller. As AEI values for both fuels in ECLIF3 are even lower than AEI values of the semisynthetic jet fuel investigated in Voigt et al. (2021), the similar PSDs for Jet A-1, HEFA-SPK, and the semisynthetic jet fuel are consistent with the conclusion of larger particles correlating with lower AEI values. Schumann et al. (2013) investigate the EI profiles of trace gases, aerosols, and ice crystals in the normalized wake vortex coordinates behind small, medium, and large aircraft. They found far higher ice particle concentrations in the upper contrail parts than in the descending primary vortex, while passive tracers showed opposite trends. Their ice particle contrail profiles are similar to the present results

for large ice particles shown in Fig. 5.8b." (Märkl et al., 2024)

5.2.5 Conclusions and outlook

This subsection is taken verbatim (figure, table, and equation numbers adapted) from Märkl et al. (2024), except where modifications are indicated by square brackets.

"In the course of the ECLIF3 campaign, a measurement flight conducted in April 2021 was identified as having suitable conditions for a side-by-side comparison of contrail properties from 100% HEFA-SPK sustainable aviation fuel and a conventional reference Jet A-1 fuel. During this flight, ice crystals, together with the trace gases CO₂ and NO_y, as well as aerosols and water vapor, were measured in situ behind a long-range Airbus A350-941 equipped with latest-generation Rolls-Royce Trent XWB-84 engines. Using data from the two forward-scattering laser spectrometers, CAS and CAPS, on board the DLR Falcon research aircraft, apparent ice emission indices for the two probed fuels were derived. Thereby, for similar atmospheric and engine operation conditions of the preceding aircraft within a single flight, a reduction in the ice number concentrations of 56% for near-zero aromatic and near-zero sulfur HEFA-SPK compared to Jet A-1 were observed, while nonvolatile particle emissions were reduced by 35%. These reductions were found to depend on the fuel composition. In particular, the lower sulfur content of the HEFA-SPK might explain the stronger reduction in ice crystals compared to the soot reduction. Also, an influence of the engine cycle, combustion parameters, combustor design, and atmospheric conditions becomes apparent when comparing the ECLIF3 AEI to results from previous campaigns where an older IAE V2527 engine with higher soot particle emissions had been probed (Voigt et al., 2021). Fuel compositions of Jet A-1 and SAF are variable in terms of their hydrogen, aromatic, and sulfur contents, which impact particle emissions and should be taken into account for the decision on strategies to reduce the climate impact from aviation by the use of sustainable aviation fuels. Also, cleaner jet fuel with a naturally (or artificially achieved) low aromatic and naphthalene content as well as a low sulfur content could reduce the contrail impact on climate.

Ice crystal particle size distributions were investigated for contrail encounters, and a clear dependence of the particle size distribution on the difference of the detection altitude to the emission altitude Δz was found. On average, larger particles were found up to 96 m above the emission altitude and smaller particles below. In all the cases, the contrail ice crystals had equivalent spherical diameters of 1.3 to 2.5 μm . Here, the experimental data highlight the sensitivity of the ice crystal size distribution to the location within the contrail. The contrail cirrus model CoCiP was applied [by Ulrich Schumann] to compute apparent ice particle emission index values for fuels with a higher hydrogen content and modeled soot emission indices with a one-dimensional Gaussian plume mixing model. The computed AEI values show less variability compared to the measurements but very similar median values. Hence, the model is able to capture the measured soot and ice particle reductions based on the fuel hydrogen content parameterization.

In order to assess the mitigation potential of the climate impact from contrails by the use of 100%

SAF, [Ulrike Burkhardt and Cornelius Weiß-Rehm] performed global model simulations by applying experimentally derived ice particle reductions. The results suggest a reduction of approximately 26 % in contrail radiative forcing for a 60 % reduction in soot number concentrations by the use of 100 % SAF applied to the global fleet average for the year 2018. These reductions are slightly lower than previous model predictions (Burkhardt et al., 2018; Teoh et al., 2022b) but are well within model uncertainties for contrail radiative forcing. Absolute reductions were largest over the main air traffic areas of Europe and the USA, with slightly lower reductions over the southern parts of the main air traffic areas. Contrail cirrus coverage was predominantly reduced downwind of the main air traffic areas, which primarily contain aged contrail cirrus, in line with a reduction in the contrail cirrus lifetimes (Burkhardt et al., 2018).

The in situ measurements of contrails at cruise altitudes in a narrow range of atmospheric, engine, and measurement conditions within a single flight provide insight into the potential benefits of the use of 100 % SAF compared to fossil Jet A-1 fuels under cruise conditions for the current fleet. Variations of external conditions such as temperature or relative humidity are expected to have an influence on the AEI, and future studies are needed to systematically quantify the influence of fuels on nvPM and ice emissions under various conditions. While measured HEFA-SPK provides a benefit regarding the climate impact from contrails, the total climate benefit of different type of SAFs depends on the method of fuel production and the type of SAF used. In addition, the aromatic composition of the kerosene plays a role. With currently limited quantities and higher monetary costs of SAF compared to fossil fuels, one approach could be to preferentially replace the "dirtier" Jet A-1 fuels containing high naphthalene, aromatics, and sulfur content with SAF. Another approach could be to try to achieve a "cleaner" Jet A-1, pending increased availability of SAF. Further, approaches such as intelligent rerouting of flights together with targeted use of SAFs on routes with a high probability of persistent contrails could be pathways to maximize effectiveness as long as SAF is a limited resource (Burkhardt et al., 2018; Teoh et al., 2022b). Finally, a complete life-cycle analysis is necessary for every individual fuel in order to evaluate its CO₂ footprint and its non-CO₂ effects in order to assess a flight's total climate impact." (Märkl et al., 2024)

CHAPTER 6

Contrails from lean-burn engines

Large in-situ campaigns such as the VOLCAN project involve many people contributing in a number of ways and parts of their contributions are shown in this chapter. A detailed statement of contributions can be found in Contributions to this study after chapter 7.

In the previous chapter it was shown that the use of 100 % SAF in RQL-type combustors can lead to a reduction in contrail ice particle formation. Modern lean-burn aircraft engines are designed for increased fuel efficiency and lower NO_x and soot emissions (Liu et al., 2017). In this chapter, the effect of these lean-burn combustors on contrail ice particle formation with the use of conventional jet fuel and SAF will be explored. This way, the formulated research questions **RQ2** (can lean-burn combustors reduce contrail ice particle numbers?) and **RQ3** (does SAF reduce contrail ice particle numbers in lean-burn combustors?) are addressed. The basis of this analysis are the in-situ measurements conducted in the course of the VOLCAN campaigns.

6.1 Measurements of lean-burn emissions and contrails

The NEOFUELS/VOLCAN (VOL avec Carburants Alternatifs Nouveaux) projects are a German-French cooperation with partners including DLR, Airbus, and Safran Aircraft Engines aimed at investigating the impact of sustainable aviation fuels and modern aircraft engines on aircraft emissions and climate. Previous in-situ flight campaigns, especially the ECLIF campaign series, built a strong foundation of expertise and knowledge within the DLR cloud physics research group. With this foundation, the VOLCAN campaign aims to expand the understanding of particle emissions and contrail formation to modern lean-burn aircraft engines as opposed to conventional rich-burn combustors. These types of engines are of particular interest to the formation of contrails as they are designed for increased fuel efficiency and lower NO_x and soot emissions (Liu et al., 2017). Strongly reduced soot emissions are predicted to lead to similarly high contrail ice particle formation at cold temperatures but a strong reduction at temperatures close to T_{SA} (Kärcher, 2018). Aerosol emissions and contrail formation of lean-burn combustors in-flight have so far not been investigated and therefore take a central position in the VOLCAN studies.

The project consists of two campaign parts, with the first part, VOLCAN1, taking place in November 2021, and the second part, VOLCAN2, taking place in February and March 2023. In both campaign parts, Airbus flight test aircraft of the A320neo family operated by Airbus flight test crew served as emission source aircraft. An A319neo was employed during VOLCAN1 and an A321neo during VOLCAN2. Both aircraft are shown in-flight in Figure 6.1 as viewed from the DLR Falcon research aircraft. Newest generation CFM LEAP-1A lean-burn engines were installed in both aircraft. A series of alternative fuels was combusted at either lean-burn, rich-burn or a split mode combustion modes, which were achieved through Full Authority Digital Engine Control (FADEC) adjustments. In order to achieve the overarching goal of measuring emitted trace gases, water vapor, nonvolatile and volatile particulate aerosols and contrail ice particles, the DLR-operated Dassault Falcon research aircraft was used as measurement platform to chase the source aircraft. Two distance regimes between the two aircraft were probed. Near-field measurements took place as close as approximately 100 m behind the emission aircraft. This way, high concentration particle and trace gas emissions could be probed almost directly after emission without the influence of ice particle formation. Far-field measurements on the other hand were taken in contrails in the age range from 24-158 s, corresponding to mean aircraft distances of 6-35 km. Far-field observations allow probing of contrails in relatively stable conditions and are therefore the primary focus in this work of contrail ice particle studies. In the following, the used fuels, test points, measurement areas and measurement conditions will be presented for the individual campaign parts.



Figure 6.1: Source flight test aircraft during the VOLCAN campaigns as viewed from the DLR Falcon research aircraft. (left panel) Airbus A319neo used during VOLCAN1 and (right panel) Airbus A321neo used during VOLCAN2, each equipped with CFM LEAP-1A lean-burn engines.

6.1.1 VOLCAN1

In the course of the first campaign within the VOLCAN project in November 2021, a series of near-field and far-field formation flights were conducted off the French Atlantic coast. An Airbus A319neo (D-AVWA) equipped with CFM LEAP-1A engines was the subject of investigation during

the measurements (Figure 6.1 left panel). A custom-processed Jet A-1 fuel (HT-fuel) was combusted and compared to a conventional Jet A-1 fuel as reference while the LEAP-1A engine was operated either in lean-burn or a forced rich-burn mode via FADEC adjustments. The forced rich-burn mode is not the default combustion mode under the conditions it was operated in during the chase flights. Therefore, this forced rich-burn mode was set via FADEC adjustments for the cruise velocities needed during chase flights. Nonetheless, this combustion mode will henceforth be referred to simply as "rich-burn" for the sake of readability.

Table 6.1: Overview of far-field contrail flights during the 2021 VOLCAN1 campaign.

Flight Number	Date	Area	Type of flight	Fuel and combustion mode	
				lean-burn	rich-burn
09	17.11.	Bordeaux, Atlantic	Contrails	Jet A-1	
13	24.11.	Bordeaux, Atlantic	Contrails	Jet A-1	Jet A-1
14	25.11.	Bordeaux, Atlantic	Contrails	HT-fuel	HT-fuel
15	27.11.	Bordeaux, Atlantic	Contrails, Emissions	Jet A-1	

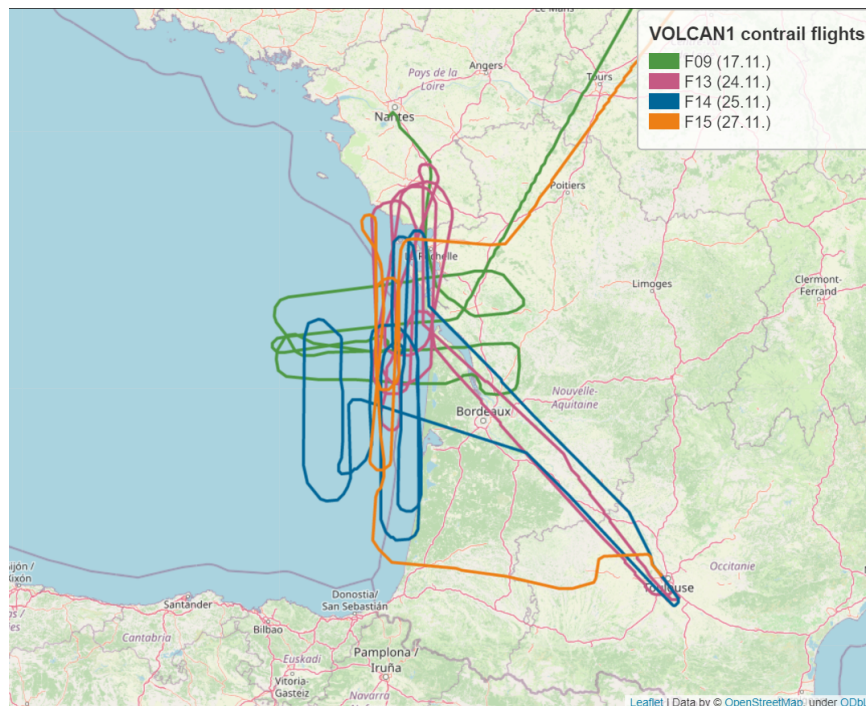


Figure 6.2: Overview of DLR Falcon flight paths of the four far-field contrail flights during the VOLCAN1 campaign. The brackets denote the flight date in the year 2021. Note that flights 13, 14, and 15 were combined flights of the VOLCAN1 and ECLIF3 Q4 campaigns. Map data from OpenStreetMap (<https://www.openstreetmap.org/copyright/en>).

Table 6.1 shows outline data of the far-field flights and the fuels and combustion modes covered. Additionally, three near-field flights were performed, where Flight 15 was a combined near-field and far-field flight. All far-field flights took place in the Bordeaux, Atlantic area as can be seen from the DLR Falcon flight paths shown in Figure 6.2. Atmospheric conditions, flight levels, and engine parameters are discussed in detail in sections 6.2 and 6.4. While the DLR Falcon took off from Nantes airport (ICAO: LFRS) for flight 09, and from Toulouse Blagnac (ICAO: LFBO) for the other three far-field flights, the emission source aircraft A319neo (paths not shown) took off from Toulouse Blagnac for all four far-field flights. Figure 6.2 clearly shows the racetrack pattern flown in either North-South or East-West directions. As was the case during the ECLIF3 campaign, the exact flight patterns and routes were chosen due to a combination of factors, including airspace restrictions from ATC, predicted contrail forming areas, and on-site evaluation of contrail visibility and conditions for contrail probing such as discernability of primary and secondary wakes.

During the campaign, a HEFA fuel and a HT-fuel were investigated and compared to a reference Jet A-1, while for far-field contrail measurements, only the HT-fuel and the Jet A-1 were available. The HT-fuel was originally a Jet A-1 fuel (different from the reference Jet A-1) that was processed specially for the project to reduce the aromatics, naphthalene, and sulfur content, as is detailed in Table 6.2. The performed processing greatly reduced fuel constituents typically responsible for soot and contrail ice particle formation while at the same time keeping the common fossil origin H:C mole fraction ratio of both fuels very similar. This provides an interesting case for fuel comparison in rich- and lean-burn combustion conditions and the effects are discussed in detail in section 6.3.

Table 6.2: *Properties of fuels used during VOLCAN1 far-field measurements.*

	unit	Jet A-1	HT-fuel
Fuel composition	%	100	100
Aromatics (ASTM D6379)*	vol%	13.1	0.5*
Naphthalenes (ASTM D1840)	vol%	0.37	< 0.08
Hydrogen content (ASTM D3701)	mass%	14.23	14.4
Carbon content**	mass%	85.77	85.60
H:C mole fraction ratio		1.98	2.00
El _{CO₂}	g/kg	3144	3138
Sulfur Total (ASTM D5453)	mass%	0.0138	0.0003
El _{H₂O}	g/kg	1.27	1.28
Combustion heat Q _{fuel}	MJ/kg	43.39	43.51

* Aromatics content of HT-fuel is determined by methods ASTM D2549 and ASTM D2425 due to the contents being below the ASTM D6379 detection limits.

**Carbon content based on the difference between 100% and hydrogen and sulfur content

6.1.2 VOLCAN2

The VOLCAN project was continued in February and March of 2023 with the second campaign part, VOLCAN2. Again, a series of formation flights consisting of nine far-field contrail flights and six near-field emission measurement flights were conducted. As for VOLCAN1, the DLR Falcon

served as research aircraft with the same suite of instrumentation. The emission source aircraft during VOLCAN2 was an Airbus A321neo (D-AVZO) as seen in the right panel of Figure 6.1. VOLCAN2 aims at expanding and consolidating the initial findings of VOLCAN1. This was achieved by systematically surveying a larger range of atmospheric conditions for a greater number of fuels. Additionally, as in VOLCAN1, engine combustion modes were varied between lean-burn, rich-burn or an intermediate split-mode via FADEC adjustments.

Table 6.3: Overview of far-field contrail flights during the 2023 VOLCAN2 campaign. Jet-A1 con1, Jet-A1 con2, HEFA con1, and Jet-A1 con2 were fuels contaminated with HEFA or Jet A-1 respectively. Details of fuel properties can be found in Table 6.4

Flight Number	Date	Area	Type of flight	Fuel and combustion mode		
				lean-burn	rich-burn	split
02	25.02.	Mediterranean	Contrails	Jet A-1 con1 HEFA con1	Jet A-1 con1 HEFA con1	
04	02.03.	Bordeaux, Atlantic	Contrails	Jet A-1 con2 HEFA con2	Jet A-1 con2 HEFA con2	
08	09.03.	Bordeaux, Atlantic	Contrails	Jet A-1	Jet A-1	Jet A-1
09	10.03.	Bordeaux, Atlantic	Contrails	SPK Low	Jet A-1 SPK Low	
11	14.03.	Bordeaux, Atlantic	Contrails	SPK Low	Jet A-1 SPK Low	
16	18.03.	Mediterranean	Contrails	Jet A-1 SPK High	Jet A-1 SPK High	
17	21.03.	Mediterranean	Contrails	Jet A-1	Jet A-1 SPK High	Jet A-1
19	22.03.	Brest, Atlantic	Contrails	Jet A-1 HEFA	Jet A-1 HEFA	
21	24.03.	Mediterranean	Contrails, Emissions	Jet A-1 HEFA		

A detailed overview of the carried out far-field contrail flights with investigated fuels and combustion modes can be found in Table 6.3. Nine far-field contrail flights took place in February and March 2023 in three measurement areas over France or off the French Atlantic coast. Thereby, eight flights were exclusively contrail flights and Flight 21 had an additional near-field sequence for the probing of emissions. In Figure 6.3, the three distinct measurement areas Brest/Atlantic in the Northwest (Flight 19), Bordeaux/Atlantic in the Southwest (Flights 04, 08, 09, 11), and Mediterranean in the South (Flights 02, 16, 17, 21) can be seen. As in VOLCAN1, racetrack patterns were flown where possible, with the exact path again determined by several factors as described in Section 6.1.1.

For the VOLCAN2 campaign part, a total of eight different fuels was investigated, of which four were pure fuels. A detailed overview of these fuels and their most important properties is given in Table 6.4. The HEFA fuel was the fuel with lowest content in aromatics, naphthalene and sulfur. In

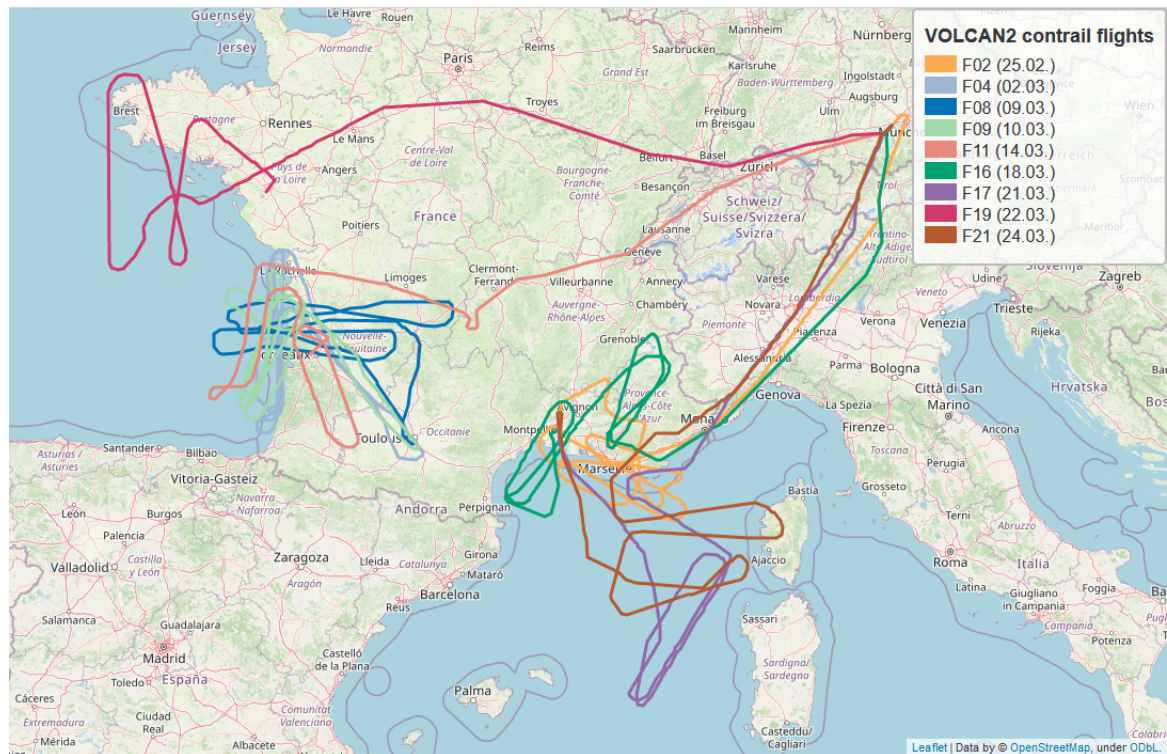


Figure 6.3: Overview of DLR Falcon flight paths from the nine far-field contrail flights during the VOLCAN2 campaign. The brackets denote the flight date in the year 2023. Map data from OpenStreetMap (<https://www.openstreetmap.org/copyright/en>). Note: A similar map has been shown by Jonas Schmidt (formerly DLR IPA) in his master's thesis (Schmidt, 2023).

order to be able to conduct a systematic series on the influence of aromatics on particle and contrail ice formation, aromatics were added to the HEFA fuel. This resulted in two fuels with extremely low sulfur and naphthalene content. One fuel had a low aromatic content (SPK Low) and the other a high aromatic content (SPK High). A conventional Jet A-1 served as reference fuel. However, due to a refueling error at the beginning of the campaign, the formerly pure fuels in the aircraft tanks were contaminated for the first set of flights. Therefore, involuntarily a set of blends of HEFA and Jet A-1 were achieved which increased the number of fuels investigated. Four of these blends were combusted during far-field flights and the resulting contrails probed. These fuels carry "con" (for contaminated) in their designation and the fuels with the "con 1" ending were used during Flight 02 and fuels containing "con 2" were used during Flight 04. The exact fuel blending ratio can be found in Table 6.4 under the fuel composition. An oddity resulting from this blending is that the Jet A-1 con 1 fuel contained more HEFA than Jet A-1, although originally intended to be pure Jet A-1.

Every contrail measurement flight is processed according to the methods described in chapter 4 to extract the findings on combustion modes and fuels discussed in the following sections. An exemplary time series of the most important measured parameters during contrail measurement flight 16 can be found in Figure 6.4. During that flight, SPK High fuel and Jet A-1 were combusted in

Table 6.4: Properties of fuels used during VOLCAN2 far-field measurements.

	unit	Jet A-1 con 1	HEFA con 1	Jet A-1 con 2	HEFA con 2	Jet A-1 con 1	HEFA con 1	Jet A-1 con 2	HEFA con 2	Jet A-1	HEFA	SPK Low	SPK High
Fuel composition (Jet:HEFA ratio for blends)	%	47:53	67:33	95:5	36:64	100	100	100	100	100	100	100	100
Aromatics (ASTM D6379)	vol%	6.05	8.58	12.13	4.66	12.8	<1	8.4	17.6	<0.1	<0.1	8.4	17.6
Naphthalenes (ASTM D1840)	vol%	0.34	0.45	0.6	0.28	0.6	<0.1	<0.1	<0.1	15.30	14.80	<0.1	<0.1
Hydrogen content (ASTM D3701)	mass%	14.69	14.43	14.07	14.83	14.1	15.30	14.80	14.3	85.9	85.2	14.80	14.3
Carbon content*	mass%	85.31	85.57	85.93	85.17	85.9	84.7	85.2	85.7	2.07	2.15	85.2	85.7
H:C mole fraction ratio		2.05	2.01	1.95	2.07	1.96	2.15	2.07	1.99	3148	3104	2.07	1.99
El _{CO₂}	g/kg	3126	3135	3149	3121	3148	3104	3122	3140	0.0195	0.00032	3122	3140
Sulfur Total (ASTM D5453)	mass%	0.0097	0.0136	0.0192	0.0075	0.0195	0.00032	0.00019	0.00005	1.26	1.37	0.00019	0.00005
El _{H₂O}	g/kg	1.31	1.29	1.26	1.33	1.26	1.37	1.32	1.28	43.42	44.07	1.32	1.28
Combustion heat Q _{fuel}	MJ/kg	43.63	43.60	43.42	43.90	43.36	44.07	43.83	43.50	43.36	44.07	43.83	43.50

Fuel composition of blends refer to Jet:HEFA blending.

*Carbon content based on the difference between 100 % and hydrogen and sulfur content

lean-burn and rich-burn combustion modes as indicated at the top of the respective sections. Single contrail encounters can be clearly discerned by the peak structures in ice particle concentrations as well as in trace gas and aerosol concentrations. The horizontal dashed blue line indicates the saturation threshold for RHi in the fourth row of the figure. Contrail encounters at supersaturated conditions above this dashed line are considered for further processing. The last row shows that the rich-burn combustion during this flight was measured at a higher flight level and therefore lower temperatures compared to the lean-burn combustion section.

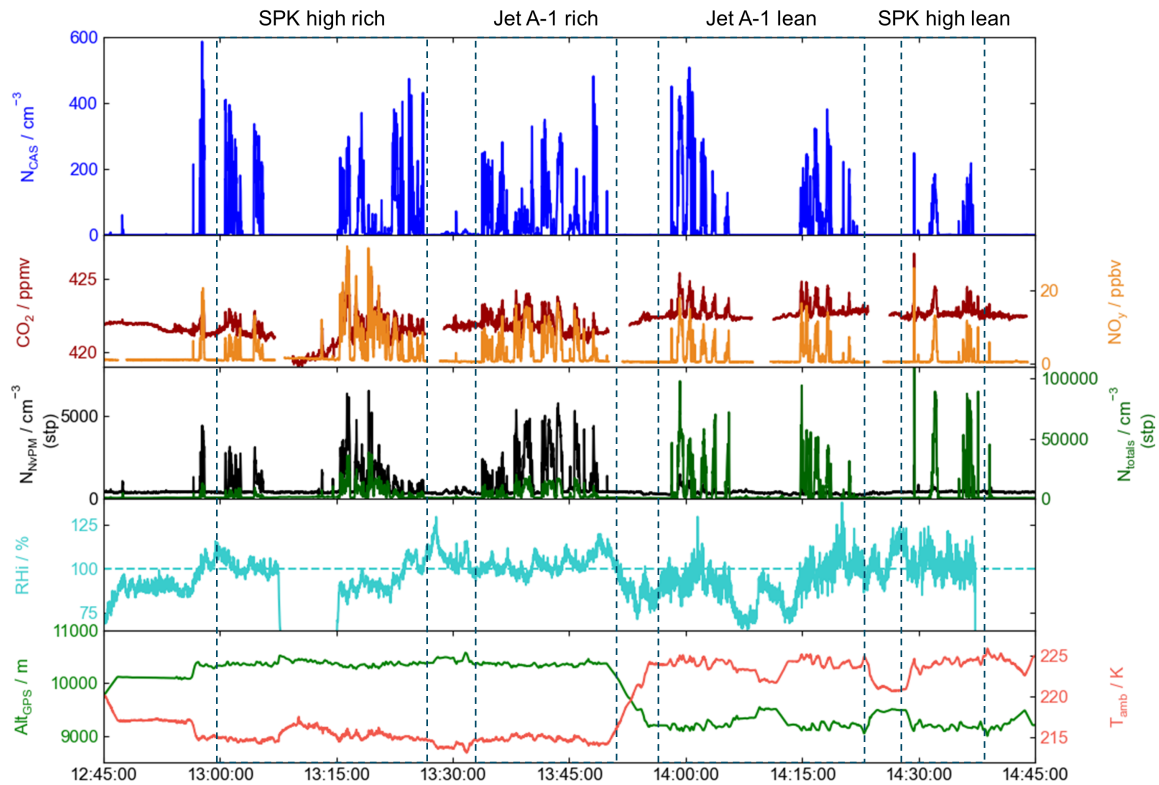


Figure 6.4: Time series of 1 Hz VOLCAN2 contrail flight F16 data during far-field measurement sequences of Jet A-1 and SPK High fuel showing number concentrations of ice crystals larger than at least $0.5 \mu\text{m}$ measured by the CAS (N_{CAS}), CO_2 and NO_y mixing ratios, number concentrations of nonvolatile particles $> 14 \text{ nm}$ (N_{nvPM}) and of total particle concentrations (N_{totals}), relative humidity over ice (RHi) during the measurements with indicated saturation (dashed line), and the GPS altitude of Falcon (Alt_{GPS}) with the Falcon-measured ambient temperature (T_{amb}).

6.2 Influence of combustion modes on AEI

This section will explore the effects of combustion modes in lean-burn engines on AEI and the relationship to aerosols using observations from the VOLCAN1 and VOLCAN2 campaigns. For this, far-field ice particle measurements will be compared to near-field aerosol emission measurements in subsection 6.2.1. The statistical method described in section 4.7 is then applied to the ice particle data set to investigate the influence of combustion mode on contrail ice crystal numbers on a

smaller scale. Finally, PSDs of combustion modes are compared.

6.2.1 Contrail formation on emitted aerosols

- *How many ice crystals are activated in the low-soot emission regime?*
- *Is there a dependence of total particles (volatile and non-volatile) on ice crystal numbers?*

The work by Kärcher (2018) describes expected ice crystal number emission indices vs. number emission indices of emitted soot particles as predicted by the parcel model described in Kärcher and Yu (2009). Expected AEI for the soot emission range from 10^{12} kg^{-1} to 10^{16} kg^{-1} are shown for two different cases of ambient conditions (see Figure 1.2). This range of soot EI roughly spans the soot emission indices expected from lean-burn engines and classical rich-burn engines and is therefore a well suited representation for discussing measurements of the VOLCAN1 and VOLCAN2 campaigns.

For temperatures close to the Schmidt-Appleman contrail formation threshold, the lower boundary of expected AEI is shown in Figure 6.5 (a). In this case, only a fraction of emitted soot particles is activated with a nearly linear dependence for nvPM EI above approximately 10^{14} kg^{-1} . Below that value, the model expects soot activation to further decrease and approach a lower limit defined by ambient aerosol concentration (Kärcher and Yu, 2009; Kärcher, 2018). For ambient temperatures 12 K below T_{SA} , the upper boundary of expected AEI (Kärcher, 2018) is formed as shown in Figure 6.5 (a). Under such conditions, soot particle activation levels are much higher so that ice particle numbers have a nearly 1:1 relationship to soot particle numbers in the high soot regime. For the low soot case below approximately 10^{14} kg^{-1} nvPM EI, the model predicts activation of UAPs so that AEI are able to reach levels similar to those in the soot-rich regime. In this type of representation, far-field AEI from the VOLCAN1 and 2 campaigns and near-field nvPM EI measured from forced rich-burn combustion are added in Figure 6.5 (b). Hereby, all far-field ice particle measurements from fuels with corresponding near-field measurements were used and small symbols in the figure represent single contrail encounters while the large symbols represent median AEI for ΔT_{SA} bins as described in subsection 4.7. This variability in ΔT_{SA} leads to the spread in AEI along the y-axis, as is expected from the relationships between AEI and ΔT_{SA} described in section 6.4. The forced rich-burn data points span and exceed the range predicted by the model (Kärcher and Yu, 2009; Kärcher, 2018) and similar soot particle emissions are measured as for a RQL-type combustor discussed in chapter 5.

In the same manner, far-field contrail ice particle AEI and near-field nvPM EI are added to this type of representation in Figure 6.5 (c). nvPM EI lie in the range between 10^{11} kg^{-1} to 10^{12} kg^{-1} . Therefore, a reduction of approximately three orders of magnitude can be observed for nvPM emissions when operating the LEAP-1A engine in the default lean-burn mode compared to the forced rich-burn combustion mode.

Median AEI on the other hand span from approximately $6 \times 10^{13} \text{ kg}^{-1}$ to $2 \times 10^{15} \text{ kg}^{-1}$ for lean-burn combustion and from $1 \times 10^{14} \text{ kg}^{-1}$ to $2 \times 10^{15} \text{ kg}^{-1}$ for the forced rich-burn mode. AEI therefore span a similar range for the two combustion modes so that the reduction in nvPM does not translate into similar reductions for contrail ice particles.

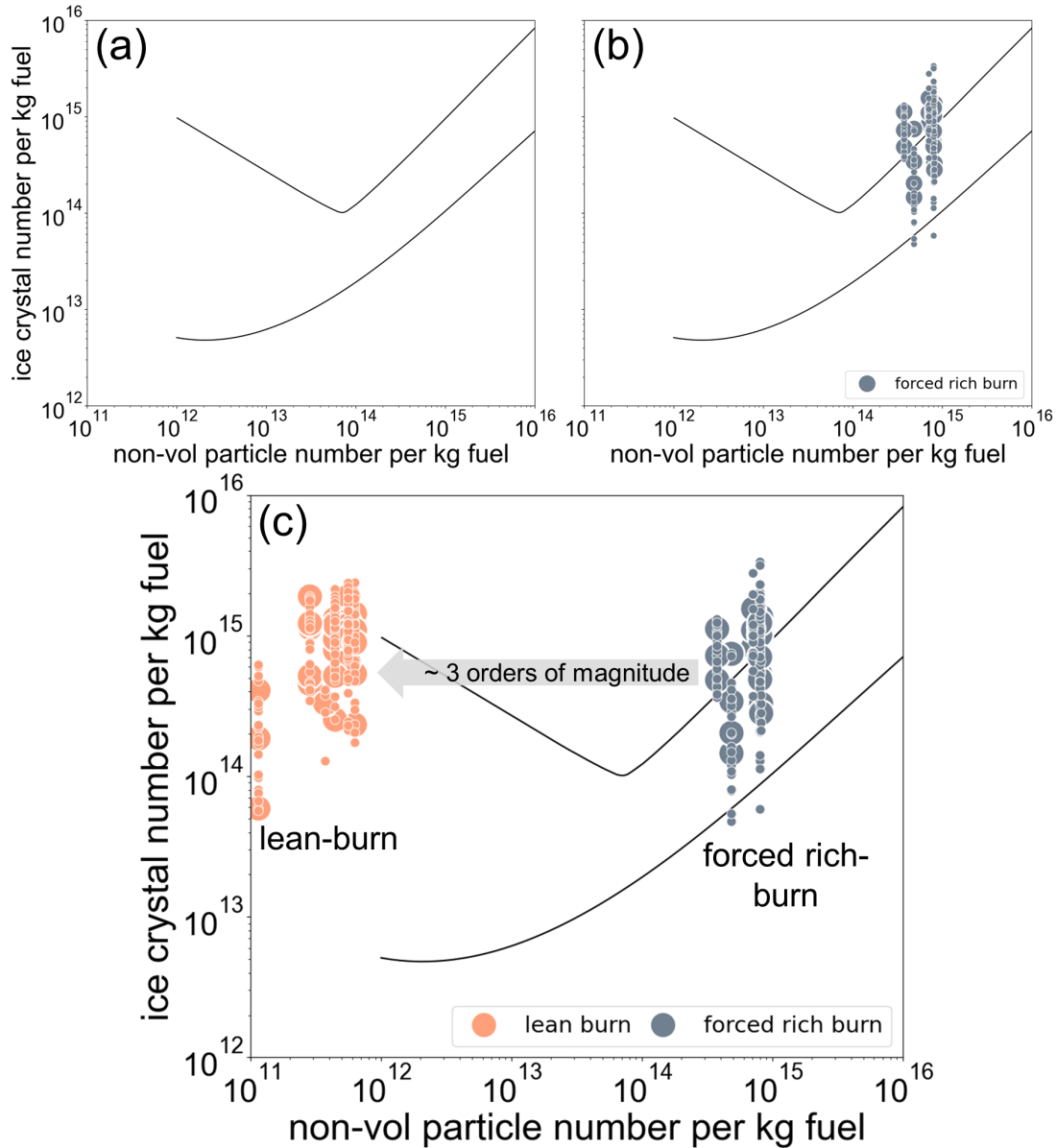


Figure 6.5: (a) Upper (far below T_{SA}) and lower (close to T_{SA}) expected AEI boundaries based on Kärcher (2018) for nvPM. Far-field VOLCAN1 and 2 contrail AEI (only CAS-DPOL) shown against near-field nvPM EI for (b) forced rich-burn combustion mode and (c) lean-burn together with forced rich-burn combustion mode. Small symbols are single contrail encounters while large symbols represent median AEI values in $1 \text{ K } \Delta T_{SA}$ range bins as described in section 4.7.

AEI and near-field total particle EIs of the lean-burn and forced rich-burn combustion mode are shown together in Figure 6.6. This representation reveals that total particle emissions are also not

affected on the order of magnitude scale by the different combustion modes as the range of total particle EI for the forced rich-burn mode lies completely within the range of the lean-burn mode. Instead, a correlation is found between AEI and near-field total particle EIs for both combustion modes. The 1:1 line and 1:1 line factored by 10^{-1} almost completely envelope the total particle EI and AEI for both combustion modes. In the rich-burn mode, near-field nvPM EI are approximately 30 % to 53 % of total particle EI, depending on the fuel. In the lean-burn mode however, the share ranges from approximately 0.02 % to 0.12 %. This means that while a large number of soot particles is available for ice particle nucleation in the rich-burn mode, the vast majority of emitted particles in the lean-burn mode must be volatile or other types of particles not detected as nvPM, such as engine oil or chemi-ions. While nvPM numbers are on the scale of ice particle numbers for the rich-burn combustion mode, particles other than nvPM must be activated to ice particles in the lean-burn combustion mode. The particle types in question for nucleation will be discussed in section 6.6.

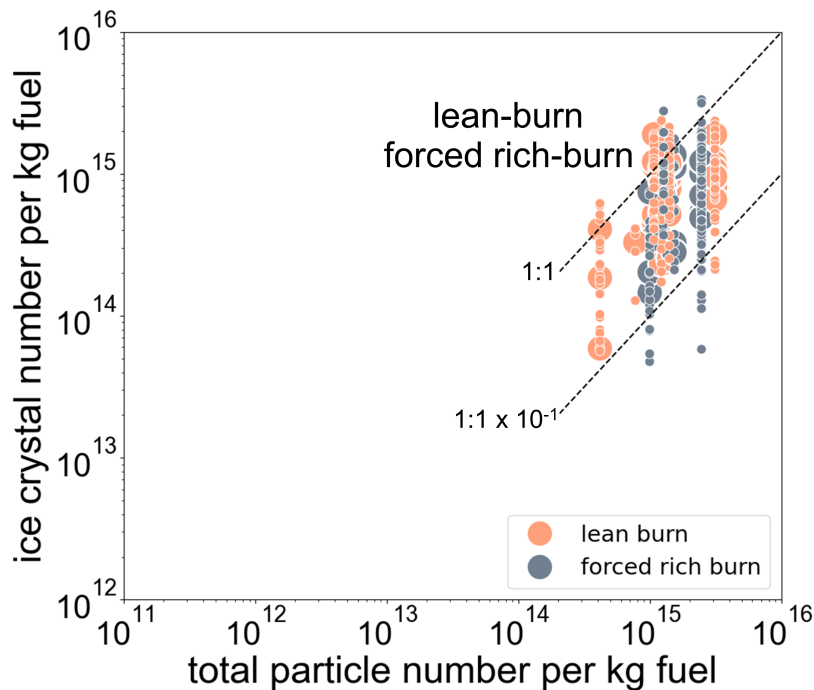


Figure 6.6: Far-field VOLCAN1 and 2 contrail AEI (only CAS-DPOL) shown against near-field total particle EI for forced rich-burn and lean-burn combustion modes. Dashed lines represent the 1:1 line and the 1:1 line factored by 10^{-1} . Small symbols are single contrail encounters while large symbols represent median AEI values in $1\text{ K } \Delta T_{SA}$ range bins as described in section 4.7.

It is important to note that due to the nature of comparing far-field with near-field measurements, the shown relationships between AEI and aerosol EI do not stem from simultaneous measurements and therefore combustor conditions and ambient conditions are not the same. Also, the rigorous narrowing down of ambient conditions by the domain method described in section 4.7 has not been applied for the data shown against near-field aerosol EIs. These relationships are therefore to be seen as approximations on the order of magnitude scale and should not be used to draw conclusions

on the effect of different fuels on AEI. Figures showing far-field AEI against near-field nvPM for the VOLCAN1 and 2 campaigns separately and resolved by fuels can be found in Figures A1 and A2 in Appendix A. The behavior of nvPM and total particle EI and of AEI between rich-burn and lean-burn combustion modes is consistent between the VOLCAN1 and VOLCAN2 campaigns and the emission indices span similar ranges. While the LEAP-1A engine type was used during both campaigns, the individual engines were mounted on different aircraft and had different ages and maintenance cycles. Therefore, the comparison of results from these two campaign parts confirms that the high number of contrail ice particles in the lean-burn mode is achieved independently of the aforementioned variabilities of engine lifecycle conditions, different individual engines, and the large range of spanned ambient conditions.

The comparison of far-field AEI with near-field aerosol EI and also the grouping together of data measured at a large range of ambient conditions is well suited to draw conclusions on the order of magnitude scale. However, conclusions on the effects of the different fuels and also possible smaller-scale effects of combustion modes on contrail ice particle formation is not possible from this approach. In order to achieve deeper insights into effects of combustion mode on a smaller scale, a statistical approach will be applied in the following subsection.

Addressing the initially formulated research questions at the beginning of section 6.2, the following summarized answers can be stated:

- **Large reductions in soot during lean-burn combustion do not translate to the same reductions of contrail ice particles. Instead, similar amounts of ice crystals are found in low-soot conditions as in high-soot conditions.**
- **Contrail ice crystal numbers correlate with total particle emissions in the low-soot and high-soot regime. The partitioning between volatile and non-volatile particles plays a secondary role.**

6.2.2 Statistical analysis of combustion mode effects on contrail ice particles

The large range of ambient conditions present during the VOLCAN campaigns necessitates the method of data structuring by domains as described in section 4.7 in order to reveal possible smaller-scale effects of combustion modes on contrail ice particle formation. The domains defined in section 4.7 allow the comparison of fuel and combustion mode effects by reducing the parameter space to the mutually linearly dependent RH_i or ΔT_{SA} . In this section, the relevant domains will be explored to extract findings regarding the effect of combustion mode on contrail ice particle number and properties. For this, six domains have been identified in VOLCAN2 and two domains in VOLCAN1 from which combustion mode comparisons can be conducted. These are listed in Table 6.5 where for each domain, at least one comparison of combustion modes is possible with a

single fuel. It needs to be kept in mind that each domain originates from a different set of ambient conditions and represents a case study in itself. Three metrics are used to evaluate the comparison between combustion modes for a single fuel, beginning with the normalized difference between compared fuel and combustion mode combination to the chosen reference. This value states the mean difference between the two compared fuel and combustion mode combinations from the four different data grouping approaches, namely from RHi binning (RHi), alternative RHi binning (RHi a), ΔT_{SA} binning (ΔT_{SA}), and alternative ΔT_{SA} binning (ΔT_{SA} a). Correspondingly, a Mann-Whitney U Rank Test p-value and statistical weight for each data grouping is given to assess the significance and to evaluate the validity of the normalized differences. In order to be able to assess the possible reasons for high p-values, the statistical weights are given. A high weight indicates a large number of data of the two compared fuel-combustion modes in same bins and therefore a good sample size for statistically relevant conclusions.

Within the six P-T domains, nine different comparisons on five different fuels can be made regarding three combustion modes. From Table 6.5, the normalized mean differences to the respective references can be extracted. Comparing lean-burn conditions to rich-burn conditions yields differences from -36 % to +67 % and comparisons to split combustion conditions yields differences from -35 % to +12 %. At first glance, some of these differences may appear large and could thereby suggest a strong effect of the combustion mode on contrail ice formation. For example, a 67 % increase in contrail ice particles for lean-burn combustion compared to rich-burn combustion in domain 9.6 could appear as a surprisingly large increase, especially when keeping the large nvPM EI reductions in the near-field in mind.

However, to properly evaluate these differences, the Mann-Whitney U test p-values and statistical weights for the respective comparison come into use. It quickly becomes apparent that there is not one single combustion mode comparison where all four p-values indicate statistically significant differences. For one comparison of the contaminated HEFA_con2 fuel in domain 1.3 and the VOL-CAN1 comparison in domain 1.1, three of the p-values lie below the threshold, while one of them lies above. For the HEFA comparison of domain 6.3 and for domain 7.3, one of the p-values lies below the significance threshold. This means that for seven of the eleven comparisons, it can be stated that the differences of the normalized AEI are not statistically significant and for four of the comparisons the statistical significance of the lean-burn AEI compared to rich-burn is inconclusive. The fact that variability can be seen in the p-values for different binning methods shows that results can be sensitive to the way they are grouped depending on ambient conditions and highlights the need to consider the totality of different binning possibilities to achieve robust results. Using the method of four different binnings, the results of normalized differences have a high level of confidence where all four p-values are conclusive, while fringe cases yielding different p-values for different binnings would likely lead to misinterpretation of results if only one binning method were used.

The statistical weights in Table 6.5 are heat map color coded with low values colored in lighter shades of blue and higher values colored in darker shades of blue. For example, the statistical

Table 6.5: Overview of results from combustion mode comparisons based on P-T domains. Defined are the reference fuel-combustion mode together with the compared fuel-combustion mode and the resulting difference of normalized mean values. For p-values and statistical weights according to the definition in subsection 4.7, four values are given respectively, where each value is obtained either from relative humidity binning (RHi), alternative relative humidity binning (RHi a), ΔT_{SA} binning (ΔT_{SA}), or alternative ΔT_{SA} binning (ΔT_{SA} a). p-values that fall below the statistical significance threshold of 0.05 are marked in green while p-values above the threshold are marked in red. Statistical weights are marked by a heat map where low weights have lighter coloring and higher weights a darker coloring. Note that CAS-DPOL and CAPS-DPOL data is used for VOLCAN1 domains.

P-T Domain	Ref. fuel comb. mode	Compared fuel comb. mode	Norm. diff. to ref.	p-values		stat. weights	
				RHi	RHi a	RHi	RHi a
				ΔT_{SA}	ΔT_{SA} a	ΔT_{SA}	ΔT_{SA} a
VOLCAN2							
1.3	HEFA_con2 rich	HEFA_con2 lean	-24 %	0.013 0.01	0.045 0.068	63 153	59 191
	Jet A-1_con2 rich	Jet A-1_con2 lean	+12 %	0.052 0.14	0.062 0.258	51 165	57 153
3.2	SPK Low rich	SPK Low lean	-30 %	0.242 0.400	0.569 0.474	99 140	66 170
	4.4	Jet A-1 split	Jet A-1 lean	+12 %	0.495 0.495	0.700 0.781	126 192
Jet A-1 split		Jet A-1 rich	-6 %	0.638 0.671	0.646 0.669	154 182	112 162
6.3	Jet A-1 rich	Jet A-1 lean	-3 %	0.320 0.189	0.708 0.560	92 275	118 330
				0.573 0.014	0.956 0.213	45 116	43 109
	HEFA rich	HEFA lean	+12 %				
7.3	Jet A-1 split	Jet A-1 rich	-35 %	0.232 0.038	0.075 0.091	25 75	28 63
				9.6	SPK Low rich	SPK Low lean	+67 %
VOLCAN1							
1.1	HT-fuel rich	HT-fuel lean	-36 %	0.003 0.005	0.001 0.115	32 60	36 40
				2.2	Jet A-1 rich	Jet A-1 lean	+5 %

weights are the lowest for the comparison in domain 9.6 where the largest difference between lean-burn and rich-burn was found. Therefore, the likely reason for the high p-values are a low number of compared data points. On the other hand, comparisons with very high statistical weights, (e.g. domain 6.3 Jet A-1 or domain 4.4) yield relatively small normalized differences between the combustion modes with additionally high p-values.

In conclusion for contrail ice particles, there was not one combustion mode comparison which yielded unambiguously statistically significant differences. When comparing combustion modes, this means that either, similar ranges of AEI are found, or that the statistical sample size is not sufficient to draw reliable conclusions. It also has to be kept in mind that in this study, contrail ice particle concentrations were measured in far-field conditions where the emissions from both engines were mixed. As will be shown in section 6.6, the two engines used during VOLCAN2 did not have the same emissions characteristics. Therefore despite these results, it can not be excluded that the combustion mode could have an effect on contrail ice particle formation and further measurements are needed to corroborate the findings of this study.

It can therefore be concluded:

The engine combustion mode has no statistically significant systematic influence on the ranges of contrail AEIs independent of the used fuel in the investigated engine/aircraft configurations.

6.2.3 Size distributions depending on combustion mode

Contrail ice particle numbers from lean-burn combustion were shown to be similar to rich-burn combustion. As significantly differing size distributions have been shown to arise from reductions in AEI (Voigt et al., 2021), similar PSDs would be expected for different combustion modes if no significant differences are found for AEI.

In order to confirm this expectation, PSDs of possible comparisons have been compiled for every P-T domain and resolved for every contrail encounter by ΔT_{SA} and RH_i. These PSDs are normalized to their respective bin with highest concentration for every plume encounter to be able to compare changes in PSD independent of absolute number concentration. By resolving ΔT_{SA} as a color gradient for every contrail encounter, it can be seen that the size distributions are sensitive to this parameters. P-T domain 4.4 has been chosen to illustrate the effect of combustion mode on PSD as all three combustion modes are covered.

In Figure A6 in Appendix A for example, it can be clearly seen that conditions at higher ΔT_{SA} temperatures produce PSDs with more small particles and less larger particles, where small particles are defined as particles with sizes below the highest bin (< approx. 1.5 μm) and large particles as particles larger than approximately 1.5 μm . This is indicated by the highest concentrations of small particles for the pink curves which are also the lowest for larger sizes and an inverse relationship for the darker blue curves. Similarly, when resolving RH_i as shown in Figure A7 in Appendix A, the pink curves for high humidity indicate a low number of small particles and a

higher number of larger particles, while less humid conditions lead to more small particles and less larger particles. These relationships indicate that for higher levels of supersaturation, more water vapor can condense to grow larger ice particles.

Compared to the PSDs shown for the ECLIF3 measurements in subsection 5.2.4, Δz plays a secondary role in the PSDs compiled for the VOLCAN campaigns. This is largely due to the large variation in ΔT_{SA} and RH_i found during the VOLCAN campaigns while the ECLIF3 measurements were taken in very similar humidities and temperatures. These variations in RH_i and ΔT_{SA} dominate the PSD shape but other influences like Δz could play a role when RH_i and ΔT_{SA} are kept constant.

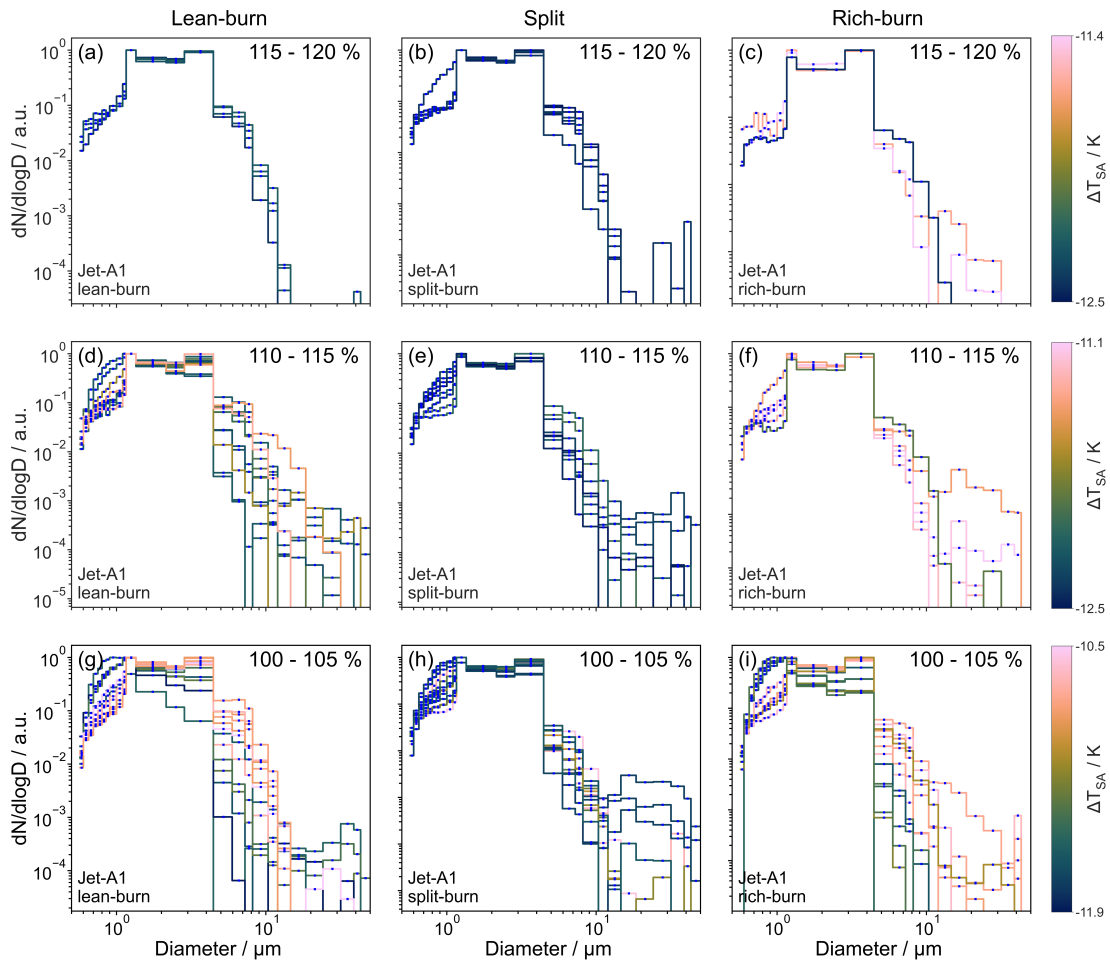


Figure 6.7: PSDs from P-T domain 4.4 from Jet A-1 combustion for the three combustion modes (a, d, g) lean-burn, (b, e, h) split, and (c, f, i) rich-burn. Conditions are narrowed to (a, b, c) high humidity (115 - 120 %), (d, e, f) medium humidity (110 - 115 %) and (g, h, i) low humidity (100 - 105 %) and resolved by ΔT_{SA} represented by a color gradient (Crameri et al., 2020; Crameri, 2021). Note: Not filtered for uncertainty or correlation.

In order to be able to attribute changes in PSD to the combustion mode and not to ambient conditions, these ambient conditions need to be narrowed down. For this, a case study is discussed

in the following where the Jet A-1 PSDs for lean-burn, split mode, and rich-burn are compared from P-T domain 4.4, as all three combustion modes can be compared in this domain. These PSDs are shown resolved by combustion mode in three columns and narrowed to ranges of similar humidity in three rows in Figure 6.7. The highest concentrations of nearly all PSDs are found in the range between 1.1 μm to 4.4 μm with variations in the ratio of smaller particles ($< 1.1 \mu\text{m}$) to larger particles ($> 4.4 \mu\text{m}$). For example, in panels (d), (g), or (i) it can be seen that a variation in particle size ratios is found depending on ΔT_{SA} . Lower ΔT_{SA} values (darker colors) are correlated with a higher number of small particles and a smaller number of large particles, while higher ΔT_{SA} values lead to an inverse relationship. However, there are also cases where the variation in PSDs cannot be attributed to the variation in ΔT_{SA} , for example in panel (b). Here, the majority of PSDs is very similar with a small number of small particles while one PSD shows a higher number of small particles and less larger particles. This effect can also be found in other instances, such as in panels (d), (f), (g), or (i). As there is not always a correlation of these outliers to ΔT_{SA} , it appears likely that another factor besides ΔT_{SA} or RH_i has a major influence on the shape of PSDs. Further conditions for which an influence on PSD shape appear reasonable include Δz , the contrail age or the correlation between ice number concentration and trace gas concentration (effectively the homogeneity of contrail sampling). For these parameters, no clear trend could be found which could explain the trend in small to large particle size ratios.

It was however found that to a certain extent, these outliers of higher small particle concentrations correlate with the occurrence of large background particles measured by the CIP instrument for particle sizes larger than 12.5 μm . These particles were found to cover a large range of sizes from the lower CIP detection limit of 12.5 μm to several hundred μm . The measurement strategy involved probing contrails close to the upper boundary of cirrus clouds where visibility of contrails was assured and humidity was high as well to allow contrail formation. This probing position could also explain the occurrence of smaller cirrus particles around 100 μm in size. To investigate the influence of these background cirrus particles on PSD shapes, contrail encounters where the CIP instrument measured particle concentrations above 0.5 cm^{-3} were filtered out to isolate contrail encounters without a significant cirrus background. These filtered PSDs are arranged analogously to Figure 6.7 in Figure 6.8. Without the presence of cirrus background particles, the outliers of many small particles in panels (b), (d), and (g) disappear. This could be an indication that nucleated contrail ice particles compete for water vapor with the preexisting larger cirrus background particles, thereby inhibiting contrail ice particle growth and leading to a relatively high number of small ice particles. However, PSDs with a low number of small ice particles are also filtered out this way. For example in panel (e), the PSDs with lowest small particle concentration are removed by using this filter, indicating that the occurrence of cirrus particles does not necessarily correlate with higher numbers of contrail ice particles.

Conversely, not all PSDs with the larger number of small particles are filtered out by disregarding contrail encounters with large background particles present as is evident from panel (i) where the darker colored PSDs with many small particles remain after filtering. These contrail encoun-

ters were found to correlate with an increased background concentration of total aerosol particles, which could indicate an analogous competition for water vapor between contrail ice particles and total aerosol particles. At the same time, these PSDs with many small particles were encountered at colder ΔT_{SA} than the other contrail encounters with larger ice particles at similar humidity in panel (i). This could indicate less available water vapor for the colder contrails, resulting in them growing less than particles under warmer conditions.

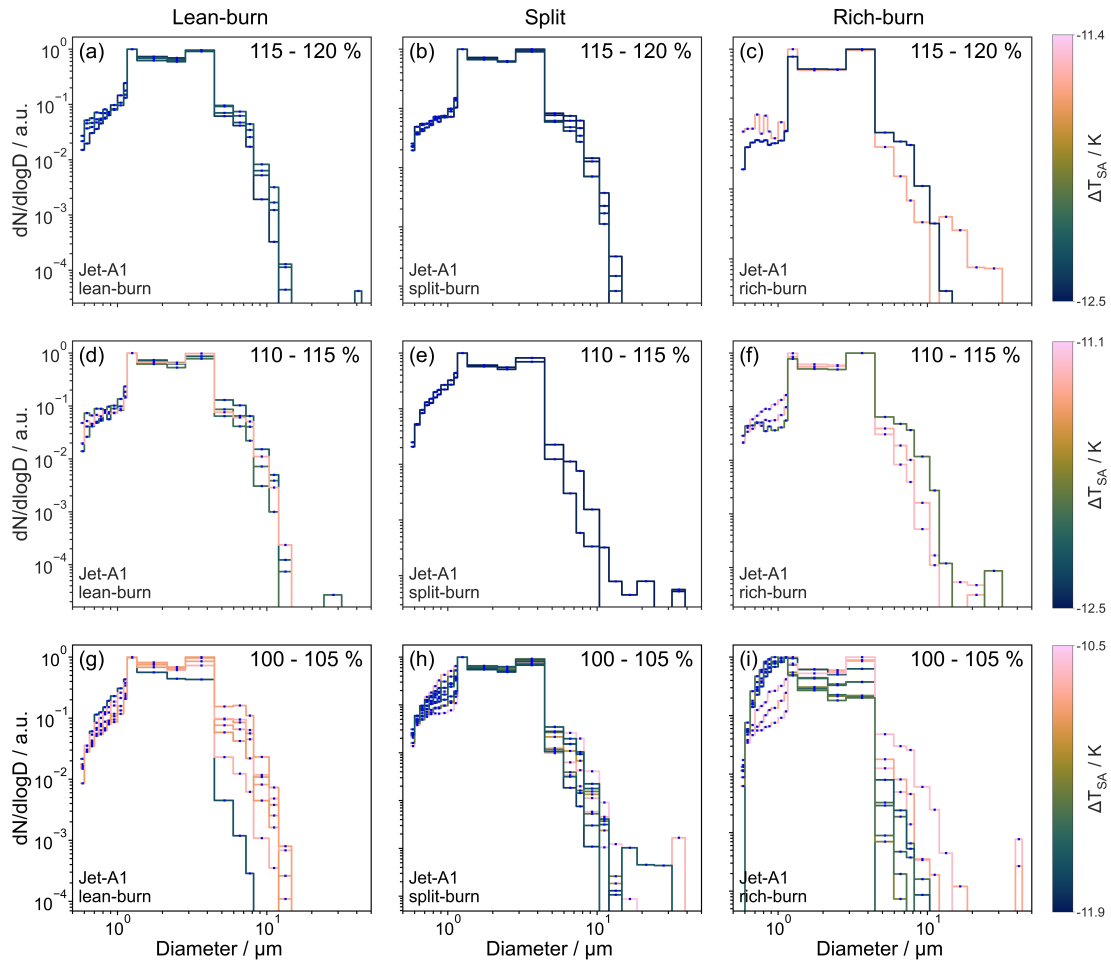


Figure 6.8: PSDs without cirrus background encounters from P-T domain 4.4 from Jet A-1 combustion for the three combustion modes (a, d, g) lean-burn, (b, e, h) split, and (c, f, i) rich-burn. Conditions are narrowed to (a, b, c) high humidity (115 - 120 %), (d, e, f) medium humidity (110 - 115 %) and (g, h, i) low humidity (100 - 105 %) and resolved by ΔT_{SA} represented by a color gradient (Crameri et al., 2020; Crameri, 2021). Note: Not filtered for uncertainty or correlation.

Finally, independent of combustion mode, one can observe an increase in PSD shape variability from high humidities to low humidities in Figure 6.8 and especially in Figure 6.7 containing a larger set of PSDs due to not being filtered for cirrus background. On a local scale, fluctuations in relative humidity can be higher than the spatial resolution of 1 Hz sampling at cruise speeds (~ 200 m/s). It is therefore possible to encounter subsaturated conditions locally, while the averaged

humidity over the sampling interval is supersaturated with respect to ice. At humidities closer to the saturation threshold (e.g. low humidities) it is more likely that subsaturated conditions are encountered compared to higher measured humidities, which delivers a likely explanation for this reduced PSD variability at high humidities.

In summary, independent of combustion mode and humidity range, the highest concentrations of contrail ice particles were in the size range between 1.1 μm to 4.4 μm with varying ratios of smaller ice particles to larger ice particles depending on a variety of ambient conditions such as humidity, ΔT_{SA} , cirrus particle background, and total aerosol particle background. Differences in PSD shape induced by these ambient conditions far outweigh possible influences of the combustion modes and therefore it can be concluded:

Particle size distributions of contrail ice particles are dominated by ambient conditions rather than the employed combustion mode.

6.3 Fuel effects at different conditions

During the VOLCAN2 campaign, four different fuels were probed and four additional fuel compositions were obtained in two contrail flights from a contamination between Jet A-1 and HEFA in their respective fuel tanks. From the P-T domain processing described in section 4.7, seven domains remain for which a comparison of fuels is possible. Three comparisons are possible for the lean-burn combustion mode, six comparisons for the rich-burn combustions mode and no fuel comparisons are available for the split combustion mode. In all cases, the fuels are compared to either Jet A-1 or the contaminated version of Jet A-1, Jet A-1_con2. This leads to a total of nine fuel comparisons from VOLCAN2 and one additional fuel comparison from VOLCAN1, where the HT-fuel was compared to Jet A-1 in the lean-burn mode. The following questions will be answered by the data and discussion presented in this section:

- *Is there a fuel-based reduction potential for AEI in the lean-burn combustion mode and is the magnitude of fuel-based reduction similar to that of the rich-burn mode?*

In order to achieve a comparison of fuels without bias from ambient conditions, the same processing was applied to the data as was done for the combustion mode comparison in section 6.2 and described in section 4.7. The result of this processing is Table 6.6 analogous to Table 6.5 shown in section 6.2. For every domain, Jet A-1 or Jet A-1_con2 was chosen as the reference to which the other fuel is compared. This normalized difference between the fuels is given in the fourth column, followed by the p-values of statistical significance for the four different binning methods and the respective statistical weights.

The p-values are an important tool in assessing whether there is a statistically significant differ-

ence between two fuels. For four of the fuel comparisons, all p-values were below the significance threshold, indicating a statistically significant difference. One domain had inconclusive statistical significance for the different binning methods and five domains showed no statistically significant difference.

Table 6.6: Overview of results from fuel comparisons based on P-T domains. Defined is the reference fuel-combustion mode together with the compared fuel-combustion mode and shown with the resulting difference of normalized mean values. For p-values and statistical weights according to the definition in subsection 4.7, four values are given respectively, where each value is obtained either from relative humidity binning (RHi), alternative relative humidity binning (RHi a), ΔT_{SA} binning (ΔT_{SA}), or alternative ΔT_{SA} binning (ΔT_{SA} a). p-values that fall below the statistical significance threshold of 0.05 are marked in green while p-values above the threshold are marked in red. Statistical weights are marked by a heat map where low weights have lighter coloring and higher weights a darker coloring. Differences in brackets are uncertain due to insufficient narrowing of ambient conditions in the P-T domain. Note that CAS-DPOL and CAPS-DPOL data is used for the VOLCAN1 domain.

P-T Domain	Ref. fuel comb. mode	Compared fuel comb. mode	Norm. diff. to ref.	p-values		stat. weights	
				RHi	RHi a	RHi	RHi a
				ΔT_{SA}	ΔT_{SA} a	ΔT_{SA}	ΔT_{SA} a
VOLCAN2							
1.2	Jet A-1 lean	SPK High lean	-49 %	0.111 0.111	0.25 0.111	20 20	15 20
1.3	Jet A-1_con2 lean	HEFA_con2 lean	-66 %	0.009 0.0004	0.010 0.0002	13 54	12 63
	Jet A-1_con2 rich	HEFA_con2 rich	-37 %	0.0001 0.0001	0.0001 0.00002	191 487	198 474
3.2	Jet A-1 rich	SPK Low rich	-32 %	0.229 0.056	0.109 0.083	18 105	14 123
6.3	Jet A-1 lean	HEFA lean	-21 %	0.013 0.0001	0.007 0.00003	101 164	96 145
	Jet A-1 rich	HEFA rich	-29 %	0.234 0.000002	0.701 0.000005	55 350	37 315
7.3	Jet A-1 rich	SPK High rich	+52 %	0.622 0.088	0.088 0.298	13 27	10 45
7.5	Jet A-1 rich	SPK High rich	+108 %	0.001 0.001	0.004 0.001	94 80	54 130
9.6	Jet A-1 rich	SPK Low rich	-34 %	0.917	0.8	8	8
				0.792	0.229	9	12
VOLCAN1							
2.2	Jet A-1 lean	HT-fuel lean	(-19 %)	0.067	0.115	324	356
				0.547	0.556	84	56

Statistically significant differences between fuels

Four of the domains produced statistically significant results. Despite the two fuels in domain 1.3 being contaminated fuels of Jet A-1 and HEFA, the differences between these two fuels are statistically significant with the rich-burn comparison producing extremely low p-values. An AEI

reduction of 66 % was achieved for the use of contaminated HEFA compared to contaminated Jet A-1 in the lean-burn mode and a reduction of 37 % was achieved in the rich-burn mode. Aromatics, naphthalene and sulfur are significantly reduced for the contaminated HEFA compared to the contaminated Jet A-1, s. Table 6.4. Considering conventional soot-based ice activation, the 37 % AEI difference between the two fuels in the rich-burn mode seems reasonable, especially comparing it to the 56 % reduction found for the pure HEFA and Jet A-1 fuels investigated during ECLIF3 (Märkl et al., 2024).

A possibly higher reduction potential is found in the lean-burn mode. From the comparison of combustion modes in section 6.2, it has been established that similar AEI are found for the lean-burn combustion mode as in the rich-burn mode. This indicates that particles other than soot particles are activated into ice particles in the lean-burn mode. For example, the reduction in sulfur for the contaminated HEFA fuel could possibly lead to a stronger reduction in sulfurous ice nuclei compared to the corresponding reduction in soot ice nuclei from the reduction in aromatics. Details of ice nucleating processes will be discussed in section 6.6. Lean-burn contaminated fuels were also compared at lower humidities compared to the rich-burn fuel comparison. The stronger measured reduction potential could therefore also be due to the encountered ambient conditions.

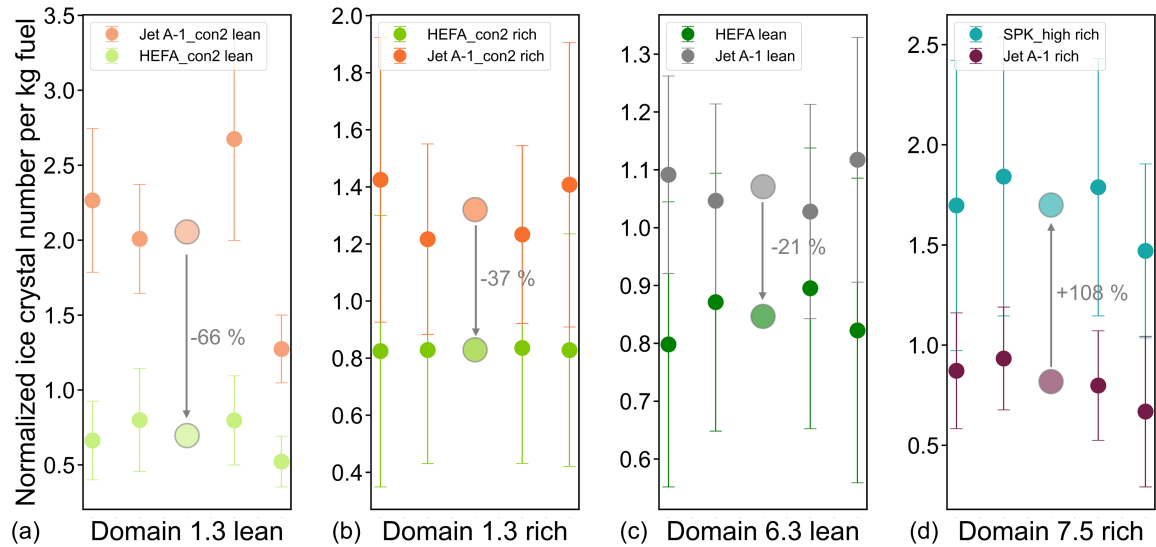


Figure 6.9: Visualization of statistically significant fuel-based differences in normalized ice crystal number concentrations during the VOLCAN campaigns for domains (a) 1.3 lean-burn, (b) 1.3 rich-burn, (c) 6.3 lean-burn, and (d) 7.5 rich-burn. Values are normalized according to the method described in section 4.7. Data points with error bars (standard deviation) for each subplot correspond to RH_i, alternative RH_i, ΔT_{SA} , and alternative ΔT_{SA} binning from left to right. Large circles are the means of all binning methods with indicated reductions between them.

HEFA fuel produced 21 % less AEI compared to Jet A-1 in domain 6.3. This general trend is as expected but the magnitude of reduction is much smaller than the 56 % reduction found during ECLIF3 (Märkl et al., 2024) and also compared to the 66 % reduction in domain 1.3 which additionally was for contaminated fuels. While the range of ΔT_{SA} was similar for the two domains,

the range of humidities differs significantly. In domain 1.3, HEFA_con2 lean was compared to Jet A-1_con2 lean up to humidities of 112.5 %, while in domain 6.3, HEFA lean was compared to Jet A-1 lean up until 145 % RHi with the majority of compared data points at high humidities. This could additionally indicate that a fuel effect is stronger at lower humidities and becomes less prominent at high humidity where more particles are likely to act as condensation nuclei due to the Kelvin effect (Rogers and Yau, 1989b; Kärcher, 2018).

SPK High fuel was found to lead to an increase in AEI by 108 % compared to Jet A-1 in domain 7.5. While the aromatics content of SPK High was 38 % higher than that of Jet A-1, it is virtually free of naphthalene and sulfur. From the higher aromatics content, a higher number of soot could be expected, which however is not confirmed in far-field nvPM measurements. From the comparison of normalized far-field nvPM, total particles and ice particles in Figure A9 in Appendix A, it can be seen that nvPM and totals are reduced in the far-field for SPK High compared to Jet A-1. As will be discussed in section 6.7, far-field nvPM and total particle EIs are not necessarily a good proxy for initial ice nucleating particles at the point of contrail formation. Near-field nvPM numbers however were similar for both fuels while total particle numbers were higher for Jet A-1 fuel as can be seen on the x-axes in Figure A10 in Appendix A. There, when comparing far-field AEI against near-field nvPM EI, ratios of emission index medians in panel (a) are above 1 for SPK High fuel and above or below 1 for Jet A-1. Therefore, more formed ice particles than emitted nvPM can be found for SPK High fuel while ice particle numbers better match near-field nvPM numbers. The ratio of AEI to near-field total particle EIs in panel (b) is higher and close to 1 for SPK High fuel and much lower for Jet A-1. Even though less total particles are emitted during SPK High combustion, a higher share of them is activated and volatile particles must have played a role for SPK High contrails while Jet A-1 contrails are dominated by nvPM nucleation. An influence of the fuel on soot particle sizes and properties could offer an explanation for this finding. For smaller primary soot particles, a higher share of volatile particle activation can be expected as the supersaturation necessary for activation of smaller particles can be achieved (Yu et al., 2024). The higher naphthalene content of Jet A-1 as well as the higher total aromatics content of SPK High both come into question as factors determining primary soot particle size which however can't be confirmed with the current data set and necessitates further measurements and/or model calculations.

The above stated statistically significant differences between fuels are also visualized in Figure 6.9. Data points are resolved by binning methods so that the variability in differences depending on binning method can also be seen. From the statistically significant differences between fuels, the question stated at the beginning of this section can be answered:

- **There is a fuel-based reduction potential in lean-burn engines for lean-burn and rich-burn combustion. HEFA produces less AEI than Jet A-1 as a pure fuel and for contaminated fuels due to the differences in fuel composition.**

Additionally, the following conclusions can be drawn that go beyond the original research question:

- **The fuel-based ice reduction potential appears to be higher at lower humidities.**
- **The lean-burn mode potentially has a higher fuel-based reduction potential compared to the forced rich-burn mode.**
- **High-aromatic fuel with no sulfur was found to produce higher AEI than lower-aromatic fuel with sulfur during rich-burn combustion. These competing ice activation effects are likely sensitive to the exact fuel composition.**

Further fuel comparisons

For five domains (1.2, 3.2, 7.3, 9.6, 2.2), the difference between fuels was not found to be statistically significant and inconclusive for one domain (6.3 rich). It is worth briefly discussing what the reasons for this statistical insignificance or inconclusiveness might be.

Domain 1.2 has relatively low statistical weights, which lead to the high p -values above the $p = 0.05$ threshold. It can therefore not be said with certainty if the 50 % reduction in AEI for SPK High compared to Jet A-1 in the lean-burn combustion mode is statistically significant.

SPK Low fuel is compared to Jet A-1 in domains 3.2 and 9.6. For both domains, a very similar difference is found with the AEI of SPK Low being 32 % lower than the AEI of Jet A-1 for domain 3.2 and 34 % lower for domain 9.6. However, the statistical weight was very low for domain 9.6 so that lack of data points can be seen as the reason for the statistically insignificant reduction of SPK Low to Jet A-1 in domain 9.6. For domain 3.2, the statistical weight is higher, but the AEI distributions for the two compared fuels are broad and the overlap of similar conditions is relatively small so that no statistically significant difference is found.

The data set obtained during VOLCAN2 therefore does not provide sufficient data to properly investigate the contrail ice particle reduction potential of the SPK Low fuel. With a larger number of data points at similar conditions, the found reductions compared to Jet A-1 would need to be confirmed in future measurements.

An increase of 52 % for AEI of SPK High compared to Jet A-1 is found in domain 7.3 but without statistical significance. Statistical weights are relatively low and/or the distributions of AEI data points span similar ranges, so that this domain neither contradicts nor confirms the findings of domain 7.5.

In the rich-burn comparison of HEFA to Jet A-1 in domain 6.3 the difference between the two fuels of 29 % is statistically significant for the ΔT_{SA} based binning methods and not significant for the RH_i based binnings. The statistical weights are also vastly higher for the ΔT_{SA} based binnings compared to the RH_i based binnings, indicating a varying overlap between the two fuels depending on the chosen binning. Higher reductions would be expected based on the results from the ECLIF3

campaign where a 56 % reduction was measured for HEFA compared to Jet A-1. The comparison from domain 6.3 therefore generally shows a consistent trend compared to ECLIF3 but lacks the even distribution of data points across RHi and ΔT_{SA} to enable a statistically sound conclusion. Finally, domain 2.2 showed a statistically insignificant difference between the HT-fuel and Jet A-1 in the lean-burn combustion mode. This is the only domain where the linear relation between RHi and ΔT_{SA} is not given across the entire domain. This is illustrated in the overview of ambient conditions for domain 2.2 in Figure A12 shown in Appendix A. There it can be seen in panel (a) that all HT-fuel points were at colder temperatures than the Jet A-1 points, and in panel (b) the HT-fuel points are clearly horizontally separated from the Jet A-1 data points as is the case for panel (c) where the water vapor mixing ratio is shown. This means that while there are data points for HT-fuel and Jet A-1 that have overlaps in the ΔT_{SA} and RHi bins, the ambient temperature was not fully comparable between the two fuels. Therefore, under comparable conditions, a significant reduction in AEI might be found for HT-fuel compared to Jet A-1. The available data however does not allow any definite conclusions for this comparison and it is therefore to be seen as an example of the necessity for checking if RHi and ΔT_{SA} are mapped linearly for valid comparisons.

6.4 Contrail dependence on ambient conditions

In the course of the VOLCAN2 campaign, a wide range of fuels, engine parameters and especially ambient conditions was probed. The goal of this section is to give an overview over the relationships between AEI and ambient conditions during VOLCAN2. In order to do this, this section will begin by showing the totality of observed AEI and then continue by breaking down their relations to ambient conditions. Note that the water vapor concentration during Flight 21 was out of the calibrated range and that the uncertainty of the resulting RHi is high. This is also reflected in corresponding ΔT_{SA} values as they are calculated by inputting RHi. Therefore for some of the shown figures, F21 data is excluded where indicated and it is discussed in further detail in section 6.5.

Figure 6.10 gives a first overview by showing all observed AEI over ΔT_{SA} . For this figure, a number of filters was applied. Their definition is described in detail in subsection 4.6 and the default filters used when showing AEI from VOLCAN2 throughout this work can be found in the top left corner of figure 6.10. Thereby, only data is shown where: Airbus A321 was the source aircraft, the average relative humidity over ice was above 100 %, measurements were taken in far-field conditions, the peak structures of ice particles coincided with those of trace gas measurements and are therefore classified as valid, the engines at time of emission were in stable operating conditions, unphysical negative AEI are neglected, the ice-tracer correlation was above 0.6, and where the AEI uncertainty was below 100 %. Also, all fuels measured during far-field measurements and their corresponding combustion modes are included and are color coded. From this figure it becomes clear that a wide ΔT_{SA} range from approximately -4.5 K to -19.0 K below the respective Schmidt-Appleman

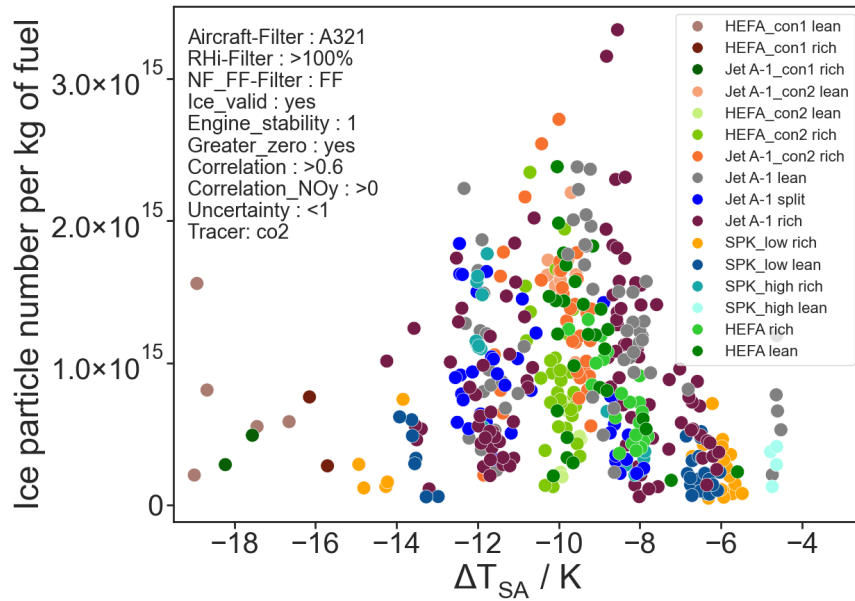


Figure 6.10: AEI from the VOLCAN2 campaign shown against ΔT_{SA} for all fuels and combustion modes. The applied filters can be found in the top left corner.

threshold temperature was probed, thereby spanning 14.5 K. AEI have a strong dependence on ΔT_{SA} where the lowest maximum AEI are measured for very high and very low temperatures. The highest maximum AEI are found between -8 K and -11 K below T_{SA} , resulting in an approximate triangular distribution of data points. However, for a given ΔT_{SA} range and fuel-combustion mode combination, AEI values are scattered from very low values to the maximum value rather homogeneously, demonstrating that ambient factors other than ΔT_{SA} must have an influence on AEI. Model predictions by Kärcher (2018) predict an increased activation of ice nucleating particles for temperatures further below T_{SA} compared to temperatures closer to the threshold. These predictions were also confirmed experimentally to some extent by Bräuer et al. (2021a) where the maximum of AEI is found at similar ΔT_{SA} as in VOLCAN2. They also find a slight decrease in maximum AEI for temperatures further below ΔT_{SA} , which is however somewhat difficult to discern in the logarithmic representation. Recent model calculations by Yu et al. (2024) also include emitted volatile particles as condensation nuclei, which are increasingly activated at higher levels of supersaturation and become highly relevant in explaining ice particle numbers in the soot-poor regime during lean-burn combustion.

To understand the influence of ambient factors on contrail ice crystal numbers measured during VOLCAN, the most important influencing factors on AEI values will be broken down in the following.

As described in section 6.1, the CFM LEAP-1A engines installed on the Airbus A321neo could be operated in their default cruise lean-burn mode, a forced rich-burn mode, or a forced intermediate split mode. To exclude possible effects from the combustion mode at this point, data from rich-burn and lean-burn combustion will be discussed separately and the split mode excluded as data

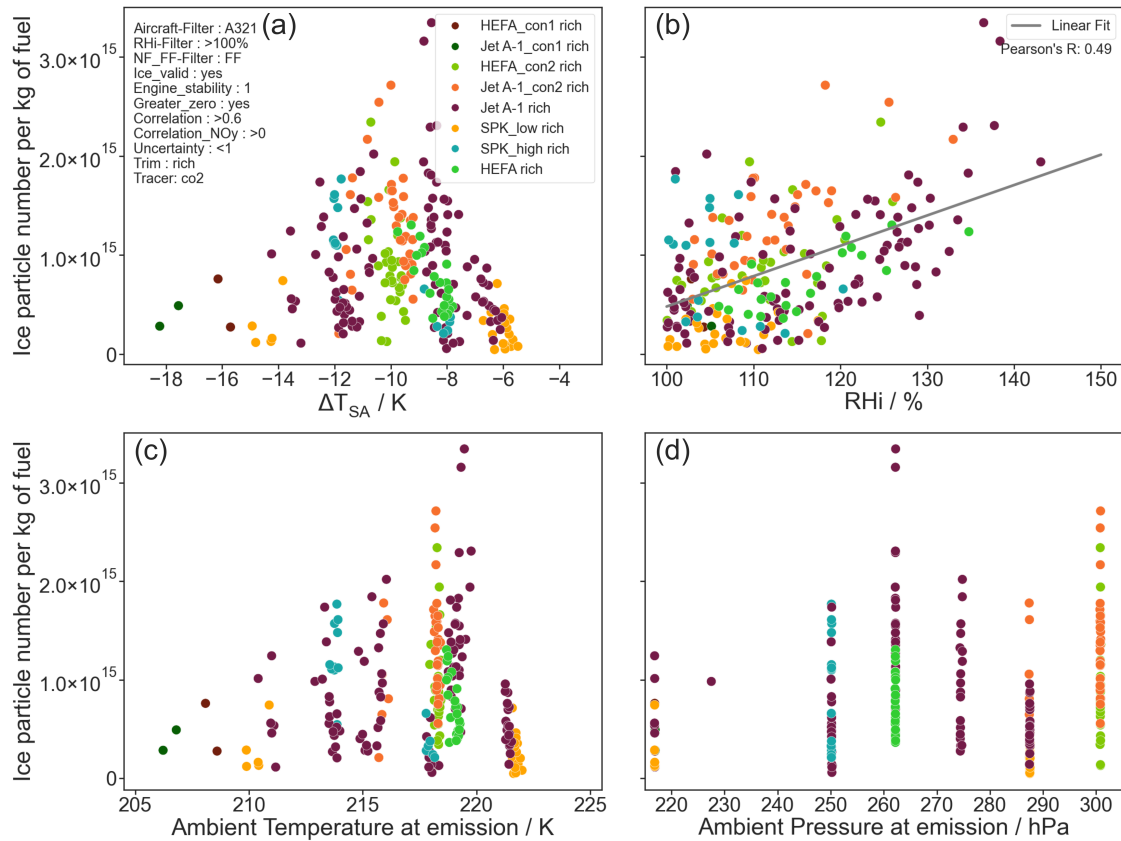


Figure 6.11: AEI from the VOLCAN2 campaign for all fuels in rich-burn combustion mode shown against (a) delta to Schmidt-Appleman threshold temperature, (b) relative humidity over ice with linear fit, (c) ambient temperature at time and point of emission, and (d) ambient pressure at time and point of emission. The applied filters can be found in the top left corner of panel (a).

recorded from this combustion mode lacks the necessary sample size and does not cover the full ΔT_{SA} range.

The full data set of AEI from contrails formed from rich-burn combustion exhaust can be found in Figure 6.11. The same filters were used to achieve this data as in the aforementioned overview in Figure 6.10. All panels in Figure 6.11 show the same AEI data against four respective different x-axes. Beginning with panel (a), AEI are shown against ΔT_{SA} . The same axes were used as in Figure 6.10 and the general triangular shape of the distributed data also appears to be similar, which is not surprising as the data in Figure 6.11 (a) is a subset of the data shown in Figure 6.10. Panel (b) of Figure 6.11 shows AEI against RHi at time of measurement. While data is spread broadly in y-axis direction, a general linear trend can be observed. This is confirmed by the gray linear fit overlaying the data points with a Pearson correlation coefficient of 0.49, indicating a moderate positive correlation. As ΔT_{SA} is defined as the difference between ambient temperature and T_{SA} , it is not surprising that the shape and distribution of AEI data points over ambient temperature shown in Figure 6.11 (c) are similar to that of panel (a). In fact, the general relative position of data points seems to be retained, with nearly linear vertical columns of data points visible for panel (c) which are skewed when viewed against ΔT_{SA} , showing the influence of varying RHi.

Finally, the AEI as shown in panel (d) seem to show no apparent correlation with ambient pressure. These strongly linear and discretely separated vertical columns show that the different pressure levels of the preceding Airbus A321neo during the measurement sequences were quasi constant for the respective flight leg. The shown range in ambient pressure corresponds to altitudes of approximately 9000 m to 11500 m.

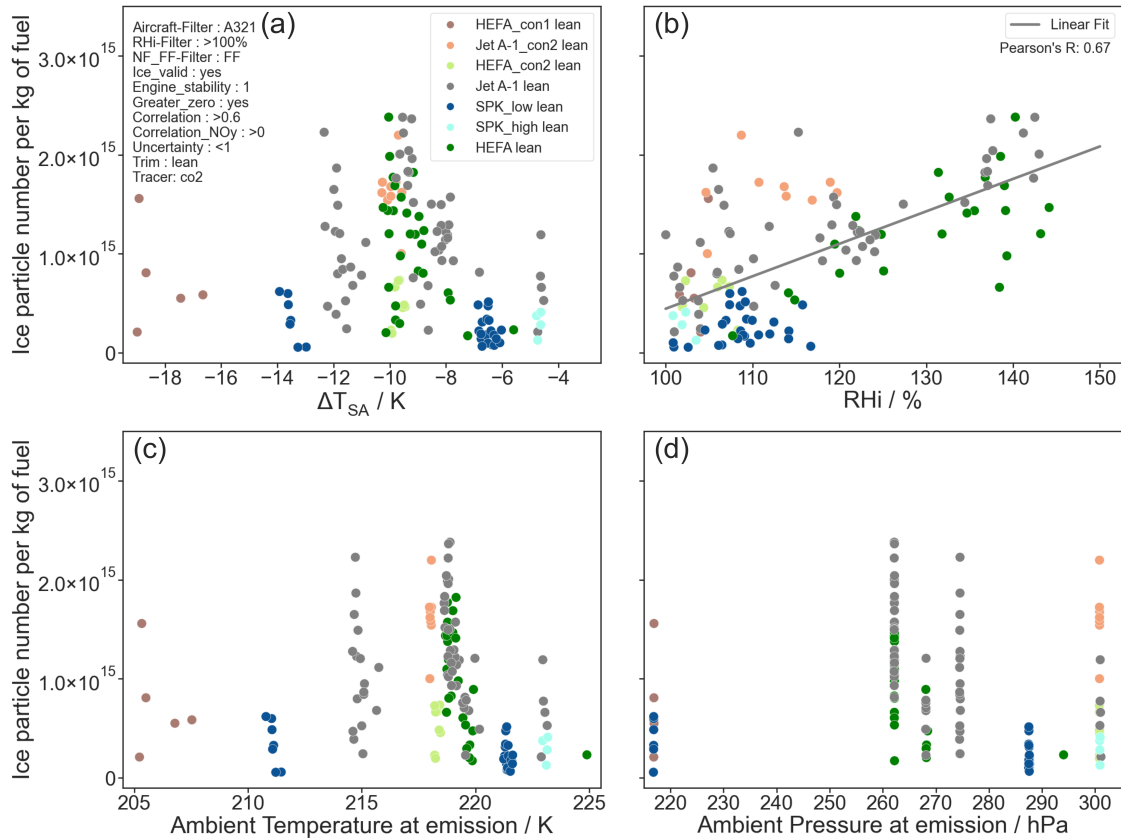


Figure 6.12: AEI from the VOLCAN2 campaign for all fuels in lean-burn combustion mode shown against (a) delta to Schmidt-Appleman threshold temperature, (b) relative humidity over ice with linear fit (excluding flight 21 due to uncertain RH_i data), (c) ambient temperature at time and point of emission, and (d) ambient pressure at time and point of emission. The applied filters can be found in the top left corner of panel (a). Panel (b) and the linear fit do not include data from Flight 21 due to uncertain water vapor measurements during this flight. The plot including Flight 21 data can be found in Figure A5 in Appendix A.

The same considerations as for rich-burn combustion can be done for lean-burn combustion and are shown in Figure 6.12 where AEI from lean-burn combustion exhaust is plotted against the same four x-axes as in Figure 6.11. Again, the same filters were used with the only difference being the consideration of lean-burn data points. AEI vs. ΔT_{SA} is shown in panel (a) and a similar distribution as for rich-burn data can be found with a nearly triangular distribution of data points. However, the lower number of lean-burn points (136) compared to rich-burn (230) leads to a less homogeneous distribution of points. Excluding individual outliers, the same trend of lowest maximum values for high and low ΔT_{SA} values, which increase towards the maximum around -9 K below T_{SA} , can be observed as is the case for rich-burn. The linear dependence of AEI on RH_i can be seen in

panel (b) where a linear function was again fitted to the data, resulting in a Pearson's R correlation coefficient of 0.67. Panel (c) shows the same effect described for rich-burn data where the relative position of vertical AEI data columns on the x-axis is similar to that in panel (a). Dependence on ambient pressure in panel (d) indicates a less homogeneous distribution of emission altitudes compared to rich-burn combustion with the majority of data recorded at pressures higher than 260 hPa. The clear delineation of pressure levels can be observed for lean-burn data as was the case for rich-burn, again indicating stable emission altitudes during the measurement flights.

As is apparent from the shown x-axis ranges in each of the respective panels, a broad set of ambient conditions was encountered. This also explains the relatively broad spread of data points for example for AEI shown against RH_i. In summary, AEI exhibit a non-linear correlation with ΔT_{SA} resulting in a triangular distribution of data points with the peak of AEI being between -8 K and -11 K below T_{SA} , while a linear correlation can be found with RH_i.

These relationships are also visualized in a representation introduced in section 6.7 and can be found in Figures A13 and A14 in Appendix A.

The following conclusions can be drawn from the findings presented above:

- **AEI have a non-linear, triangular relation to ΔT_{SA} .**
- **AEI have a nearly linear relation to RH_i.**

6.5 Warm contrails

During the VOLCAN2 campaign, the last contrail measurement flight (F21) was intended to investigate the onset of contrail formation at warm conditions. Additionally, a small number of contrail onset conditions was also measured during flight F09. These contrail encounters can be seen in the overview panel plot in Figure 4.2, especially the green and red points at highest temperatures in panel (a) or at highest water vapor mixing ratios in panel (c). These contrail encounters at temperatures close to T_{SA} are distinguishable in this panel plot as no humidity filter and less strict correlation filters (>0) were applied for this plot compared to the AEI overview plots in Figures 6.10, 6.11, and 6.12. In this section, focus is put on these contrail encounters at warm temperatures during flights F21 and F09.

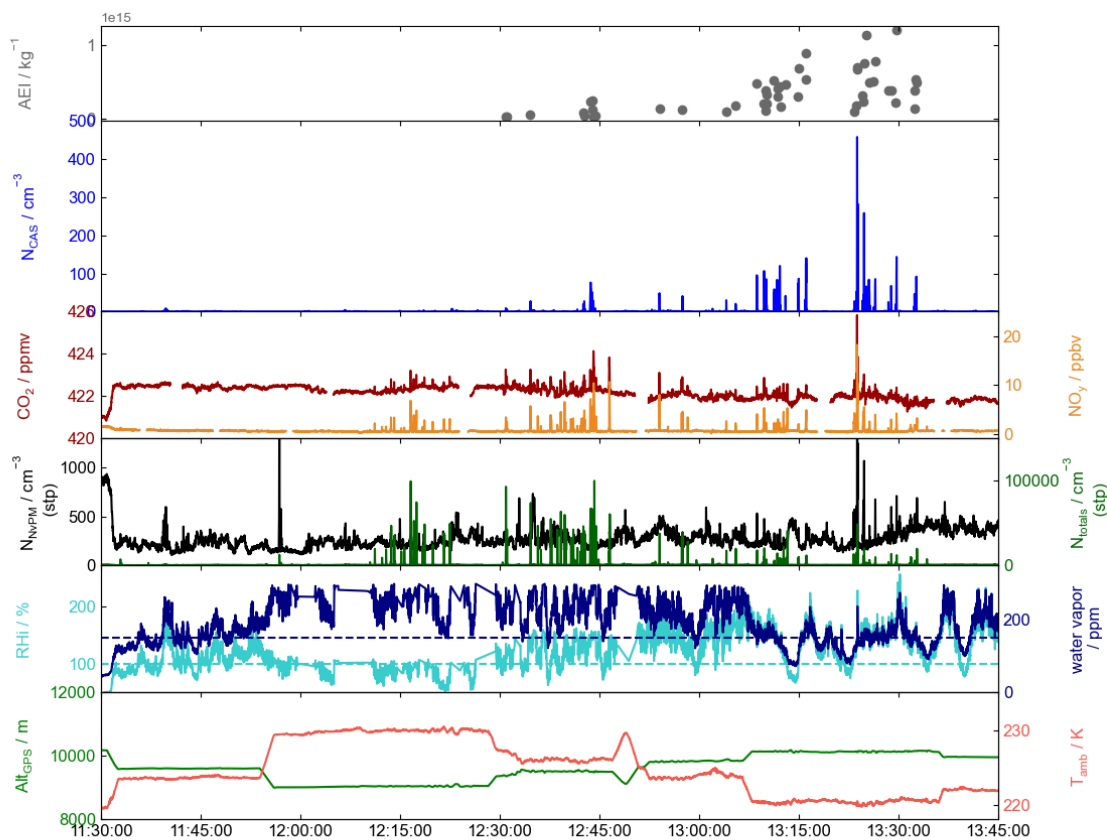


Figure 6.13: Time series of 1 Hz VOLCAN2 warm contrail flight F21 data during far-field measurement sequences of Jet A-1 and HEFA-SPK fuel showing AEI for every contrail encounter, number concentrations of ice crystals larger than at least $0.5\ \mu\text{m}$ measured by the CAS (N_{CAS}), CO_2 and NO_y mixing ratios, number concentrations of nonvolatile particles $> 14\text{nm}$ (N_{NVPM}) and of total particle concentrations (N_{totals}), relative humidity over ice (RHi) during the measurements with indicated saturation (dashed line) and water vapor mixing ratio with indicated uncertainty threshold, and the GPS altitude of Falcon (Alt_{GPS}) with the Falcon-measured ambient temperature (T_{amb}).

The majority of contrail encounters at conditions close to T_{SA} were found during Flight F21, which is why it is worth investigating the measurement time series during this flight in Figure 6.13. In the top row, the progression of AEI from low values during the first contrail encounters beginning around 12:30 UTC to an increasingly larger spread of AEI and higher values during the later encounters up until approximately 13:30 UTC. This trend is a direct result of the similarly increasing maximum contrail ice particle number concentrations as seen in the second row while the trace gas peaks seen in the third row do not exhibit this increase in average peak height throughout the flight. This behavior can also be observed for the number concentrations of total aerosol particles in the fourth row where the first two plume encounter clusters up until 12:45 UTC show higher

average concentrations than the latter two plume clusters after 12:45 UTC. The measured ambient conditions in rows five and six are especially interesting during this flight. The dark blue timeline in row five shows the water vapor mixing ratio measured at the time of contrail detection. The corresponding dashed dark blue line is positioned at 150 ppm and denotes the threshold at which the uncertainty of water vapor measurements begins to rise dramatically due to decreased sensitivity of the instrument at higher water vapor mixing ratios.

Flight 21 is characterized by a long period of the water vapor measurement surpassing this threshold nearly continuously from approximately 11:50 until approximately 13:05 UTC. After 13:05 UTC the average mixing ratio is lower but still repeatedly surpasses the high uncertainty threshold. This increased uncertainty can be directly seen in the mentioned continuous sequence of high mixing ratios as the fluctuations are on the scale of over 100 ppm as a result of amplified noise at high mixing ratios. Also, the measurement repeatedly fails completely as can be seen exemplary by the interpolation around 12:05 UTC. Directing attention to the last row of the figure shows that the flight strategy involved flying at several discreet steps of altitude, corresponding to inverse steps in ambient temperature. When comparing the steps in temperature to ice number concentrations or AEI, it can be seen that no ice particles are measured for the warmest step between 11:55 UTC and 12:30 UTC. The maximum values and spread of ice particle concentration then increases for every subsequent colder temperature step. Going back to row four, the RHi timeline can be seen in light blue. The average RHi seems to increase continuously throughout the flight until 13:10 UTC where the strong fluctuations follow the mixing ratio quite well. The increase of average RHi during the period of high mixing ratios may be due to the steps in temperature as the water vapor measurement fluctuates strongly and erratically around the very high values. Therefore, the RHi in this sequence can only be seen as a rough estimate of humidity with approximately 30 % uncertainty. These uncertainties strongly limit an analysis of contrail onset conditions based on RHi and ΔT_{SA} as it also depends on humidity.

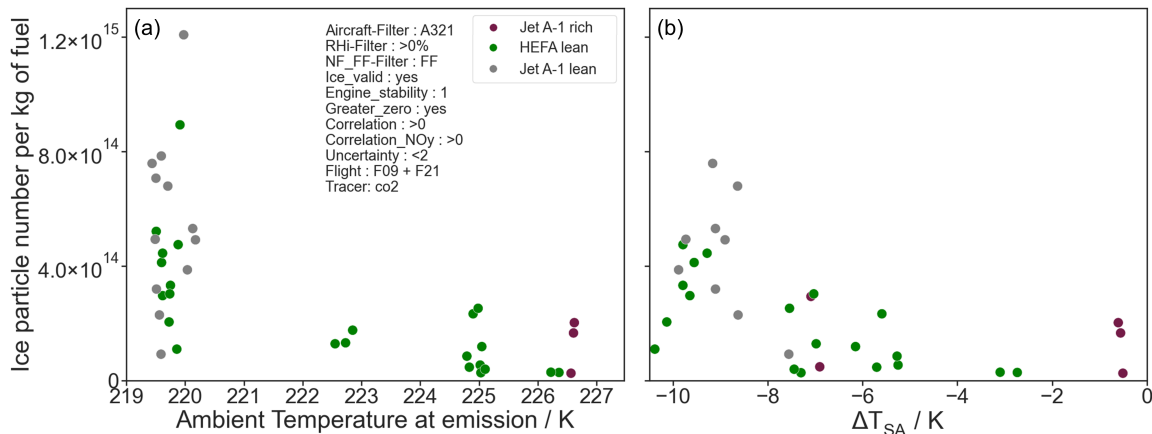


Figure 6.14: AEI against (a) ambient temperature at time of emission and (b) ΔT_{SA} for warm temperature contrail onset conditions during flights F09 and F21. Note: Panel (a) is cut off at 219 K and panel (b) at -10.5 K to focus on the contrail onset. Note: ΔT_{SA} values have high uncertainty resulting from the 30 % uncertainty in water vapor mixing ratio in high mixing ratio sequences.

In the following, focus is therefore drawn towards the comparison of AEI to ambient temperature and also to ΔT_{SA} , which needs to be taken with caution due to the high RH_i uncertainties. Figure 6.14 shows these AEI against (a) ambient temperature and (b) ΔT_{SA} at the highest temperatures found during flights F09 and F21. Dark red Jet A-1 rich points are all from flight F09 while all others originate from flight F21. In panel (a), the increase of AEI for lower temperatures hinted at in the timelines of Figure 6.13 can be confirmed. This trend for the discreet temperature steps is smoothed out due to the influence of RH_i in panel (b). The three red points at highest ΔT_{SA} values originate from a sequence in Flight 09 where the water vapor mixing ratio also continuously surpassed the uncertainty threshold. Therefore, these ΔT_{SA} values are also burdened by high uncertainties. However, within this uncertainty of approximately 30 %, the points of highest ΔT_{SA} likely still represent the contrail onset at high temperatures. The lowest AEI for the lowest red point at highest temperatures and the lowest lean-burn HEFA points lie below $3 \times 10^{13} \text{ kg}^{-1}$. This is slightly below the predictions for the soot-rich regime and slightly above the predictions for the soot-poor regime by Kärcher (2018) and gives an indication of the lowest expected AEI at warm conditions.

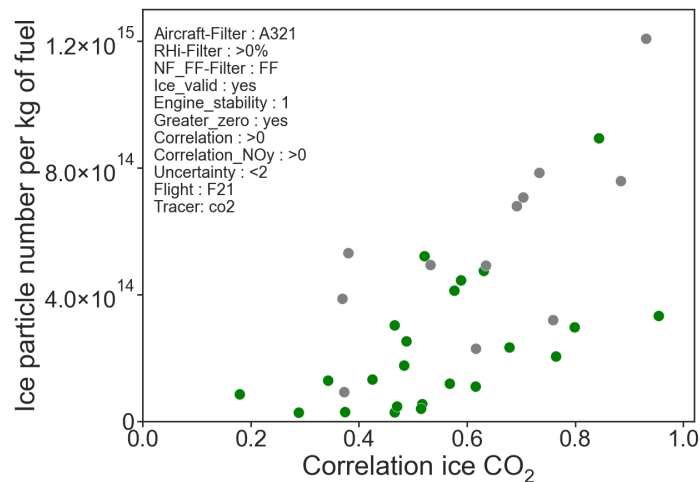


Figure 6.15: AEI against the correlation of ice particle and CO_2 concentration. Low AEI at contrail forming conditions are found especially below the standard correlation threshold of 0.6.

Finally, this contrail onset study also gives insight into the validity of applied correlation filters between ice number concentrations and CO_2 . At warmer temperatures and lower AEI, ice particles are either more likely to be affected by sublimation effects or less likely to form at all. Therefore, it is expected that correlation between ice particle number concentrations to the quasi-inert tracer is worse for conditions close to the formation threshold. This is confirmed by the trend found in Figure 6.15 where AEI are shown against the ice- CO_2 correlation. Lower AEI corresponding to warmer temperatures are found predominantly below the standard cutoff correlation threshold of 0.6 while the higher values corresponding to lower temperatures are found beyond this cutoff value. Sublimation and/or incomplete activation effects are therefore found predominantly at warmer temperatures, leading to a worse correlation between ice particle and trace gas time series.

6.6 Ice nucleation in lean-burn engines

In the previous sections it has been established that contrail ice particles number concentrations are not reduced by the employment of lean-burn combustion compared to rich-burn combustion in the investigated engine/aircraft configuration. Additionally, fuel-based reductions in ice number concentrations could be achieved in rich-burn and lean-burn combustion modes. This raises the question on the ice nucleation processes for lean-burn engines as particles other than soot must be activated to result in the high number of contrail ice particle concentrations. In this chapter, the possible nucleation pathways for lean-burn engines will be explored with the central questions being:

- *What are the main ice forming particles in lean-burn engines?*
- *Are volatile particles activated to ice in the absence of soot?*

6.6.1 Engine comparison

To be able to properly interpret near-field and far-field aerosol emission indices, one first needs to compare the emission characteristics of the two engines on board the A321 source aircraft used during VOLCAN2. No engine comparison was done for VOLCAN1, which is why all discussions will be based on VOLCAN2 data. Figure 6.16 shows near-field (a) nvPM EI and (b) total particle EIs from flight 24, which was the only flight where engine 1 was probed in the near-field. All other near-field measurements were conducted behind engine 2. nvPM EI shown in panel (a) are very similar for both engines, especially given the uncertainties. Therefore, no systematic difference in nvPM EI is found between engine 1 and engine 2 for both combustion modes. A very different picture is presented when viewing panel (b) and comparing total particle EI between the two engines. For both combustion modes, engine 1 emits approximately one order of magnitude more total particles than engine 2. This is a very important finding to keep in mind when interpreting and comparing far-field EIs to near-field EIs as far-field data contains emissions mixed from both engines, while all other near-field data only contains data from engine 2. The two engines were at different points in their maintenance cycle and therefore had different exhaust gas temperature margin (EGTM) values, which are an indicator of engine deterioration (Apostolidis and Stamoulis, 2021). This is the most likely explanation for the much higher total particle emission index of engine 1.

During near-field flight 03, contrail ice forming conditions as well as non contrail ice forming conditions were encountered and many of the transitions were captured with the Falcon cockpit mounted GoPro video camera, as well as from instrument operator photographs and videos taken through a side window in the cabin of the Falcon. In the following, several of these ice forming

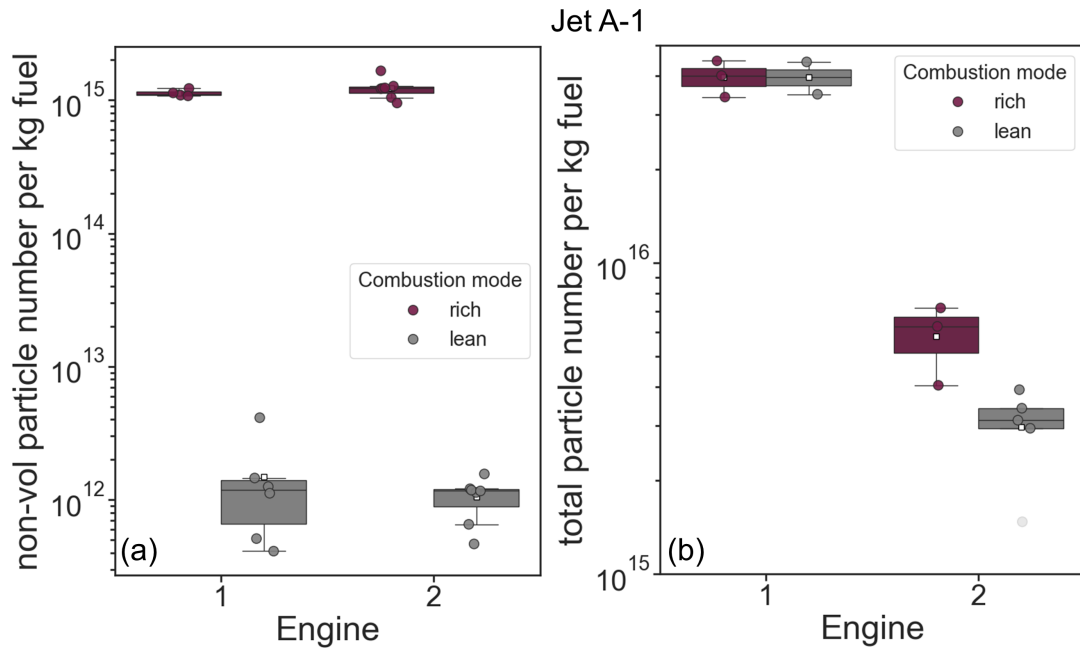


Figure 6.16: VOLCAN2 comparison of engines during near-field measurements of (a) nvPM EIs and (b) total particle EIs. Courtesy of and with permission from Rebecca Dischl and Daniel Sauer. Note that the lowest lean-burn total particle value for engine 2 is likely affected by large uncertainties due to coincidence effects and is therefore faded.

encounters will be presented and discussed as they give first indications for the nucleation processes behind the two engines. In Figure 6.17, several photographs are presented that were taken aboard the DLR Falcon while chasing the Airbus A321 before and after the actual near-field measurement sequences during flight 03 on February 28, 2023. The pictures shown here were chosen to have been taken at a time where both engines were operating in the same combustion mode and the T30 of both engines were comparable while combusting Jet A-1 fuel. During the actual near-field measurement sequences where only engine 2 was probed, the T30s between the two engines differed strongly as it was kept constant in engine 2 and variable in engine 1. For the presented sequences in Figure 6.17, the difference in T30 between the two engines was approximately 9 K in panel (a), 3 K in panel (b) and 2 K in panel (c). The engines can therefore be assumed to have operated under similar, albeit not in steady-state, conditions for the selected times. The photograph in panel (a) was taken from the Falcon cockpit with a GoPro video camera while the A321 was operating in the lean-burn combustion mode. A visible contrail forms behind the aircraft but there are clearly visible differences in the contrail forming behind engine 1 and engine 2. The contrail behind engine 1 appears whiter and seems to reflect/scatter sunlight stronger than the contrail forming behind engine 2. This could indicate either a higher number concentration of contrail ice crystals behind engine 2 or larger ice crystals or both. This photograph was taken before the near-field measurements conducted during that flight. The same observations could however be made approximately 1 hour and 40 minutes later after the near-field measurement sequence as shown in panel (b). Again, the contrail forming behind engine 1 appears to be optically thicker

than the contrail forming behind engine 2 for lean-burn combustion. Unfortunately, no section in the video footage could be found where the engines were operating at comparable conditions, contrails were forming and the perspective was such that the two contrails could be visually well discerned while both engines were operating in the rich-burn mode. Panel (c) shows a point in time where the engines were operating in the rich-burn mode but the perspective and lighting do not allow to draw any conclusions on the optical thickness of the two individual contrails forming behind the engines.

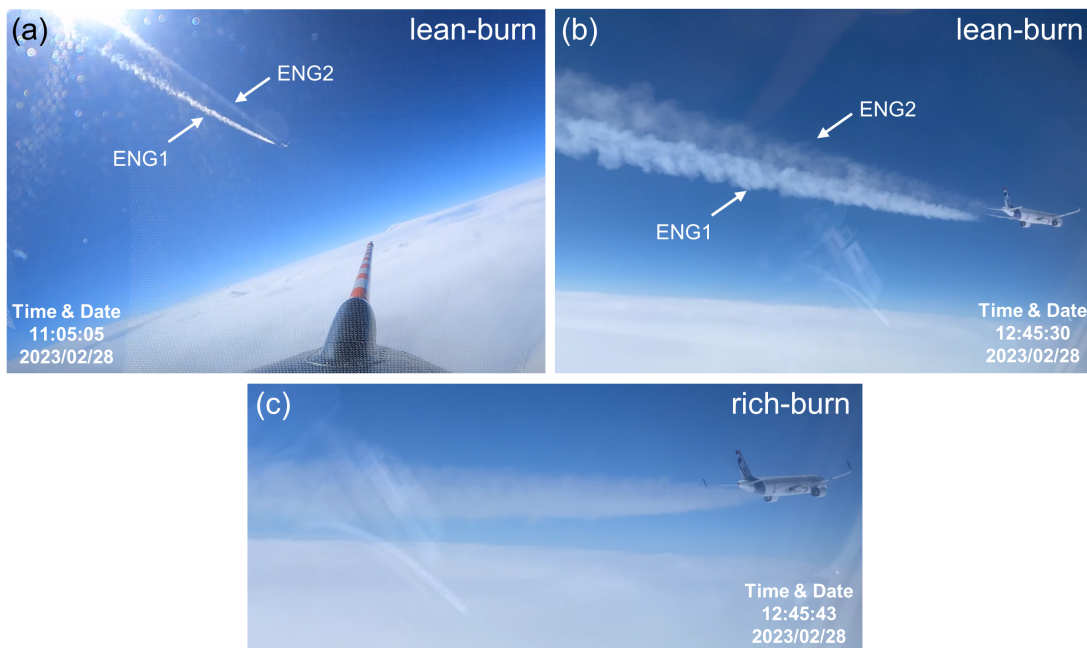


Figure 6.17: Photographs of contrails produced by the A321 source aircraft during flight 03 on February 28, 2023 of VOLCAN2. (a) Falcon cockpit mounted GoPro camera footage of contrails with visually different appearance from engine 1 (ENG1) and engine 2 (ENG2) while operating in the lean-burn combustion mode. (b-c) Photograph taken from the ice instrument operator seat onboard the Falcon with (b) differences visually apparent between the two engines while operating in the lean-burn combustion mode and (c) differences between engines not discernible due to the perspective while operating in the rich-burn combustion mode. The time and date of recording is indicated in UTC in every panel. Image in panel (a) courtesy of Monika Scheibe.

Keeping Figure 6.16 in mind, very low nvPM emissions are expected for the lean-burn combustion mode on both engines. These EI are approximately two orders of magnitude lower than the typical AEI found in far-field contrails. This already indicates that particles other than nvPM must act as condensation nuclei, which are included in the total particle number concentrations. The higher total particle EI found for engine 1 compared to engine 2 appear to directly translate into optically thicker contrails with likely higher ice particle numbers as is indicated by optically thicker contrails from engine 1 in the photographs. While this is not a scientifically quantifiable measurement, it provides a visual illustration and indication of the role of (semi-)volatile particles in the nucleation of contrail ice crystals in the quasi-absence of soot emissions.

The strong differences in total particle emissions between the two engines also need to always be kept in mind when interpreting far-field emission indices of ice and aerosols as both engine emissions are mixed. Also, near-field aerosol EI are only partially representative of initial emissions as only engine 2 was probed during all other near-field measurements of VOLCAN2. This can be summarized as:

- **Engine 1 emitted almost an order of magnitude more total particles than Engine 2.**
- **Contrails forming directly behind engine 1 are optically much thicker than contrails forming behind engine 2.**

6.6.2 Types of contrail ice condensation nuclei

The previous sections have established that for the lean-burn combustion mode, volatile particles play a major role in the contrail ice nucleation process. These volatile particles possibly also play a role in contrail ice nucleation in the rich-burn combustion mode as in some instances, AEI are higher than corresponding nvPM EI.

For the soot-rich regime with soot emissions higher than approximately 10^{14} kg^{-1} , the relationship between nvPM EI and AEI is nearly linear while for the soot-poor regime, AEI values are predicted to be anticorrelated with nvPM emissions for conditions far below T_{SA} and up to two orders of magnitude lower for conditions near T_{SA} (Kärcher and Yu, 2009; Kärcher, 2018). The majority of current emissions is in the soot-rich regime where soot particles are the preferred condensation nuclei due to their larger size (Kärcher and Yu, 2009; Wong and Miake-Lye, 2010; Heymsfield et al., 2010; Schumann and Heymsfield, 2017; Bier et al., 2022). These originally hydrophobic particles can become coated by sulfur compounds (Kärcher, 1998; Kärcher et al., 2015), thereby increasing their hygroscopicity and propensity to act as ice condensation nuclei (Popovicheva et al., 2004; Petzold et al., 2005; Wong and Miake-Lye, 2010; Kärcher et al., 2015). Indications for this behavior predicted by model calculations are also found in experimental data (Jones and Miake-Lye, 2023). In the soot-poor regime $< 10^{14} \text{ kg}^{-1}$, particles other than soot must act as ice condensation nuclei. Following particle types come into question and will be discussed briefly in the following: Ultra-fine aqueous particles (UAPs), chemi-ions, lubrication oil, (semi-)volatile particles, ambient aerosol particles, secondary aerosol.

Kärcher (2018) mentions UAPs which originate from gaseous emitted substances as likely ice condensation nuclei, especially the larger mode of ionized gas molecules also called chemi-ions (Yu and Turco, 1997; Arnold et al., 1999). Kärcher (2018) attributes high AEI for the soot-poor regime mainly to nucleation on UAPs and also indicates that the range of achievable AEI depends on ΔT_{SA} , the latter of which was partially confirmed experimentally during the VOLCAN campaigns as the direct relationship was found with RH_i rather than to ΔT_{SA} , see Figure A13. For the comparison

of AEI to near-field aerosol EI shown in section 6.2, there are cases where AEI exceed the upper boundary predicted by Kärcher (2018) in the high-soot rich-burn regime. This could indicate that the "kink point" where the upper boundary has its minimum does not necessarily reach such low AEI. Rather, it is possible that the upper boundary could be more flat due to activation of volatile particles for lower soot emissions. This would indicate that particles aside from the UAPs considered in Kärcher (2018) take part in ice nucleation.

From several ground-based experiments, engine lubrication oil has been identified as a major contributor to organic particulate engine emissions (Timko et al., 2010b; Fushimi et al., 2019; Ungeheuer et al., 2022). Recent work by Ponsonby et al. (2024a) has shown that insoluble and hydrophobic lubrication oil droplets could nonetheless compete for plume supersaturations, especially under soot-poor conditions, and thereby form contrail ice crystals. During the conducted flight experiments in VOLCAN, there was no real time monitoring of lubrication oil use, thereby inhibiting a direct correlation to measured total particle numbers. The higher total particle emission indices observed for engine 1 compared to engine 2 during VOLCAN 2 could possibly be explained by a higher oil consumption for engine 1, which was further along in its maintenance cycle.

Volatile particulate matter is not found in significant amounts at the engine exit plane but rather after dilution and cooling of the exhaust when the volatile precursors condense from the gas phase (Timko et al., 2010b; Yu et al., 2019). Thereby, the volatile material can either condense onto soot particles, through which they are coated, or nucleate into liquid droplets (Petzold et al., 1998; Timko et al., 2010b). In the same study by Timko et al. (2010b), sulfate and organic materials are found to be the main volatile species of particulate matter. Organic materials include mostly lubrication oil and products of incomplete combustion, with lubrication oil dominating at high power engine settings (Timko et al., 2010b). This finding is confirmed by Yu et al. (2019) who state that organic particles are dominated by aromatic species at engine idle and by lubrication oil at higher thrust. Micro-physical processes and mainly gas-to-particle conversion form a nucleation/growth mode within seconds of emission and the resulting particles grow over the time period of several minutes by condensation of additional precursors and subsequent coagulation (Timko et al., 2013). These gas-to-particle conversions lead to a decrease in total particle number concentration and an increase in total particle mass and size (Timko et al., 2013). It has to be kept in mind that these observations are from ground-based measurements where no contrail ice forms and therefore possible processing and interaction with ice particles is not considered in the mentioned literature. Cross et al. (2013) additionally find that intermediate volatility organic compounds and semivolatile organic compounds that partition between gas and particle phases are strongly present in aircraft emissions.

Ambient aerosol particles are assumed as the only source for contrail ice crystals at conditions near T_{SA} in Kärcher (2018). This is however directly caveated by the low concentration of particles which would not be able to explain the high contrail ice particle number concentrations. Ambient aerosol particles can therefore likely be neglected as a major source of contrail ice nucleating particles. Similarly, secondary aerosol particles can be ruled out as contrail ice nucleating particles as nucleation happens within the first second of emission while secondary aerosol forms over a

longer time period of minutes to hours under sunlight exposure (Miracolo et al., 2011; Miracolo et al., 2012).

In summary, several types of particles come into question as contrail ice condensation particles. From the current set of measurements conducted during the VOLCAN campaigns it is not possible to say with certainty which particles are responsible for nucleation as the available information on particle concentrations and sizes does not unambiguously reveal particle composition. A study with quantified and controlled lubrication oil emissions using low-sulfur, low aromatic fuel might be one way to experimentally verify hypotheses regarding lubrication oil as main ice nucleating particles in the low-soot regime. The impact of fuel composition on contrail ice particle formation may also differ from known interactions of gaseous emission with soot, such as sulfur coatings on soot. Comparing fuels at low-soot conditions with controlled lubrication oil use could also reveal effects in this regard. Currently, work is being conducted (Ponsonby et al., 2024b) to update the parcel model of Kärcher et al. (2015) to include the activation of volatile particles in the soot-poor regime. Yu et al. (2024) have recently published model results including volatile particles, which however do not yet include condensable organic species. These developments are to be closely followed and it would be of great value to conduct comparisons of experimental results with these updated models to be able to verify the model and to possibly gain reciprocal insights into nucleation processes.

In summary:

- **A number of particles come into question as ice nucleating particles, especially UAPs, lubrication oil and other organic and inorganic (semi-) volatile particles.**

6.7 Ice processing

6.7.1 Effects of ice formation on aerosol numbers

In section 6.2, far-field contrail ice particle measurements were compared to near-field aerosol measurements. There, a three orders of magnitude reduction of nvPM for the lean-burn combustion mode compared to the rich-burn combustion mode did not translate to similar contrail ice particle reductions. Far-field aerosol measurements taken at the same time as contrail ice particle detection however reveal that the near-field emissions do not remain at their original values under the presence of contrail ice particles. nvPM measured in far-field is therefore not only soot but a more fitting description would be non-volatile interstitial and ice residual particles. For sake of simplicity, this will be further referred to as nvPM with the explicit notice that it does not only contain soot. The following question is raised by the higher far-field aerosol numbers:

- Why do nvPM and total particle numbers increase from near-field to far-field?

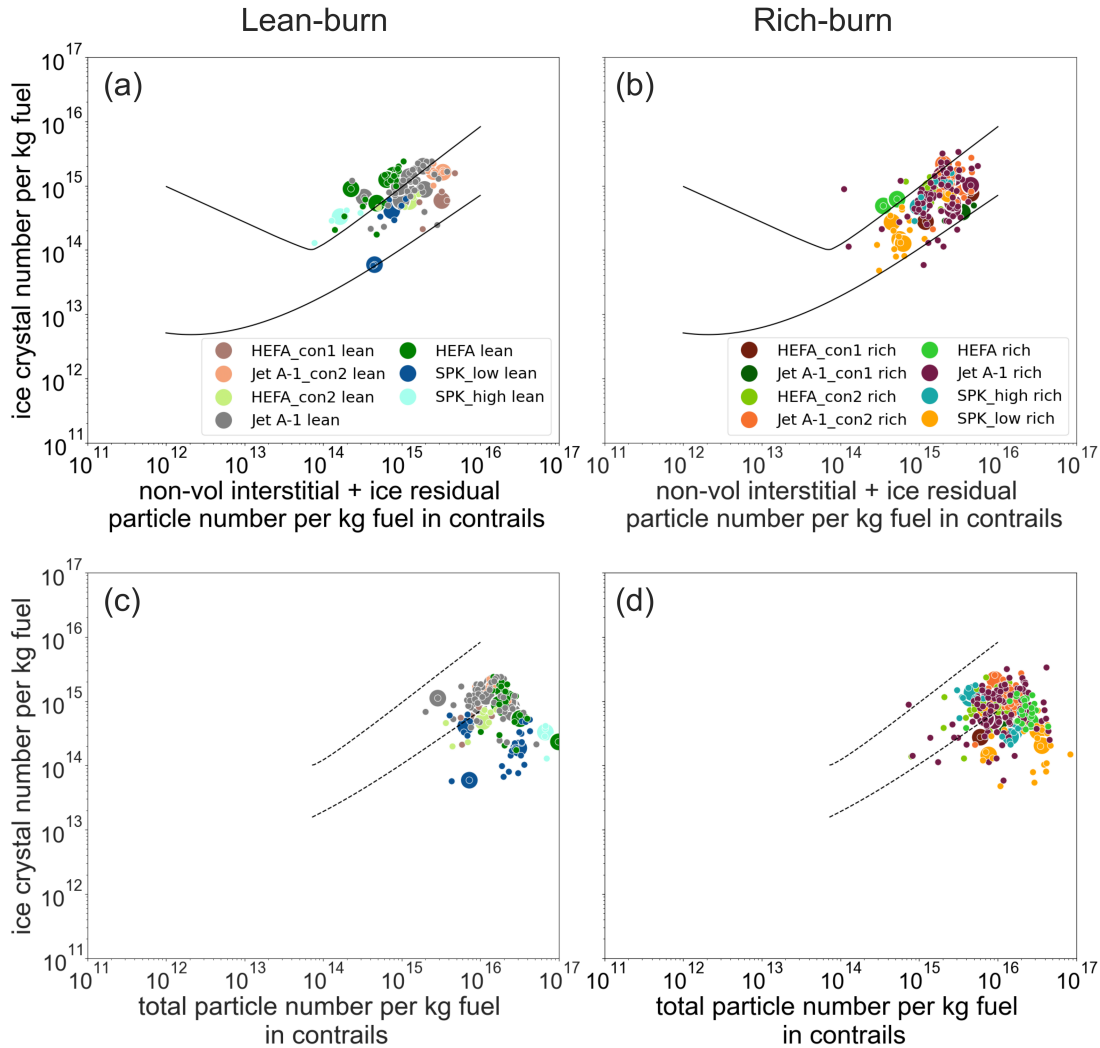


Figure 6.18: VOLCAN2 far-field AEI vs. (a, b) far-field nvPM emission indices and vs. (c, d) far-field total particle emission indices in (a, c) lean-burn combustion mode and in (b, d) rich-burn combustion mode. Continuous lines represent the upper and lower expected AEI boundaries based on Kärcher (2018) for nvPM and dashed lines represent the high soot regime nvPM based boundaries shown as guide to the eye in total particle number plots. Small symbols are single contrail encounters while large symbols represent median AEI values in $1\text{ K } \Delta T_{\text{SA}}$ range bins as described in subsection 4.7. Panels (a) and (b) only contain encounters where the forward-facing aerosol inlet was used.

For VOLCAN2, all AEI from forward-facing inlet measurements are shown against respective far-field nvPM EI in Figure 6.18 (a, b) and all AEI from both inlets against respective total particle EIs in Figure 6.18 (c, d). Lean-burn nvPM EI medians span a range from approximately $2 \times 10^{14} \text{ kg}^{-1}$ to $3 \times 10^{15} \text{ kg}^{-1}$ and rich-burn nvPM EI medians span a very similar range from approximately $4 \times 10^{14} \text{ kg}^{-1}$ to $5 \times 10^{15} \text{ kg}^{-1}$. Median AEIs from forward-facing inlet measurements span a range from approximately $6 \times 10^{13} \text{ kg}^{-1}$ to $2 \times 10^{15} \text{ kg}^{-1}$ for lean-burn conditions and from $1 \times 10^{14} \text{ kg}^{-1}$ to

$2 \times 10^{15} \text{ kg}^{-1}$ for rich-burning conditions. Considering a very broad range of atmospheric conditions was present during formation of measured contrails, the AEI from both combustion modes cover a similar range and fit well within the boundaries predicted by Kärcher (2018), especially for the rich-burn mode. Median total particle EIs shown in Figure 6.18 (c, d) cover a range from $3 \times 10^{15} \text{ kg}^{-1}$ to $1 \times 10^{17} \text{ kg}^{-1}$ for the lean-burn mode and from $4 \times 10^{15} \text{ kg}^{-1}$ to $4 \times 10^{16} \text{ kg}^{-1}$ for the rich-burn mode. Rich-burn median total particle EIs therefore span a smaller range lying completely within the range of lean-burn values. On a order of magnitude scale, no significant differences can be therefore found between lean-burn and rich-burn combustor conditions for far-field nvPM EI and far-field total particle EI.

Striking differences are however found when comparing the far-field aerosol EI in Figure 6.18 to those measured in near-field conditions in Figure A1 in Appendix A. Rich-burn nvPM EI are spread more broadly in far-field but otherwise cover a similar order of magnitude compared to near-field, while lean-burn nvPM EI in far-field are approximately three orders of magnitude higher compared to near-field. Total particle EI in far-field on the other hand are about one order of magnitude higher for both combustion modes compared to near-field.

These strong differences between near-field and far-field aerosol EI likely indicate processing of volatile aerosol particles in or on contrail ice particles. For the lean-burn mode, AEI are much higher than nvPM in the near-field, meaning that ice particles must have nucleated on particles not measured as nvPM. The fact that a similar number of nvPM as ice is measured in far-field suggests that the original ice nucleating particles must have been processed within the ice particles so that they are then measured as nvPM in far-field after the ice has been evaporated in the thermodeuder.

The increase of total particle number by an order of magnitude compared to near-field measurements could at first glance also hint at processing in contrail ice particles leading to an increased number concentration of total particles. However, this seems unlikely as total particle EI are similar for the forward-facing and backward-facing inlet, meaning that total particles minus nvPM are likely not bound in ice particles. Instead, these particles appear to increase in number from the point of emission to the point of detection in far-field.

Several pathways for this are possible, which however cannot be proven with the available data set and this discussion should therefore serve as an inspiration for future measurements in this regard. The processes leading to increases in particle numbers from near-field to far-field measurements are illustrated for the lean-burn combustion mode in Figure 6.19, where the arrow leading from panel (c) to (b) indicates the transition of (semi-) volatile particles to non-volatile interstitial and ice residual particles.

One mechanism could be that the high number concentrations of nvPM and total particles found in the far-field are already emitted at the engine exit but are too small for detection in the near-field. These particles could grow through condensation of volatiles and semivolatiles over time so that they grow into the aerosol measurement range by the time of far-field measurements.

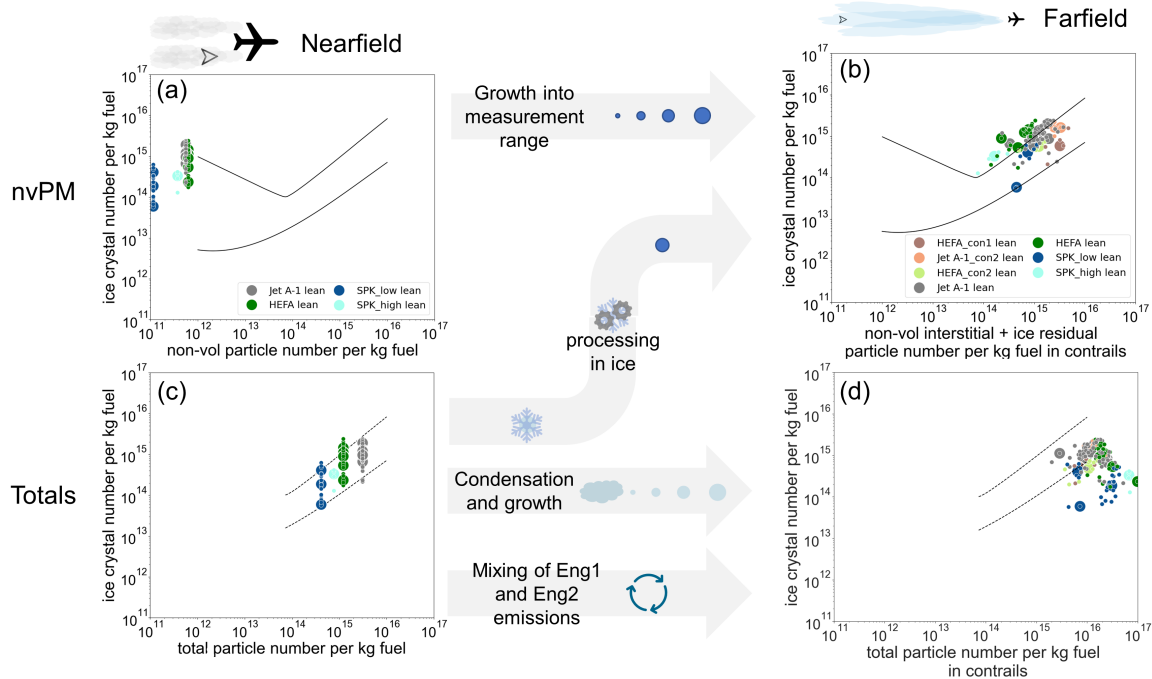


Figure 6.19: Comparison of VOLCAN2 lean-burn AEI shown against near-field (a) nvPM EI and (c) total particle EI and against far-field (b) non-volatile interstitial and ice residual particle numbers and (d) total particle EI with possible processes indicated between the near-field and far-field plots. Small symbols are single contrail encounters while large symbols represent median AEI values in $1\text{ K } \Delta T_{SA}$ range bins as described in subsection 4.7. The analog figure for rich-burn combustion can be found in Figure A4 in Appendix A.

It was shown in section 6.6 that engine 1 emitted approximately one order of magnitude more total particles than engine 2. As far-field measurements sample the combined emissions from both engines, these higher total particle emissions from engine 1 could also be a reason for the supposed increase in total particles when comparing far-field total particle EI to near-field total particle EI from engine 2 emissions. This increase is also found when comparing near-field and far-field total particle EI from VOLCAN1, for which no measurements of engine 1 were conducted. Therefore, an influence of higher total particle emissions for engine 1 on the difference of near-field and far-field total particle EI can be neither proven nor disproven. While the increase in total particles from near-field to far-field could possibly be due to the different EIs from the two different engines, the approximately three orders of magnitude increase of nvPM EI from near-field to far-field for lean-burn combustion cannot be explained by this circumstance.

Finally, processing of (semi-) volatile particles to nonvolatile ice residuals could possibly explain the increase in nvPM from near-field to far-field measurements. It is conceivable that once ice crystals have formed, the large surface area provides a good condensation site for (semi-)volatile material, which then coagulates and remains as a particulate ice residual even after passing the thermode-nuder of the nvPM measurement system. In this case, several volatile particles condensing onto the ice crystal might result in a single ice residual. This is however a speculative mechanism that

requires further research to quantify the interaction between (semi-)volatile aerosols and contrail ice particles. A small set of nvPM measurements conducted in the far-field under non contrail forming conditions showed that nvPM stayed at levels similar to those in near-field measurements. This strongly suggests that the presence of contrail ice particles leads to the increase in nvPM EI measured in the far-field under contrail forming conditions and supports the theory of ice particles processing (semi-) volatile particles to nonvolatile ice residuals.

In summary:

- **Non-volatile interstitial and ice residuals measured in far-field are approximately three orders of magnitude higher than nvPM measured in near-field, likely due to processing in contrail ice particles.**
- **Total particle numbers increase from near-field to far-field by growth into the measurement range or mixing of emissions from both engines.**

Similar findings consistent with those of VOLCAN2 can be found in VOLCAN1 data shown in Figure A3 in Appendix A for the differences between near-field and far-field on the order of magnitude scale. During VOLCAN1 however, slightly lower far-field nvPM and total particle EI are found compared to VOLCAN2. This is an interesting observation as near-field nvPM and total particle EIs are similar between the two campaigns. During VOLCAN2 therefore, more particles are either processed in or on contrail ice particles, form after the initial emission phase or result from the higher total particle emissions from engine 1.

Here it must be noted that during VOLCAN2, two different inlet configurations (forward-facing (FW) and backward-facing (BW) (Fiebig, 2001)) were employed. While with the forward-facing inlet configuration, interstitial aerosol as well as aerosols enclosed in ice particles are measured, only interstitial aerosol is measured in the backward-facing configuration. As nvPM EI are on a similar order of magnitude as AEI, values obtained using the backward-facing inlet yield strongly reduced emission indices that do not include the condensation nuclei. Therefore, all shown nvPM EI only include measurements from the forward-facing inlet, as do the corresponding AEI shown together with nvPM EI. AEI are at least an order of magnitude smaller than total particle EIs and the impact of AEI on the reduction of total particles is therefore relatively small (see subsection 6.7.2). In order to be able to use the large number of measured contrail encounters, those with both inlet configurations were used when comparing AEI against far-field total particle EIs. This means that the data set is different for AEI vs nvPM EI (only forward-facing inlet) and AEI vs total EI (both inlets), leading to slightly varying median AEI.

6.7.2 Influence of ambient conditions on processing

In the following, the ratios of far-field AEI and aerosol EI are discussed in order to gain insight into the mechanisms behind ice activation and processes affecting aerosol numbers. The P-T domain 6.3 has been selected to discuss these relationships as a large range of RHi is spanned while other variables such as altitude and water vapor availability are narrowed down.

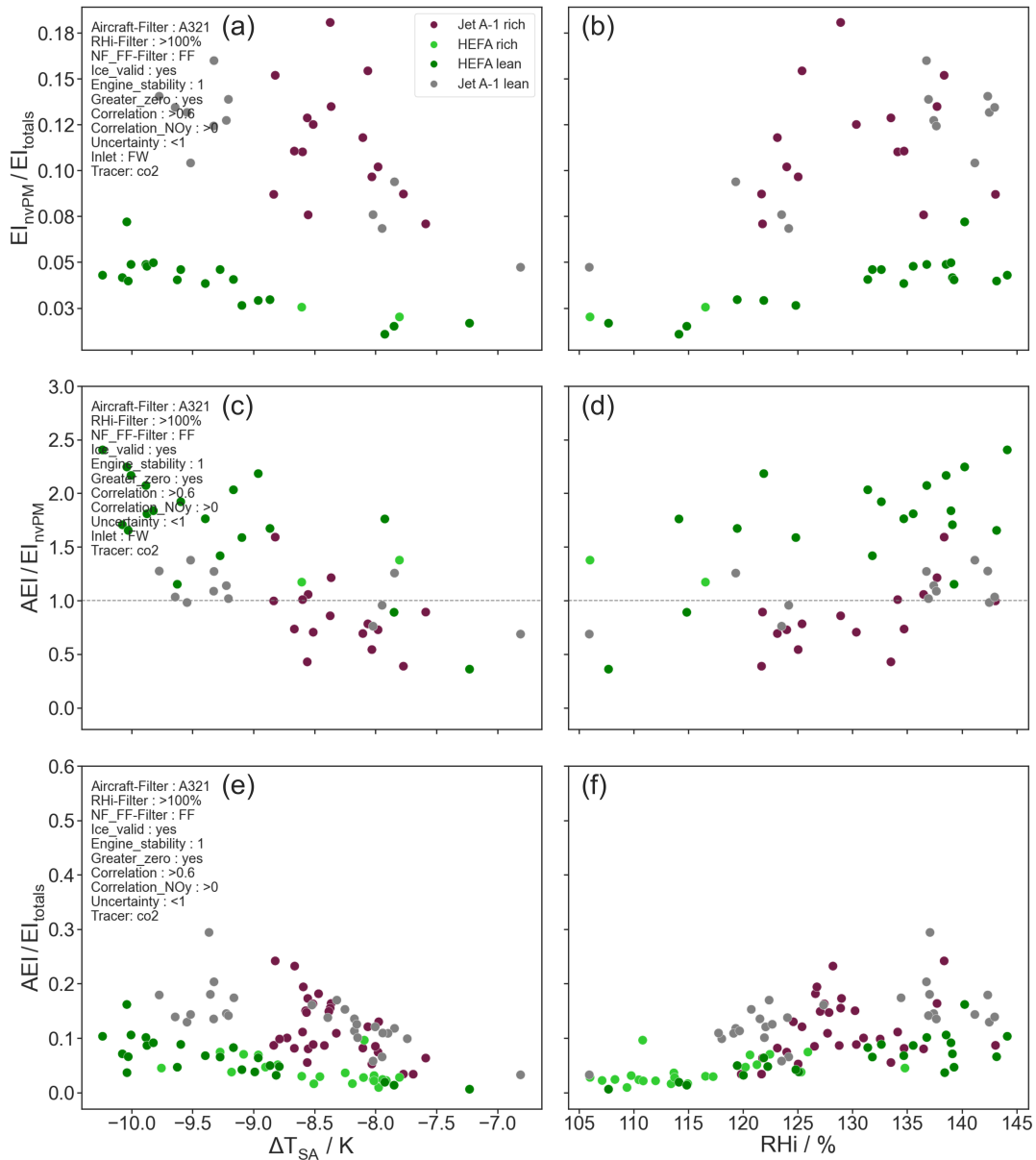


Figure 6.20: Ratios of emission indices for VOLCAN2 far-field contrail encounters of domain 6.3 shown against (a, c, e) ΔT_{SA} and (b, d, f) RHi. (a, b) The ratios of far-field nvPM EI to far-field total particle EI considering only data where the forward-facing inlet (FW) was used, (c, d) the ratios of AEI to far-field nvPM EI where only the FW inlet was used, and (e, f) the ratios of AEI to far-field total particle EI with both inlet configurations.

Figure 6.20 shows ratios of emission indices of ice and aerosols during contrail encounters from domain 6.3. Panels (a) and (b) show the share of nvPM EI to total particle EI $EI_{\text{nvPM}} / EI_{\text{totals}}$ for the forward-facing aerosol inlet against (a) ΔT_{SA} and (b) RHi. This ratio appears to have a linear relationship to ΔT_{SA} and RHi for the respective fuels, where the share of nvPM to total particles increases with increasing RHi and with increasing temperature difference to T_{SA} . Data points for Jet A-1 and HEFA are clearly separated vertically with Jet A-1 points having systematically higher shares of nvPM to total particles compared to HEFA.

To understand this separation, it is worth reviewing the plots comparing normalized AEI, nvPM EI, and total particle EI of the respectively compared fuels in Figure A8 in Appendix A and Figure 4.8. There, a direct proportionality is found between normalized AEI and nvPM EI while normalized AEI are inversely proportional to normalized total particle EI. This inverse proportionality is the reason for the vertical separation of Jet A-1 and HEFA data points in Figure 6.20 (a, b).

A similar trend as in panels (a, b) can be found for the other two shown ratios AEI / EI_{nvPM} in panels (c, d) and AEI / EI_{totals} in panels (e, f) as well. This is a plausible relation for the ratios relating ice to aerosol EIs as it has been established that AEI increase with RHi and larger differences to T_{SA} . It is interesting that this relation is also found for $EI_{\text{nvPM}} / EI_{\text{totals}}$ as it means that at higher humidities, the proportion of nvPM to total particles increases similarly to the proportion of ice particles to total particles. A reason could be the aforementioned processing of originally volatile particles to a nonvolatile ice residual in or on ice particles. A causality could be that the more ice particles are available, the more volatile particles are processed into nonvolatile ice residuals.

Another interesting aspect found in Figure 6.20 (c, d) is the high number of contrail encounters where AEI / EI_{nvPM} is above 1. This means that more contrail ice particles than nvPM were measured and that for the cases of the ratio being above 1, there are cases where no ice residual was measured. It is interesting to see that mostly encounters from lean-burn combustion have AEI / EI_{nvPM} above 1, leading to the suggestion that the volatile particles that served as condensation nuclei were not fully processed to nonvolatile particles or are not measured as such due to being either evaporated by the thermodenuder or because their size is below the detection limit. The processing of (semi-)volatile aerosols on ice particles is likely sensitive to a number of external factors and changes the number of measured far-field nvPM and total particles. Several originally volatile particles could therefore also possibly be processed into a smaller number of (semi-)volatile ice residuals. However, also rich-burn encounters are found with AEI / EI_{nvPM} above 1 so that volatile particles might also play a role in ice nucleation during rich-burn combustion.

The findings of this subsection can be summarized as:

- **The ratios $EI_{\text{nvPM}} / EI_{\text{totals}}$, AEI / EI_{nvPM} , and AEI / EI_{totals} increase with increasing humidity and larger differences to T_{SA} . This likely indicates a correlation between the number of contrail ice particles and the number of ice residuals.**
- **Especially for lean-burn combustion, the number of ice particles can exceed that of non-volatile interstitial and ice residual particles.**

CHAPTER 7

Summary and Outlook

7.1 Summary

Can contrails be reduced with the use of 100 % SAF or with modern lean-burn engines? The investigation of these two technological approaches as measures to mitigating the climate impact of contrails and contrail cirrus was the overarching motive of this work. Lower contrail ice particle numbers have been shown to lead to decreased radiative forcing (Burkhardt et al., 2018; Schumann et al., 2013; Bock and Burkhardt, 2019; Teoh et al., 2022b) and previous studies (Kärcher and Yu, 2009; Wong and Miake-Lye, 2010; Kärcher et al., 2015; Kleine et al., 2018; Rojo et al., 2015) have asserted soot particles as being the dominant contrail condensation nuclei. With an extensive instrumentation onboard the DLR Falcon research aircraft including the two forward-scattering laser spectrometers CAS-DPOL and CAPS-DPOL, in-flight in-situ measurements of contrails were conducted behind an Airbus A350-941 equipped with Rolls-Royce Trent XWB-84 engines in the course of the ECLIF3 campaign to study the influence of 100 % SAF combustion on contrail formation. Using the same measurement platform and methodology, an Airbus A319neo and A321neo powered by CFM International LEAP-1A lean-burn engines were chased during the NEOFUELS/VOLCAN campaign and contrails forming from the lean-burn combustion mode were compared to those from a reference forced rich-burn combustion mode. Central to this study was the question whether strongly reduced soot emissions in the lean-burn combustion mode lead to likewise reduced contrail ice particle numbers, or if other particles take over as condensation nuclei as predicted by parcel model simulations (Kärcher and Yu, 2009; Kärcher, 2018; Yu et al., 2024). Measurements of contrail ice crystal numbers were correlated with aerosol particle numbers and fuel properties from data sets obtained across a broad range of ambient conditions and a statistical method for ensuring comparability of data was developed. In the following, the major research questions and conclusions obtained from the ECLIF3 and VOLCAN campaigns will be summarized.

The first major research question (RQ) of this work was:

RQ1 What is the effect of 100 % SAF combustion on particle emissions and contrail formation?

→Chapter 5, Figures 5.5, 5.6

This question was discussed and answered by data measured during the ECLIF3 campaign where contrails from 100 % SAF combustion were probed in-flight for the first time. A HEFA-type SAF was combusted in an RQL-type Rolls-Royce Trent XWB-84 engine onboard an Airbus A350-941 operated by Airbus so that engine parameters could be controlled and similar ambient conditions targeted. From five contrail flights in April and November 2021, one flight performed on April 16 2021 stood out as offering contrail measurements in stable ice-supersaturated conditions with sufficient statistics from HEFA and reference fuel Jet A-1 combustion. The data obtained during this flight was therefore ideal to answer **RQ1** and it was processed and discussed in the publication Märkl et al. (2024) and from which the following conclusions are taken.

Contrail ice crystals were measured together with the trace gases CO₂ and NO_y, aerosol particles and water vapor. NO_y was used as a dilution tracer due to the lower uncertainties from background fluctuations during this flight, which had also been previously suggested by Kleine (2019). From the data measured by the two forward-scattering laser spectrometers CAS-DPOL and CAPS-DPOL, apparent ice emission indices (AEI) were calculated for the two investigated fuels for similar engine parameters and ambient conditions, resulting in 56 % lower apparent ice emission indices for 100 % HEFA combustion compared to the reference Jet A-1. Nonvolatile aerosol particle EI measured in the far-field contrails were reduced by 35 %. Lower AEI and nvPM EI were attributed to the lower aromatics and naphthalene content of the HEFA while the stronger reduction in ice particles compared to nvPM is suspected to be due to lower ice activation from the low-sulfur HEFA. Comparisons to similar measurements during the previous ECLIF1 and 2 campaigns presented in Voigt et al. (2021) showed that beyond the fuel composition, the type of engine also plays a large role in nvPM emission and contrail ice particle formation. The current generation Rolls-Royce Trent XWB-84 engine showed a significant reduction in contrail ice particle numbers compared to the older IAE V2527 engine for conventional fuel. The variable composition (hydrogen, aromatic, and naphthalene content) of jet fuels and SAFs as well as the type of engine are therefore seen as major influencing factors for contrail formation and the associated climate impact.

Contrail ice crystal PSDs measured during this flight were also studied and a dependence on the difference to emission altitude Δz was found. Ice crystals measured at higher positive Δz (above emission altitude) were largest and smaller particles were found the lower they were detected below emission altitude, thereby showing a high variability of ice crystal PSDs within contrails.

Contrail ice crystal number concentration predictions from CoCiP were performed by Ulrich Schumann (DLR IPA) and compared to the experimental findings. A good agreement was found for median values while the experimentally observed values had a larger spread due to CoCiP not being able to resolve small-scale inhomogeneities in the contrail.

By assuming a 60 % soot particle reduction for the use of 100 % SAF and applying this assumption to the global fleet average for the year 2018, a 26 % reduction in contrail radiative forcing was calculated by Ulrike Burkhardt and Cornelius Weiß-Rehm using the GCM ECHAM5 general circulation model coupled to the Hamburg Aerosol Module and using the contrail cirrus module CCMoD informed by the in-flight measurements.

The findings from the ECLIF3 campaign extend previous in-situ measurements on contrails of SAF

blends (Bräuer et al., 2021b; Voigt et al., 2021) that showed a similar relative reduction but compared to a much "dirtier" reference Jet A-1 (higher aromatics, naphthalene, and sulfur content). Therefore, the role of fuel parameters and the engine type on soot emissions and contrail formation are highlighted so that no generalized statements can be made about the influence of SAF and conventional jet fuels on soot emissions and contrail formation. Instead, fuels and their contrail reduction potential must be evaluated based on their composition and the type of engine they are combusted in.

Modern lean-burn combustion technologies are primarily an approach to reducing NO_x emissions and to increase fuel efficiency (Liu et al., 2017). Test stand measurements have also shown reduced particle number emissions (ICAO, 2024) so that possible nvPM emission reductions under cruise conditions raised the second major research question:

RQ2 Can contrail ice particle numbers be reduced by the use of modern lean-burn combustion technologies and if so, how much? →Section 6.2, Figures 6.5, 6.6

The data needed to answer this question were measured during the NEOFUELS/VOLCAN campaign, which was split into two parts in November 2021 (VOLCAN1) and February and March 2023 (VOLCAN2). CFM International LEAP-1A lean-burn engines installed on the Airbus A319neo and A321neo were staged via FADEC adjustments to operate in a lean-burn combustion mode or a forced rich-burn combustion mode. This allowed emissions and contrails from the respective combustion modes to be intercepted by the DLR Falcon and measured by its onboard instrumentation. In the course of four contrail flights during VOLCAN1 and nine contrail flights during VOLCAN2, a data set from a broad range of ambient conditions was obtained. Additionally, three ice-free near-field emission measurement flights were performed during VOLCAN1 and six such flights during VOLCAN2.

Compared to the relatively constrained ambient conditions found during the investigated ECLIF3 flight, the number of measurement flights performed at a variety of ambient conditions necessitates data to be grouped by similar ambient conditions in order to find influences of combustion mode or fuel on contrail ice particles. On the local scale with otherwise similar ambient conditions, a linear relation was found between AEI and RH_i while a linear anticorrelation was found between AEI and ΔT_{SA} . Likely, higher supersaturations allow a greater number of particles to become activated and lead to the higher contrail ice particle concentrations.

Across the entire data set and all encountered conditions however, a non-linear, triangular relation between AEI and ΔT_{SA} with highest AEI around -9 K to -10 K below T_{SA} could be observed. This is mostly due to a sampling bias from avoiding very cold and humid areas where natural cirrus impede the visibility needed for contrail chasing. Lower AEI at higher temperatures result from incomplete activation of condensation nuclei. To avoid biases from sampling at different RH_i or ΔT_{SA} , a method was developed where VOLCAN data was grouped into so-called P-T domains in which data points were recorded at similar ambient pressures and appear as clustered groups in

a T vs ΔT_{SA} diagram. Within these domains, AEI is assumed to depend mostly on R_{Hi} and ΔT_{SA} and data points are grouped into bins thereof. The data was then normalized and the statistical significance of AEI differences between different fuels or combustion modes evaluated according to Mann-Whitney U rank test p-values. This new method was applied to the VOLCAN data set and allowed answering research questions **RQ2** and **RQ3** from a broad set of data.

Near-field nvPM measurements comparing lean-burn combustion to rich-burn combustion revealed a reduction of approximately three orders of magnitude in soot particles for lean-burn combustion. Interestingly, this reduction does not translate into the same reduction for contrail ice crystals in the far-field on the order of magnitude scale in the investigated engine/aircraft configurations. Instead, a correlation is found between AEI and near-field total particle EIs for both combustion modes. A clear indication was found that the number of ice crystals formed in the young contrails correlate with the number of total aerosol (volatile and nonvolatile) particles larger than 5 nm. The partitioning between nonvolatile and volatile particles seems to play a minor role for ice crystal activation. From this large-scale view, it is not possible to judge if the combustion mode might have an influence on contrail ice crystals on the smaller scale.

For this, the P-T domain method comes into use to compare combustion modes in the far-field under similar conditions. No statistically significant differences in AEI ranges could be found unambiguously across all four binning methods for any P-T domain, so that a contrail ice particle reduction potential by the use of lean-burn combustion could not be found for these measurements. In line with the similarity of AEI for different combustion modes, no significant difference in contrail ice particle size distributions could be observed. Instead, a number of ambient conditions and conditions of contrail probing outweigh any effects the combustion mode might have on PSDs.

As approximately three orders of magnitude less nvPM than total particles were available as nucleating particles for the lean-burn mode, other particle types such as (semi-)volatile aerosols must have acted as condensation nuclei. A strong indication for this was also found by comparing emissions from the two engines during VOLCAN2 as engine 1 had significantly higher total particle emissions than engine 2 in both combustion modes. From sequences of stable engine conditions, the contrail forming behind engine 1 appeared much more optically dense than the one forming behind engine 2 in the lean-burn combustion mode, which is likely attributed to the higher total particle emissions of engine 1.

These results partially confirm the parcel model simulations (Kärcher and Yu, 2009) presented in Kärcher (2018) and shown in Figure 1.2 that predict similar AEI in the soot-poor regime for conditions well below the Schmidt-Appleman threshold temperature T_{SA} . Unlike the predictions for conditions close to T_{SA} , a strong reduction in AEI on the order of magnitude scale could not be confirmed experimentally for the soot-poor regime and instead, contrail ice particle formation seems to be dominated by (semi-)volatile emissions such as ultrafine aqueous particles (UAPs), lubrication oil, unburned hydrocarbons or other organic and inorganic (semi-)volatile particles (Yu et al., 2024).

The aerosol measurements performed by Daniel Sauer and Rebecca Dischl (DLR IPA) showed that the number of nvPM is approximately three orders of magnitude and total particles approximately one order of magnitude higher in far-field contrail measurements compared to the ice-free near-field measurements in the lean-burn combustion mode. While the same increase in total particles could be found for the rich-burn combustion mode when comparing far-field to near-field measurements, no significant increase was found for nvPM. A connection of the increase in nvPM from near-field to far-field measurements in the lean-burn mode to the presence of contrail ice particles is therefore suggested.

Ice activation rates either with respect to far-field nvPM or total particles increase with increasing RH_i and larger differences to T_{SA}. The number of contrail ice particles was found to exceed the number of far-field non-volatile interstitial and ice residual particles in some cases, especially for lean-burn combustion. This indicates that not all original ice condensation nuclei necessarily remain as ice residuals but might also be reduced or increased in number by processing in or on ice particles or evaporate in the thermodenuder. Additionally, the share of far-field nvPM with respect to total particles also increases with increasing RH_i and larger differences to T_{SA}, indicating a larger share of ice residuals for conditions where more contrail ice particles were present.

Processing of (semi-)volatile particles to a nonvolatile ice residual in or on contrail ice particles could be an explanation for this finding. Therefore, nvPM in the far-field are not simply termed as soot or nvPM but as non-volatile interstitial and ice residuals. All near-field emissions measurements were performed behind engine 2, so that the mixing of higher total particle numbers from engine 1 into the contrail could be an explanation for the increase in total particles from near-field to far-field. As it appears that some kind of processing happens between emission and far-field detection, far-field aerosol EI can't be used as a good indicator of initial ice nucleation processes in the lean-burn combustion mode.

Several types of fuel including 100 % SAF and SAF modified through the addition of aromatics were probed during the VOLCAN campaigns. With this set of measurements, the third research question could be answered:

RQ3 Can contrail ice particle numbers be reduced by the use of SAFs in modern lean-burn combustion technologies in the lean-burn and forced rich-burn combustion mode? →Section 6.3, Table 6.6, Figure 6.9

In both combustion modes, a fuel-based ice particle number reduction potential could be found where the HEFA fuel led to lower AEI compared to Jet A-1. A higher fuel-based ice particle reduction potential was also found for lower RH_i compared to higher RH_i. The lean-burn combustion mode also showed possible indications of a higher reduction potential compared to the rich-burn combustion mode for the contaminated fuels. This might be due to the lower sulfur content of HEFA leading to a stronger reduction in (semi-) volatile condensation nuclei compared to the possible reduction in soot particles for the rich-burn mode. However, this could also be an effect of the aforementioned lower humidities for the lean-burn comparison. A somewhat surprising result

was found for the comparison of a high-aromatic but sulfur-free modified SAF fuel (SPK High) to the reference Jet A-1 in the rich-burn combustion mode. The SPK High fuel led to higher AEI compared to Jet A-1 in the rich-burn mode at similar near-field nvPM and lower total particle numbers. Possibly, the higher aromatic content of the SPK High or the higher naphthalene content of Jet A-1 modify primary soot particle sizes and influence the share of volatile particle activation. This could however could not be fully verified in this work.

The fact that a fuel effect can be detected in the lean-burn combustion mode for the use of low-aromatic, low-sulfur HEFA fuel indicates that condensation nuclei other than soot must be reduced by the type of fuel as well. Assuming that lubrication oil droplet emissions are independent of the type of fuel, other particle types such as unburned hydrocarbons, chemi-ions, or other (semi-) volatile particles acting as condensation nuclei are likely to be influenced by the type of fuel.

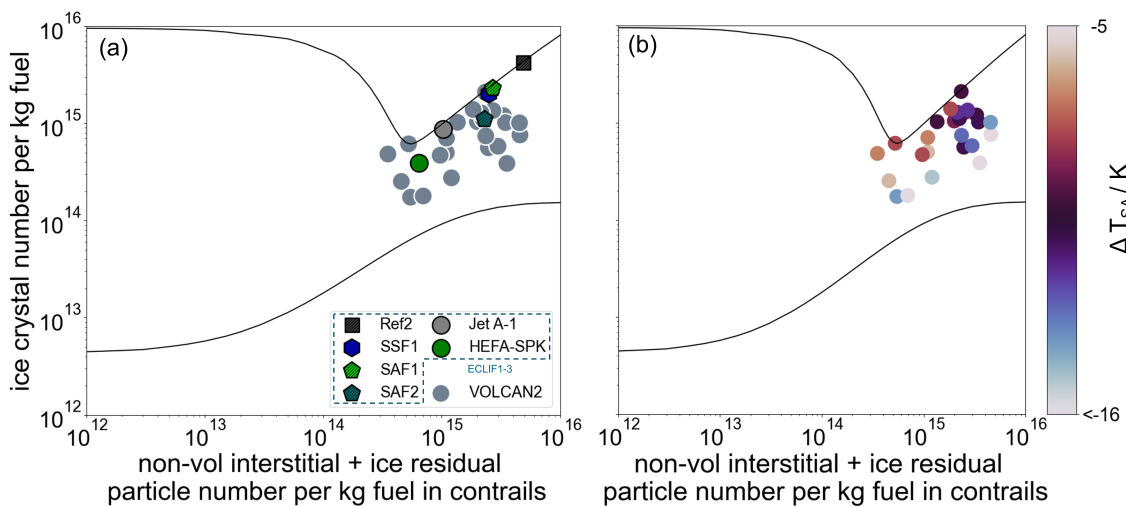


Figure 7.1: (a) Far-field mean AEIs and nonvolatile interstitial and ice residual particle numbers (forward-facing (FW) inlet) of forced rich-burn combustion mode data of the VOLCAN2 campaign (blue-gray data points) and the ECLIF campaigns (Märkl et al., 2024; Voigt et al., 2021) (all other colors). (b) VOLCAN2 mean AEI for a given color-coded ΔT_{SA} range. Continuous lines are boundaries for conditions well below T_{SA} (top) and for conditions close to T_{SA} (bottom) from Yu et al. (2024).

Figure 7.1 (a) combines far-field data from the ECLIF campaigns (Voigt et al., 2021; Märkl et al., 2024) and the VOLCAN2 campaign and allows a comparison of spanned ice particle number and nonvolatile interstitial and ice residual particle number ranges. VOLCAN2 data points cover a large portion of the y-axis range within the borders defined in Yu et al. (2024), which represent a recently updated version of the borders defined in Kärcher (2018) and based on Kärcher and Yu (2009). In this updated model, primary soot particles determine contrail formation rather than aggregates, leading to increased plume supersaturations and higher probabilities of volatile particle activation (Yu et al., 2024). The model however does not yet include the effect of condensable organics (Yu et al., 2024), which could possibly further align model results with experimental observations. ECLIF3 data points on the other hand are confined to the top of the y-axis range at a similar x-axis range. Figure 7.1 (b) shows the same VOLCAN2 data points but resolved by their respective ΔT_{SA} value.

Here, a color bar was chosen with light colors at very warm and very cold temperatures and dark colors for the intermediate ΔT_{SA} values. Consequentially, intermediate ΔT_{SA} values can be found for higher AEI while lower AEI correlate with very warm or very cold temperatures. Hence, the strong influence of ΔT_{SA} on AEI as predicted by Kärcher and Yu (2009) is shown. The comparison of the two campaigns highlights that AEI measured during the ECLIF campaigns are found at the upper predicted boundary defined by Yu et al. (2024) and meaning nearly complete soot particle activation (Kleine et al., 2018; Voigt et al., 2021). On the other hand, almost the entire y-axis range is spanned for VOLCAN2 data. Even for one single engine type, the range of measured AEI and nonvolatile interstitial and ice residual particle numbers therefore strongly depends on ambient conditions and the type of used fuel.

Overall, the formulated research questions could be answered in the course of this work with additional findings materializing from the comprehensive data set. As is often the case with research, when questions are answered, new ones are raised. These will be discussed in the next section together with suggestions on how they could be answered and what further research is planned in this respect in the future.

7.2 Outlook

This work answered several questions with regard to contrails from 100 % SAF combustion and the use of modern lean-burn engines. While the obtained data sets covered a broad range of ambient conditions, fuels, and engine parameters, there are still gaps in experimental findings that will be discussed in the following. Subsequently, possibilities to fill these gaps in future campaigns will be presented together with suggestions for instrumentation and data analysis. Finally, the potential and likely future development of the investigated technological climate impact mitigation measures will be discussed.

7.2.1 Open questions and future contrail campaigns

The ECLIF3 campaign showed the reduction potential for the use of 100 % SAF in RQL combustors compared to a relatively "clean" conventional reference jet fuel. Comparisons to previous in-situ measurements of SAF blends showed that the type of engine also has a large influence on nvPM emissions and contrail formation. Hence, the reference Jet A-1 during ECLIF3 showed lower nvPM EI and AEI compared to the SAF blends combusted in an older engine. Simulations by Teoh et al. (2022b) predict a decreasingly steep contrail reduction potential for increasing blending ratio. This has however not been confirmed experimentally from in-situ measurements at cruise conditions. Measurements similar to those conducted during ECLIF3 with SAF blends at varying blending ratios (e.g. 25 %, 50 %, 100 %) and ideally a world-average conventional reference jet fuel could be

useful in verifying predictions and determining the ideal blending ratio to maximize the climate warming mitigation potential of SAF.

Some of the conclusions from the VOLCAN data set can be drawn with fairly high confidence such as that contrail ice particle numbers are not significantly influenced by the combustion mode in the investigated aircraft/engine configuration despite developing from different condensation nuclei. Other findings are indicated but would benefit from confirmation through further measurements. Overall, the following open questions emerge from the VOLCAN campaign and could serve as research questions for future campaigns regarding contrail formation from lean-burn engines:

- *Can a higher fuel-based reduction potential for low humidity compared to high humidity be systematically confirmed?*
- *Can a higher fuel-based reduction potential be confirmed in the lean-burn combustion mode compared to rich-burn combustion?*
- *Can higher AEI for SPK High combustion compared to Jet A-1 be confirmed and can the underlying particles or particle properties for ice nucleation be identified?*
- *What type of (semi-)volatile particles is mainly responsible for contrail ice nucleation in the lean-burn mode?*
- *Can lubrication oil use be monitored in real time and controlled to systematically investigate its role in contrail ice nucleation?*
- *What are the exact processes leading to the increase in nvPM and total particles in the far-field compared to near-field?*

The first three research questions can be answered by conducting measurements similar to those during the VOLCAN campaigns. Repeating measurements from HEFA and Jet A-1 combustion at lean-burn and rich-burn conditions preferably at low humidity and at high humidity could provide the data set needed to answer the first two questions. Finding the right conditions for this type of comparison has proven challenging in the past. Areas are needed where humidity and visibility are simultaneously high enough for contrail formation and large enough to provide an airspace suitable for contrail sampling. Finding these types of air masses took considerable time during the VOLCAN campaign, even in areas with predicted contrail-forming conditions. Repeating the comparison of SPK High fuel to Jet A-1 at lean-burn and rich-burn conditions would also give the opportunity to confirm the higher AEI for SPK high and to check if SPK High inversely produces lower AEI than Jet A-1 in the lean-burn mode. Model calculations similar to those conducted by Yu et al. (2024) for these specific fuels could also offer insight into possible nucleation mechanisms

and underlying condensation nucleus properties. During VOLCAN, the statistical sample size for contrails from SPK Low fuel was small. Repeating measurements comparing Jet A-1 and SPK Low at similar conditions would provide insight if a statistically significant difference can be found. Similarly, the ambient conditions for the comparison of HT-fuel to Jet A-1 during VOLCAN1 were not similar enough to clearly investigate the difference of these two fuels on contrail ice formation. Repeating measurements with these two fuels at similar RH_i , ΔT_{SA} and ambient pressure would therefore be recommended. The confirmation of these findings could be implemented in models to evaluate the climate impact mitigation value under specific conditions. For example, if it is confirmed that SAF reduces contrails more at low RH_i in the lean-burn combustion mode, SAF could be preferentially allocated to routes where these conditions are met.

To determine the exact type of (semi-)volatile particles mainly responsible for ice nucleation in the lean-burn mode, monitored and controlled lubrication oil use during inflight measurements could show if contrail ice formation can be tuned this way. Also, it would be helpful to use two engines with a similar maintenance cycle to avoid possible additional effects such as additional particle emissions that might arise from the use of two engines at different stages of maintenance cycle. Combustion of low-sulfur, low aromatic fuel during this study of lubrication oil could additionally minimize the possible influence of fuel constituents and reduce the study to particulate lubrication oil emissions. Findings from a study of such type would also be of importance for future hydrogen combustors. For the design and interpretation of these measurements, the current work by Ponsonby et al. (2024b) on the inclusion of volatile particle activation in the soot-poor regime could be closely followed. The recent work by Yu et al. (2024) already includes volatile particles as condensation nuclei and provides an updated view to the boundaries presented in Kärcher (2018). Volatile organic particles are however not yet included in the model and the findings from the VOLCAN campaigns presented in this work should be considered for implementation in future model versions, especially for predictions in the low-soot regime.

Urbanek et al. (2018) and Groß et al. (2023) have found indications of an effect of aviation emitted aerosols on cirrus cloud properties. Non-volatile ice residuals processed from volatile aerosols could therefore have implications for the formation of natural cirrus, even after sublimation of contrail ice crystals. To understand the processing of particles in or on ice particles it could be useful to perform a distance profile from near-field to far-field conditions under ice-free conditions and under contrail-forming conditions. This way, it could be confirmed if the increase in $nvPM$ from near-field to far-field in the lean-burn mode is dependent on the presence of ice. It thereby also might be possible to quantify rates of conversion from (semi-)volatile particles to nonvolatile ice residuals and to gain further insight into the processes responsible for this conversion. An experimental campaign performed in autumn 2023 is the EcoDemonstrator experiment where the NASA DC-8 research aircraft chased a Boeing 737-10 equipped with CFM International LEAP-1B engines, which are very similar to the LEAP-1A engines used during VOLCAN. During these measurements, contrails were probed from SAF and ultra-low sulfur Jet A fuel combustion in newly manufactured engines, offering the opportunity for comparing VOLCAN campaign results (Bräuer et al., 2024).

7.2.2 Future developments in instrumentation and data analysis

The instrumentation and methods used in the course of this work have been developed and iterated over the course of several years and campaigns. While this led to continuous advancements in measurements and data processing, this work has also revealed remaining room for improvement for future measurements and campaigns.

Instrumentation

The employed CAS-DPOL and CAPS-DPOL instruments were used to measure ice particle number concentrations and sizes. As discussed in subsection 3.2.4, there was a certain, likely size-dependent, variability in particle counting agreement between the two instruments. Here, an independent particle counting calibration method, ideally covering a range of particle sizes, would be a useful way to test if the instruments overcount or undercount particles of certain sizes. Correction functions could thereby be derived for each instruments so that their size-dependent particle counting efficiencies match those of the calibration method. Simulating scattering events electronically could be one solution as well as creating a particle air flow with a defined concentration in the laboratory. Methods exist to calibrate the counting efficiency of OPCs at low particle concentrations in the size range relevant for contrails (Vasilatou et al., 2020) so that it is conceivable to adapt similar methods to CAS instrumentation.

Another limit of the CAS instruments is the maximum number of particles recorded by the pbp file. In subsection 4.1, the two different methods for calculating number concentrations based on the CAS bulk file or pbp file were mentioned. The bulk file based method was chosen despite its lower size resolution due to expected uncertainties from concentration extrapolations necessary when using the pbp file not containing every encountered particle. In future instrumentation versions, it would be desirable to record all encountered particles in a pbp file despite the high requirements for data processing and storage. This would avoid the rigid ADC size binning in the bulk file and at the same time ensure accurate number concentration determination even in rapidly varying concentration settings.

Particle sizing with forward-scattering laser spectroscopy methods is physically limited by Mie ambiguities in the relationship between SCS and size for a given laser wavelength and scattering angle range. These Mie oscillations could be shifted to each other for different wavelengths so that two or more chosen laser wavelengths could in principle be combined to reduce ambiguities. This type of measurement principle would however come with the disadvantages of the weight and volume of a second laser source and optical system and detector, as well as data processing. A system using two laser wavelengths exists (Nagy et al., 2007) and has been used on the ground to characterize urban aerosols (Nagy et al., 2016).

There are not many feasible alternatives to the CAS instrument system for the in-flight in-situ measurement of contrail ice particles. In principle, the FFSSP (upgraded version of Forward Scattering Spectrometer Probe (FSSP)) and Fast Cloud Droplet Probe (FCDP) instruments from SPECinc are

light-scattering instruments designed for the counting and sizing of cloud particles. The CAS instrument has been developed based on the older FSSP (Baumgardner et al., 2001) making it obsolete, while the FCDP is not able to measure particles smaller than $1.5 \mu\text{m}$ (practically $3 \mu\text{m}$) (Kirschler et al., 2022). Another measurement principle is the Phase Doppler Interferometer (PDI) implemented by Artium Technologies for cloud microphysical measurements (Chuang et al., 2008). In contrast to other forward-scattering probes, the PDI's measured quantity is the light's wavelength after undergoing interference at the measured particle and not the scattering intensity, leading to advantages regarding uncertainties for example due to coincidence (Chuang et al., 2008). While the detectable size range down to approximately $0.5 \mu\text{m}$ covers typical contrail ice particles, accurate sizing is only possible if their shape is close to spherical (Chuang et al., 2008), which can't be assumed for contrail ice particles aged several minutes (Gayet et al., 2012; Voigt et al., 2011).

Beyond improvements in ice particle detection, the questions raised by this work also require certain modifications and improvements in the non ice particle instrumentation. Aerosol measurements could be improved by extending the size detection range of the CPCs towards the nucleation mode of volatile particles (\sim several nm) and also adding additional channels to achieve higher size resolution in the range of 3 to 20 nm (currently detection only goes down to 7 nm and no size resolution). This could be realized by connecting several CPCs in series, each with a respective lower cutoff size. This together with the use of several thermodenuders operated at different temperatures could shed light on the types of particles responsible for ice particle nucleation in the soot-poor regime by characterizing the size and volatility of (semi-)volatile particles. It is also conceivable to install instrumentation capable of measuring ion clusters, for example using a Cluster Ion Counter (CIC) (Airel OÜ, 2024) or previously used instrumentation such as a Neutral Cluster - Air Ion Spectrometer (NAIS) (Mirme et al., 2010) or mass spectrometer (Arnold et al., 1999) in order to be able to quantify the role of chemi-ions on contrail ice particle nucleation.

RHi values used for filtering data as well as for the calculation of T_{SA} in this work were obtained from the AIMS onboard the DLR Falcon aircraft. While it has been discussed in subsection 3.4 that these measurements are a good approximation for these purposes, the ideal solution would be the measurement of water vapor mixing ratios in the undisturbed atmosphere onboard the preceding emission source aircraft. A relatively compact instrument that could come into question is the Sophisticated Hygrometer for Atmospheric ResearCh (SHARC) (Kaufmann et al., 2018), which has an extremely large measurement range able to cover very low to very high humidity from the ground to the stratosphere. This instrument is also a desirable addition to the DLR Falcon instrumentation for future campaigns and would for example solve the problem of low measurement accuracy for mixing ratios over 150 ppm in AIMS.

Data processing

Due to variable backgrounds of tracers, especially CO₂, and aerosols, there is still a lot of manual work involved in classifying plumes. While certain criteria are used (e.g. dipping of concentrations below 15 % of the neighboring peak maximum) and plume definitions are iterated and discussed with expert colleagues, there is currently no fully objective and automatic algorithm that can satisfactorily define plume times across ice particle, aerosol, and trace gas measurements. Such an algorithm would save the analyzing scientist a lot of time and could reduce subjectivity in plume definitions. It could also be investigated to train a machine learning algorithm to classify plumes from existing data sets but this would again reduce the traceability of plume definition as no clear and objective criteria would again be used.

7.2.3 Technology outlook

This work has shown that the use of 100 % SAF has the potential to reduce contrail ice particle numbers and thereby radiative forcing, in RQL combustors as well as in lean-burn engines. In subsection 2.2.4 it has been discussed that the projected demand for SAF will present fuel producers with the challenge of producing and delivering enough sustainably produced SAF. This constrained supply leads Teoh et al. (2022b) to suggest a targeted use of SAFs in a way that maximizes climate impact reduction. They recommend achieving this by using higher SAF blending ratios for a small share of flights with the highest contrail energy forcing instead of uniformly distributing SAF supply across a larger share of flights with lower blending ratios. The use of 100 % non drop-in SAF will likely not be certified before the year 2030 (EASA, 2023) so that for the time being, blends or drop-in SAFs are the only implementation options. In principle, conventional jet fuel could also be hydrotreated to remove or reduce the chemical compounds (mainly sulfur and aromatics) responsible for producing contrail ice condensation nuclei (Faber et al., 2022; Quante et al., 2024). However, this process actually increases the fuel's CO₂ net emissions due to the additional processing so that this pathway might be feasible only when used on flights where a strong contrail energy forcing is expected that could be reduced by the use of hydrotreated conventional jet fuel (Quante et al., 2024).

Current research indicates that the use of blended or pure SAF can lead to reduced contrail radiative forcing (Voigt et al., 2021; Bräuer et al., 2021b; Teoh et al., 2022b; Märkl et al., 2024) and can therefore be a valuable tool in combating aviation's climate impact. SAF is a term incorporating many fuels with different chemical characteristics and varying degrees of sustainability. As discussed in subsection 2.2.3, the overall climate impact of SAFs depends strongly on the type of feedstock and production pathway so that a full life cycle analysis is necessary for a nuanced assessment. In order to cover the growing SAF demand, several types of feedstock and production pathways (see subsection 2.2.2) need to be explored. Recently, first in-flight emission measurements of Power to Liquid (PtL) fuel were performed by DLR to investigate the non-CO₂ effects of this type of fuel that

could play a large role in future SAF supply (DLR, 2024).

New propulsion technologies such as electrically powered aircraft or the use of hydrogen fuel are also currently under development (Llewellyn and Miftakhov, 2022; Ying, 2022). These have the advantage of producing no local CO₂ emissions and in the case of electric propulsion, no local emissions at all. For the foreseeable future, electric propulsion will only be feasible for urban and regional traffic due to limitations in energy and power density of batteries and the fundamentally different mode of propulsion compared to jet engines (Ying, 2022; Hungerland et al., 2024). Hydrogen on the other hand can be used as fuel for hybrid-electric propulsion using fuel cells or to create jet propulsion in direct combustion (Llewellyn and Miftakhov, 2022). The primary emission during hydrogen fuel use is liquid or gaseous water, but so far there is no experimental verification of the effect on contrail formation. Especially during direct hydrogen combustion, potential contrail condensation nuclei can be found in the atmosphere or they can be emitted, either consisting of lubrication oil droplets or nitrogen compounds from high temperature NO_x formation (Bier et al., 2024). Long technology implementation cycles together with the currently high cost of hydrogen and low availability of sustainably produced hydrogen are large barriers that would need to be overcome (Nikolaidis and Poullikkas, 2017; Llewellyn and Miftakhov, 2022). There are however efforts to characterize contrail formation behavior of hydrogen combustion, for example the BlueCondor campaign where a glider equipped with a hydrogen combusting engine is used as the emission source aircraft to study contrail forming behavior without interference from conventional jet engine emissions (Airbus, 2023).

While lean-burn engine technologies such as the TAPS combustor concept can improve engine efficiency and reduce soot emissions, the results of this work have shown that contrail ice particle numbers from the lean-burn mode remain similar to those in the forced rich-burn mode. This work has however also shown that the use of SAFs in these combustors can lead to reductions in contrail ice particles in the lean-burn combustion mode. Further measurements are needed to confirm if a higher fuel-based contrail ice particle reduction potential can be achieved in the lean-burn combustion mode and determine if a contrail mitigation benefit can be achieved in this way after all.

Beyond direct technological solutions at the aircraft or the fuels, air traffic management and operations are a sector where climate impact mitigation can be achieved with the currently available fleet and fuels (EASA, 2023). For example, the European air traffic management (ATM) Master Plan includes measures to reduce operational and routing inefficiencies and associated excess fuel consumption by harmonizing the different ATM systems and modernizing operations (SESAR Joint Undertaking, 2020; EASA, 2023). Especially the avoidance of contrail forming regions could be a way to reduce contrail radiative forcing without modifications to aircraft or fuels. Past research work has investigated the feasibility and efficacy of flight rerouting with the purpose of avoiding contrail formation while also pointing to the risks of increased fuel consumption and additional

CO₂ emissions (Schumann et al., 2011; Teoh et al., 2020a,b; Sausen et al., 2023; Lee et al., 2023; Martin Frias et al., 2024). Current efforts in this regard include the 100 flights trial, a collaboration between four airlines, Deutsche Flugsicherung (DFS), DLR, and Deutscher Wetterdienst (DWD) where contrail forming regions are predicted and flight routes adapted on 100 flights to avoid contrail formation (BMDV and BMWK, 2024). The study will then further use satellite observations and numerical models to verify the successful prediction and contrail avoidance (BMDV and BMWK, 2024).

As only a small portion of flights are responsible for the majority of contrail energy forcing (Teoh et al., 2024), rerouting efforts might be supplemented with other technological measures such as SAF in order to maximize climate impact mitigation. A sensible use for the still limited SAF supply could for example be combustion of higher blending ratios on a small share of flights that can not be rerouted without a significant fuel penalty so that both climate impact mitigation options are used in parallel and complementarily. Currently, there is not one approach or solution that can be used to make aviation sustainable on its own. On the path forward, technological and operational approaches will need to be further developed and used in conjunction to maximize reductions in CO₂ and non-CO₂ radiative effects and assure feasibility in implementation. Likely, SAFs and modern combustion technologies will play a major role and policymakers and the industry as well as the general public deserve to be guided by reliable data and information, which is why further research regarding these technologies and their impact on emissions and contrail formation is extremely important and strongly recommended for the future.

Contributions to this study

*Persons formerly affiliated with the indicated institution are marked with an asterisk *.*

ECLIF3

Author contribution statement from the publication Märkl et al. (2024): Christiane Voigt^{1,2}, Stefan Kaufmann¹, Charles Renard³, and Andreas Dörnbrack¹ planned and coordinated the flight experiment. Raphael Satoru Märkl^{1,2}, Daniel Sauer¹, Rebecca Katharina Dischl^{1,2}, Stefan Kaufmann¹, Theresa Harlaß^{1*}, Valerian Hahn¹, Andreas Marsing¹, Anke Roiger¹, and Monika Scheibe¹ performed the in-flight measurements and analyzed the data. Raphael Satoru Märkl^{1,2} performed the contrail ice data evaluation and wrote the paper. Christiane Voigt^{1,2} conceptualized the study. Cornelius Weiß-Rehm¹ and Ulrike Burkhardt¹ performed the climate model calculations and authored the respective sections. Ulrich Schumann¹ performed a contrail model comparison and authored the respective sections. Maxime Gauthier³ assisted in aircraft data analysis. Peter Swann⁴, Paul Madden^{4*}, and Darren Luff^{4*} performed NO_x model analysis and provided EI_{NO_x} data. Reetu Sallinen⁵ provided the fuels and fuel analysis. Tobias Schripp^{6*} and Patrick Le Clerq⁶ performed the ground measurements and fuel analysis. All the authors contributed to the paper. Additionally, Charles Renard³, Maxime Gauthier³, Ashog Kulathasan³, and Gauthier Le Chenadec³ performed fuel analyses.

VOLCAN

Large in-situ campaigns such as the VOLCAN project involve many people contributing in a number of ways and parts of their contributions are shown in chapter 6. Christiane Voigt^{1,2}, Charles Renard³, and Katharina Seeliger³ conceptualized the campaigns, Daniel Sauer¹ and Rebecca Dischl^{1,2} measured and analyzed aerosol data, Theresa Harlaß¹, Tiziana Bräuer^{1,2}, and Lisa Eirenschmalz^{1*} measured and analyzed trace gas data, Stefan Kaufmann¹ and Laura Tomsche^{1,2} measured and analyzed water vapor data, Katharina Seeliger³, Maxime Gauthier³, and Charles Renard³ provided information on fuels and Airbus flight data, and Emmanuel Greslin⁷ of Safran provided engine parameters. I operated the cloud probes during many flights, evaluated and analyzed all data regarding ice particle measurements, performed the shown inter-instrumental analyses, wrote the text, and produced all figures and tables with the aforementioned restrictions or where indicated otherwise.

¹Institut für Physik der Atmosphäre, Deutsches Zentrum für Luft- und Raumfahrt, Oberpfaffenhofen, Germany

²Institute of Atmospheric Physics, Johannes Gutenberg-Universität, Mainz, Germany

³Airbus Operations SAS, Toulouse, France

⁴Rolls-Royce plc., Derby, UK

⁵Neste Corporation, Innovation, Porvoo, Finland

⁶Institute of Combustion Technology, Deutsches Zentrum für Luft- und Raumfahrt, Stuttgart, Germany

⁷Safran Aircraft Engines, Villaroche, France

Parts of the VOLCAN2 results presented here build upon work conducted by Jonas Schmidt^{1*} whom I supervised at DLR in the course of his master thesis (Schmidt, 2023) (not published) at DLR IPA where he focused on fuel comparisons in the rich-burn combustion mode. Specifically, he co-performed CAS-DPOL and CAPS-DPOL calibrations and measurement flights with me during the campaign and defined contrail encounters for flights F04, F11, F17, and F19 based on code written largely by me. The analyses of the mentioned flights performed by Jonas Schmidt have been widely extended and the flights have been re-analyzed with new methods in the course of my work.

¹Institut für Physik der Atmosphäre, Deutsches Zentrum für Luft- und Raumfahrt, Oberpfaffenhofen, Germany

Appendix A: Additional VOLCAN information

Table A1: Overview of VOLCAN 2 P-T domains with the flights included in the respective domain, the total number of data points, the filtered number of data points and the fuels and combustion modes contained in the data for the respective domains. Domains with insufficient data for comparisons are marked in red while domains used for further analysis are marked green. Domain 5.3 is not considered due to the low number of comparable points at similar conditions.

P-T domain	Flights	# of data points	# of filtered data points	Fuels (combustion mode) comparisons
1.1	F21	2	0	-
1.2	F16	36	9	Jet A-1, SPK High (lean)
1.3	F04	136	79	Jet A-1 con2, HEFA con2 (rich, lean)
2.1	F21	8	1	-
3.1	F09	2	0	-
3.2	F11	70	56	SPK Low (rich, lean), Jet A-1 (rich)
3.4	F04	9	6	-
4.4	F08	155	62	Jet A-1 (lean, split, rich)
5.3	F21	13	9	Jet A1, HEFA (lean)
6.3	F19	132	102	Jet A-1, HEFA (rich, lean)
7.3	F09, F17	50	28	Jet A-1 (rich, split), SPK High (rich)
7.5	F16	46	25	SPK High, Jet A-1 (rich)
8.5	F09	2	1	-
9.6	F09	54	18	Jet A-1 (rich), SPK Low (rich, lean)
9.7	F02	63	9	HEFA con1 (lean, rich), Jet A-1 con1 (rich)

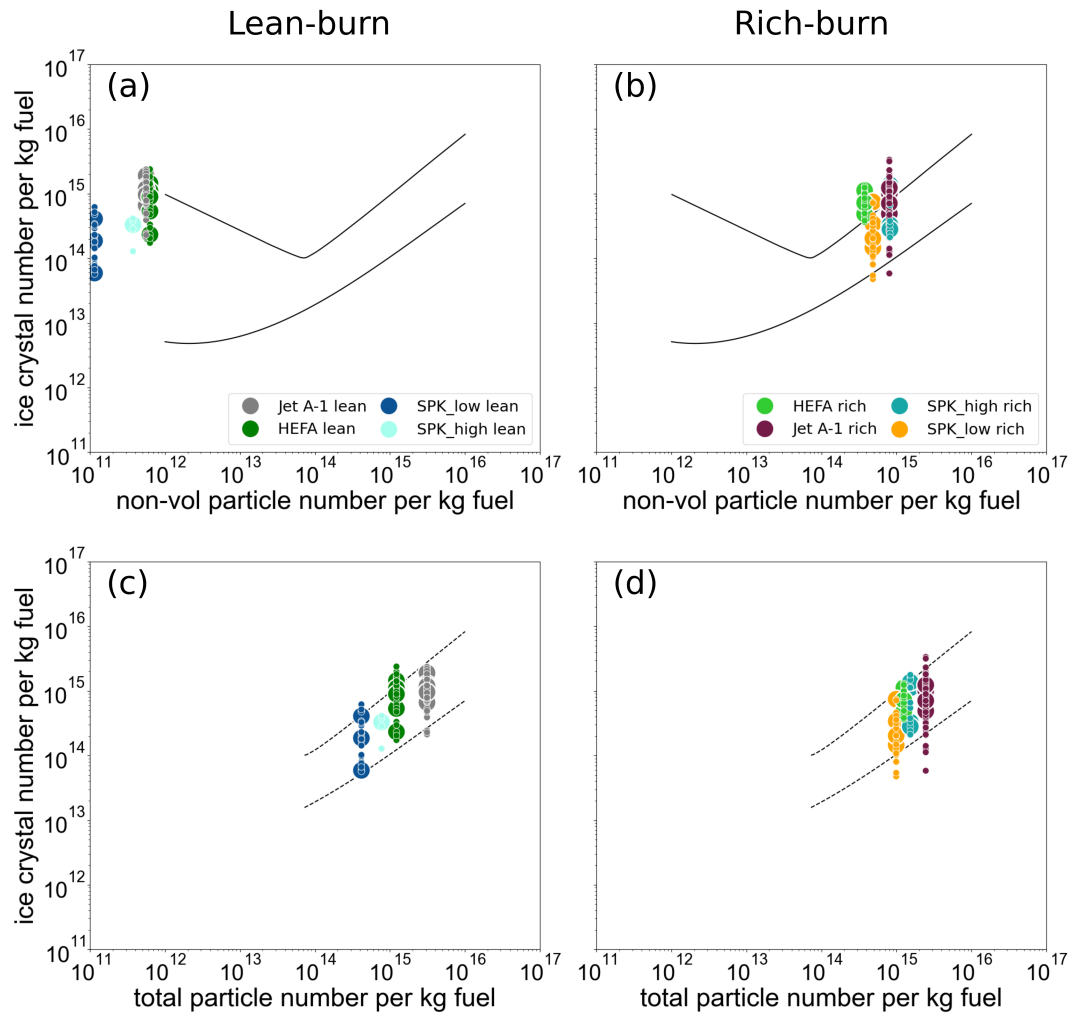


Figure A1: VOLCAN2 far-field AEI vs. (a, b) near-field nvPM emission indices and vs. (c, d) near-field total particle emission indices in (a, c) lean-burn combustion mode and in (b, d) rich-burn combustion mode. Continuous lines represent the upper and lower expected AEI boundaries based on Kärcher (2018) for nvPM and dashed lines represent the high soot regime nvPM based boundaries shown as guide to the eye in total particle number plots. Small symbols are single contrail encounters while large symbols represent median AEI values in $1\text{ K } \Delta T_{SA}$ range bins as described in subsection 4.7.

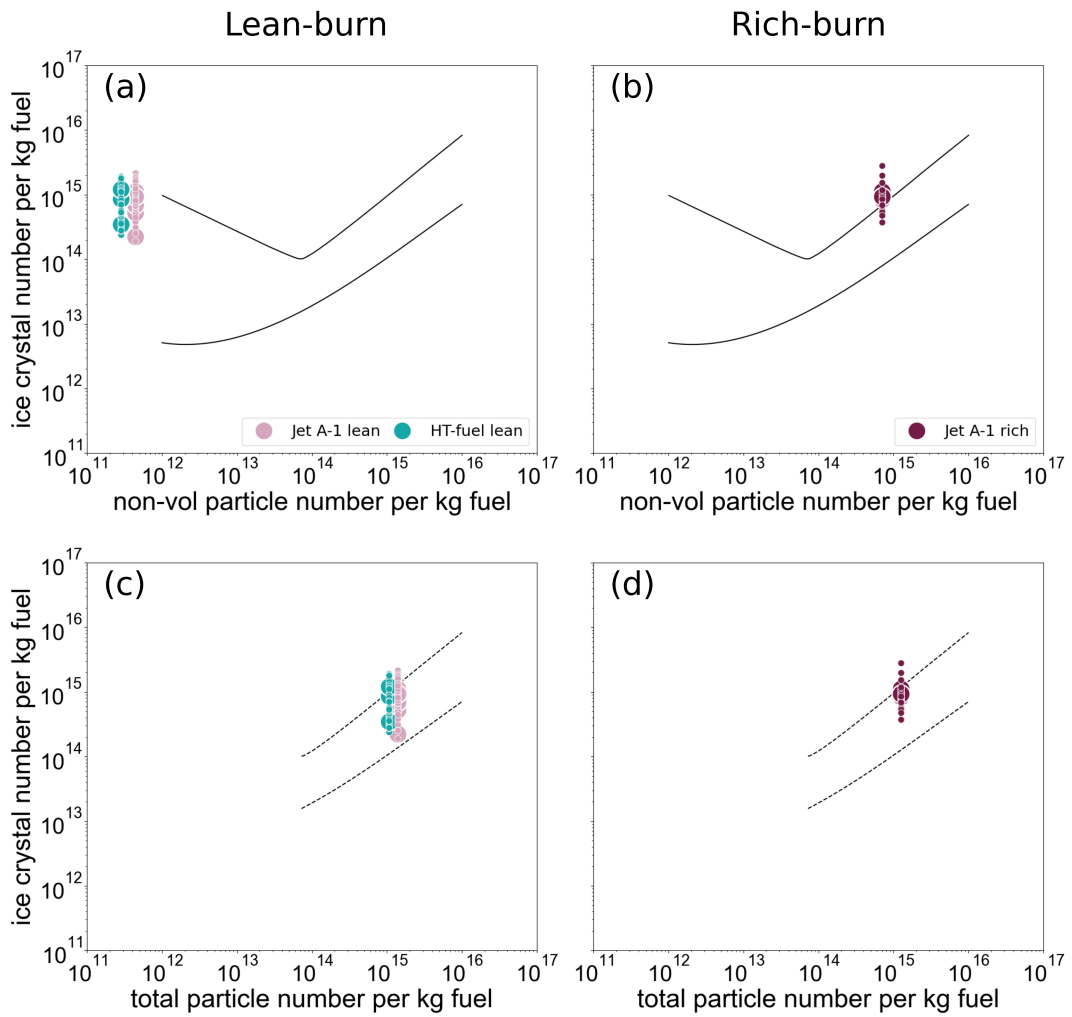


Figure A2: VOLCAN1 far-field AEI vs. (a, b) near-field nvPM emission indices and vs. (c, d) near-field total particle emission indices in (a, c) lean-burn combustion mode and in (b, d) rich-burn combustion mode. Continuous lines represent the upper and lower expected AEI boundaries based on Kärcher (2018) for nvPM and dashed lines represent the high soot regime nvPM based boundaries shown as guide to the eye in total particle number plots. Small symbols are single contrail encounters while large symbols represent median AEI values in $1\text{ K } \Delta T_{SA}$ range bins as described in subsection 4.7. Note that for VOLCAN1, data from the CAS-DPOL and CAPS instruments are shown together.

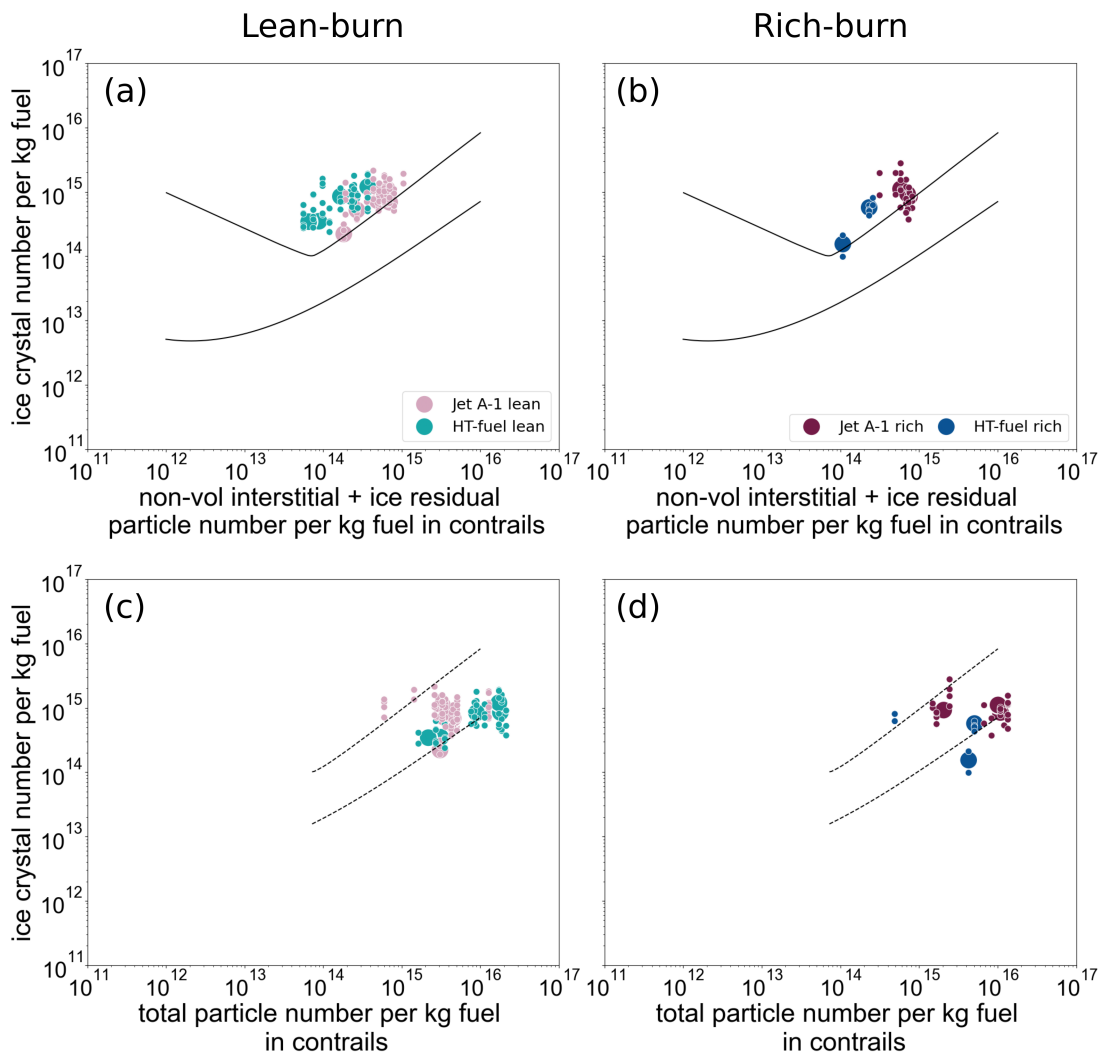


Figure A3: VOLCAN1 far-field AEI vs. (a, b) far-field nvPM emission indices and vs. (c, d) far-field total particle emission indices in (a, c) lean-burn combustion mode and in (b, d) rich-burn combustion mode. Continuous lines represent the upper and lower expected AEI boundaries based on Kärcher (2018) for nvPM and dashed lines represent the high soot regime nvPM based boundaries shown as guide to the eye in total particle number plots. Small symbols are single contrail encounters while large symbols represent median AEI values in $1\text{ K } \Delta T_{SA}$ range bins as described in subsection 4.7. Note that for VOLCAN1, data from the CAS-DPOL and CAPS instruments are shown together. Note also that in panel (d), two Jet A-1 medians lie nearly on top of each other and are therefore difficult to discern. The total particle measurement corresponding to the third Jet A-1 Median was not valid.

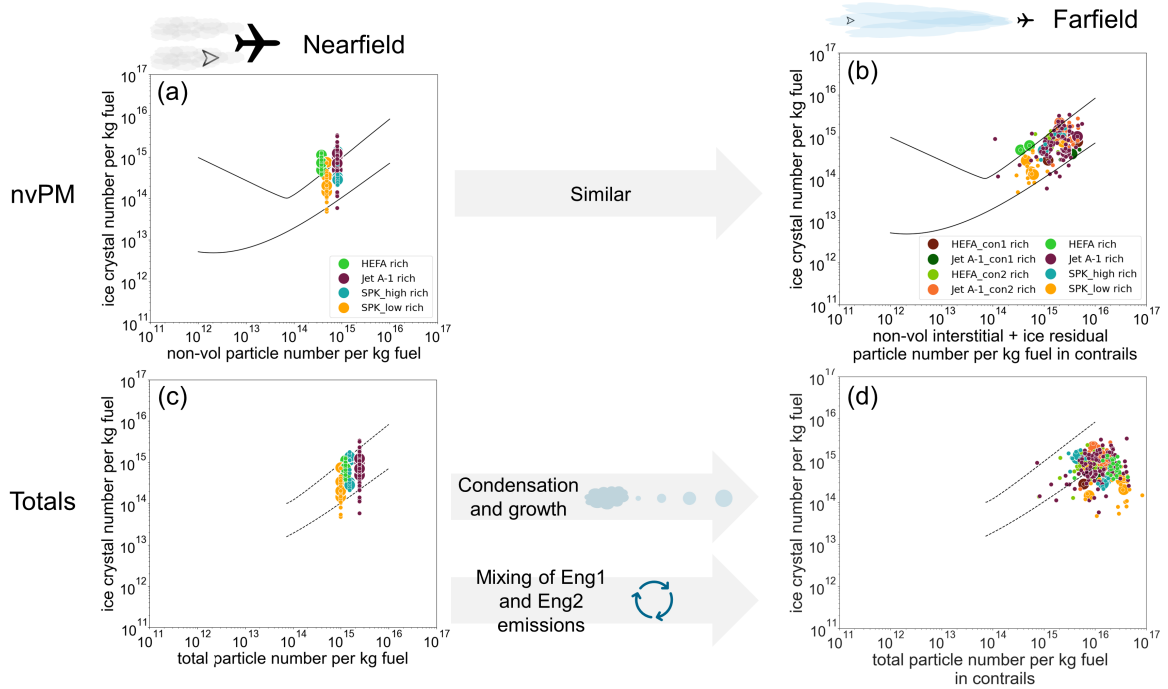


Figure A4: Comparison of VOLCAN2 rich-burn AEI shown against near-field (a) nvPM EI and (c) total particle EI and against far-field (b) non-volatile interstitial and ice residual particle numbers and (d) total particle EI with possible processes indicated between the near-field and far-field plots. Small symbols are single contrail encounters while large symbols represent median AEI values in $1\text{ K } \Delta T_{SA}$ range bins as described in subsection 4.7

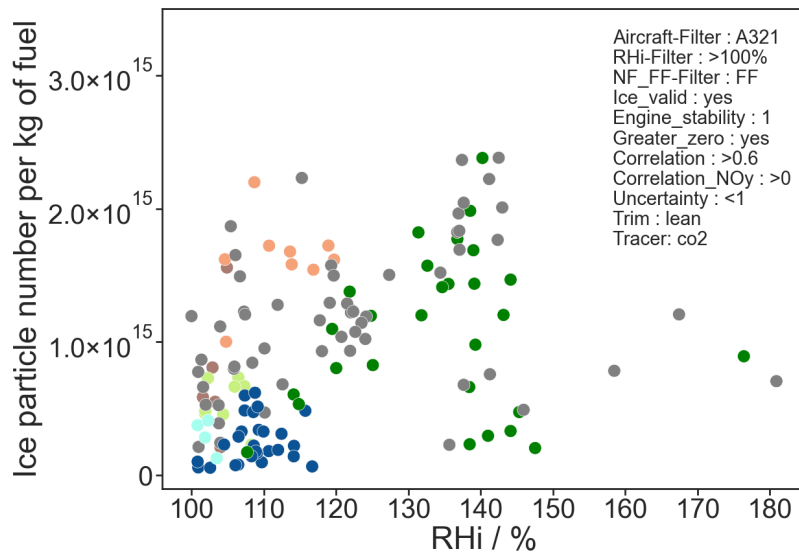


Figure A5: AEI from the VOLCAN2 campaign for all fuels in lean-burn combustion mode shown against relative humidity over ice for the entire RH_i range including Flight 21.

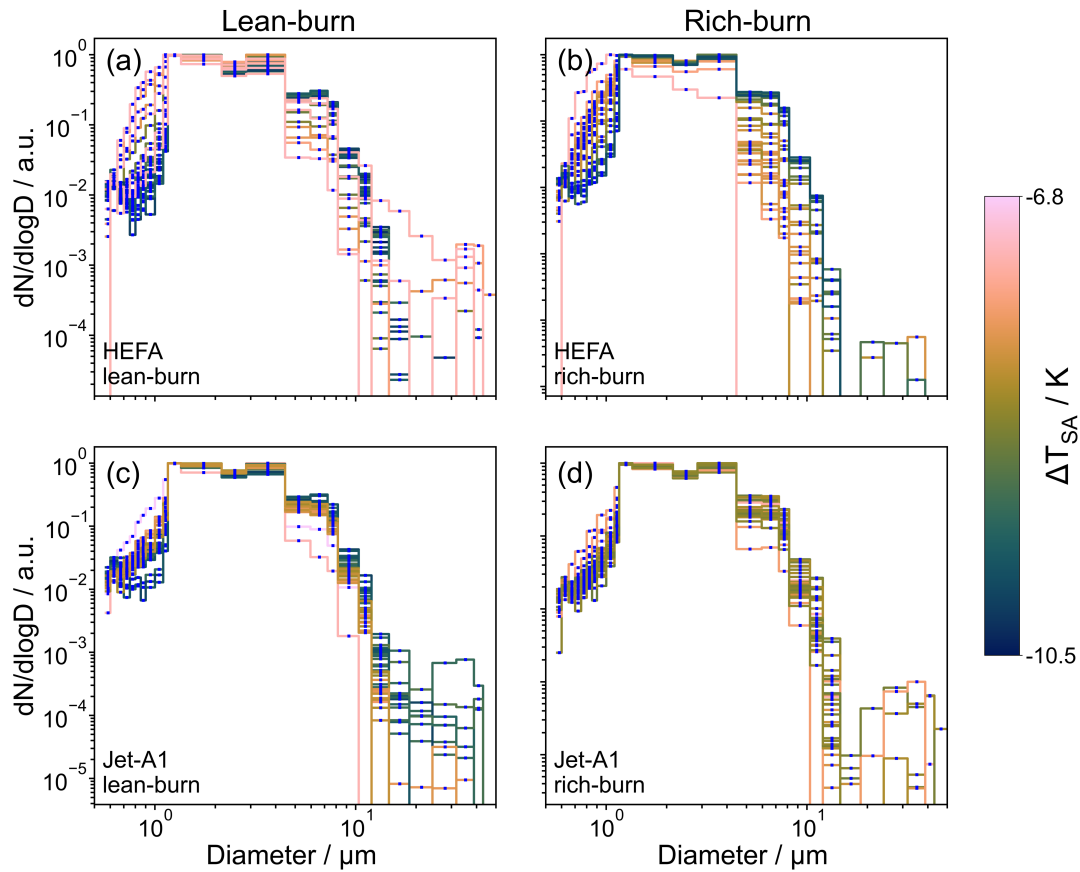


Figure A6: ΔT_{SA} resolved PSDs of P-T domain 6.3 for HEFA (a) lean-burn and (b) rich-burn conditions and for Jet A-1 (c) lean-burn and (d) rich-burn conditions. Note: The scientific color map batlow (Crameri et al., 2020; Crameri, 2021) is used.

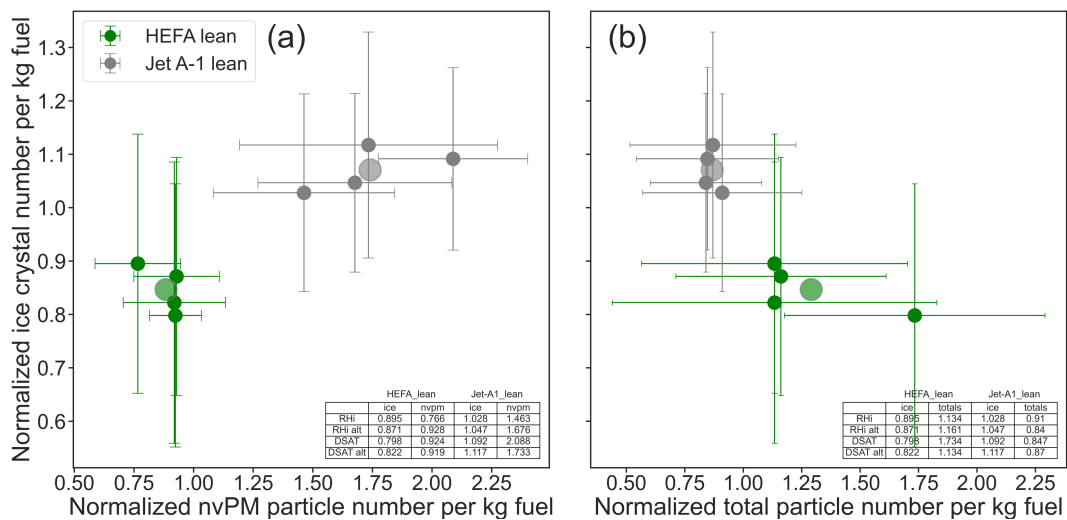


Figure A8: Median normalized AEI comparing domain 6.3 HEFA lean-burn to Jet A-1 fuel lean-burn from the four different binning methods (small points) and the mean of all four medians (large points) against (a) respective normalized median nvPM EI and (b) respective normalized total particle EIs.

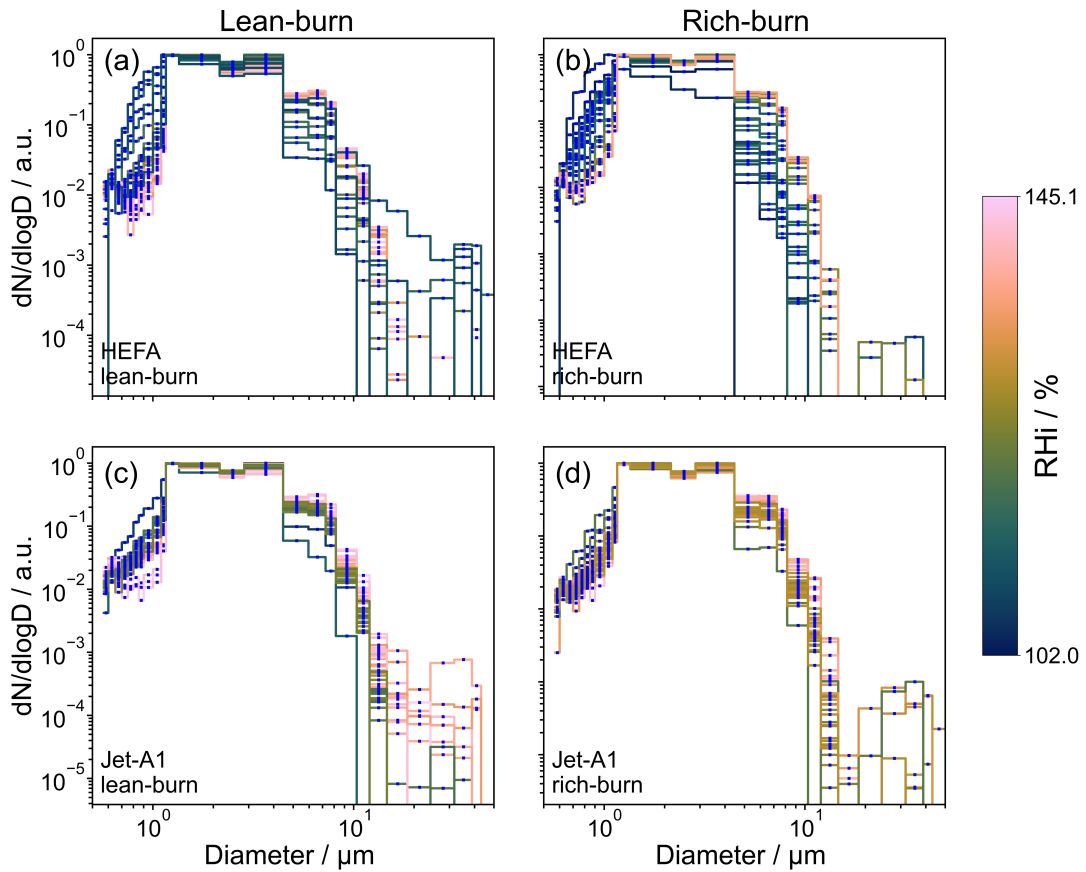


Figure A7: RH_i resolved PSDs of P-T domain 6.3 for HEFA (a) lean-burn and (b) rich-burn conditions and for Jet A-1 (c) lean-burn and (d) rich-burn conditions. Note: The scientific color map batlow (Crameri et al., 2020; Crameri, 2021) is used.

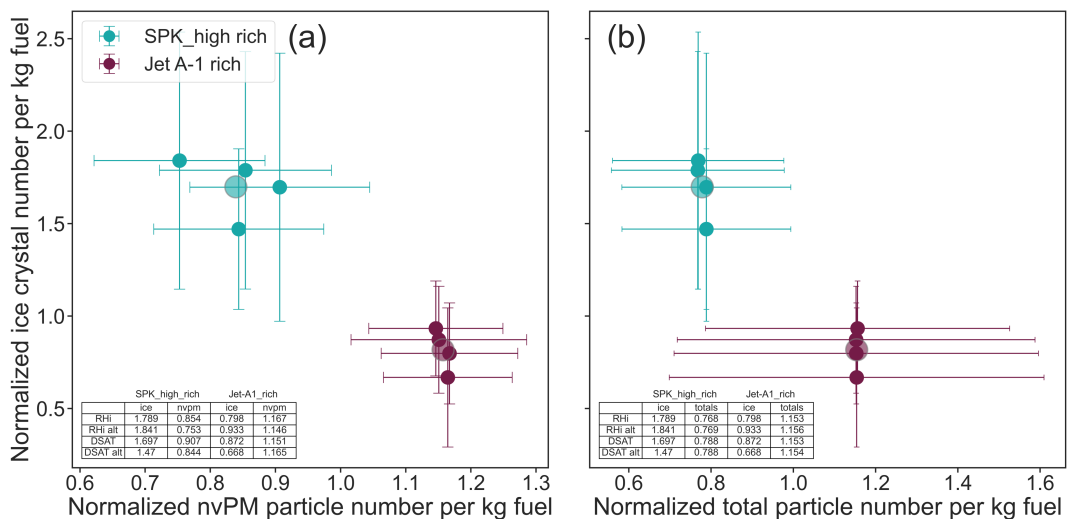


Figure A9: Median normalized AEI comparing domain 7.5 SPK High fuel rich-burn against Jet A-1 rich-burn from the four different binning methods (small) points and the mean of all four medians (large points) against (a) respective normalized median nvPM EI and (b) respective normalized total particle EIs.

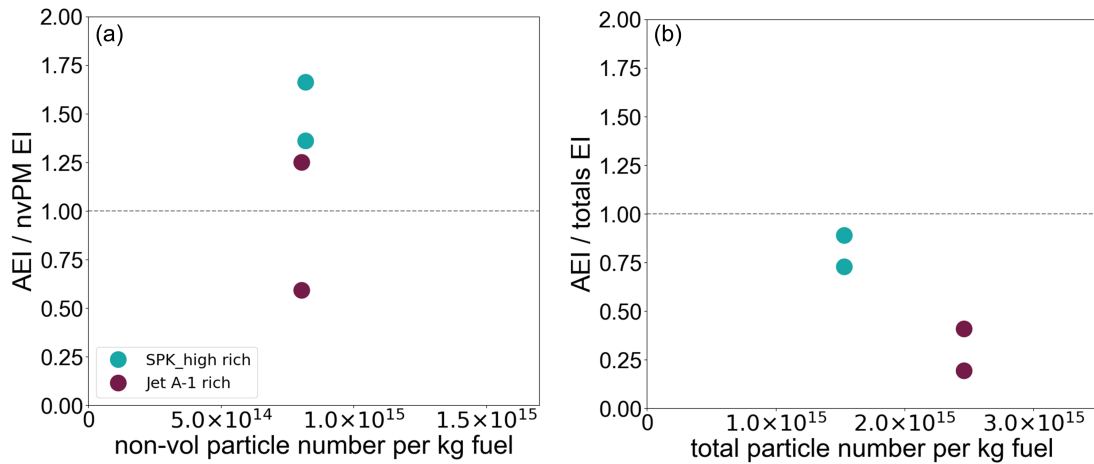


Figure A10: Far-field contrail AEI medians of ΔT_{SA} binning from P - T domain 7.5 versus near-field (a) nvPM EI and (b) total particle EIs. Note: far-field AEI and near-field aerosol EI were measured at different ambient conditions and engine parameters. These comparisons therefore only serve to qualitatively illustrate trends.

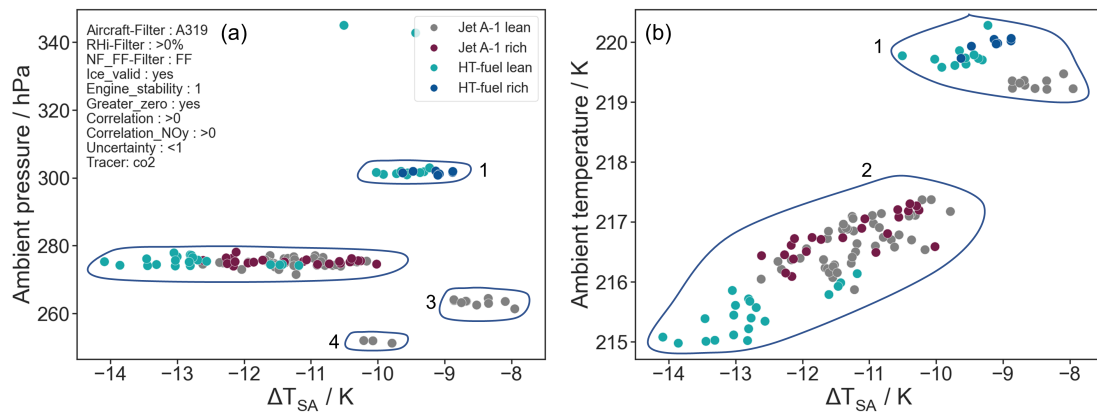


Figure A11: VOLCAN1 data from contrail encounters vs. ΔT_{SA} . Ambient conditions shown are (a) ambient pressure and (b) ambient temperature. Additionally, domains in the respective parameter space are marked and numbered.

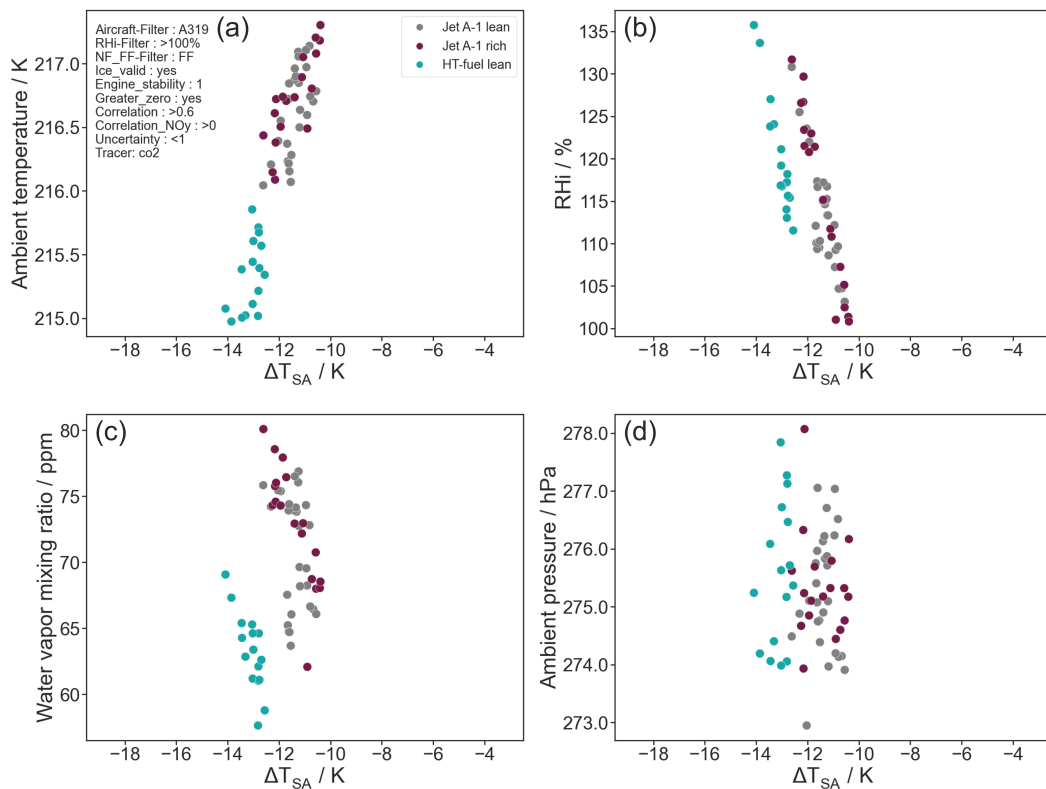


Figure A12: Ambient conditions of P - T domain 2.2 at time and point of contrail detection. (a) ambient temperature including applied filters, (b) relative humidity over ice, (c) water vapor mixing ratio, and (d) ambient pressure shown against ΔT_{SA} .

Contrail ice particle and aerosol numbers resolved by RHi and T_{SA}

The triangular and linear relationships shown in section 6.4 can also be illustrated by median AEI against median far-field nvPM EI for the forward-facing inlet as shown in Figure A13. Every median results from grouping the data in either 5 % RHi bins as shown in panels (a) and (b) or by 1 K ΔT_{SA} bins as shown in panels (c) and (d). The corresponding RHi or ΔT_{SA} bins are indicated by the continuous color gradient shown for each panel. For RHi binning, a general trend can be seen where low humidities are found at lower AEI and higher humidities at higher AEI. This trend is especially clear for rich-burn combustion in panel (b) where in addition to the vertical trend, a horizontal trend can be seen with higher humidities found more at higher nvPM EIs. The trends are more difficult to discern for ΔT_{SA} binning in panels (c) and (d) but it is clearer in panel (d). High and low ΔT_{SA} values are found at lower AEI and the highest AEI correspond to ΔT_{SA} values in the middle of the color bar range. This reflects the previously mentioned triangular relationship between AEI and ΔT_{SA} . nvPM EI on the other hand appear to show a linear trend depending on ΔT_{SA} with higher ΔT_{SA} values found for lower nvPM EI and lower ΔT_{SA} values corresponding to higher nvPM EI. These plots in principle are a different visualization of the linear trends for RHi dependence and triangular trends for ΔT_{SA} dependence shown in Figures 6.11 and 6.12 while

additionally putting ice emission indices in context with far-field nvPM EI. An additional collection of plots in this type of representation can be found in Figure A14 where AEI are shown against far-field total particle EI for all inlet types. There, the trends for AEI regarding RHi and ΔT_{SA} are very similar to those in Figure A13, differing only by the enhanced data set due to the use of both aerosol inlet configurations. The trends on the x-axis on the other hand are different for far-field nvPM and total particles. While a linear relationship between AEI and nvPM is seen for the RHi binning, no clear trend is visible for the total particles in this binning. For the ΔT_{SA} binning, a linear relationship is found between total particle EI and ΔT_{SA} which is inverse to that found for nvPM EI. High ΔT_{SA} are found for high total particle EI and low ΔT_{SA} for low total particle EI.

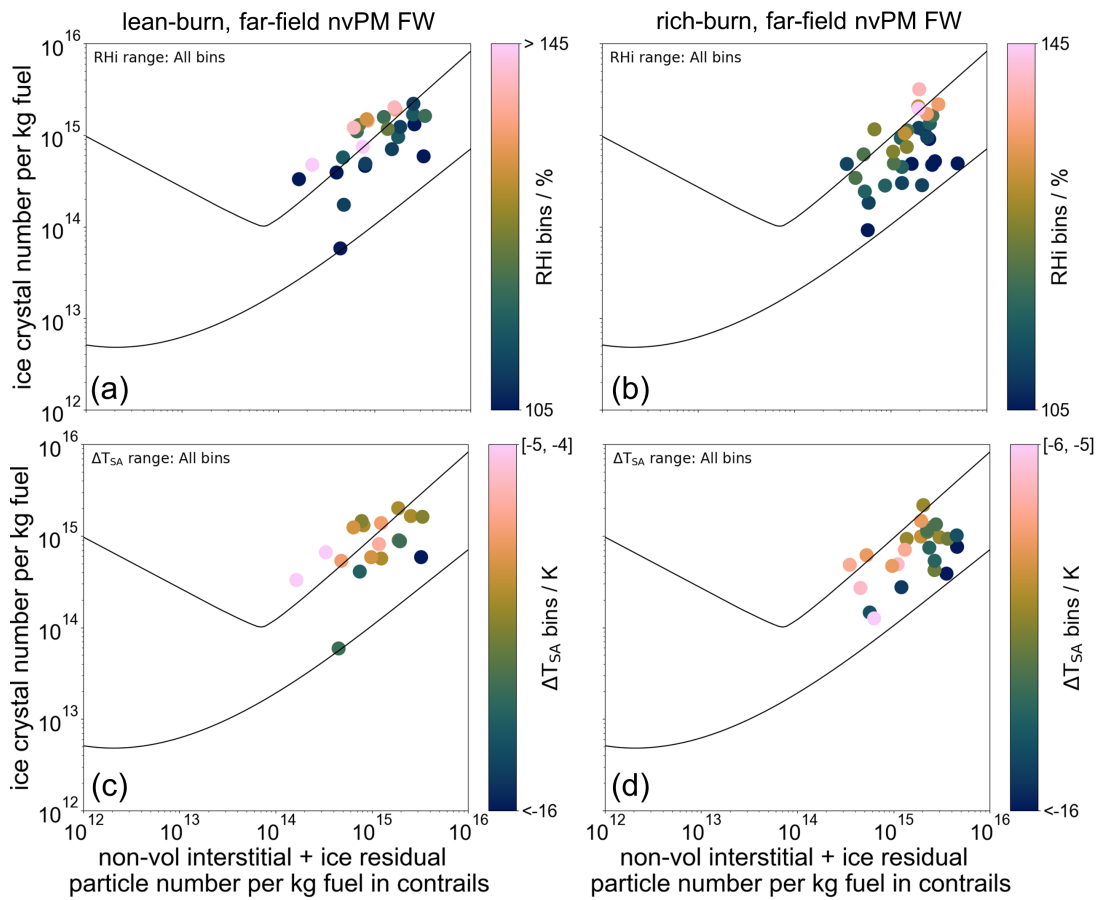


Figure A13: VOLCAN2 far-field median AEI (only FW inlet) shown against median nvPM EI of (a, b) RHi bins, and (c, d) ΔT_{SA} bins for (a, c) lean-burn combustion and (b, d) rich-burn combustion. Continuous lines represent the upper and lower expected AEI boundaries based on Kärcher (2018). Note: Some points of flight F21 with invalid water vapor measurements are not included in this figure. The scientific color map batlow (Crameri et al., 2020; Crameri, 2021) is used.

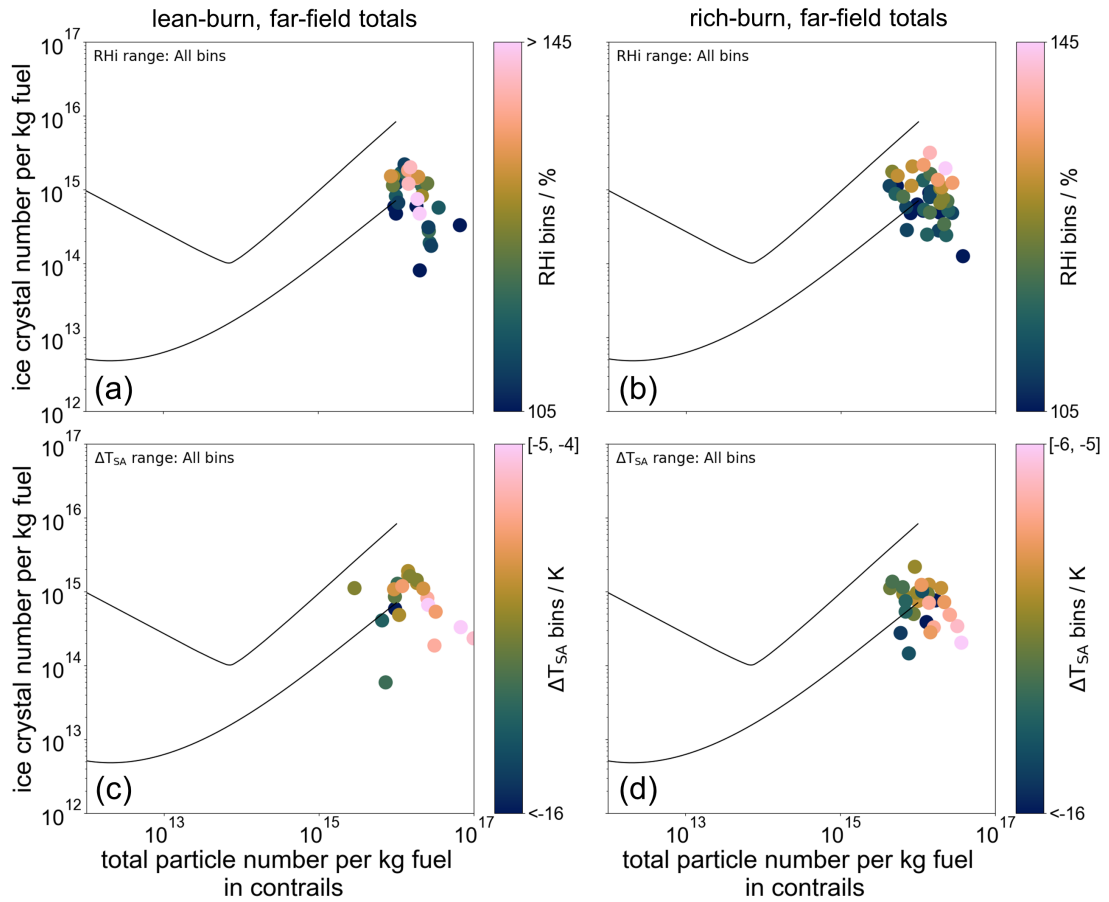


Figure A14: VOLCAN2 far-field median AEI shown against median total particle EI of (a, b) RHi bins, and (c, d) ΔT_{SA} bins for (a, c) lean-burn combustion and (b, d) rich-burn combustion. Continuous lines represent the upper and lower expected AEI boundaries based on Kärcher (2018) for nvPM and are shown here as guide to the eye. Note: Some points of flight F21 with invalid water vapor measurements are not included in this figure. The scientific color map batlow (Crameri et al., 2020; Crameri, 2021) is used.

Appendix B: Sensitivity of T_{SA} and ΔT_{SA} on ambient conditions

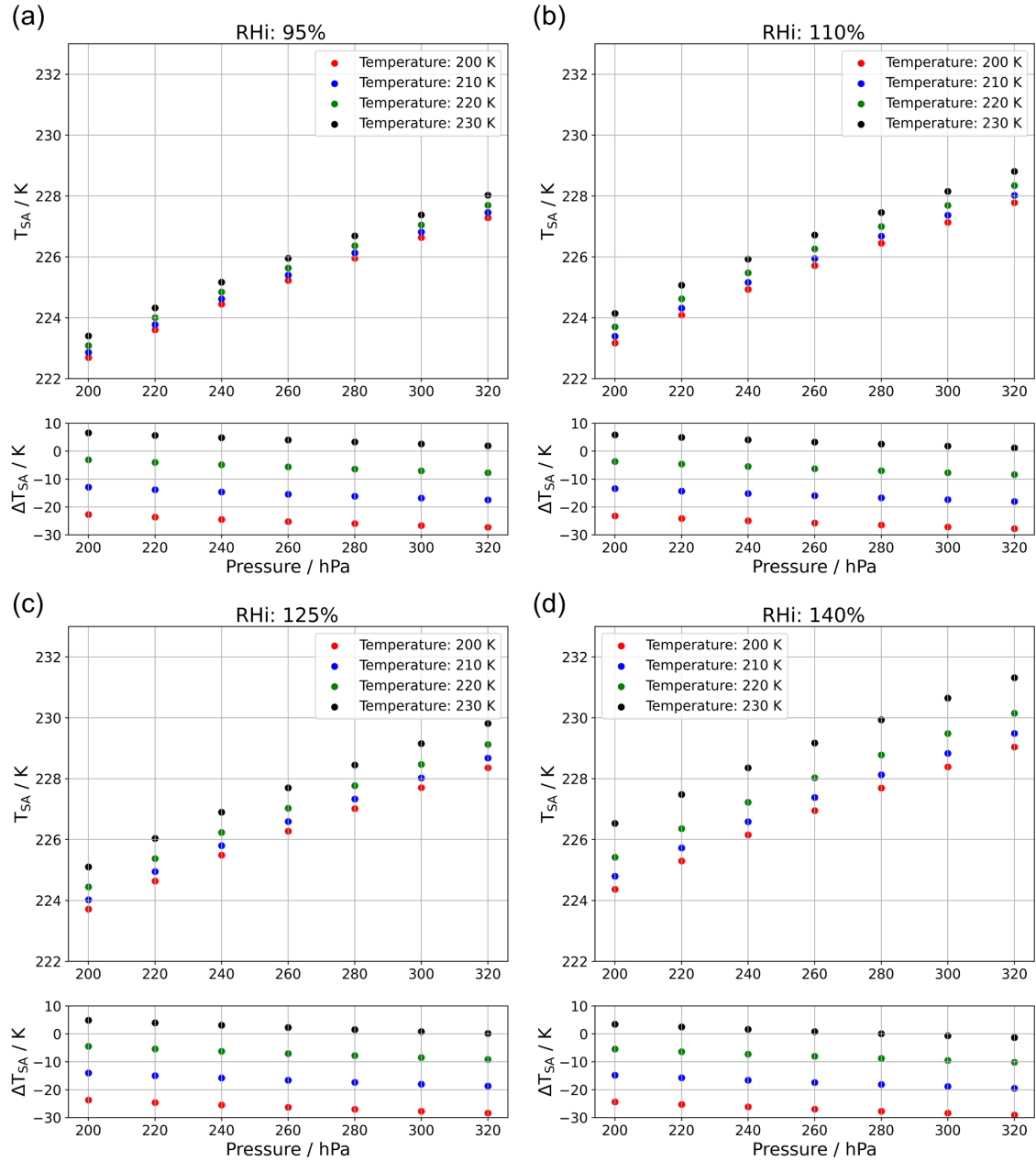


Figure B1: Overview of the sensitivity of T_{SA} and ΔT_{SA} on the ambient conditions temperature (200 K – 230 K), pressure (200 hPa – 320 hPa), and RH_i ((a) 95 %, (b) 110 %, (c) 125 %, (d) 140 %).

Figure B1 shows values of T_{SA} and $\Delta T_{SA} = (T_{amb, emission} - T_{SA})$, with $T_{amb, emission}$ being the ambient temperature at time of emission, for a variety of ambient temperatures, pressures and RH_i values typically encountered during in-flight measurements at cruise conditions. Every panel of the figure

shows values for one fixed RH_i value (a) 95 %, (b) 110 %, (c) 125 %, and 140 %, while the x-axis gives a range of ambient pressure values and four different ambient temperatures are color coded. The upper plot in every panel shows T_{SA} while the lower plot shows ΔT_{SA} . In all panels, it can be seen that T_{SA} increases with increasing pressure and temperature while the difference between T_{SA} values for one pressure value also increases with increasing temperature. When comparing the different panels, it can also be seen that higher values of RH_i lead to higher T_{SA} values with a larger spread. Therefore, the uncertainty of T_{SA} determination is highest for high humidity and high ambient temperature ($\pm \sim 2.5$ K) and lowest for low humidity and low temperature ($\pm \sim 0.5$ K) based on a temperature uncertainty of 0.5 K, a pressure uncertainty of 0.5 hPa, and RH_i uncertainty of 15 % (s. sections 3.5 and 3.4).

Appendix C: Additional information for instrumentation

CAS-DPOL gain stage voltage adjustment

The baseline voltage adjustment was conducted with the assistance of Jonas Schmidt (formerly DLR IPA) and a variation of Figure C1 has been shown by him in his master's thesis (Schmidt, 2023).

At the beginning of the VOLCAN2 campaign, many counts were observed in the gain stage overlap area between HGS and MGS as shown in panel (a) of Figure C1. There, the highest number of ADC counting effects falls within the gain stage overlap area with the peak being at over 300 counts (not shown). This was noticed at the beginning of the campaign and under remote supervision of the manufacturer DMT, the MGS baseline voltage was readjusted from 0.28 V to the correct value of 0.39 V. The reason for the wrongly adjusted baseline voltage at the beginning of the campaign is not known and can result from simple aging of the instrument and its electronics or from physical impacts to the probe during transport or in-flight operation. After this adjustment, the number of counts in the gain stage overlap area was strongly reduced as can be seen in panel (b). Instead, the ratios of the peak heights has shifted such that the main peak of the 4.6 μm calibration beads is also the highest and the size allocation has been corrected. One contrail measurement flight was conducted with the baseline voltage of 0.28 V (28. Feb. 2023) which however was not used for any of the combustion mode or fuel comparisons discussed in chapter 6.

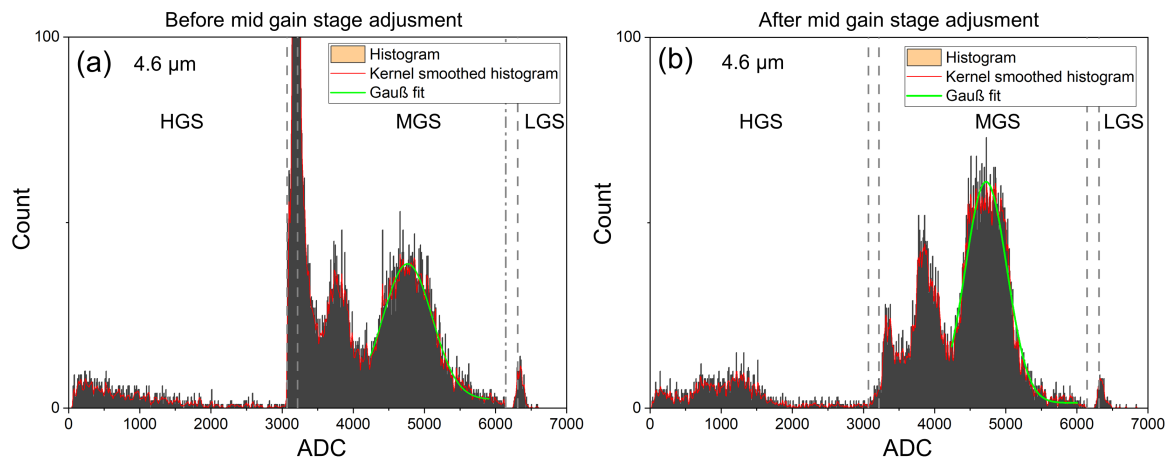


Figure C1: Histogram over 4.6 μm calibration bead measurements with red kernel smoothed function and green Gauss fits over the main peak. (a) Calibration measurements conducted before the VOLCAN2 campaign with a mid gain baseline voltage of 0.28 V. (b) Calibration measurements conducted after the VOLCAN2 campaign during which the mid gain stage baseline voltage was set to 0.39 V.

CAS-DPOL binning

Table C1: Size binnings of the CAS-DPOL probe during the different campaigns for volume equivalent diameters of ice particles with aspect ratio of 0.75. Note that bins with a width of (near) zero are defined for the gain stage overlaps (bins 11 and 21) for ECLIF3 Q4 / VOLCAN1 and VOLCAN2 and only for the second gain stage overlap (bins 21 and 22) for ECLIF3 Q2. Note: VOLCAN2 binning has been shown by Jonas Schmidt (formerly DLR IPA) in his master's thesis (Schmidt, 2023).

Bin	ECLIF3 Q2		ECLIF3 Q4 / VOLCAN1		VOLCAN2	
	D_{\max} / μm	ADC	D_{\max} / μm	ADC	D_{\max} / μm	ADC
min	0.66	60	0.61	50	0.57	30
1	0.74	218	0.70	198	0.6	46
2	0.76	298	0.74	316	0.65	109
3	0.79	384	0.80	482	0.7	196
4	0.82	518	0.85	690	0.75	311
5	0.87	710	0.89	928	0.8	453
6	0.92	971	0.94	1231	0.85	651
7	0.97	1315	1.00	1617	0.9	885
8	1.04	1811	1.05	2022	1	1515
9	1.13	2425	1.09	2448	1.1	2353
10	1.19	3072	1.17	3071	1.16	3071
11	1.29	3319	1.17	3158	1.16	3218
12	1.85	3654	1.42	3308	1.35	3351
13	2.51	3992	1.61	3413	2.15	3527
14	3.52	4414	1.69	3458	2.85	3643
15	4.46	4751	1.98	3608	3.1	4114
16	5.43	5073	2.75	3954	4.45	4565
17	6.17	5328	4.30	4502	5.95	5013
18	6.87	5584	6.57	5218	7.25	5450
19	7.67	5916	8.16	5838	8.15	5811
20	8.16	6144	8.81	6144	8.86	6144
21	8.15	6299	8.82	6308	8.86	6312
22	8.16	6327	11.00	6385	10.35	6360
23	9.79	6389	13.33	6500	12	6430
24	11.72	6476	15.00	6604	14.65	6578
25	13.68	6592	16.48	6707	18.5	6853
26	17.30	6868	18.97	6895	24.1	7156
27	22.38	7211	27.33	7412	31.7	7796
28	27.33	7588	31.58	7801	38.8	8530
29	34.79	8408	36.89	8325	43.1	9038
30	40.96	9216	43.81	9216	50	9948

CAPS-DPOL binning

Table C2: Size binnings of the CAPS-DPOL probe during the different campaigns for volume equivalent diameters of ice particles with aspect ratio of 0.75. The original ADC bins are shown, which were then modified for ECLIF3 / VOLCAN1 to increase size resolution. ADC values for VOLCAN2 were obtained from the described calibration.

Bin	Original DMT	ECLIF3 / VOLCAN1		VOLCAN2	
	ADC	D_{\max} / μm	ADC	D_{\max} / μm	ADC
min	83	0.51	83	0.5	83
1	227	0.61	227	0.6	362
2	523	0.71	523	0.7	576
3	1063	0.81	1063	0.8	944
4	1862	0.91	1862	0.9	1564
5	3112	1.01	3112	1	2465
6	4503	1.1	4503	1.1	3665
7	16555	1.45	14334	1.35	7774
8	16910	1.62	16384	2.15	11873
9	17187	2.45	16555	2.85	14571
10	17336	5.08	16600	3.1	16819
11	17433	6.2	16910	4.45	16916
12	17578	7.3	17187	5.95	17012
13	17832	9.39	17336	7.25	17106
14	18514	10.67	17433	8.15	17184
15	18943	10.71	17578	8.95	17263
16	19400	14.69	17832	10.35	17434
17	20005	15.61	18514	12	17696
18	20314	15.95	18943	13.8	18052
19	21039	17.25	19400	14.65	18246
20	21660	21.33	20005	16.8	18796
21	22343	22.93	20314	18.5	19271
22	23281	26.77	21660	22.2	19907
23	23938	29.25	22343	24.1	20405
24	24510	31.33	23281	27.4	21383
25	25708	34.53	23938	31.7	22792
26	26580	37.58	25708	34.7	23904
27	27615	39.62	26580	38.8	25532
28	28817	42.68	27615	43.1	27427
29	29333	44.92	28817	45.9	28747
30	30689	49.1	30689	50	30821

To improve data recording resolution, several additional size bins were added in the size areas of interest and bins removed in larger areas of lesser interest. The original ADC bins are shown in Table C2 without allocated ice particle sizes. This original binning was used in the first ECLIF3 measurement flight which however was not used for any comparisons. In preparation of the VOLCAN2 campaign, a first own calibration was performed after discussing data processing with DMT and after several attempts and iterations of working with CAPS-DPOL pbp data. Following this calibration, an AR 0.75 aspherical ice particle allocation was directly set and used during the VOLCAN2 campaign. In an attempt to isolate the CAPS-DPOL's "dead zone" and to be able to process the high gain stage and low gain stage separately in the bulk file, a bin with upper threshold of 16383 ADC, the highest high gain stage ADC value, was tentatively set in the measurement flight on 25. Feb. 2023. This however led to no data being recorded in the low gain stage and the binning was switched to the originally calibrated size binning.

Processing of PSDs

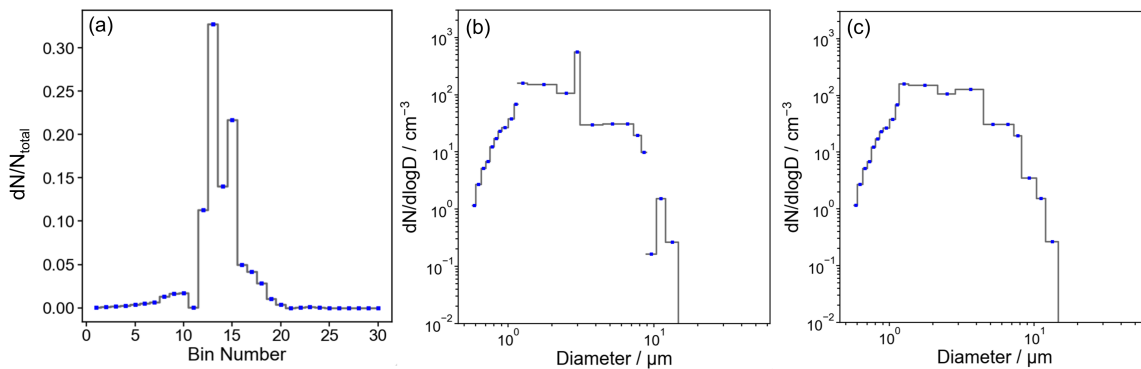


Figure C2: Particle size distribution for one contrail encounter (VOLCAN2 flight F16 13:05:15-13:05:36 UTC) with (a) originally recorded binning and (b) modified binning where bins 11 and 21 are removed and bins 15 and 16 and bins 20 and 22 are combined respectively.

The effect of the normalization by the difference of logarithmic bin boundaries can be nicely seen in Figure C2. Panel (a) shows the particle size distribution represented by the concentrations in every bin as a share of the total measured concentration during the chosen time sequence for each of the 30 bins on linear scales. It can be seen that most of the contrail ice particles were measured in bins 12-15. The gain stage overlap bins in this case are bins 11 and 21 with an allocated width of 0 μm (s. Table C1). Only very few counts fall into these bins, which also shows in the size distribution. Panel (b) shows the same size distribution as $(dN/d \log D)$ for all 30 bins in a double-logarithmic representation. A gap is found for bins 11 and 21 due to their width of zero. Due to Mie ambiguities and instrument uncertainties, it is possible that more particles are counted within a bin than would be expected from its nominal size width. In the shown example, bin 15 has a small width but a very high number of counts. Here, the set bin resolution was higher than can be reliably measured by the instrument. Therefore, bins 15 and 16 are combined which was also done

for bins 20 and 22 across the second gap. This reduction of apparent resolution leads to smoothed size distributions and a more conservative view regarding the instrument's size resolution. The result of this processing can be found in panel (c) where the gain stage overlap bins 11 and 21 have also been removed completely. This bin processing was done for all PSDs of VOLCAN2, while for ECLIF3, bins 21 and 22 were removed and no bins merged due to only the second gain stage overlap being isolated.

Agreement between CAS-DPOL and CAPS-DPOL during VOLCAN2

Three examples of the different levels of agreement during VOLCAN2 between CAS-DPOL and CAPS-DPOL are found in Figure C3. During flight F19 in panel (a), the CAS-DPOL measured several times higher number concentrations compared to the CAPS-DPOL. This behavior was found during three of the nine contrail flights. Panel (b) shows good agreement between CAS-DPOL and CAPS-DPOL, which was also found for flight F02 and parts of F16. Finally, during flight F17 in panel (c), the mentioned strong overcounting of the CAPS-DPOL in its first bin becomes apparent. In light of all the described issues of the CAPS-DPOL during the VOLCAN2 campaign, it was decided to only use CAS-DPOL data for further scientific evaluation as there was no apparent reason to mistrust CAS-DPOL particle number concentration data.

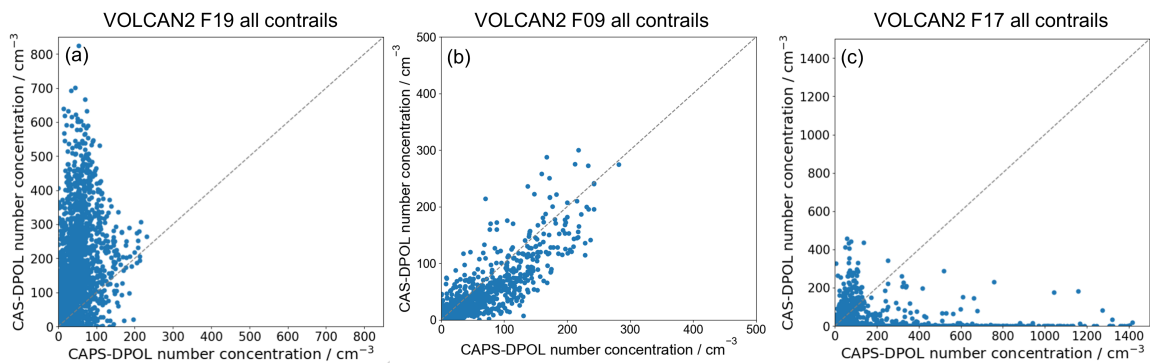


Figure C3: 1 Hz CAS-DPOL vs. CAPS-DPOL number concentrations during the respective VOLCAN2 contrail measurement sequences in (a) flight F19, (b) flight F09, and (c) flight F17. Note: F09 CAPS data was shifted by 1 s to match CAS-DPOL data for this figure.

Bibliography

- Afchine, A., C. Rolf, A. Costa, N. Spelten, M. Riese, B. Buchholz, V. Ebert, R. Heller, S. Kaufmann, A. Minikin, C. Voigt, M. Zöger, J. Smith, P. Lawson, A. Lykov, S. Khaykin, and M. Krämer (2018). “Ice particle sampling from aircraft – influence of the probing position on the ice water content”. In: *Atmospheric Measurement Techniques* 11.7, pp. 4015–4031. DOI: 10.5194/amt-11-4015-2018.
- Airbus (Nov. 2023). *Contrail-chasing Blue Condor makes Airbus’ first full hydrogen-powered flight*. Last accessed: Sept. 05, 2024. URL: <https://www.airbus.com/en/newsroom/stories/2023-11-contrail-chasing-blue-condor-makes-airbus-first-full-hydrogen-powered>.
- Airel OÜ (Aug. 2024). *Cluster Ion Counter (CIC), Model: 201.2*. Last accessed: Sept. 05, 2024. URL: <https://www.arel.ee/products/cic/cic-brochure.pdf>.
- Apostolidis, A. and K. P. Stamoulis (2021). “A Health Monitoring Modelling Case Study: Humidity Effects on Engine Deterioration Prediction”. In: *MATEC Web of Conferences* 349. Ed. by S. Pantelakis, G. Lampeas, and K. Tserpes, p. 03011. ISSN: 2261-236X. DOI: 10.1051/mateconf/202134903011.
- Appleman, H. (Jan. 1953). “The Formation of Exhaust Condensation Trails by Jet Aircraft”. In: *Bulletin of the American Meteorological Society* 34.1, pp. 14–20. DOI: 10.1175/1520-0477-34.1.14.
- Arnold, F., J. Curtius, B. Sierau, V. Bürger, R. Busen, and U. Schumann (June 1999). “Detection of massive negative chemiions in the exhaust plume of a jet aircraft in flight”. In: *Geophys. Res. Lett.* 26.11, pp. 1577–1580. ISSN: 1944-8007. DOI: 10.1029/1999GL900304.
- ASTM (Apr. 2024a). *ASTM Standard D1655-24: Standard Specification for Aviation Turbine Fuels*. Tech. rep. ASTM International. DOI: 10.1520/D1655-24.
- (Apr. 2024b). *ASTM Standard D7566-24a: Standard Specification for Aviation Turbine Fuel Containing Synthesized Hydrocarbons*. Tech. rep. ASTM International. DOI: 10.1520/d7566-24a.
- Baumgardner, D., S. J. Abel, D. Axisa, R. Cotton, J. Crosier, P. Field, C. Gurganus, A. Heymsfield, A. Korolev, M. Krämer, P. Lawson, G. McFarquhar, Z. Ulanowski, and J. Um (Jan. 2017). “Cloud Ice Properties: In Situ Measurement Challenges”. In: *Meteorological Monographs* 58, pp. 9.1–9.23. ISSN: 0065-9401. DOI: 10.1175/AMSMONOGRAPHS-D-16-0011.1.
- Baumgardner, D, H Jonsson, W Dawson, D O'Connor, and R Newton (2001). “The cloud, aerosol and precipitation spectrometer: a new instrument for cloud investigations”. In: *Atmospheric Research* 59-60, pp. 251–264. DOI: 10.1016/S0169-8095(01)00119-3.
- Baumgardner, D. (June 1986). “A New Technique for the Study of Cloud Microstructure”. In: *Journal of Atmospheric and Oceanic Technology* 3.2, pp. 340–343. ISSN: 1520-0426. DOI: 10.1175/1520-0426(1986)003<0340:ANTFTS>2.0.CO;2.
- Baumgardner, D. and B. E. Gandrud (Apr. 1998). “A comparison of the microphysical and optical properties of particles in an aircraft contrail and mountain wave cloud”. In: *Geophysical Research Letters* 25.8, pp. 1129–1132. ISSN: 1944-8007. DOI: 10.1029/98gl00035.

- Becken, S., B. Mackey, and D. S. Lee (Aug. 2023). “Implications of preferential access to land and clean energy for Sustainable Aviation Fuels”. In: *Science of the Total Environment* 886, p. 163883. ISSN: 0048-9697. DOI: 10.1016/j.scitotenv.2023.163883.
- Benjah-bmm27 (username) (Oct. 2006). *Dodecane-3D-balls.png*. Last accessed: 23 Nov. 2024. Wikimedia Commons. URL: <https://commons.wikimedia.org/wiki/File:Dodecane-3D-balls.png>.
- (May 2007). *Benzene-aromatic-3D-balls.png*. Last accessed: 23 Nov. 2024. Wikimedia Commons. URL: <https://commons.wikimedia.org/wiki/File:Benzene-aromatic-3D-balls.png>.
- (Mar. 2009). *Naphthalene-from-xtal-3D-balls.png*. Last accessed: 23 Nov. 2024. Wikimedia Commons. URL: <https://commons.wikimedia.org/wiki/File:Naphthalene-from-xtal-3D-balls.png>.
- Bergthorson, J. M. and M. J. Thomson (Feb. 2015). “A review of the combustion and emissions properties of advanced transportation biofuels and their impact on existing and future engines”. In: *Renewable Sustainable Energy Rev* 42, pp. 1393–1417. ISSN: 1364-0321. DOI: 10.1016/j.rser.2014.10.034.
- Beyersdorf, A. J., M. T. Timko, L. D. Ziemba, D. Bulzan, E. Corporan, S. C. Herndon, R. Howard, R. Miake-Lye, K. L. Thornhill, E. Winstead, C. Wey, Z. Yu, and B. E. Anderson (2014). “Reductions in aircraft particulate emissions due to the use of Fischer–Tropsch fuels”. In: *Atmospheric Chemistry and Physics* 14.1, pp. 11–23. DOI: 10.5194/acp-14-11-2014.
- Bier, A. and U. Burkhardt (2019). “Variability in Contrail Ice Nucleation and Its Dependence on Soot Number Emissions”. In: *Journal of Geophysical Research: Atmospheres* 124.6, pp. 3384–3400. DOI: 10.1029/2018JD029155.
- Bier, A., U. Burkhardt, and L. Bock (2017). “Synoptic Control of Contrail Cirrus Life Cycles and Their Modification Due to Reduced Soot Number Emissions”. In: *J. Geophys. Res. Atmos.* 122.21, pp. 11,584–11,603. DOI: 10.1002/2017JD027011.
- Bier, A., S. Unterstrasser, and X. Vancassel (2022). “Box model trajectory studies of contrail formation using a particle-based cloud microphysics scheme”. In: *Atmospheric Chemistry and Physics* 22.2, pp. 823–845. DOI: 10.5194/acp-22-823-2022.
- Bier, A., S. Unterstrasser, J. Zink, D. Hillenbrand, T. Jurkat-Witschas, and A. Lottermoser (Feb. 2024). “Contrail formation on ambient aerosol particles for aircraft with hydrogen combustion: a box model trajectory study”. In: *Atmospheric Chemistry and Physics* 24.4, pp. 2319–2344. ISSN: 1680-7324. DOI: 10.5194/acp-24-2319-2024.
- Blakey, S., L. Rye, and C. W. Wilson (2011). “Aviation gas turbine alternative fuels: A review”. In: *Proceedings of the Combustion Institute* 33.2, pp. 2863–2885. ISSN: 1540-7489. DOI: 10.1016/j.proci.2010.09.011.
- BMDV and BMWK (May 2024). *Ergebnisse des Arbeitskreises klimaneutrale Luftfahrt - Zentrale Handlungsfelder auf dem Weg zu einem umwelt- und klimaschonenden Luftverkehrssystem der Zukunft*. Tech. rep. Last accessed: Sept. 05, 2024. Bundesministerium für Digitales und Verkehr, Bundesministerium für Wirtschaft und Klimaschutz.
- Bock, L. and U. Burkhardt (2016). “The temporal evolution of a long-lived contrail cirrus cluster: Simulations with a global climate model”. In: *Journal of Geophysical Research: Atmospheres* 121.7, pp. 3548–3565. DOI: 10.1002/2015JD024475.

- (2019). “Contrail cirrus radiative forcing for future air traffic”. In: *Atmospheric Chemistry and Physics* 19.12, pp. 8163–8174. DOI: 10.5194/acp-19-8163-2019.
- Bohren, C. F. and D. R. Huffman (Apr. 1998a). “Absorption and Scattering by an Arbitrary Particle”. In: *Absorption and Scattering of Light by Small Particles*. Wiley. Chap. 3, pp. 57–81. ISBN: 9780471293408. DOI: 10.1002/9783527618156.ch3.
- (Apr. 1998b). “Geometrical Optics”. In: *Absorption and Scattering of Light by Small Particles*. Wiley. Chap. 7, pp. 166–180. ISBN: 9780471293408. DOI: 10.1002/9783527618156.ch7.
- Borrmann, S., B. Luo, and M. Mishchenko (2000). “Application of the T-matrix method to the measurement of aspherical (ellipsoidal) particles with forward scattering optical particle counters”. In: *Journal of Aerosol Science* 31.7, pp. 789–799. DOI: 10.1016/S0021-8502(99)00563-7.
- Boshell, F., S. Kang, R. Gorini, and M. A. Kadir (2022). “The role of renewables in decarbonising the aviation sector”. In: *Innovation for a green transition, 2022 environmental report*. ICAO, pp. 187–190.
- Brem, B. T., L. Durdina, F. Siegerist, P. Beyerle, K. Bruderer, T. Rindlisbacher, S. Rocci-Denis, M. G. Andac, J. Zelina, O. Penanhoat, and J. Wang (2015). “Effects of Fuel Aromatic Content on Non-volatile Particulate Emissions of an In-Production Aircraft Gas Turbine”. In: *Environmental Science and Technology* 49.22, pp. 13149–13157. DOI: 10.1021/acs.est.5b04167.
- Bräuer, T., C. Voigt, D. Sauer, S. Kaufmann, V. Hahn, M. Scheibe, H. Schlager, G. S. Diskin, J. B. Nowak, J. P. DiGangi, F. Huber, R. H. Moore, and B. E. Anderson (2021a). “Airborne Measurements of Contrail Ice Properties—Dependence on Temperature and Humidity”. In: *Geophysical Research Letters* 48.8. DOI: 10.1029/2020GL092166.
- Bräuer, T., R. Märkl, M. Scheibe, D. Sauer, R. Dischl, C. Heckl, H. Aufmhoff, L. Stremming, C. Voigt, J. Digangi, G. Diskin, S. Baughcum, W. Griffin, T. Rahmes, C. Miller, and R. Moore (Mar. 2024). “In-flight Measurements of Contrails in the Low Soot Regime during the ecoDemonstrator Experiment”. In: *EGU General Assembly 2024, Vienna, Austria, 14-19 Apr 2024, EGU24-10277*. DOI: 10.5194/egusphere-egu24-10277.
- Bräuer, T., C. Voigt, D. Sauer, S. Kaufmann, V. Hahn, M. Scheibe, H. Schlager, F. Huber, P. L. Clercq, R. H. Moore, and B. E. Anderson (2021b). “Reduced ice number concentrations in contrails from low-aromatic biofuel blends”. In: *Atmospheric Chemistry and Physics* 21.22, pp. 16817–16826. DOI: 10.5194/acp-21-16817-2021.
- Burkhardt, U., L. Bock, and A. Bier (2018). “Mitigating the contrail cirrus climate impact by reducing aircraft soot number emissions”. In: *npj Climate and Atmospheric Science* 1.37. DOI: 10.1038/s41612-018-0046-4.
- Burkhardt, U. and B. Kärcher (2011). “Global radiative forcing from contrail cirrus”. In: *Nature Climate Change* 1.1, pp. 54–58. DOI: 10.1038/nclimate1068.
- Busen, R. and U. Schumann (June 1995). “Visible contrail formation from fuels with different sulfur contents”. In: *Geophysical Research Letters* 22.11, pp. 1357–1360. ISSN: 1944-8007. DOI: 10.1029/95GL01312.

- Bögel, W. and R. Baumann (1991). “Test and Calibration of the DLR Falcon Wind Measuring System by Maneuvers”. In: *Journal of Atmospheric and Oceanic Technology* 8.1, pp. 5–18. DOI: 10.1175/1520-0426(1991)008<0005:TACOTD>2.0.CO;2.
- Cain, J., M. J. DeWitt, D. Blunck, E. Corporan, R. Striebich, D. Anneken, C. Klingshirn, W. M. Roquemore, and R. V. Wal (2013). “Characterization of Gaseous and Particulate Emissions From a Turbo-shaft Engine Burning Conventional, Alternative, and Surrogate Fuels”. In: *Energy Fuels* 27.4, pp. 2290–2302. DOI: 10.1021/ef400009c.
- Chauvigné, A., O. Jourdan, A. Schwarzenboeck, C. Goubeyre, J. F. Gayet, C. Voigt, H. Schlager, S. Kaufmann, S. Borrmann, S. Molleker, A. Minikin, T. Jurkat, and U. Schumann (2018). “Statistical analysis of contrail to cirrus evolution during the Contrail and Cirrus Experiment (CONCERT)”. In: *Atmospheric Chemistry and Physics* 18.13, pp. 9803–9822. DOI: 10.5194/acp-18-9803-2018.
- Chen, C.-C. and A. Gettelman (Dec. 2013). “Simulated radiative forcing from contrails and contrail cirrus”. In: *Atmospheric Chemistry and Physics* 13.24, pp. 12525–12536. ISSN: 1680-7324. DOI: 10.5194/acp-13-12525-2013.
- Chen, T., W. B. Rossow, and Y. Zhang (Jan. 2000). “Radiative Effects of Cloud-Type Variations”. In: *Journal of Climate* 13.1, pp. 264–286. ISSN: 1520-0442. DOI: 10.1175/1520-0442(2000)013<0264:REOCTV>2.0.CO;2.
- Chevron Products Company (2007). *Aviation Fuels Technical Review*. Tech. rep. Last accessed: Sept. 03, 2024. URL: <https://www.chevron.com/-/media/chevron/operations/documents/aviation-tech-review.pdf>.
- Chin, J. S. and A. H. Lefebvre (1990). “Influence of Fuel Chemical Properties on Soot Emissions from Gas Turbine Combustors”. In: *Combustion Science and Technology* 73.1-3, pp. 479–486. DOI: 10.1080/00102209008951664.
- Chuang, P. Y., E. W. Saw, J. D. Small, R. A. Shaw, C. M. Sipperley, G. A. Payne, and W. D. Bachalo (June 2008). “Airborne Phase Doppler Interferometry for Cloud Microphysical Measurements”. In: *Aerosol Science and Technology* 42.8, pp. 685–703. ISSN: 1521-7388. DOI: 10.1080/02786820802232956.
- Crameri, F. (2021). *Scientific colour maps (7.0.1)*. en. DOI: 10.5281/zenodo.5501399.
- Crameri, F., G. E. Shephard, and P. J. Heron (2020). “The misuse of colour in science communication”. In: *Nature Communications* 11.5444. DOI: 10.1038/s41467-020-19160-7.
- Cross, E. S., J. F. Hunter, A. J. Carrasquillo, J. P. Franklin, S. C. Herndon, J. T. Jayne, D. R. Worsnop, R. C. Miake-Lye, and J. H. Kroll (Aug. 2013). “Online measurements of the emissions of intermediate-volatility and semi-volatile organic compounds from aircraft”. In: *Atmospheric Chemistry and Physics* 13.15, pp. 7845–7858. ISSN: 1680-7324. DOI: 10.5194/acp-13-7845-2013.
- Crow, S. C. (Dec. 1970). “Stability theory for a pair of trailing vortices”. In: *AIAA Journal* 8.12, pp. 2172–2179. ISSN: 1533-385X. DOI: 10.2514/3.6083.
- Csonka, S., K. C. Lewis, and M. Rumizen (2022). “New Sustainable Aviation Fuels (SAF) technology pathways under development”. In: *Innovation for a green transition, 2022 environmental report*. ICAO. Chap. Chapter seven: Climate Change Mitigation: Sustainable Aviation Fuels, pp. 195–198.

- Czyrnek-Delêtre, M. M., A. Chiodi, J. D. Murphy, and B. P. Ó Gallachóir (Mar. 2016). “Impact of including land-use change emissions from biofuels on meeting GHG emissions reduction targets: the example of Ireland”. In: *Clean Technologies and Environmental Policy* 18.6, pp. 1745–1758. ISSN: 1618-9558. DOI: 10.1007/s10098-016-1145-8.
- Dischl, R., S. Kaufmann, and C. Voigt (2022). “Regional and Seasonal Dependence of the Potential Contrail Cover and the Potential Contrail Cirrus Cover over Europe”. In: *Aerospace* 9.9, p. 485. DOI: 10.3390/aerospace9090485.
- Dischl, R., D. Sauer, C. Voigt, T. Harlaß, F. Sakellariou, R. Märkl, U. Schumann, M. Scheibe, S. Kaufmann, A. Roiger, A. Dörnbrack, C. Renard, M. Gauthier, P. Swann, P. Madden, D. Luff, M. Johnson, D. Ahrens, R. Sallinen, T. Schripp, G. Eckel, U. Bauder, and P. Le Clercq (Oct. 2024). “Measurements of particle emissions of an A350-941 burning 100 % sustainable aviation fuels in cruise”. In: *Atmospheric Chemistry and Physics* 24.19, pp. 11255–11273. ISSN: 1680-7324. DOI: 10.5194/acp-24-11255-2024.
- Divine, G. W., H. J. Norton, A. E. Barón, and E. Juárez-Colunga (Mar. 2018). “The Wilcoxon–Mann–Whitney Procedure Fails as a Test of Medians”. In: *The American Statistician* 72.3, pp. 278–286. ISSN: 1537-2731. DOI: 10.1080/00031305.2017.1305291.
- DLR (Oct. 2024). *Climate-compatible aviation: flying lab measures emissions from turboprop using 100 percent synthetic fuel for first time*. Last accessed: 03. November 2024. URL: <https://www.dlr.de/en/latest/news/2024/climate-compatible-aviation-flying-lab-measures-emissions-from-turboprop-using-100-percent-synthetic-fuel-for-first-time>.
- DMT (2011). *Particle Analysis and Display System (PADS) 3.6.3 Overview Manual*. DOC-0300, Rev C-3. Droplet Measurement Technologies. 2400 Trade Centre Avenue Longmont, CO 80503 USA.
- (2018). *Cloud Aerosol Spectrometer Depolarization Option (CAS-DPOL) Operator Manual DOC-0167 Revision E-3*. Droplet Measurement Technologies. 2400 Trade Centre Avenue Longmont, CO 80503 USA.
- EASA (2019). *Type-Certificate Data Sheet No. EASA E.111 for Engine Trent XWB series engines*. Tech. rep. 12.
- (2023). *European aviation environmental report 2022*. Tech. rep. DOI: 10.2822/04357.
- EIA (July 2012). *Crude oils have different quality characteristics*. Last accessed: August 07, 2024. URL: <https://www.eia.gov/todayinenergy/detail.php?id=7110>.
- Epstein, A. H. (2014). “Aeropropulsion for Commercial Aviation in the Twenty-First Century and Research Directions Needed”. In: *AIAA J.* 52.5, pp. 901–911. DOI: 10.2514/1.J052713.
- Eyring, V., N. P. Gillett, K. M. A. Rao, R. Barimalala, M. B. Parillo, N. Bellouin, C. Cassou, P. J. Durack, Y. Kosaka, S. McGregor, S.-K. Min, O. Morgenstern, and Y. Sun (July 2021). “Human Influence on the Climate System”. In: *In Climate Change 2021: The Physical Science Basis. Contribution of Working Group I to the Sixth Assessment Report of the Intergovernmental Panel on Climate Change*. Ed. by V. Masson-Delmotte, P. Zhai, A. Pirani, S. L. Connors, C. Péan, S. Berger, N. Caud, Y. Chen, L. Goldfarb, M. I. Gomis, M. Huang, K. Leitzell, E. Lonnoy, J. R. Matthews, T. K. Maycock, T. Waterfield, O. Yelekçi, R. Yu, and B. Zhou. Cambridge, United Kingdom and New York, NY, USA: Cambridge University Press, pp. 423–552. ISBN: 9781009157896. DOI: 10.1017/9781009157896.005.

- Faber, J., J. Király, D. Lee, B. Owen, and A. O’Leary (Feb. 2022). *Potential for reducing aviation non-CO₂ emissions through cleaner jet fuel*. Tech. rep. Last accessed: Sept. 03, 2024. CE Delft. URL: https://cedelft.eu/wp-content/uploads/sites/2/2022/03/CE_Delft_210410_Potential_reducing_aviation_non-CO2_emissions_cleaner_jet_fuel_FINAL.pdf.
- Fay, M. P. and M. A. Proschan (Jan. 2010). “Wilcoxon-Mann-Whitney or t-test? On assumptions for hypothesis tests and multiple interpretations of decision rules”. In: *Statistics Surveys* 4, pp. 1–39. ISSN: 1935-7516. DOI: 10.1214/09-SS051.
- Feistel, R. and W. Wagner (June 2006). “A New Equation of State for H₂O Ice Ih”. In: *Journal of Physical and Chemical Reference Data* 35.2, pp. 1021–1047. ISSN: 1529-7845. DOI: 10.1063/1.2183324.
- Feldpausch, P., M. Fiebig, L. Fritzsche, and A. Petzold (2006). “Measurement of ultrafine aerosol size distributions by a combination of diffusion screen separators and condensation particle counters”. In: *Journal of Aerosol Science* 37.5, pp. 577–597. DOI: 10.1016/j.jaerosci.2005.04.009.
- Ferrone, A. (2011). “Aviation and climate change in Europe : from regional climate modelling to policy-options”. PhD thesis. UNIVERSITÉ CATHOLIQUE DE LOUVAIN.
- Fiebig, M. (2001). “Das troposphärische Aerosol in mittleren Breiten - Mikrophysik, Optik und Klimaantrieb am Beispiel der Feldstudie LACE 98”. PhD thesis. Ludwig-Maximilians-Universität München.
- Field, P. R., R. Wood, P. R. A. Brown, P. H. Kaye, E. Hirst, R. Greenaway, and J. A. Smith (Feb. 2003). “Ice Particle Interarrival Times Measured with a Fast FSSP”. In: *Journal of Atmospheric and Oceanic Technology* 20.2, pp. 249–261. ISSN: 1520-0426. DOI: 10.1175/1520-0426(2003)020<0249:IPITMW>2.0.CO;2.
- Fleming, G. G., I. de Lépinay, and R. Schaufele (2022). “Environmental Trends in Aviation to 2050”. In: *Innovation for a green transition, 2022 environmental report*. ICAO. Chap. Chapter one: Aviation & Environmental Outlook, pp. 24–31.
- Forster, P., T. Storelvmo, K. Armour, W. Collins, J.-L. Dufresne, D. Frame, D. J. Lunt, T. Mauritsen, M. D. Palmer, M. Watanabe, M. Wild, and H. Zhang (2021). “The Earth’s Energy Budget, Climate Feedbacks and Climate Sensitivity”. In: *In Climate Change 2021: The Physical Science Basis. Contribution of Working Group I to the Sixth Assessment Report of the Intergovernmental Panel on Climate Change*. Ed. by V. Masson-Delmotte, P. Zhai, A. Pirani, S. L. Connors, C. Péan, S. Berger, N. Caud, Y. Chen, L. Goldfarb, M. I. Gomis, M. Huang, K. Leitzell, E. Lonnoy, J. R. Matthews, T. K. Maycock, T. Waterfield, O. Yelekçi, R. Yu, and B. Zhou. Cambridge, United Kingdom and New York, NY, USA: Cambridge University Press, pp. 923–1054. DOI: 10.1017/9781009157896.009.
- Foust, M., D. Thomsen, R. Stickles, C. Cooper, and W. Dodds (2012). “Development of the GE Aviation Low Emissions TAPS Combustor for Next Generation Aircraft Engines”. In: *50th AIAA Aerospace Sciences Meeting including the New Horizons Forum and Aerospace Exposition*. American Institute of Aeronautics and Astronautics. DOI: 10.2514/6.2012-936.
- Fox-Kemper, B., H. T. Hewitt, C. Xiao, G. Aðalgeirsdóttir, S. S. Drijfhout, T. L. Edwards, N. R. Golledge, M. Hemer, R. E. Kopp, G. Krinner, A. Mix, D. Notz, S. Nowicki, I. S. Nurhati, L. Ruiz, J.-B. Sallée, A. B. Slangen, and Y. Yu (2021). “Ocean, Cryosphere and Sea Level Change”. In: *In Climate Change 2021: The Physical Science Basis. Contribution of Working Group I to the Sixth As-*

- essment Report of the Intergovernmental Panel on Climate Change. Ed. by V. Masson-Delmotte, P. Zhai, A. Pirani, S. L. Connors, C. Péan, S. Berger, N. Caud, Y. Chen, L. Goldfarb, M. I. Gomis, M. Huang, K. Leitzell, E. Lonnoy, J. R. Matthews, T. K. Maycock, T. Waterfield, O. Yelekçi, R. Yu, and B. Zhou. Cambridge, United Kingdom and New York, NY, USA: Cambridge University Press, pp. 1211–1362. doi: 10.1017/9781009157896.011.
- Freudenthaler, V., F. Homburg, and H. Jäger (1995). “Contrail observations by ground-based scanning lidar: Cross-sectional growth”. In: *Geophysical Research Letters* 22.24, pp. 3501–3504. doi: 10.1029/95GL03549.
- Fuglestad, J., K. Shine, T. Berntsen, J. Cook, D. Lee, A. Stenke, R. Skeie, G. Velders, and I. Waitz (2010). “Transport impacts on atmosphere and climate: Metrics”. In: *Atmospheric Environment* 44.37, pp. 4648–4677. doi: 10.1016/j.atmosenv.2009.04.044.
- Fushimi, A., K. Saitoh, Y. Fujitani, and N. Takegawa (2019). “Identification of jet lubrication oil as a major component of aircraft exhaust nanoparticles”. In: *Atmospheric Chemistry and Physics* 19.9, pp. 6389–6399. doi: 10.5194/acp-19-6389-2019.
- Gayet, J.-F., V. Shcherbakov, C. Voigt, U. Schumann, D. Schäuble, P. Jessberger, A. Petzold, A. Minikin, H. Schlager, O. Dubovik, and T. Lapyonok (2012). “The evolution of microphysical and optical properties of an A380 contrail in the vortex phase”. In: *Atmospheric Chemistry and Physics* 12.14, pp. 6629–6643. doi: 10.5194/acp-12-6629-2012.
- Gayet, J.-F., G. Febvre, G. Brogniez, H. Chepfer, W. Renger, and P. Wendling (Jan. 1996). “Microphysical and Optical Properties of Cirrus and Contrails: Cloud Field Study on 13 October 1989”. In: *Journal of the Atmospheric Sciences* 53.1, pp. 126–138. ISSN: 1520-0469. doi: 10.1175/1520-0469(1996)053<0126:MAOPOC>2.0.CO;2.
- Gerz, T., T. Dürbeck, and P. Konopka (1998). “Transport and effective diffusion of aircraft emissions”. In: *Journal of Geophysical Research: Atmospheres* 103.D20, pp. 25905–25913. doi: 10.1029/98JD02282.
- Gierens, K. (2021). “Theory of Contrail Formation for Fuel Cells”. In: *Aerospace* 8.6, p. 164. doi: 10.3390/aerospace8060164.
- Gierens, K., P. Spichtinger, and U. Schumann (2012). “Ice Supersaturation”. In: *Atmospheric Physics*. Ed. by U. Schumann. Springer Berlin Heidelberg. Chap. 9, pp. 135–150. ISBN: 978-3-642-30182-7. doi: 10.1007/978-3-642-30183-4_9.
- Giez, A., C. Mallaun, V. Nenakhov, and M. Zöger (2021). *Calibration of a Nose Boom Mounted Airflow Sensor on an Atmospheric Research Aircraft by Inflight Maneuvers*. Tech. rep. Deutsches Zentrum für Luft- und Raumfahrt, Flugexperimente, Forschungsflugabteilung Oberpfaffenhofen. URL: <https://elib.dlr.de/145969/>.
- Giez, A., C. Mallaun, M. Zöger, A. Dörnbrack, and U. Schumann (2017). “Static Pressure from Aircraft Trailing-Cone Measurements and Numerical Weather-Prediction Analysis”. In: *Journal of Aircraft* 54.5, pp. 1728–1737. doi: 10.2514/1.C034084.
- Giez, A., M. Zöger, V. Dreiling, and C. Mallaun (2020). *Static Source Error Calibration of a Nose Boom Mounted Air Data System on an Atmospheric Research Aircraft Using the Trailing Cone*

- Method.* Tech. rep. Deutsches Zentrum für Luft- und Raumfahrt, Flugexperimente, Forschungsflugabteilung Oberpfaffenhofen. URL: <https://elib.dlr.de/145770/>.
- Giez, A., M. Zöger, C. Mallaun, V. Nenakhov, M. Schimpf, Christoph Grad, A. Numberger, and K. Raynor (2023). *Determination of the Measurement Errors for the HALO Basic Data System BAHAMAS by Means of Error Propagation*. Tech. rep. Deutsches Zentrum für Luft- und Raumfahrt, Flugexperimente, Forschungsflugabteilung Oberpfaffenhofen. DOI: 10.57676/5rdc-q708. URL: <https://elib.dlr.de/193175/>.
- Goobie, S., R. Dubebout, G. Steinmetz, E. Upton, B. Parry, L. Knappen, M. F. G. Claro, M. Huising, W. Lee, and A. Bonnet (2022). “Advancing aviation technology towards industry decarbonisation”. In: *Innovation for a green transition, 2022 environmental report*. ICAO. Chap. Chapter five: Climate Change Mitigation: Aircraft Technologies, pp. 106–112.
- Grewe, V. and K. Dahlmann (2015). “How ambiguous are climate metrics? And are we prepared to assess and compare the climate impact of new air traffic technologies?” In: *Atmospheric Environment* 106, pp. 373–374. DOI: 10.1016/j.atmosenv.2015.02.039.
- Groß, S., T. Jurkat-Witschas, Q. Li, M. Wirth, B. Urbanek, M. Krämer, R. Weigel, and C. Voigt (July 2023). “Investigating an indirect aviation effect on mid-latitude cirrus clouds – linking lidar-derived optical properties to in situ measurements”. In: *Atmospheric Chemistry and Physics* 23.14, pp. 8369–8381. ISSN: 1680-7324. DOI: 10.5194/acp-23-8369-2023.
- Gössling, S., P. Hanna, J. Higham, S. Cohen, and D. Hopkins (Oct. 2019). “Can we fly less? Evaluating the ‘necessity’ of air travel”. In: *Journal of Air Transport Management* 81, p. 101722. ISSN: 0969-6997. DOI: 10.1016/j.jairtraman.2019.101722.
- Gössling, S. and A. Humpe (Nov. 2020). “The global scale, distribution and growth of aviation: Implications for climate change”. In: *Global Environmental Change* 65, p. 102194. ISSN: 0959-3780. DOI: 10.1016/j.gloenvcha.2020.102194.
- Hadaller, O. J. and J. M. Johnson (2006). *World Fuel Sampling Program*. Final Report CRC Report No. 647. Coordinating Research Council, Inc.
- Hahn, V. (2019). “Development of a Calibration Setup for Cloud Spectrometers and In-Situ Measurements of Low Level Clouds in West Africa”. MA thesis. LMU.
- Harlass, T., R. Dischl, S. Kaufmann, R. Märkl, D. Sauer, M. Scheibe, P. Stock, T. Bräuer, A. Dörnbrack, A. Roiger, H. Schlager, U. Schumann, M. Pühl, T. Schripp, T. Grein, L. Bondorf, C. Renard, M. Gauthier, M. Johnson, D. Luff, P. Madden, P. Swann, D. Ahrens, R. Sallinen, and C. Voigt (Oct. 2024). “Measurement report: In-flight and ground-based measurements of nitrogen oxide emissions from latest-generation jet engines and 100% sustainable aviation fuel”. In: *Atmospheric Chemistry and Physics* 24.20, pp. 11807–11822. ISSN: 1680-7324. DOI: 10.5194/acp-24-11807-2024.
- Haywood, J. M., R. P. Allan, J. Bornemann, P. M. Forster, P. N. Francis, S. Milton, G. Rädcl, A. Rap, K. P. Shine, and R. Thorpe (Dec. 2009). “A case study of the radiative forcing of persistent contrails evolving into contrail-induced cirrus”. In: *Journal of Geophysical Research: Atmospheres* 114.D24. ISSN: 0148-0227. DOI: 10.1029/2009JD012650.

- Hermann, M. and A. Wiedensohler (2001). "Counting efficiency of condensation particle counters at low-pressures with illustrative data from the upper troposphere". In: *Journal of Aerosol Science* 32.8, pp. 975–991. DOI: 10.1016/S0021-8502(01)00037-4.
- Heymsfield, A., D. Baumgardner, P. DeMott, P. Forster, K. Gierens, and B. Kärcher (Apr. 2010). "Contrail Microphysics". In: *Bulletin of the American Meteorological Society* 91.4, pp. 465–472. ISSN: 0003-0007. DOI: 10.1175/2009BAMS2839.1. URL: <https://doi.org/10.1175/2009BAMS2839.1>.
- Hinds, W. C. (1999). "Sampling and Measurement of Concentration". In: *Aerosol Technology: Properties, Behavior, and Measurement of Airborne Particles*. 2. John Wiley and Sons. Chap. 10, pp. 206–232. ISBN: 0471194107.
- Hungerland, T., L. Meißner, S. Abel, L. Nögel, and J. Czerniak-Wilmes (Apr. 2024). *Innovative Antriebe und Kraftstoffe für einen klimaverträglicheren Luftverkehr*. de. Tech. rep. 6. Büro für Technikfolgen-Abschätzung beim Deutschen Bundestag (TAB). DOI: 10.5445/IR/1000170399.
- IATA (June 2023). *Global Outlook for Air Transport, Highly Resilient, Less Robust*. Tech. rep. Last accessed: Aug 27, 2024. URL: <https://www.iata.org/en/iata-repository/publications/economic-reports/global-outlook-for-air-transport---june-2023/>.
- IATA (2023). *SAF Deployment, Policy*. Last accessed: August 08, 2024. URL: <https://www.iata.org/contentassets/d13875e9ed784f75bac90f000760e998/saf-policy-2023.pdf>.
- ICAO (2010). *Introduction: Aviation Outlook*. Tech. rep. ICAO Environmental Report.
- (Dec. 2018). *Sustainable aviation fuels guide*. Tech. rep. 2.
 - (June 2022a). *CORSIA Default Life Cycle Emissions Values for CORSIA Eligible Fuels*. Tech. rep.
 - (June 2022b). *CORSIA Supporting Document "CORSIA Eligible Fuels – Life Cycle Assessment Methodology"*. Tech. rep. 5. URL: https://www.icao.int/environmental-protection/CORSIA/Documents/CORSIA_Eligible_Fuels/CORSIA_Supporting_Document_CORSIAEligibleFuels_LCA_Methodology_V5.pdf.
 - (July 2024). *ICAO Aircraft Engine Emissions Databank Issue 30*.
- Immler, F., R. Treffeisen, D. Engelbart, K. Krüger, and O. Schrems (Mar. 2008). "Cirrus, contrails, and ice supersaturated regions in high pressure systems at northern mid latitudes". In: *Atmospheric Chemistry and Physics* 8.6, pp. 1689–1699. ISSN: 1680-7324. DOI: 10.5194/acp-8-1689-2008.
- Jeßberger, P., C. Voigt, U. Schumann, I. Sölch, H. Schlager, S. Kaufmann, A. Petzold, D. Schäuble, and J.-F. Gayet (2013). "Aircraft type influence on contrail properties". In: *Atmospheric Chemistry and Physics* 13.23, pp. 11965–11984. DOI: 10.5194/acp-13-11965-2013.
- Jing, L., H. M. El-Houjeiri, J.-C. Monfort, J. Littlefield, A. Al-Qahtani, Y. Dixit, R. L. Speth, A. R. Brandt, M. S. Masnadi, H. L. MacLean, W. Peltier, D. Gordon, and J. A. Bergerson (Dec. 2022). "Understanding variability in petroleum jet fuel life cycle greenhouse gas emissions to inform aviation decarbonization". In: *Nature Communications* 13.1. ISSN: 2041-1723. DOI: 10.1038/s41467-022-35392-1.
- Jones, S. H. and R. C. Miake-Lye (2023). "Contrail Modeling of ECLIF2/ND-MAX flights: Effects of nvPM Particle Numbers and Fuel Sulfur Content". In: *Meteorologische Zeitschrift*. DOI: 10.1127/metz/2023/1180.

- Jurkat, T., C. Voigt, F. Arnold, H. Schlager, J. Kleffmann, H. Aufmhoff, D. Schäuble, M. Schaefer, and U. Schumann (2011). “Measurements of HONO, NO, NO_y and SO₂ in aircraft exhaust plumes at cruise”. In: *Geophysical Research Letters* 38.10. DOI: 10.1029/2011GL046884.
- Kaufmann, S. (2013). “Massenspektrometrische Wasserdampfmessung in der oberen Troposphäre und unteren Stratosphäre”. PhD thesis.
- Kaufmann, S., R. Dischl, and C. Voigt (Dec. 2024). “Regional and seasonal impact of hydrogen propulsion systems on potential contrail cirrus cover”. In: *Atmospheric Environment: X* 24, p. 100298. ISSN: 2590-1621. DOI: 10.1016/j.aeaoa.2024.100298.
- Kaufmann, S., C. Voigt, R. Heller, T. Jurkat-Witschas, M. Krämer, C. Rolf, M. Zöger, A. Giez, B. Buchholz, V. Ebert, T. Thornberry, and U. Schumann (2018). “Intercomparison of midlatitude tropospheric and lower-stratospheric water vapor measurements and comparison to ECMWF humidity data”. In: *Atmospheric Chemistry and Physics* 18.22, pp. 16729–16745. DOI: 10.5194/acp-18-16729-2018.
- Kaufmann, S., C. Voigt, P. Jeßberger, T. Jurkat, H. Schlager, A. Schwarzenboeck, M. Klingebiel, and T. Thornberry (2014). “In situ measurements of ice saturation in young contrails”. In: *Geophysical Research Letters* 41.2, pp. 702–709. DOI: 10.1002/2013GL058276.
- Kaufmann, S., C. Voigt, T. Jurkat, T. Thornberry, D. W. Fahey, R.-S. Gao, R. Schlage, D. Schäuble, and M. Zöger (2016). “The airborne mass spectrometer AIMS –Part 1: AIMS-H₂O for UTLS water vapor measurements”. In: *Atmospheric Measurement Techniques* 9.3, pp. 939–953. DOI: 10.5194/amt-9-939-2016.
- Kirschler, S., C. Voigt, B. Anderson, R. Campos Braga, G. Chen, A. F. Corral, E. Crosbie, H. Dadas-hazar, R. A. Ferrare, V. Hahn, J. Hendricks, S. Kaufmann, R. Moore, M. L. Pöhlker, C. Robinson, A. J. Scarino, D. Schollmayer, M. A. Shook, K. L. Thornhill, E. Winstead, L. D. Ziemba, and A. Sorooshian (June 2022). “Seasonal updraft speeds change cloud droplet number concentrations in low-level clouds over the western North Atlantic”. In: *Atmospheric Chemistry and Physics* 22.12, pp. 8299–8319. ISSN: 1680-7324. DOI: 10.5194/acp-22-8299-2022.
- Kleine, J., C. Voigt, D. Sauer, H. Schlager, M. Scheibe, T. Jurkat-Witschas, S. Kaufmann, B. Kärcher, and B. E. Anderson (2018). “In Situ Observations of Ice Particle Losses in a Young Persistent Contrail”. In: *Geophysical Research Letters* 45.24, pp. 13,553–13,561. DOI: 10.1029/2018gl079390.
- Kleine, J. (2019). “Flugzeuggetragene Messungen von Eis- und Rußpartikeln in Kondensstreifen bei Verwendung konventioneller und synthetischer Treibstoffe”. PhD thesis. Johannes Gutenberg-Universität Mainz. DOI: 10.25358/openscience-3574.
- Knollenberg, R. G. (Oct. 1972). “Measurements of the Growth of the Ice Budget in a Persisting Contrail”. In: *Journal of the Atmospheric Sciences* 29.7, pp. 1367–1374. ISSN: 1520-0469. DOI: 10.1175/1520-0469(1972)029<1367:MOTGOT>2.0.CO;2.
- Kotz, M., A. Levermann, and L. Wenz (Apr. 2024). “The economic commitment of climate change”. In: *Nature* 628.8008, pp. 551–557. ISSN: 1476-4687. DOI: 10.1038/s41586-024-07219-0.
- Krautstrunk, M. and A. Giez (2012). “The Transition From FALCON to HALO Era Airborne Atmospheric Research”. In: *Atmospheric Physics*. Ed. by U. Schumann. Springer Berlin Heidelberg. Chap. 37, pp. 609–624. ISBN: 978-3-642-30182-7. DOI: 10.1007/978-3-642-30183-4_37.

- Krämer, M., C. Schiller, A. Afchine, R. Bauer, I. Gensch, A. Mangold, S. Schlicht, N. Spelten, N. Sitnikov, S. Borrmann, M. de Reus, and P. Spichtinger (June 2009). “Ice supersaturations and cirrus cloud crystal numbers”. In: *Atmospheric Chemistry and Physics* 9.11, pp. 3505–3522. ISSN: 1680-7324. DOI: 10.5194/acp-9-3505-2009.
- Krämer, M. and A. Afchine (2004). “Sampling characteristics of inlets operated at low U/U₀ ratios: new insights from computational fluid dynamics (CFX) modeling”. In: *Journal of Aerosol Science* 35.6, pp. 683–694. DOI: 10.1016/j.jaerosci.2003.11.011.
- Kärcher, B. (May 1998). “On the potential importance of sulfur-induced activation of soot particles in nascent jet aircraft exhaust plumes”. In: *Atmospheric Research* 46.3–4, pp. 293–305. ISSN: 0169-8095. DOI: 10.1016/S0169-8095(97)00070-7.
- Kärcher, B., U. Burkhardt, A. Bier, L. Bock, and I. J. Ford (2015). “The microphysical pathway to contrail formation”. In: *Journal of Geophysical Research: Atmospheres* 120.15, pp. 7893–7927. DOI: 10.1002/2015JD023491.
- Kärcher, B., J. Kleine, D. Sauer, and C. Voigt (2018). “Contrail Formation: Analysis of Sublimation Mechanisms”. In: *Geophysical Research Letters* 45.24, pp. 13179–13561. DOI: 10.1029/2018GL079391.
- Kärcher, B., R. P. Turco, F. Yu, M. Y. Danilin, D. K. Weisenstein, R. C. Miake-Lye, and R. Busen (Dec. 2000). “A unified model for ultrafine aircraft particle emissions”. In: *Journal of Geophysical Research: Atmospheres* 105.D24, pp. 29379–29386. ISSN: 0148-0227. DOI: 10.1029/2000JD900531.
- Kärcher, B. and F. Yu (2009). “Role of aircraft soot emissions in contrail formation”. In: *Geophysical Research Letters* 36.1. DOI: 10.1029/2008GL036649.
- Kärcher, B. (2018). “Formation and radiative forcing of contrail cirrus”. In: *Nature Communications* 9.1824. DOI: 10.1038/s41467-018-04068-0.
- Lance, S. (2012). “Coincidence Errors in a Cloud Droplet Probe (CDP) and a Cloud and Aerosol Spectrometer (CAS), and the Improved Performance of a Modified CDP”. In: *Journal of Atmospheric and Oceanic Technology* 29.10, pp. 1532–1541. DOI: 10.1175/JTECH-D-11-00208.1.
- Laven, P. (Nov. 2021). *MiePlot v4.6.21*. Last accessed: Nov. 28, 2024. URL: <http://www.philiplaven.com/mieplot.htm>.
- Lee, D. S., M. R. Allen, N. Cumpsty, B. Owen, K. P. Shine, and A. Skowron (2023). “Uncertainties in mitigating aviation non-CO₂ emissions for climate and air quality using hydrocarbon fuels”. In: *Environmental Science: Atmospheres* 3.12, pp. 1693–1740. ISSN: 2634-3606. DOI: 10.1039/d3ea00091e.
- Lee, D., D. Fahey, A. Skowron, M. Allen, U. Burkhardt, Q. Chen, S. Doherty, S. Freeman, P. Forster, J. Fuglestvedt, A. Gettelman, R. D. León, L. Lim, M. Lund, R. Millar, B. Owen, J. Penner, G. Pitari, M. Prather, R. Sausen, and L. Wilcox (Jan. 2021). “The contribution of global aviation to anthropogenic climate forcing for 2000 to 2018”. In: *Atmospheric Environment* 244, p. 117834. DOI: 10.1016/j.atmosenv.2020.117834.
- Lewellen, D. C., O. Meza, and W. W. Huebsch (2014). “Persistent Contrails and Contrail Cirrus. Part I: Large-Eddy Simulations from Inception to Demise”. In: *J. Atmospheric Sci.* 71.12, pp. 4399–4419. DOI: 10.1175/JAS-D-13-0316.1.

- LI-7000 CO₂ /H₂O Analyzer Instruction Manual (Aug. 2007). 4th ed. LI-COR Inc. 4647 Superior Street, Lincoln, Nebraska.
- Liu, G., B. Yan, and G. Chen (Sept. 2013). “Technical review on jet fuel production”. In: *Renewable and Sustainable Energy Reviews* 25, pp. 59–70. ISSN: 1364-0321. DOI: 10.1016/j.rser.2013.03.025.
- Liu, Y., X. Sun, V. Sethi, D. Nalianda, Y.-G. Li, and L. Wang (Oct. 2017). “Review of modern low emissions combustion technologies for aero gas turbine engines”. In: *Progress in Aerospace Sciences* 94, pp. 12–45. ISSN: 0376-0421. DOI: 10.1016/j.paerosci.2017.08.001.
- Llewellyn, G. and V. Miftakhov (2022). “Hydrogen power – boldly going to the heart of climate-neutral aviation”. In: *Innovation for a green transition, 2022 environmental report*. ICAO. Chapter five: Climate Change Mitigation: Aircraft Technologies, pp. 126–130.
- Lobo, P., D. E. Hagen, and P. D. Whitefield (2011). “Comparison of PM Emissions from a Commercial Jet Engine Burning Conventional, Biomass, and Fischer–Tropsch Fuels”. In: *Environmental Science and Technology* 45.24, pp. 10744–10749. DOI: 10.1021/es201902e.
- Malina, R., M. Prussi, and F. Taheripour (2022). “Method for establishing lifecycle greenhouse gas emission factors for sustainable aviation fuels”. In: *Innovation for a green transition, 2022 environmental report*. ICAO. Chapter seven: Climate Change Mitigation: Sustainable Aviation Fuels, pp. 207–211.
- Mann, H. B. and D. R. Whitney (1947). “On a Test of Whether one of Two Random Variables is Stochastically Larger than the Other”. In: *The Annals of Mathematical Statistics* 18.1, pp. 50–60. URL: <https://www.jstor.org/stable/2236101>.
- Martin Frias, A, M. L. Shapiro, Z Engberg, R Zopp, M Soler, and M. E. J. Stettler (Mar. 2024). “Feasibility of contrail avoidance in a commercial flight planning system: an operational analysis”. In: *Environmental Research: Infrastructure and Sustainability* 4.1, p. 015013. ISSN: 2634-4505. DOI: 10.1088/2634-4505/ad310c.
- Maxwell, J. C. (Dec. 1865). “VIII. A dynamical theory of the electromagnetic field”. In: *Philosophical Transactions of the Royal Society of London* 155, pp. 459–512. ISSN: 2053-9223. DOI: 10.1098/rstl.1865.0008.
- Meerkötter, R., U. Schumann, D. R. Doelling, P. Minnis, T. Nakajima, and Y. Tsushima (1999). “Radiative forcing by contrails”. In: *Annales Geophysicae* 17.8, pp. 1080–1094. DOI: 10.1007/s00585-999-1080-7.
- Megill, L., K. Deck, and V. Grewe (May 2024). “Alternative climate metrics to the Global Warming Potential are more suitable for assessing aviation non-CO₂ effects”. In: *Communications Earth & Environment* 5.1. ISSN: 2662-4435. DOI: 10.1038/s43247-024-01423-6.
- Mie, G. (1908). “Beiträge zur Optik trüber Medien, speziell kolloidaler Metallösungen”. In: *Annalen der Physik* 330.3, pp. 377–445. DOI: 10.1002/andp.19083300302.
- Minnis, P., J. K. Ayers, R. Palikonda, and D. Phan (Apr. 2004). “Contrails, Cirrus Trends, and Climate”. In: *Journal of Climate* 17.8, pp. 1671–1685. ISSN: 1520-0442. DOI: 10.1175/1520-0442(2004)017<1671:CCTAC>2.0.CO;2.
- Miracolo, M. A., C. J. Hennigan, M. Ranjan, N. T. Nguyen, T. D. Gordon, E. M. Lipsky, A. A. Presto, N. M. Donahue, and A. L. Robinson (May 2011). “Secondary aerosol formation from photochem-

- ical aging of aircraft exhaust in a smog chamber”. In: *Atmospheric Chemistry and Physics* 11.9, pp. 4135–4147. ISSN: 1680-7324. DOI: 10.5194/acp-11-4135-2011.
- Miracolo, M. A., G. T. Drozd, S. H. Jathar, A. A. Presto, E. M. Lipsky, E. Corporan, and A. L. Robinson (July 2012). “Fuel Composition and Secondary Organic Aerosol Formation: Gas-Turbine Exhaust and Alternative Aviation Fuels”. In: *Environmental Science and Technology* 46.15, pp. 8493–8501. ISSN: 1520-5851. DOI: 10.1021/es300350c.
- Mirme, S., A. Mirme, A. Minikin, A. Petzold, U. Hörrak, V. M. Kerminen, and M. Kulmala (Jan. 2010). “Atmospheric sub-3 nm particles at high altitudes”. In: *Atmospheric Chemistry and Physics* 10.2, pp. 437–451. ISSN: 1680-7324. DOI: 10.5194/acp-10-437-2010.
- Mirón, I. J., C. Linares, and J. Díaz (Jan. 2023). “The influence of climate change on food production and food safety”. In: *Environmental Research* 216, p. 114674. ISSN: 0013-9351. DOI: 10.1016/j.envres.2022.114674.
- Moore, R. H., K. L. Thornhill, B. Weinzierl, D. Sauer, E. D’Ascoli, J. Kim, M. Lichtenstern, M. Scheibe, B. Beaton, A. J. Beyersdorf, J. Barrick, D. Bulzan, C. A. Corr, E. Crosbie, T. Jurkat, R. Martin, D. Riddick, M. Shook, G. Slover, C. Voigt, R. White, E. Winstead, R. Yasky, L. D. Ziemba, A. Brown, H. Schlager, and B. E. Anderson (2017). “Biofuel blending reduces particle emissions from aircraft engines at cruise conditions”. In: *Nature* 543.7645, pp. 411–415. DOI: 10.1038/nature21420.
- Myhre, G., D. Shindell, F.-M. Bréon, W. Collins, J. Fuglestedt, J. Huang, D. Koch, J.-F. Lamarque, D. Lee, B. Mendoza, T. Nakajima, A. Robock, G. Stephens, T. Takemura, and H. Zhang (2013). “Anthropogenic and Natural Radiative Forcing”. In: *Climate Change 2013: The Physical Science Basis. Contribution of Working Group I to the Fifth Assessment Report of the Intergovernmental Panel on Climate Change*. Ed. by T. F. Stocker, D. Qin, G.-K. Plattner, M. M. Tignor, S. K. Allen, J. Boschung, A. Nauels, Y. Xia, V. Bex, and P. M. Midgley. Cambridge, United Kingdom and New York, NY, USA: Cambridge University Press.
- Märkl, R. S., C. Voigt, D. Sauer, R. K. Dischl, S. Kaufmann, T. Harlaß, V. Hahn, A. Roiger, C. Weiß-Rehm, U. Burkhardt, U. Schumann, A. Marsing, M. Scheibe, A. Dörnbrack, C. Renard, M. Gauthier, P. Swann, P. Madden, D. Luff, R. Sallinen, T. Schripp, and P. Le Clercq (Mar. 2024). “Powering aircraft with 100% sustainable aviation fuel reduces ice crystals in contrails”. In: *Atmospheric Chemistry and Physics* 24.6, pp. 3813–3837. ISSN: 1680-7324. DOI: 10.5194/acp-24-3813-2024.
- Nagy, A., W. Szymanski, P. Gál, A. Golczewski, and A. Czitrovsky (Apr. 2007). “Numerical and experimental study of the performance of the dual wavelength optical particle spectrometer (DWOPS)”. In: *Journal of Aerosol Science* 38.4, pp. 467–478. ISSN: 0021-8502. DOI: 10.1016/j.jaerosci.2007.02.005.
- Nagy, A., A. Czitrovsky, A. Kerekes, M. Veres, and W. W. Szymanski (2016). “Real-Time Determination of Absorptivity of Ambient Particles in Urban Aerosol in Budapest, Hungary”. In: *Aerosol and Air Quality Research* 16.1, pp. 1–10. ISSN: 2071-1409. DOI: 10.4209/aaqr.2015.05.0356.
- Neuling, U. and M. Kaltschmitt (Aug. 2017a). “Biokerosene from Vegetable Oils – Technologies and Processes”. In: *Biokerosene*. Ed. by M. Kaltschmitt and U. Neuling. Springer Berlin Heidelberg. Chap. 19, pp. 475–496. ISBN: 978-3-662-53063-4. DOI: 10.1007/978-3-662-53065-8_19.

- Neuling, U. and M. Kaltschmitt (Aug. 2017b). “Conversion Routes from Biomass to Biokerosene”. In: *Biokerosene*. Ed. by M. Kaltschmitt and U. Neuling. Springer Berlin Heidelberg. Chap. 18, pp. 435–473. ISBN: 978-3-662-53063-4. DOI: 10.1007/978-3-662-53065-8_18.
- Newinger, C. and U. Burkhardt (2012). “Sensitivity of contrail cirrus radiative forcing to air traffic scheduling”. In: *Journal of Geophysical Research: Atmospheres* 117.D10. DOI: 10.1029/2011JD016736.
- Newman, R. and I. Noy (Sept. 2023). “The global costs of extreme weather that are attributable to climate change”. In: *Nature Communications* 14.1. ISSN: 2041-1723. DOI: 10.1038/s41467-023-41888-1.
- Newman, S. M., L. Clarisse, D. Hurtmans, F. Marengo, B. Johnson, K. Turnbull, S. Havemann, A. J. Baran, D. O’Sullivan, and J. Haywood (Feb. 2012). “A case study of observations of volcanic ash from the Eyjafjallajökull eruption: 2. Airborne and satellite radiative measurements”. In: *Journal of Geophysical Research: Atmospheres* 117.D20. ISSN: 0148-0227. DOI: 10.1029/2011JD016780.
- Niklaß, M., K. Dahlmann, V. Grewe, S. Maertens, M. Plohr, J. Scheelhaase, J. Schwieger, U. Brodmann, C. Kurzböck, M. Repmann, N. Schweizer, and M. von Unger (2020). *Integration of Non-CO2 Effects of Aviation in the EU ETS and under CORSIA*. Tech. rep. Umweltbundesamt.
- Nikolaidis, P. and A. Poullikkas (Jan. 2017). “A comparative overview of hydrogen production processes”. In: *Renewable and Sustainable Energy Reviews* 67, pp. 597–611. ISSN: 1364-0321. DOI: 10.1016/j.rser.2016.09.044.
- Noone, K. J. and H.-C. Hansson (1990). “Calibration of the TSI 3760 Condensation Nucleus Counter for Nonstandard Operating Conditions”. In: *Aerosol Science and Technology* 13.4, pp. 478–485. DOI: 10.1080/02786829008959462.
- Onissen, H. (2014). “Antriebe”. In: *Handbuch der Luftfahrzeugtechnik*. Ed. by C.-C. Rossow, K. Wolf, and P. Horst. Carl Hanser Verlag München. Chap. 5, pp. 444–641. ISBN: 978-3-446-42341-1.
- Paoli, R. and K. Shariff (2016). “Contrail Modeling and Simulation”. In: *Annual Review of Fluid Mechanics* 48.1, pp. 393–427. DOI: 10.1146/annurev-fluid-010814-013619.
- Paugam, R., R. Paoli, and D. Cariolle (2010). “Influence of vortex dynamics and atmospheric turbulence on the early evolution of a contrail”. In: *Atmospheric Chemistry and Physics* 10.8, pp. 3933–3952. DOI: 10.5194/acp-10-3933-2010.
- Pavlenko, N., S. Searle, and A. Christensen (2019). “The cost of supporting alternative jet fuels in the European Union”. In: *ICCT*.
- Pavri, R. and G. D. Moore (2001). “Gas Turbine Emissions and Control”. In: *Atlanta: GE Energy Services* GER-4211.
- Pechstein, J. and A. Zschocke (Aug. 2017). “Blending of Synthetic Kerosene and Conventional Kerosene”. In: *Biokerosene*. Ed. by M. Kaltschmitt and U. Neuling. Springer Berlin Heidelberg. Chap. 25, pp. 665–686. ISBN: 978-3-662-53063-4. DOI: 10.1007/978-3-662-53065-8_25.
- Petzold, A., R. Busen, F. P. Schröder, R. Baumann, M. Kuhn, J. Ström, D. E. Hagen, P. D. Whitefield, D. Baumgardner, F. Arnold, S. Borrmann, and U. Schumann (1997). “Near-field measurements on contrail properties from fuels with different sulfur content”. In: *Journal of Geophysical Research: Atmospheres* 102.D25, pp. 29867–29880. DOI: 10.1029/97JD02209.

- Petzold, A., M. Gysel, X. Vancassel, R. Hitzenberger, H. Puxbaum, S. Vrochticky, E. Weingartner, U. Baltensperger, and P. Mirabel (Dec. 2005). “On the effects of organic matter and sulphur-containing compounds on the CCN activation of combustion particles”. In: *Atmospheric Chemistry and Physics* 5.12, pp. 3187–3203. ISSN: 1680-7324. DOI: 10.5194/acp-5-3187-2005.
- Petzold, A, J Ström, S Ohlsson, and F. Schröder (Aug. 1998). “Elemental composition and morphology of ice-crystal residual particles in cirrus clouds and contrails”. In: *Atmospheric Research* 49.1, pp. 21–34. ISSN: 0169-8095. DOI: 10.1016/S0169-8095(97)00083-5.
- Ponsonby, J., L. King, B. J. Murray, and M. E. J. Stettler (Feb. 2024a). “Jet aircraft lubrication oil droplets as contrail ice-forming particles”. In: *Atmospheric Chemistry and Physics* 24.3, pp. 2045–2058. ISSN: 1680-7324. DOI: 10.5194/acp-24-2045-2024.
- Ponsonby, J., R. Teoh, and M. Stettler (Mar. 2024b). “Towards an improved treatment of (semi) volatile particle activation in contrail models”. In: *EGU General Assembly 2024*. Copernicus GmbH. DOI: 10.5194/egusphere-egu24-17410.
- Popovicheva, O. B., N. M. Persiantseva, E. E. Lukhovitskaya, N. K. Shonija, N. A. Zubareva, B. Demirdjian, D. Ferry, and J. Suzanne (June 2004). “Aircraft engine soot as contrail nuclei”. In: *Geophysical Research Letters* 31.11. ISSN: 1944-8007. DOI: 10.1029/2003GL018888.
- Quante, G., S. Voß, N. Bullerdiek, C. Voigt, and M. Kaltschmitt (Apr. 2024). “Hydroprocessing of fossil fuel-based aviation kerosene – Technology options and climate impact mitigation potentials”. In: *Atmospheric Environment: X* 22, p. 100259. ISSN: 2590-1621. DOI: 10.1016/j.aeaoa.2024.100259.
- Rauch, R., H. Hofbauer, U. Neuling, and M. Kaltschmitt (Aug. 2017). “Biokerosene Production from Bio-Chemical and Thermo-Chemical Biomass Conversion and Subsequent Fischer-Tropsch Synthesis”. In: *Biokerosene*. Ed. by M. Kaltschmitt and U. Neuling. Springer Berlin Heidelberg. Chap. 20, pp. 497–542. ISBN: 978-3-662-53063-4. DOI: 10.1007/978-3-662-53065-8_20.
- Roeckner, E, G Bäuml, L. Bonaventura, R Brokopf, M. Esch, M. Giorgetta, S. Hagemann, I. Kirchner, L. Kornblueh, E. Manzini, A. Rhodin, U Schlese, U. Schulzweida, and A Tompkins (Jan. 2003). *The atmospheric general circulation model ECHAM 5. PART I: model description*. Tech. rep. 349. Max Planck Institute for Meteorology. URL: <https://hdl.handle.net/11858/00-001M-0000-0012-0144-5>.
- Rogers, R. R. and M. K. Yau (1989a). “Formation and Growth of Ice Crystals”. In: *A Short Course in Cloud Physics*. Ed. by D. T. Haar. 3rd ed. Vol. 113. International Series in Natural Philosophy. Butterworth Heinemann. Chap. 9, pp. 150–169. ISBN: 0-7506-3215-1.
- (1989b). “Formation of Cloud Droplets”. In: *A Short Course in Cloud Physics*. Ed. by D. T. Haar. 3rd ed. Vol. 113. International Series in Natural Philosophy. Butterworth Heinemann. Chap. 6, pp. 81–98. ISBN: 0-7506-3215-1.
- (1989c). “Water Vapor and its Thermodynamic Effects”. In: *A Short Course in Cloud Physics*. Ed. by D. T. Haar. 3rd ed. Vol. 113. International Series in Natural Philosophy. Butterworth Heinemann. Chap. 2, pp. 12–27. ISBN: 0-7506-3215-1.
- Rojo, C., X. Vancassel, P. Mirabel, J.-L. Ponche, and F. Garnier (Mar. 2015). “Impact of alternative jet fuels on aircraft-induced aerosols”. In: *Fuel* 144, pp. 335–341. ISSN: 0016-2361. DOI: 10.1016/j.fuel.2014.12.021.

- Rosenberg, P. D., A. R. Dean, P. I. Williams, J. R. Dorsey, A. Minikin, M. A. Pickering, and A. Petzold (2012). “Particle sizing calibration with refractive index correction for light scattering optical particle counters and impacts upon PCASP and CDP data collected during the Fennec campaign”. In: *Atmospheric Measurement Techniques* 5.5, pp. 1147–1163. DOI: 10.5194/amt-5-1147-2012.
- Roth, A., F. Riegel, and V. Batteiger (Aug. 2017). “Potentials of Biomass and Renewable Energy: The Question of Sustainable Availability”. In: *Bioerosene*. Ed. by M. Kaltschmitt and U. Neuling. Springer Berlin Heidelberg. Chap. 6, pp. 95–122. ISBN: 978-3-662-53063-4. DOI: 10.1007/978-3-662-53065-8_6.
- Sausen, R., S. Hofer, K. Gierens, L. Bugliaro, R. Ehrmanntraut, I. Sitova, K. Walczak, A. Burridge-Diesing, M. Bowman, and N. Miller (Jan. 2023). “Can we successfully avoid persistent contrails by small altitude adjustments of flights in the real world?” In: *Meteorologische Zeitschrift*. ISSN: 0941-2948. DOI: 10.1127/metz/2023/1157.
- Schmidt, E. (1940). “Die Entstehung von Eisnebel aus den Auspuffgasen von Flugmotoren”. In: *Schriften der Deutschen Akademie der Luftfahrtforschung* 44.5, pp. 1–22. URL: <https://elib.dlr.de/107948/>.
- Schmidt, J. (2023). “Messung mikrophysikalischer Parameter von Kondensstreifen eines modernen Passagierflugzeuges (Unpublished)”. MA thesis. Technische Universität München.
- Schripp, T., B. Anderson, E. C. Crosbie, R. H. Moore, F. Herrmann, P. Oßwald, C. Wahl, M. Kapernaum, M. Köhler, P. L. Clercq, B. Rauch, P. Eichler, T. Mikoviny, and A. Wisthaler (2018). “Impact of Alternative Jet Fuels on Engine Exhaust Composition During the 2015 ECLIF Ground-Based Measurements Campaign”. In: *Environmental Science and Technology* 52.8, pp. 4969–4978. DOI: 10.1021/acs.est.7b06244.
- Schripp, T., B. E. Anderson, U. Bauder, B. Rauch, J. C. Corbin, G. J. Smallwood, P. Lobo, E. C. Crosbie, M. A. Shook, R. C. Mlake-Lye, Z. Yu, A. Freedman, P. D. Whitefield, C. E. Robinson, S. L. Achterberg, M. Köhler, P. Oßwald, T. Grein, D. Sauer, C. Voigt, H. Schlager, and P. LeClercq (2022). “Aircraft engine particulate matter emissions from sustainable aviation fuels: Results from ground-based measurements during the NASA/DLR campaign ECLIF2/ND-MAX”. In: *Fuel* 325, p. 124764. DOI: 10.1016/j.fuel.2022.124764.
- Schröder, F., B. Kärcher, C. Duroure, J. Ström, A. Petzold, J.-F. Gayet, B. Strauss, P. Wendling, and S. Borrmann (2000). “On the Transition of Contrails into Cirrus Clouds”. In: *Journal of the Atmospheric Sciences* 57.4, pp. 464–480. DOI: 10.1175/1520-0469(2000)057<0464:ottoci>2.0.co;2.
- Schulte, P. and H. Schlager (1996). “In-flight measurements of cruise altitude nitric oxide emission indices of commercial jet aircraft”. In: *Geophys. Res. Lett.* 23.2, pp. 165–168. DOI: 10.1029/95gl03691.
- Schulte, P., H. Schlager, H. Ziereis, U. Schumann, S. L. Baughcum, and F. Deidewig (1997). “NO_x emission indices of subsonic long-range jet aircraft at cruise altitude: In situ measurements and predictions”. In: *Journal of Geophysical Research: Atmospheres* 102.D17, pp. 21431–21442. DOI: 10.1029/97JD01526.
- Schumann, U. (2012). “A contrail cirrus prediction model”. In: *Geoscientific Model Development* 5.3, pp. 543–580. DOI: 10.5194/gmd-5-543-2012.

- Schumann, U., F. Arnold, R. Busen, J. Curtius, B. Kärcher, A. Kiendler, A. Petzold, H. Schlager, F. Schröder, and K.-H. Wohlfrom (2002). "Influence of fuel sulfur on the composition of aircraft exhaust plumes: The experiments SULFUR 1-7". In: *Journal of Geophysical Research* 107.D15, AAC 2-1 –AAC 2-27. DOI: 10.1029/2001jd000813.
- Schumann, U., B. Mayer, K. Graf, and H. Mannstein (July 2012). "A Parametric Radiative Forcing Model for Contrail Cirrus". In: *Journal of Applied Meteorology and Climatology* 51.7, pp. 1391–1406. ISSN: 1558-8432. DOI: 10.1175/JAMC-D-11-0242.1.
- Schumann, U., J. Ström, R. Busen, R. Baumann, K. Gierens, M. Krautstrunk, F. P. Schröder, and J. Stingl (1996). "In situ observations of particles in jet aircraft exhausts and contrails for different sulfur-containing fuels". In: *Journal of Geophysical Research: Atmospheres* 101.D3, pp. 6853–6869. DOI: 10.1029/95JD03405.
- Schumann, U. (1996). "On Conditions for Contrail Formation from Aircraft Exhausts". In: *Meteorologische Zeitschrift* 5.1, pp. 4–23. DOI: 10.1127/metz/5/1996/4. URL: <https://elib.dlr.de/32128/>.
- (2000). "Influence of propulsion efficiency on contrail formation". In: *Aerospace Science and Technology* 4.6, pp. 391–401. DOI: 10.1016/S1270-9638(00)01062-2.
- (2002). "Aircraft Emissions". In: *Causes and consequences of global environmental change*. Ed. by I. Douglas. Vol. 3. Encyclopedia of Global Environmental Change. John Wiley & Sons, Ltd, Chichester, pp. 178–186. ISBN: 0-471-97796-9.
- Schumann, U., R. Baumann, D. Baumgardner, S. T. Bedka, D. P. Duda, V. Freudenthaler, J.-F. Gayet, A. J. Heymsfield, P. Minnis, M. Quante, E. Raschke, H. Schlager, M. Vázquez-Navarro, C. Voigt, and Z. Wang (2017). "Properties of individual contrails: a compilation of observations and some comparisons". In: *Atmospheric Chemistry and Physics* 17.1, pp. 403–438. DOI: 10.5194/acp-17-403-2017.
- Schumann, U. and K. Graf (2013). "Aviation-induced cirrus and radiation changes at diurnal timescales". In: *Journal of Geophysical Research: Atmospheres* 118.5, pp. 2404–2421. DOI: 10.1002/jgrd.50184.
- Schumann, U., K. Graf, and H. Mannstein (2011). "Potential to reduce the climate impact of aviation by flight level changes". In: *3rd AIAA Atmospheric Space Environments Conference*. American Institute of Aeronautics and Astronautics. DOI: 10.2514/6.2011-3376.
- Schumann, U. and A. J. Heymsfield (Jan. 2017). "On the Life Cycle of Individual Contrails and Contrail Cirrus". In: *Meteorological Monographs* 58, pp. 3.1–3.24. ISSN: 0065-9401. DOI: 10.1175/AMSMONOGRAPHS-D-16-0005.1.
- Schumann, U., P. Jeßberger, and C. Voigt (2013). "Contrail ice particles in aircraft wakes and their climatic importance". In: *Geophysical Research Letters* 40.11, pp. 2867–2872. DOI: 10.1002/grl.50539.
- Schöberl, M., M. Dollner, J. Gasteiger, P. Seibert, A. Tipka, and B. Weinzierl (May 2024). "Characterization of the airborne aerosol inlet and transport system used during the A-LIFE aircraft field experiment". In: *Atmospheric Measurement Techniques* 17.9, pp. 2761–2776. ISSN: 1867-8548. DOI: 10.5194/amt-17-2761-2024.

- Seinfeld, J. H. and S. N. Pandis (2006). “Interaction of Aerosols with Radiation”. In: *Atmospheric Chemistry and Physics*. 2nd ed. John Wiley & Sons, Inc. Chap. 15, pp. 691–719. ISBN: 978-0-471-72018-8.
- Seneviratne, S. I., X. Zhang, M. Adnan, W. Badi, C. Dereczynski, A. D. Luca, S. Ghosh, I. Iskandar, J. Kossin, S. Lewis, F. Otto, I. Pinto, M. Satoh, S. M. Vicente-Serrano, M. Wehner, and B. Zhou (2021). “Weather and Climate Extreme Events in a Changing Climate”. In: *In Climate Change 2021: The Physical Science Basis. Contribution of Working Group I to the Sixth Assessment Report of the Intergovernmental Panel on Climate Change*. Ed. by V. Masson-Delmotte, P. Zhai, A. Pirani, S. L. Connors, C. Péan, S. Berger, N. Caud, Y. Chen, L. Goldfarb, M. I. Gomis, M. Huang, K. Leitzell, E. Lonnoy, J. R. Matthews, T. K. Maycock, T. Waterfield, O. Yelekçi, R. Yu, and B. Zhou. Cambridge, United Kingdom and New York, NY, USA: Cambridge University Press, pp. 1513–1766. DOI: 10.1017/9781009157896.013.
- SESAR Joint Undertaking (2020). *European ATM Master Plan: Digitalising Europe’s aviation infrastructure : executive view*. Tech. rep. DOI: 10.2829/695700.
- Stickles, R. and J. Barrett (2013). *TAPS II Combustor Final Report*. Tech. rep. General Electric.
- Stuber, N., P. Forster, G. Rädcl, and K. Shine (2006). “The importance of the diurnal and annual cycle of air traffic for contrail radiative forcing”. In: *Nature* 441.7095, pp. 864–867. DOI: 10.1038/nature04877.
- Teoh, R., Z. Engberg, U. Schumann, C. Voigt, M. Shapiro, S. Rohs, and M. E. J. Stettler (May 2024). “Global aviation contrail climate effects from 2019 to 2021”. In: *Atmospheric Chemistry and Physics* 24.10, pp. 6071–6093. ISSN: 1680-7324. DOI: 10.5194/acp-24-6071-2024.
- Teoh, R., U. Schumann, E. Gryspeerdt, M. Shapiro, J. Molloy, G. Koudis, C. Voigt, and M. E. J. Stettler (2022a). “Aviation contrail climate effects in the North Atlantic from 2016 to 2021”. In: *Atmospheric Chemistry and Physics* 22.16, pp. 10919–10935. DOI: 10.5194/acp-22-10919-2022.
- Teoh, R., U. Schumann, A. Majumdar, and M. E. J. Stettler (2020a). “Mitigating the Climate Forcing of Aircraft Contrails by Small-Scale Diversions and Technology Adoption”. In: *Environmental Science and Technology* 54.5, pp. 2941–2950. DOI: 10.1021/acs.est.9b05608.
- Teoh, R., U. Schumann, and M. E. J. Stettler (2020b). “Beyond Contrail Avoidance: Efficacy of Flight Altitude Changes to Minimise Contrail Climate Forcing”. In: *Aerospace* 7.9, p. 121. DOI: 10.3390/aerospace7090121.
- Teoh, R., U. Schumann, C. Voigt, T. Schripp, M. Shapiro, Z. Engberg, J. Molloy, G. Koudis, and M. E. J. Stettler (2022b). “Targeted Use of Sustainable Aviation Fuel to Maximize Climate Benefits”. In: *Environmental Science and Technology* 56.23, pp. 17246–17255. DOI: 10.1021/acs.est.2c05781.
- Timko, M. T., E. Fortner, J. Franklin, Z. Yu, H. W. Wong, T. B. Onasch, R. C. Miake-Lye, and S. C. Herndon (Mar. 2013). “Atmospheric Measurements of the Physical Evolution of Aircraft Exhaust Plumes”. In: *Environmental Science and Technology* 47.7, pp. 3513–3520. ISSN: 1520-5851. DOI: 10.1021/es304349c.
- Timko, M. T., Z. Yu, T. B. Onasch, H.-W. Wong, R. C. Miake-Lye, A. J. Beyersdorf, B. E. Anderson, K. L. Thornhill, E. L. Winstead, E. Corporan, M. J. DeWitt, C. D. Klingshirn, C. Wey, K. Tacina, D. S. Liscinsky, R. Howard, and A. Bhargava (Nov. 2010a). “Particulate Emissions of Gas Turbine

- Engine Combustion of a Fischer-Tropsch Synthetic Fuel”. In: *Energy & Fuels* 24.11, pp. 5883–5896. ISSN: 1520-5029. DOI: 10.1021/ef100727t.
- Timko, M. T., T. B. Onasch, M. J. Northway, J. T. Jayne, M. R. Canagaratna, S. C. Herndon, E. C. Wood, R. C. Miake-Lye, and W. B. Knighton (2010b). “Gas Turbine Engine Emissions—Part II: Chemical Properties of Particulate Matter”. In: *Journal of Engineering for Gas Turbines and Power* 132.6, p. 061505. DOI: 10.1115/1.4000132.
- TSI Incorporated (2012). *Aerosol Statistics, Lognormal Distributions, and dN/dlogDp*. Last accessed: 12 Sept. 2024. URL: https://www.tsi.com/getmedia/1621329b-f410-4dce-992b-e21e1584481a/PR-001-RevA_Aerosol-Statistics-AppNote?ext=.pdf.
- Ungeheuer, F., L. Caudillo, F. Ditas, M. Simon, D. van Pinxteren, D. Kılıç, D. Rose, S. Jacobi, A. Kürten, J. Curtius, and A. L. Vogel (2022). “Nucleation of jet engine oil vapours is a large source of aviation-related ultrafine particles”. In: *Communications Earth & Environment* 3.319. DOI: 10.1038/s43247-022-00653-w.
- United Nations, U. (2015). “Adoption of the Paris Agreement”. In: *Conference of the Parties, Twenty-first session Paris, 30 November to 11 December 2015*. FCCC/CP/2015/L.9/Rev.1.
- Unterstrasser, S. (2014). “Large-eddy simulation study of contrail microphysics and geometry during the vortex phase and consequences on contrail-to-cirrus transition”. In: *Journal of Geophysical Research: Atmospheres* 119.12, pp. 7537–7555. DOI: 10.1002/2013JD021418.
- Unterstrasser, S. and K. Gierens (2010a). “Numerical simulations of contrail-to-cirrus transition – Part 2: Impact of initial ice crystal number, radiation, stratification, secondary nucleation and layer depth”. In: *Atmospheric Chemistry and Physics* 10.4, pp. 2037–2051. DOI: 10.5194/acp-10-2037-2010.
- (Feb. 2010b). “Numerical simulations of contrail-to-cirrus transition – Part 1: An extensive parametric study”. In: *Atmospheric Chemistry and Physics* 10.4, pp. 2017–2036. ISSN: 1680-7324. DOI: 10.5194/acp-10-2017-2010.
- Urban, M. C. (May 2015). “Accelerating extinction risk from climate change”. In: *Science* 348.6234, pp. 571–573. ISSN: 1095-9203. DOI: 10.1126/science.aaa4984.
- Urbanek, B., S. Groß, M. Wirth, C. Rolf, M. Krämer, and C. Voigt (Dec. 2018). “High Depolarization Ratios of Naturally Occurring Cirrus Clouds Near Air Traffic Regions Over Europe”. In: *Geophysical Research Letters* 45.23. ISSN: 1944-8007. DOI: 10.1029/2018GL079345.
- U.S. Department of Energy, U.S. Department of Transportation, U.S. Department of Agriculture, and U.S. Environmental Protection Agency (2022). *SAF Grand Challenge Roadmap*. Tech. rep. Last accessed: August 09, 2024. URL: <https://www.energy.gov/sites/default/files/2022-09/beto-saf-gc-roadmap-report-sept-2022.pdf>.
- Vasilatou, K., K. Dirscherl, K. Iida, H. Sakurai, S. Horender, and K. Auderset (Feb. 2020). “Calibration of optical particle counters: first comprehensive inter-comparison for particle sizes up to 5 μm and number concentrations up to 2 cm^{-3} ”. In: *Metrologia* 57.2, p. 025005. ISSN: 1681-7575. DOI: 10.1088/1681-7575/ab5c84.

- Vázquez-Navarro, M., H. Mannstein, and S. Kox (2015). “Contrail life cycle and properties from 1 year of MSG/SEVIRI rapid-scan images”. In: *Atmospheric Chemistry and Physics* 15.15, pp. 8739–8749. DOI: 10.5194/acp-15-8739-2015.
- Virent (2024). *Sustainable Aviation Fuel (SAF)*. Last accessed: August 07, 2024. URL: <https://www.virent.com/products/sustainable-aviation-fuel/>.
- Voigt, C., U. Schumann, P. Jessberger, T. Jurkat, A. Petzold, J.-F. Gayet, M. Krämer, T. Thornberry, and D. W. Fahey (2011). “Extinction and optical depth of contrails”. In: *Geophysical Research Letters* 38.11. DOI: 10.1029/2011GL047189.
- Voigt, C., U. Schumann, T. Jurkat, D. Schäuble, H. Schlager, A. Petzold, J.-F. Gayet, M. Krämer, J. Schneider, S. Borrmann, J. Schmale, P. Jessberger, T. Hamburger, M. Lichtenstern, M. Scheibe, C. Gourbeyre, J. Meyer, M. Kübbeler, W. Frey, H. Kalesse, T. Butler, M. G. Lawrence, F. Holzäpfel, F. Arnold, M. Wendisch, A. Döpelheuer, K. Gottschaldt, R. Baumann, M. Zöger, I. Sölch, M. Rautenhaus, and A. Dörnbrack (2010). “In-situ observations of young contrails – overview and selected results from the CONCERT campaign”. In: *Atmospheric Chemistry and Physics* 10.18, pp. 9039–9056. DOI: 10.5194/acp-10-9039-2010.
- Voigt, C., J. Kleine, D. Sauer, R. H. Moore, T. Bräuer, P. L. Clercq, S. Kaufmann, M. Scheibe, T. Jurkat-Witschas, M. Aigner, U. Bauder, Y. Boose, S. Borrmann, E. Crosbie, G. S. Diskin, J. DiGangi, V. Hahn, C. Heckl, F. Huber, J. B. Nowak, M. Rapp, B. Rauch, C. Robinson, T. Schripp, M. Shook, E. Winstead, L. Ziemba, H. Schlager, and B. E. Anderson (2021). “Cleaner burning aviation fuels can reduce contrail cloudiness”. In: *Communications Earth & Environment* 2.114. DOI: 10.1038/s43247-021-00174-y.
- Voigt, C., R. Maerkl, and D. Sauer (2023a). *Dataset #9662, Version v1*. HALO database [data set]. DOI: 10.17616/R39Q0T. URL: <https://halo-db.pa.op.dlr.de/dataset/9662>.
- Voigt, C., R. Maerkl, D. Sauer, T. Harlass, S. Kaufmann, A. Roiger, R. Dischl, and A. Giez (2023b). *Dataset #9661, Version v1*. HALO database [data set]. DOI: 10.17616/R39Q0T. URL: <https://halo-db.pa.op.dlr.de/dataset/9661>.
- Voigt, C., U. Schumann, A. Minikin, A. Abdelmonem, A. Afchine, S. Borrmann, M. Boettcher, B. Buchholz, L. Bugliaro, A. Costa, J. Curtius, M. Dollner, A. Dörnbrack, V. Dreiling, V. Ebert, A. Ehrlich, A. Fix, L. Forster, F. Frank, D. Fütterer, A. Giez, K. Graf, J.-U. Grooß, S. Grooß, K. Heimerl, B. Heinold, T. Hüneke, E. Järvinen, T. Jurkat, S. Kaufmann, M. Kenntner, M. Klingebiel, T. Klimach, R. Kohl, M. Krämer, T. C. Krisna, A. Luebke, B. Mayer, S. Mertes, S. Molleker, et al. (2017). “ML-CIRRUS: The Airborne Experiment on Natural Cirrus and Contrail Cirrus with the High-Altitude Long-Range Research Aircraft HALO”. In: *Bulletin of the American Meteorological Society* 98.2, pp. 271–288. DOI: 10.1175/BAMS-D-15-00213.1.
- Wallace, J. M. and P. V. Hobbs (2006). “Cloud Microphysics”. In: *Atmospheric Science: an introductory survey*. Ed. by R. Dmowska, D. Hartmann, and H. T. Rossby. 2nd ed. Vol. 92. International Geophysics Series. Elsevier. Chap. 6, pp. 209–269. ISBN: 978-0-12-732951-2.
- Wang, Z., L. Bugliaro, T. Jurkat-Witschas, R. Heller, U. Burkhardt, H. Ziereis, G. Dekoutsidis, M. Wirth, S. Grooß, S. Kirschler, S. Kaufmann, and C. Voigt (2023). “Observations of microphysical

- properties and radiative effects of a contrail cirrus outbreak over the North Atlantic”. In: *Atmospheric Chemistry and Physics* 23.3, pp. 1941–1961. DOI: 10.5194/acp-23-1941-2023.
- Wendisch, M. and P. Yang (2012). “Interactions of EM Radiation and Individual Particles”. In: *Theory of Atmospheric Radiative Transfer: A Comprehensive Introduction*. John Wiley & Sons. Chap. 4, pp. 59–132. ISBN: 978-3-527-40836-8.
- Wild, M., D. Folini, M. Z. Hakuba, C. Schär, S. I. Seneviratne, S. Kato, D. Rutan, C. Ammann, E. F. Wood, and G. König-Langlo (Dec. 2015). “The energy balance over land and oceans: an assessment based on direct observations and CMIP5 climate models”. In: *Climate Dynamics* 44.11–12, pp. 3393–3429. ISSN: 1432-0894. DOI: 10.1007/s00382-014-2430-z.
- Wiscombe, W. J. (May 1980). “Improved Mie scattering algorithms”. In: *Applied Optics* 19.9, p. 1505. ISSN: 1539-4522. DOI: 10.1364/AO.19.001505.
- Wong, H.-W. and R. C. Miake-Lye (2010). “Parametric studies of contrail ice particle formation in jet regime using microphysical parcel modeling”. In: *Atmospheric Chemistry and Physics* 10.7, pp. 3261–3272. DOI: 10.5194/acp-10-3261-2010.
- Ying, S. X. (2022). “Electric Aircraft”. In: *Innovation for a green transition, 2022 environmental report*. ICAO. Chap. Chapter five: Climate Change Mitigation: Aircraft Technologies, pp. 120–123.
- Yu, F., B. Kärcher, and B. E. Anderson (Sept. 2024). “Revisiting Contrail Ice Formation: Impact of Primary Soot Particle Sizes and Contribution of Volatile Particles”. In: *Environmental Science & Technology*. ISSN: 1520-5851. DOI: 10.1021/acs.est.4c04340.
- Yu, F. and R. P. Turco (Aug. 1997). “The role of ions in the formation and evolution of particles in aircraft plumes”. In: *Geophysical Research Letters* 24.15, pp. 1927–1930. ISSN: 1944-8007. DOI: 10.1029/97GL01822.
- Yu, Z., M. T. Timko, S. C. Herndon, C. Miake-Lye Richard, A. J. Beyersdorf, L. D. Ziemba, E. L. Winstead, and B. E. Anderson (Dec. 2019). “Mode-specific, semi-volatile chemical composition of particulate matter emissions from a commercial gas turbine aircraft engine”. In: *Atmospheric Environment* 218, p. 116974. ISSN: 1352-2310. DOI: 10.1016/j.atmosenv.2019.116974.
- Ziereis, H., P. Hoor, J.-U. Grooß, A. Zahn, G. Stratmann, P. Stock, M. Lichtenstern, J. Krause, V. Bense, A. Afchine, C. Rolf, W. Woiwode, M. Braun, J. Ungermann, A. Marsing, C. Voigt, A. Engel, B.-M. Sinnhuber, and H. Oelhaf (2022). “Redistribution of total reactive nitrogen in the lowermost Arctic stratosphere during the cold winter 2015/2016”. In: *Atmospheric Chemistry and Physics* 22.5, pp. 3631–3654. DOI: 10.5194/acp-22-3631-2022.

Abbreviations and Symbols

Acronyms

1D	one-dimensional
2D	two-dimensional
AC	alternating current
ACCESS	Alternative Fuel Effects on Contrails and Cruise Emissions Study
ADC	analog-to-digital counts
ADS-B	Automatic Dependent Surveillance–Broadcast
AEI	Apparent Ice Emission Index
AIMS	Airborne Mass Spectrometer
AR	aspect ratio
ASTM	American Society for Testing and Materials
ATC	air traffic control
ATM	air traffic management
ATRA	Advanced Technology Research Aircraft
BS	borosilicate
CAPS-DPOL	Cloud, Aerosol, and Precipitation Spectrometer with Depolarization
CAS	Cloud and Aerosol Spectrometer
CAS-DPOL	Cloud and Aerosol Spectrometer with Depolarization

CFD	computational fluid dynamics
CIC	Cluster Ion Counter
CIP	Cloud Imaging Probe
CLD	chemiluminescence detector
CoCiP	Contrail Cirrus Prediction Tool
CONCERT	CONtrail and Cirrus ExpeRimenT
CORSIA	Carbon Offsetting and Reduction Scheme for International Aviation
CPC	condensation particle counter
CRDS	Cavity Ring-Down Spectrometer
DAC	double annular combustor
DC	direct current
DFS	Deutsche Flugsicherung
DLR	Deutsches Zentrum für Luft- und Raumfahrt / German Aerospace Center
dLUC	direct land use change
DMT	Droplet Measurement Technologies
DSHC	direct sugars to hydrocarbon
DWD	Deutscher Wetterdienst
ECLIF	Emission and Climate Impact of Alternative Fuels
ECMWF	European Centre for Medium-Range Weather Forecasts
EGTM	exhaust gas temperature margin

EI	Emission Index
ERF	effective radiative forcing
ETS	Emissions Trading Scheme
EU	European Union
FADEC	Full Authority Digital Engine Control
FCDP	Fast Cloud Droplet Probe
FFSSP	Fast Forward Scattering Spectrometer Probe
FSC	fuel sulfur content
FSSP	Forward Scattering Spectrometer Probe
FT	Fischer-Tropsch
FW	forward-facing
GCM	global climate model
GFS	Global Forecast System
GWP	Global Warming Potential
HALO	High Altitude and Long Range Research Aircraft
HEFA	hydrotreated esters and fatty acids
HGS	high gain stage
HT-fuel	custom-processed Jet A-1 fuel
IAE	International Aero Engines
ICAO	International Civil Aviation Organization

iLUC	indirect land use change
ILUC	induced land use change
IPA	Institute of Atmospheric Physics
IPT	inter-particle time
IWC	ice water content
LCA	life cycle assessment
LEC	Low-Emissions Combustor
LGS	low gain stage
LIDAR	light detection and ranging
LTO	Landing and Take Off Cycle
LUC	land use change
LWC	liquid water content
MGS	mid gain stage
MVD	median volume diameter
NAIS	Neutral Cluster - Air Ion Spectrometer
NASA	National Aeronautics and Space Administration
NCAR	National Center for Atmospheric Research
nvPM	nonvolatile particulate matter
OPC	optical particle counter
PADS	Particle Analysis and Display System

PAS	particle air speed
pbp	particle-by-particle
PDI	Phase Doppler Interferometer
PSD	particle size distribution
PSL	polystyrene latex
PtL	Power to Liquid
Q2	second quarter
Q4	fourth quarter
RQL	Rich-Quench-Lean
SAF	sustainable aviation fuel
SAS	sample air speed
SCS	scattering cross section
SHARC	Sophisticated Hygrometer for Atmospheric ResearCh
SIP	synthetic isoparaffins
SKA	Synthetic Kerosene with Aromatics
SL	soda-lime
SPECinc	Stratton Park Engineering
SPK	Synthetic Paraffinic Kerosene
STP	standard temperature and pressure
TAPS	Twin Annular Premixing Swirler

- TAS true air speed
- TD thermodenuder
- TOA top of the atmosphere
- UAP ultrafine aqueous particles
- UHC unburned hydrocarbons
- VOLCAN VOL avec Carburants Alternatifs Nouveaux
- vPM volatile particulate matter
- WGS84 World Geodetic System 1984

Symbols

- CO_{2e} CO₂ equivalent emissions
- Δz delta of detection altitude to emission altitude
- ΔT_{SA} delta to Schmidt-Appleman threshold temperature
- P_{amb} ambient pressure
- RHi relative humidity over ice
- T_{SA} Schmidt-Appleman threshold temperature
- T_{amb} ambient temperature
- T30 combustor inlet temperature
- U relative humidity over liquid water

List of Figures

1.1	Contrail net radiative forcing	2
1.2	Contrail ice crystal numbers depending on number of emitted soot particles	5
2.1	T_{SA} determination	10
2.2	Contrail formation stages	13
2.3	GWP time horizon comparison	17
2.4	RF increase 2006 to 2050	18
2.5	ECLIF 1 and 2 emission indices and size distributions	19
2.6	Main constituents of jet fuel	21
2.7	Radiative forcing and particle reduction	24
2.8	SAF blending ratio effect	24
2.9	Schematic of RQL combustor	27
2.10	Schematic of lean-burn combustor in rich-burn mode	29
2.11	Schematic of lean-burn combustor in lean-burn mode	30
3.1	Scattering cross section depending on particle size for water	34
3.2	Scattering cross section depending on particle size for ice	36
3.3	Mie scattering polar plots	38
3.4	Front view of CAPS-DPOL instrument	39
3.5	Top view and beam paths of CAS instrument	40
3.6	Calibration data processing steps	46
3.7	CAPS-DPOL calibration ADC	49
3.8	CAPS-DPOL VOLCAN2 transfer functions	50
3.9	Particle size distribution resolved and average	52
3.10	CAS-DPOL vs CAPS-DPOL matching and non-matching	54
3.11	CAS-DPOL vs. CAPS-DPOL ECLIF3 and VOLCAN1 + 2	56
3.12	Aerosol inlet	58
3.13	DLR Falcon	63
4.1	IPT analysis	71
4.2	VOLCAN2 ambient conditions vs. delta to Schmidt-Appleman temperature	79
4.3	VOLCAN2 domains for ambient pressure and temperature	80
4.4	VOLCAN2 domain 6.3 RH _i vs ΔT_{SA}	81
4.5	VOLCAN2 P-T Domain 6.3 Overview	82
4.6	VOLCAN2 domain 6.3 binning normalization example	83
4.7	Normalization reference example	84
4.8	Domain 6.3 normalized AEI and aerosol EI	86
5.1	ECLIF3 aircraft photos	90
5.2	ECLIF3 far-field flight paths	91
5.3	ECLIF3 ambient conditions vs. delta to Schmidt-Appleman temperature	93
5.4	ECLIF3 flight 04 time series	95
5.5	ECLIF3 AEI vs soot EI and fuel properties	100
5.6	AEI vs soot EI for ECLIF campaigns	102
5.7	AEI vs fuel properties for ECLIF campaigns	103

5.8	Jet A-1 PSDs Δz resolved from ECLIF3	106
5.9	Jet A-1 normalized number concentrations Δz resolved from ECLIF3	107
6.1	VOLCAN source aircraft	112
6.2	VOLCAN1 far-field flight paths	113
6.3	VOLCAN2 far-field flight paths	116
6.4	Contrail flight F16 timeline	118
6.5	VOLCAN1 + 2 near-field nvPM and far-field contrail comparison rich-lean	120
6.6	VOLCAN1 + 2 near-field totals and far-field contrail comparison rich-lean	121
6.7	VOLCAN2 domain 4.4 PSDs	126
6.8	VOLCAN2 domain 4.4 PSDs without cirrus	128
6.9	VOLCAN2 fuel differences	131
6.10	VOLCAN2 AEI dependence on delta to Schmidt-Appleman temperature	135
6.11	VOLCAN2 AEI dependence on ambient conditions rich-burn	136
6.12	VOLCAN2 AEI dependence on ambient conditions lean-burn	137
6.13	Warm contrail flight F21 timeline	139
6.14	Warm contrail AEI vs temperatures	140
6.15	Warm contrail AEI vs ice-co2 correlation	141
6.16	VOLCAN2 engine comparison aerosol near-field	143
6.17	VOLCAN2 engine comparison photos	144
6.18	VOLCAN2 far-field contrail ice to aerosol comparison rich-lean	148
6.19	VOLCAN2 near-field to far-field comparison	150
6.20	VOLCAN2 domain 6.3 ratios of AEI and aerosol EI	152
7.1	VOLCAN and ECLIF campaign comparison	160
A1	VOLCAN2 contrail ice to near-field aerosol comparison rich-lean	172
A2	VOLCAN1 contrail ice to near-field aerosol comparison rich-lean	173
A3	VOLCAN1 contrail ice to far-field aerosol comparison rich-lean	174
A4	VOLCAN2 near-field to far-field comparison	175
A5	VOLCAN2 AEI vs RHi lean-burn full range	175
A6	VOLCAN2 P-T Domain 6.3 PSDs ΔT_{SA} resolved	176
A8	VOLCAN2 P-T Domain 6.3 HEFA to Jet A-1 comparison lean	176
A7	VOLCAN2 P-T Domain 6.3 PSDs RHi resolved	177
A9	VOLCAN2 P-T Domain 7.5 SPK High to Jet A-1 comparison rich	177
A10	Ice particle to near-field aerosol ratios for domain 7.5	178
A11	VOLCAN1 domains for ambient pressure and temperature	178
A12	VOLCAN2 P-T Domain 2.2 ambient conditions	179
A13	VOLCAN2 AEI vs. nvPM EI by RHi and ΔT_{SA} color coded	180
A14	VOLCAN2 AEI vs. total particle EI by RHi and ΔT_{SA} color coded	181
B1	Sensitivity of T_{SA} on ambient conditions	183
C1	CAS-DPOL mid gain stage adjustment effect	185
C2	Particle size distribution processing	188
C3	CAS-DPOL vs. CAPS-DPOL VOLCAN2	189

List of Tables

3.1	CAS-DPOL transfer function parameters	48
3.2	CAPS-DPOL transfer function parameters	50
4.1	Median AEI uncertainties during investigated campaigns.	77
5.1	ECLIF3 far-field flights	91
5.2	Fuel properties ECLIF3	92
5.3	Contrail measurement conditions for flight 04 in ECLIF3	97
5.4	ECLIF3 AEI and nvPM EI medians and means	103
6.1	VOLCAN1 far-field flights	113
6.2	Fuel properties VOLCAN1	114
6.3	VOLCAN2 far-field flights	115
6.4	Fuel properties VOLCAN2	117
6.5	VOLCAN2 and VOLCAN1 domain-based combustion mode comparisons	124
6.6	VOLCAN2 and VOLCAN1 domain-based fuel comparisons	130
A1	VOLCAN2 domain overview	171
C1	CAS-DPOL binnings	186
C2	CAPS-DPOL binnings	187

Acknowledgments

An experimental work based on flight campaigns is a complex project that could never be done alone in an office. Many people have supported me with my work or even made it possible. I owe many thanks to all of them and especially to the following:

Prof. Dr. Christiane Voigt for making this dissertation possible by accepting me as a doctoral candidate in the DLR Cloud Physics department. I learned a lot from the many discussions and academic guidance she provided over the years and of course could never have conducted these analyses without her organization and leadership during the campaigns. The experiences I had during campaigns, conferences, and the daily work in the laboratory and the office are unforgettable and I am very grateful to have had this opportunity.

Prof. Dr. Stephan Borrmann for acting as reviewer of this dissertation.

Prof. Dr. Markus Rapp for making it possible to work with excellent people and state of the art equipment at the DLR Institute of Atmospheric Physics and for providing the rare opportunity to work on aircraft flight campaigns.

Dr. Daniel Sauer and Rebecca Dischl performed the aerosol measurements and provided data, analyses and all necessary information to be able to interpret the relations between aerosols and contrail ice particles encountered during the flight campaigns. We had many fruitful discussions which often required lots of patience and a combined effort to obtain our goals but at the same time were always friendly, professional, and productive.

Dr. Stefan Kaufmann, Dr. Andreas Marsing, and Dr. Laura Tomsche for performing the water vapor measurements and providing this very critical data for the analysis of contrail ice data.

Dr. Theresa Harlaß for performing the trace gas measurements and processing and providing this data that is essential to calculating apparent ice emission indices.

Valerian Hahn for patiently introducing me to all the technical aspects of the ice particle instrumentation as well as data analysis and always taking time for troubleshooting and discussions.

Dr. Tiziana Bräuer for performing trace gas measurements as well as supporting ice particle measurements during the campaigns. We also discussed many scientific and non-scientific topics, data analysis and working with her was always productive and fun.

Dr. Tina Jurkat-Witschas, Elena De La Torre Castro, Dr. Simon Kirschler, and Dr. Manuel Moser

for troubleshooting work on the instruments, many discussions on data analysis and the physics behind our measurements as well as for campaign preparation.

Dr. Johanna Mayer for being an amazing office partner and lots of shared snacks, coffee, plant maintenance and funny moments.

Monika Scheibe for her engineering expertise and patient and friendly way in dealing with technical problems in the lab and during campaigns.

Jonas Schmidt for defining contrail times of several VOLCAN flights and conducting first analyses of rich-burn fuel effects.

Natalie Keur for the great support in all administrative questions.

Prof. Dr. Ulrich Schumann for performing CoCiP calculations based on the ECLIF3 data and collaboration for the resulting publication as well as honest and very productive discussions.

Dr. Ulrike Burkhardt und Cornelius Weiß-Rehm for global climate model calculations based on the ECLIF3 data and collaboration for the resulting publication.

The DLR flight department for maintaining and flying the Falcon research aircraft and especially Georg Dietz for all the logistics, organization, and planning of flight campaigns.

The industry partners involved in the ECLIF3 and VOLCAN campaigns. Airbus and especially Charles Renard, Katharina Seeliger, Maxime Gauthier, Ashog Kulathasan, Emiliano Requena-Esteban, and Frederic Gass for letting us chase their aircraft as well as for the great campaign preparation, organization and many scientific discussions. Rolls-Royce and especially Peter Swann, Paul Madden and Darren Luff for providing engine data for the Trent XWB-84 during the ECLIF3 campaign and the performed prediction calculations as well as for great scientific input. Neste and especially Reetu Sallinen for providing the HEFA fuel and corresponding data during the ECLIF3 campaign. CFM and especially Emmanuel Greslin for providing engine data on the LEAP-1A engine during the VOLCAN campaign.

All other colleagues of the DLR clouds physics department and the atmospheric trace species department who were a pleasure to work with on a professional and on a human level.

Finally, my family for supporting me from the beginning and always being there for me. My friends for all the sports, games, trips, meals, laughs and fun in my life. Amanda for being there through all ups and downs and being my main moral support since long before this doctoral work.

Curriculum Vitae

Personal details

Raphael Satoru Maerkl
Born on February 19, 1994 in Munich, Germany

School Education

2004 - 2012 Gymnasium Tutzing
Abitur (German grade average: 1.2), June 2012

University Education

10/2012 - 02/2016 B.Sc. in Physics (German grade average: 1.95)
Ludwig Maximilian University of Munich

08/2017 - 01/2018 ERASMUS grant supported studies
Instituto Superior Técnico, Lisbon, Portugal

10/2016 - 05/2019 M.Sc. in Applied and Engineering Physics (German grade average:
1.4)
Technical University of Munich

Doctoral Studies

since 06/2020 Doctoral candidate
Johannes Gutenberg University Mainz and the Cloud Physics department of the Institute of Atmospheric Physics, Deutsches Zentrum für Luft- und Raumfahrt (DLR), Weßling, under supervision of Prof. Dr. Christiane Voigt

Work Experience

01/2015 - 01/2019 Technical translator for European patent applications
Self-employed, based in Munich, Germany

10/2019 - 04/2020 Junior Associate
Strategy consulting firm Munich Strategy GmbH & Co. KG